



THE UNIVERSITY  
*of* ADELAIDE

SOOT EVOLUTION IN  
ACOUSTICALLY FORCED  
LAMINAR NON-PREMIXED JET  
FLAMES

KAE KEN FOO

School of Mechanical Engineering  
The University of Adelaide  
South Australia 5005  
Australia

*Thesis submitted for the degree of Ph. D. on 24/8/2018.*

[This page is intentionally left blank]

**Ph. D. Thesis**

January 7, 2019

School of Mechanical Engineering  
The University of Adelaide  
South Australia 5005  
Australia

Typeset by the author using L<sup>A</sup>T<sub>E</sub>X.  
Printed in Australia.

Copyright © 2019 Kae Ken Foo, and The University of Adelaide,  
Australia.

*All right reserved. No part of this report may be used or reproduced in  
any form or by any means, or stored in a database or retrieval system  
without prior written permission of the university except in the case of  
brief quotations embodied in critical articles and reviews.*

[This page is intentionally left blank]

*To my wife Shufang Tang  
and my son Zeno.*

[This page is intentionally left blank]

# Declarations

I certify that this work contains no material which has been accepted for the award of any other degree or diploma in my name, in any university or other tertiary institution and, to the best of my knowledge and belief, contains no material previously published or written by another person, except where due reference has been made in the text. In addition, I certify that no part of this work will, in the future, be used in a submission in my name, for any other degree or diploma in any university or other tertiary institution without the prior approval of the University of Adelaide and where applicable, any partner institution responsible for the joint-award of this degree.

I acknowledge that copyright of published works contained within this thesis resides with the copyright holder(s) of those works.

I also give permission for the digital version of my thesis to be made available on the web, via the University's digital research repository, the Library Search and also through web search engines, unless permission has been granted by the University to restrict access for a period of time.

I acknowledge the support I have received for my research through the provision of an Australian Government Research Training Program Scholarship.

---

**Kae Ken Foo**

[This page is intentionally left blank]



# Acknowledgements

As a research student, I have as many doubts as there are stars in the sky, but there is one thing I have no doubt with, which is the fact that I could never have finished the thesis without the advice, guidance, support and contributions of many people. Foremost among them is, of course, my supervisors, Prof. Bassam Dally, Prof. Graham 'Gus' Nathan, Assoc. Prof. Paul Medwell and Assoc. Prof. Zeyad Alwahabi. Their inexhaustible passion for science and immovable insistence on improving the quality of my work have always motivated me to (and believe in myself that I can) become a better researcher. It has been a great pleasure working with them. I consider myself very fortunate to have this rare opportunity. For that, I am indebted to Assoc. Prof. Maziar Arjomandi who has successfully persuaded me to submit my application for a postgraduate program on the very last day. Also, he introduced me to Prof. Bassam Dally, who has later become my principal supervisor.

I want to thank Prof. Bassam Dally for his mentorship over the years. He has toughened me up and taught me how to be an independent researcher. I am also grateful to Prof. Graham Nathan, who has shown me the way of formulating problems scientifically and presenting ideas using precise terminology in well-structured writing. Additionally, I owe my gratitude to Assoc. Prof. Paul Medwell, who has made available his support in many ways, two of which are emotional and technical. While working with him, I have learned a variety of laboratory skills and the utmost importance of having a nicely structured bibliography. I am also thankful to Assoc. Prof. Zeyad Alwahabi for his valuable support in the area of laser diagnostic. Additionally, it is also necessary for me to thank Dr Zhiwei Sun, for his knowledge and expertise, which have proved invaluable in helping me produce experimental measurements.

I am also thankful that I got to share an office with Dr Eshodrar 'Esho' Sureshku-mar, Dr Houzhi Wang, Dr Amy Lewis and Dominic 'Dom' Davis, Francesco 'Frank' Larizza, Long Shen, Orddom Leav, David 'Dave' Haydon and Sammu-el 'Sam' Sobey. It was enlightening and intriguing to share our passion for A Song of Ice and Fire, AGC (anime, games and cartoons) and a long list of philosophical questions. I am also very happy that I got to know Dr Michael Evans, Dr Jingjing Ye, Dr Dahe Gu, Dr Alfonso Chinnici, Dr Chia Xiong Thong, Kimberley Kueh and many other friendly, helpful and intelligent people during my PhD. I would also like to acknowledge the support I have received from the staff at the school of Mechanical Engineering, particularly the workshop staff. It is impossible to thank all those people whom I have met. I apologise to those whom I missed in this acknowledgements.

I owe my deepest gratitude to my parents, Ah Hong Foo and Yoke Mui Hooi, and my brothers, Kae Shyan Foo and Kae Liang Foo for their encouragements. Above all, my newly formed family - my wife, Shufang Tang and our first-born child, Zinuo 'Zeno' Fu - without their unconditional love and endless support, I cannot imagine how I could have accomplished this.

# Abstract

With current concerns for sustainability, the ability to control pollutant emissions is a crucial factor in the design of modern combustion systems. Among pollutants of concern is soot, a type of particulate matter that is emitted from flames and fires due to incomplete hydrocarbon combustion. Interest in soot study spans a diverse range of combustion systems from simple laminar jet flames on a stove, to large-scale boilers and furnaces and complex aircraft turbine operating under high pressure. This thesis reports on work performed to advance understanding of soot evolution in a series of time-varying laminar non-premixed ethylene–nitrogen flames. Time-varying laminar flames offer diverse combinations of residence time, temperature histories, local stoichiometries and strain rates, that are inaccessible under steady conditions. These parameters are not only interdependent but also significantly influential to soot evolution. The thesis aims to provide a deeper understanding of interactions between flame chemistry, time-dependent flow field and soot evolution through a combined experimental and computational study. In the experiments, optical-based techniques are utilised to study the effects of acoustically induced flow modulations on the macroscopic aspects of time-varying laminar flames. The computational study focuses on the chemistry of soot evolution under unsteady combustion.

This thesis consists of a compilation of four journal articles, presenting results and findings from a combination of experimental and computational studies. The experiments examine three operating parameters, namely, the forcing frequency, the burner diameter and the fuel flow modulation. Various optical-based techniques were used, including Two-Line Atomic Fluorescence (TLAF), Laser-Induced Incandescence (LII), Time-Resolved LII (TiRe-LII), Planar Laser-Induced Fluorescence of OH (OH-PLIF) and Particle Imaging Velocimetry (PIV).

The experimental data set comprises simultaneous two-dimensional measurements of gas temperature, soot volume fraction, primary particle diameter and OH radical with a subsequent measurement of velocity field. All measurements, except OH-PLIF, are quantitative. Nevertheless, the qualitative measurement of OH serves as a reliable indicator for flame location. Furthermore, the experimental data spans a wide range of flame conditions, which is not only valuable for advancing current knowledge of soot evolution but also particularly useful for model development and validation.

The results reveal that the coupling between the flame structure and time-varying flow field is most effective at frequencies near to the flame natural flickering frequency, which is approximately 10 Hz for low-velocity flows, independent of

the burner diameter. The peak soot concentrations in 10-Hz time-varying flames are 120% larger than that measured in a steady flame burning with the same averaged fuel volumetric flow rate, whereas the enhancement for the 20- and 40-Hz time-varying laminar flames is only 87% and 10%, respectively. The same trend evident in the relative peak soot concentrations between steady and forced flames can be found in the primary soot particle diameter as well.

Under the same flow and forcing conditions (a frequency of 10 Hz at a 50% amplitude of fuel flow modulation), time-varying flames with different diameters of fuel nozzles (4.0, 5.6 and 8.0 mm inner diameters) exhibit different structures of the soot field. Time-varying flames with smaller burner diameters, 4.0 and 5.6 mm, exhibit a low-soot region on the centreline, encompassed by highly sooting region. In contrast, such a structure is not observed in the time-varying flame with an 8.0-mm-diameter burner. Consequently, the peak volume-integrated soot volume fraction in the time-varying flame with a 4.0-mm-diameter burner is 50% larger than that with an 8.0-mm-diameter burner.

The experimental study also examined the response of flame structure and the soot behaviour at different amplitudes of fuel flow modulation. The results show that the soot production increases as the amplitude of fuel flow modulation increases. This trend is found for amplitudes up to 50% where soot production is enhanced in these ethylene–nitrogen flames. However, further increasing the fuel flow modulation from 50% to 75% does not increase the soot production. On the contrary, the time-varying flame with a 75% fuel flow modulation exhibits a lower peak soot concentration compared with the 50% case.

A numerical study simulating the steady and time-varying flames with a 5.6-mm-diameter burner predicts the temperature, mixture fraction, species concentrations and kinetic rate of reaction as a function of the spatial coordinates and time. The computational results show that the prolonged ethylene pyrolysis in the neck of the time-varying laminar flame leads to the increase in the spatial extent of high acetylene concentration, which in turn contributes to the higher peak soot concentrations and larger maximum primary particle diameter measured in the time-varying flame relative to its steady counterpart. Furthermore, the residence time analysis shows that the soot growth rate in the early stages of time-varying flame is comparable or even slower than that in the steady equivalent. Additionally, in the later stages of the time-varying flame, the soot growth rate on the centreline is quicker than those in the annular region of the flame. The different combinations of time–temperature–mixture fraction histories not only help deepen understanding of soot evolution in unsteady combustion but also potentially useful to the development of soot models by serving as validation cases.

# Contents

<b>1</b>	<b>Introduction</b>	<b>1</b>
1.1	Background . . . . .	1
1.2	Overview of soot particles . . . . .	3
1.3	Soot particle studies . . . . .	4
1.4	Thesis outline . . . . .	6
<b>2</b>	<b>Background literature</b>	<b>9</b>
2.1	Mechanisms of soot formation and destruction . . . . .	9
2.2	Physical parameters affecting soot evolution . . . . .	13
2.3	Vortex–flame interactions . . . . .	18
2.4	Research gaps and aims . . . . .	25
<b>3</b>	<b>Methodology</b>	<b>37</b>
3.1	Co-flow burner . . . . .	37
3.2	Studied flame conditions . . . . .	40
3.3	Optical diagnostic techniques . . . . .	42
3.4	Time-Resolved Laser-Induced Incandescence . . . . .	44
3.5	Two-Line Atomic Fluorescence . . . . .	47
3.6	OH Planar Laser-Induced Fluorescence . . . . .	51
3.7	Particle Image Velocimetry . . . . .	54
3.8	CCD and ICCD cameras . . . . .	55
3.9	Image pre-processing . . . . .	56
3.10	Computational approach . . . . .	58
3.11	Summary . . . . .	60
<b>4</b>	<b>Experimental investigation of acoustic forcing on temperature, soot volume fraction and primary particle diameter in non-premixed laminar flames</b>	<b>65</b>
4.1	Introduction . . . . .	68
4.2	Experimental details . . . . .	71
4.3	Results . . . . .	75
4.4	Discussion . . . . .	98
4.5	Conclusions . . . . .	99
<b>5</b>	<b>Influence of nozzle diameter on soot evolution in acoustically forced laminar non-premixed flames</b>	<b>107</b>
5.1	Introduction . . . . .	110
5.2	Experimental details . . . . .	112
5.3	Results and discussion . . . . .	117
5.4	Conclusions . . . . .	132

<b>6</b>	<b>Soot evolution and flame response to acoustic forcing of laminar non-premixed jet flames at varying amplitudes</b>	<b>139</b>
6.1	Introduction	142
6.2	Experimental details	144
6.3	Results and discussion	148
6.4	Conclusions	176
<b>7</b>	<b>Calculated concentration distributions and time histories of key species in an acoustically forced laminar flame</b>	<b>183</b>
7.1	Introduction	186
7.2	Methodology	188
7.3	Results and discussion	192
7.4	Conclusions	216
<b>8</b>	<b>Conclusions and outlook</b>	<b>221</b>
8.1	Conclusions	221
8.2	Outlook	223
<b>A</b>	<b>List of publications</b>	<b>225</b>

## List of Figures

1.1	Global primary energy production by source, regenerated using data.	2
1.2	Picture of soot particles extracted from a diesel engine taken with a scanning electron microscope.	4
2.1	A conceptual schematic of soot evolution.	11
2.2	Soot yield versus temperature in acetylene pyrolysis.	14
2.3	Maximum soot volume fraction as a function of strain rate for different fuels: ethylene ( $C_2H_4$ ), propane ( $C_3H_8$ ), methane ( $CH_4$ ) and blended propane/methane ( $CH_4+C_3H_8$ ).	19
2.4	Full width at half maximum (FWHM) of axial soot volume fraction profiles for a propane-air counterflow non-premixed flame at various strain rates, presented as a function of the square root of strain rate.	19
2.5	Flame flickering frequency as a function of fuel jet velocity.	21
2.6	Relation between the Strouhal number and the inverse Froude number for a wide range of experimental studies involving flickering flames.	23
3.1	Cross-sectional diagram of the co-flow burner.	39

3.2	Experimental setup of burner and the simultaneous measurements of Laser-Induced Incandescence (LII), Time-Resolved LII (TiRe-LII), Non-Linear regime of Two-Line Atomic Fluorescence thermometry (NTLAF) and Planar Laser-Induced Fluorescence for hydroxyl radical (OH-PLIF). . . . .	42
3.3	Schematic diagram of the fluorescence processes for indium: Stokes and Anti-Stokes fluorescences. . . . .	47
3.4	Fluorescence versus irradiance for (a) Stokes and (b) anti-Stokes transitions. Solid line represents the curve fit. . . . .	50
3.5	Schematic of a laser ablation indium seeding system. . . . .	50
3.6	A simulation of LIF excitation spectra by LIFBASE (assumed a resolution of 0.01 nm, Gaussian line shape), showing the Q-branch transitions of the $A^2\Sigma^+(v' = 1) \leftarrow X^2\Pi_i(v'' = 0)$ OH band. The $Q_1(8)$ at 283.6 nm was used to excite OH. . . . .	53
3.7	Potential energy curves for the ground state ( $X^2\Pi_i$ ) and the first excitation state ( $A^2\Sigma^+$ ) of OH. The upward arrow represents the absorption of a photon near 283.6 nm, $A^2\Sigma^+(v' = 1) \leftarrow X^2\Pi_i(v'' = 0)$ , while the downward arrow represents the subsequent fluorescence emission near 308 nm. The internuclear separation is given in the unit of Bohr radius, $1 a_0 \approx 5.29 \times 10^{-11}$ m. . . . .	53
4.1	Amplitude of the perturbation to the axial component of the centreline velocity for the non-reacting flow, $\alpha = \frac{v_c - \bar{v}_c}{\bar{v}_c}$ , where $v_c$ is the centreline velocity measured at 2 mm above the burner using a constant temperature anemometer, and $\bar{v}_c$ is the time-averaged centreline velocity. The measured $v_c$ is presented together with the components of the fundamental and the first harmonic derived using a Fourier-transformation analysis. The average centreline velocities, $\bar{v}_c$ for (a) $St = 0.23$ and (b) $St = 0.46$ cases were both 0.7 m/s. . . . .	72
4.2	Planar pseudo-colour images (each at the same spatial scale) of the steady laminar non-premixed flames (32% ethylene diluted by nitrogen), with showing (a) gas temperature, $T_g$ measured with NTLAF; (b) soot volume fraction, $f_v$ measured with LII; (c) diameter of primary soot particles, $d_p$ measured with TiRe-LII. . . . .	77
4.3	Axial evolution of gas temperature along the centreline and soot volume fraction as a function of height above the burner ( $x/D$ ) for steady $C_2H_4$ /air flame with a fuel bulk exit velocity of 0.35 m/s. Current measured gas temperature and soot volume fraction results are compared with Connelly's soot temperature and two sets of soot volume fractions measured with LII and derived from pyrometry. For clarity, only every fifth measurement point is shown. . . . .	79

4.4	Planar images of (a) gas temperature, (b) soot volume fraction and (c) diameter of primary soot particles for flame with $St = 0.23$ at 50% modulation. The time interval between the panels is 5 ms, corresponding to phase angle of $36^\circ$ . Panels $\phi = 36^\circ$ , $252^\circ$ and $288^\circ$ are cropped because these regions exhibit poor SNR. . . . .	83
4.5	Temporal evolution of the distribution of $\text{OH}^*$ chemiluminescence for the flame with $St = 0.23$ . The phase angle difference between panels is $10^\circ$ , starts from $\phi = 288^\circ$ to $18^\circ$ . . . . .	85
4.6	Contours of (a) soot volume fraction and (b) diameter of primary particles superimposed onto the planar image of gas temperature for the flame with $St = 0.23$ at $\phi = 288^\circ$ . The soot volume fraction and diameter of primary soot particles are normalised by the maximum values, $f_{v,max} = 0.45$ ppm and $d_{p,max} = 73.6$ nm. . . . .	87
4.7	Planar images of (a) gas temperature, (b) soot volume fraction and (c) primary particles diameter for the flame with $St = 0.46$ at 50% modulation. The time interval between the panels is 2.5 ms, corresponding to phase angle of $36^\circ$ . Panels $\phi = 36^\circ$ and $180^\circ$ are cropped as these regions exhibit poor SNR. . . . .	89
4.8	Contours of (a) soot volume fraction and (b) diameter of primary particles superimposed onto the planar image of gas temperature for the flame with $St = 0.46$ at $\phi = 288^\circ$ . The soot volume fraction and diameter of primary soot particles are normalised by the maximum values, $f_{v,max} = 0.27$ ppm and $d_{p,max} = 56.4$ nm. . . . .	91
4.9	Distribution of gas temperature calculated from the three-dimensional revolution of corresponding images of gas temperature. It presents the fraction ( $n$ ) of the total flame volume ( $N$ ) that exhibits the temperatures range from 800-2000 K, with an increment of 50 K. The vertical lines correspond to the mean temperature for each flame. . . . .	92
4.10	The dependence of $d_p/d_{p,max}$ upon $f_v/f_{v,max}$ at selected HABs for the flames with (a) $St = 0.23$ ( $f_{v,max} = 0.45$ ppm and $d_{p,max} = 73.6$ nm), and (b) $St = 0.46$ ( $f_{v,max} = 0.27$ ppm and $d_{p,max} = 56.4$ nm) at $\phi = 288^\circ$ . These data are obtained only from the left hand side of the flame. . . . .	93
4.11	Temporal evolution of the volume-integrated soot volume fraction and maximum diameter of primary particles for the flames with $St = 0.23$ and $St = 0.46$ during one period. The solid lines indicate the volume-integrated soot volume fraction, and the dashed lines represent the maximum diameter of primary particles. . . . .	95
4.12	Growth rates of volume-integrated soot volume fraction at each phase for flame with $St = 0.23$ and $St = 0.46$ . . . . .	95



4.13	A comparison between the radial profiles of the gas temperature (solid lines), the soot volume fraction (dashed lines) and the diameter of primary particles (dotted lines) for (a, b, c) the flames with $St = 0.23$ (left half of the plots) , $St = 0.46$ (right half of the plots) and (d, e, f) the steady flame. The values of $f_{v,max}$ and $d_{p,max}$ for the flames are given in Table 4.1. . . . .	97
4.14	The dependence of $d_p/d_{p,max}$ upon $f_v/f_{v,max}$ at selected HABs for the flames with $St = 0.23$ (normalised to local maximum values) at $\phi = 288^\circ$ . These data are obtained only from the left hand side of the flame. . . . .	104
4.15	The dependence of $d_p/d_{p,max}$ upon $f_v/f_{v,max}$ at selected HABs for the flames with $St = 0.46$ (normalised to local maximum values) at $\phi = 288^\circ$ . These data are obtained only from the left hand side of the flame. . . . .	105
5.1	Schematic representation of the co-flow burner, including coordinate orientation and a typical axisymmetric toroidal vortex structure. . . .	113
5.2	Comparison of (a) soot interfered axial velocity field and (b) interpolated velocity field for the steady flame S-1 ( $D = 4.0$ mm). The axial velocities along the centreline for both cases are plotted in panel (c) for a better comparison. . . . .	116
5.3	Normalised power spectral density of the flame luminosity signals acquired for S-1 ( $D = 4.0$ mm), S-2 ( $D = 5.6$ mm) and S-3 ( $D = 8.0$ mm) at natural flickering mode without a co-flow. . . . .	117
5.4	Planar measurements of flame temperature for the steady flames S-1 ( $D = 4.0$ mm), S-2 ( $D = 5.6$ mm) and S-3 ( $D = 8.0$ mm) superimposed with isopleths of corresponding OH-PLIF marking the location of the reaction zones. Five images at different heights have been stacked together to constitute the full-field images presented here. . . . .	119
5.5	Velocity fields for the steady flames S-1 ( $D = 4.0$ mm), S-2 ( $D = 5.6$ mm) and S-3 ( $D = 8.0$ mm) superimposed with contours of soot volume fraction and diameter of primary soot particle on the left half and right half of the plots, respectively. . . . .	119
5.6	Planar measurements of gas temperature, $T_g$ , superimposed with the corresponding OH layer collected for the forced flames (a)F-1 with $D = 4.0$ mm, (b) F-2 with $D = 5.6$ mm and (c) F-3 with $D = 8.0$ mm. The flames are forced at 10 Hz 50% amplitude. The oscillation cycle is divided into eight phases with $45^\circ$ phase angle difference, equivalent to a time interval of 12.5 ms. . . . .	123

5.7	Contour of Galilean-transformed velocity magnitudes superimposed with the OH layer indicating the reaction zone and the planar measurements of soot volume fraction, $f_v$ (LHS), and diameter of primary soot particle, $d_p$ (RHS), collected for the forced flames (a) F-1 with $D = 4.0$ mm, (b) F-2 with $D = 5.6$ mm and (c) F-3 with $D = 8.0$ mm. In the velocity contour, the mean flow velocity ( $\bar{u} \sim 0.8$ m/s) is subtracted from all the velocity magnitudes. The black stripe at the top part of the plots represents no data as it is beyond the field of view of the PIV camera. . . . .	125
5.8	Contour of shear strain rate superimposed with vorticity fields presented in the form of streamlines derived from the Galilean-transformed velocity fields, the OH layer and the planar measurements of soot volume fraction, $f_v$ (LHS), and diameter of primary soot particle, $d_p$ (RHS), collected for the forced flames (a) F-1 with $D = 4.0$ mm, (b) F-2 with $D = 5.6$ mm and (c) F-3 with $D = 8.0$ mm. The black stripe at the top part of the plots represents no data as it is beyond the field of view of the PIV camera. . . . .	127
5.9	Temporal evolution of the volume-integrated soot volume fraction ( $f_{v,int}$ ) and the local maximum diameter of primary soot particle ( $d_{p,max}$ ) for steady (dashed lines) and forced flames, F-1 ( $D = 4.0$ mm), F-2 ( $D = 5.6$ mm) and F-3 ( $D = 8.0$ mm). . . . .	131
5.10	A fluid parcel traced along a streamline as a function of time ( $t$ ) in the Cartesian ( $r, x$ ) and streamline ( $s, n$ ) coordinate systems. . . . .	131
5.11	Measurements of soot volume fraction ( $f_v$ ), diameter of primary soot particle ( $d_p$ ) and flame temperature ( $T_g$ ) along the tracked fluid parcel pathlines as a function of the total residence time for the steady (dashed lines) and forced flames (open symbols). . . . .	133
6.1	Cross-sectional diagram of the co-flow burner, which is identical to that of Dworkin et al. . . . .	145
6.2	Isopleths of the residence time superimposed on the spatial distribution of soot volume fraction in pseudo-colour for laminar steady flames, from left to right, S-1 ( $D = 4.0$ mm), S-2 ( $D = 5.6$ mm) and S-3 ( $D = 8.0$ mm). For reference, the location of the OH-PLIF is plotted in purple. . . . .	149
6.3	Soot volume fractions along the centreline as a function of residence time. Filled markers represent the temperatures and diameters of primary particle corresponding to the maximum soot volume fraction. . . . .	151
6.4	Interdependence of the normalised soot volume fraction, $\hat{f}_v$ and primary particle diameter, $\hat{d}_p$ , and the temperature, $T_g$ , for the steady laminar flame S-1 ( $D = 4.0$ mm). . . . .	153
6.5	Interdependence of the normalised soot volume fraction, $\hat{f}_v$ and primary particle diameter, $\hat{d}_p$ , and the temperature, $T_g$ , for the steady laminar flame S-2 ( $D = 5.6$ mm). . . . .	155

6.6	Interdependence of the normalised soot volume fraction, $\hat{f}_v$ and primary particle diameter, $\hat{d}_p$ , and the temperature, $T_g$ , for the steady laminar flame S-3 ( $D = 8.0$ mm). . . . .	157
6.7	Bivariate correlation between the normalise soot volume fraction, $\hat{f}_v$ and primary particle diameter, $\hat{d}_p$ for the three steady flames (a) S-1 ( $D = 4.0$ mm), (b) S-2 ( $D = 5.6$ mm) and (c) S-3 ( $D = 8.0$ mm). The black solid line corresponds to an exponential function fitted from experimental data, $\hat{f}_v = a \cdot e^{n \cdot \hat{d}_p}$ , while the blue dashed lines represent the 99% confidence bounds. . . . .	159
6.8	Amplitudes of the centreline velocity, $\alpha = (U_{c,forced} - U_{c,steady}) / U_{c,steady}$ , measured with PIV technique under cold-flow condition at $x = 0.5$ mm as a function of phase angle, $\phi$ , for (a) 4.0-mm-diameter-burner, (b) 5.6-mm-diameter-burner and (c) 8.0-mm-diameter-burner. . . . .	161
6.9	Level of residence times superimposed on planar measurements of diameter of primary particle (LHS) and soot volume fraction (RHS) for the laminar flames with a 4.0-mm-diameter burner, F-4 and F-1, forced at $\alpha = 25$ and 50%, respectively. For reference, the location of the OH-PLIF is plotted in purple. . . . .	163
6.10	Level of residence times superimposed on planar measurements of diameter of primary particle (LHS) and soot volume fraction (RHS) for the laminar flames with a 5.6-mm-diameter burner, F-2 and F-5, forced at $\alpha = 50$ and 75%, respectively. For reference, the location of the OH-PLIF is plotted in purple. . . . .	165
6.11	Level of residence times superimposed on planar measurements of diameter of primary particle (LHS) and soot volume fraction (RHS) for the laminar flames with an 8.0-mm-diameter burner, F-6 and F-3, forced at $\alpha = 25$ and 50%, respectively. For reference, the location of the OH-PLIF is plotted in purple. . . . .	167
6.12	Volume-integrated soot volume fraction as a function of residence time measured for all six forced flames at various forcing amplitudes. . . . .	169
6.13	Galilean-transformed streamlines relative to the mean flow, superimposed on the soot volume fraction profiles for forced flames F-2 and F-5 ( $D = 5.6$ mm), at $\alpha = 50\%$ (upper) and 75% (lower) while both at $\tau = 62.5$ ms. Only the streamlines in the co-flow region are shown for clarity. Three arbitrary lines normal to the soot sheet are selected for each flame. Normalised quantities (soot volume fraction, $\hat{f}_v$ , diameter of primary particle, $\hat{d}_p$ , temperature, $T_g$ , and OH intensity, $\hat{I}_{OH}$ ) are plotted along the normal transects. . . . .	171
6.14	Interdependence of the normalised soot volume fraction, $\hat{f}_v$ and primary particle diameter, $\hat{d}_p$ , and the temperature, $T_g$ , for the forced flame F-2 ( $D = 5.6$ mm, $\alpha = 50\%$ ) at $\tau = 62.5$ ms. . . . .	172

6.15	Interdependence of the normalised soot volume fraction, $\hat{f}_v$ and primary particle diameter, $\hat{d}_p$ , and the temperature, $T_g$ , for the forced flame F-5 ( $D = 5.6$ mm, $\alpha = 75\%$ ) at $\tau = 62.5$ ms. . . . .	173
6.16	Bivariate correlation between normalised soot volume fraction and primary particle for six of the forced flames (a) F-1 ( $D = 4.0$ mm; $\alpha = 50\%$ ), (b) F-4 ( $D = 4.0$ mm; $\alpha = 25\%$ ), (c) F-2 ( $D = 5.6$ mm; $\alpha = 50\%$ ), (d) F-5 ( $D = 5.6$ mm; $\alpha = 75\%$ ), (e) F-3 ( $D = 8.0$ mm; $\alpha = 50\%$ ) and (f) F-6 ( $D = 8.0$ mm; $\alpha = 25\%$ ). The phase chosen is $\tau = 62.5$ ms. The black solid line corresponds to an exponential function fitted from experimental data, $\hat{f}_v = a \cdot e^{n \cdot \hat{d}_p}$ , while the blue dashed lines represent the 99% confidence bounds. . . . .	175
6.17	Soot volume fraction, $f_v$ , temperature, $T_g$ , and primary particle diameter, $d_p$ , are presented as functions of dimensionless axial coordinate ( $x/x_{T,max}$ , where $x_{T,max}$ is the location of the maximum $T_g$ ) for steady laminar flames with burner diameters, $D = 4.0, 5.6$ and $8.0$ mm. . . .	181
7.1	Cross-sectional diagram of the computational domain of the axisymmetric nozzle for steady and forced laminar flames simulations. Boundaries include inlets for fuel and co-flow (blue), no-slip wall (black), jet exit plane (purple), axis of symmetry (dark green) and opening (red). For the transient case, the temporal profile of the time-dependent fuel inlet velocity, $U(t)$ , is defined as a sum of sinusoids. . . . .	191
7.2	Comparisons between the planar cross-sections of the experimental (left) and numerical data (right) for the steady laminar $C_2H_4/N_2$ non-premixed flame: (a) normalised OH distribution, (b) velocity, $U$ , and (c) flame temperature, $T_g$ . The black dashed lines in (c) represent the radial location of peak values of $T_{g,E}$ and $T_{g,C}$ at all heights. . . . .	193
7.3	Comparisons between experimental (symbols) and computed (lines) axial profiles of temperature, $T_g$ , at the centreline. Additionally, the normalised computed number density of OH, $\hat{n}_{OH,C}$ , is compared with the normalised experimental OH-PLIF intensity, $\hat{I}_{OH,E}$ . For reference, the location of measured and computed normalised soot volume fraction, $\hat{f}_{v,E}$ and $\hat{f}_{v,C}$ , respectively, at the centreline is included. . . . .	195
7.4	Quantitative comparisons between the experimental (symbols) and numerical (lines) results: (a) the axial profiles of velocity, $U$ , on the axis (for clarity, only every tenth point is shown) and the radial profiles of the jet exit velocity probed at selected axial heights, $x =$ (b) $0.5$ mm, (c) $5$ mm and (d) $10$ mm. . . . .	197

7.5	Two-dimensional cross-sections for the steady laminar $C_2H_4/N_2$ non-premixed flame: (a) the measured and computed soot volume fraction, $f_{v,E}$ (left) and $f_{v,C}$ (right), respectively; (b) the calculated contours of mole fractions of ethylene, $X_{C_2H_4,C}$ (left) and acetylene, $X_{C_2H_2,C}$ (right). The isopleth of the stoichiometric mixture fraction, $Z_{stoic}$ , is presented in black and white colours in panels (a) and (b), respectively. The white dashed contour in (b) represents the location of the computed mole fraction of vinyl, $X_{C_2H_3,C}$ . . . . .	199
7.6	Pseudo-colour images of OH-PLIF with normalised intensity, $\hat{I}_{OH,E}$ (left), and the normalised computed number density of OH, $\hat{n}_{OH,C}$ (right), for the time-varying laminar $C_2H_4/N_2$ non-premixed flame in which the inlet fuel flow rate is varied with a 10-Hz sinusoidal wave with a 50% amplitude (defined as the ratio between the maximum jet exit velocity at the exit plane of the time-varying and steady laminar flames). The images are obtained at 12.5-ms intervals. . . . .	201
7.7	Pseudo-colour images of the measured temperature, $T_{g,E}$ (left), and the computed temperature, $T_{g,C}$ (right), for the time-varying laminar $C_2H_4/N_2$ non-premixed flame obtained at 12.5-ms intervals. Black dashed-lines represent the radial location of peak values of $T_{g,E}$ and $T_{g,C}$ at all heights. . . . .	201
7.8	Pseudo-colour images of computed mole fractions of ethylene, $X_{C_2H_4}$ (left), and acetylene, $X_{C_2H_2}$ (right), for the time-varying laminar $C_2H_4/N_2$ non-premixed flame for time-steps of 12.5 ms. The calculated isopleth of the stoichiometric mixture fraction, $Z_{stoic}$ , is presented in white solid lines. . . . .	203
7.9	Pseudo-colour images of computed net molar reaction rates of ethylene, $R_{C_2H_4,C}$ (left), and acetylene, $R_{C_2H_2,C}$ (right), for the time-varying laminar $C_2H_4/N_2$ non-premixed flame, also at 12.5-ms intervals. The calculated isopleth of the stoichiometric mixture fraction, $Z_{stoic}$ , is presented in black solid lines. . . . .	203
7.10	Pseudo-colour images of the computed kinetic rate of reaction of $C_2H_4+H\rightarrow C_2H_3+H_2$ (left) and $C_2H_3+H\rightarrow C_2H_2+H_2$ (right) for the time-varying laminar $C_2H_4/N_2$ non-premixed flame for time-steps of 12.5 ms. The calculated isopleth of the stoichiometric mixture fraction, $Z_{stoic}$ , is presented in black solid line. . . . .	205
7.11	Pseudo-colour images of computed strain rate, $S_{rx,C}$ (left), and heat release rate (right) for the time-varying laminar non-premixed flame at 12.5-ms intervals. the calculated isopleth of stoichiometric mixture fraction, $Z_{stoic}$ , is presented in white solid lines. . . . .	205

- 7.12 Images of the measured soot volume fraction,  $f_{v,E}$ , showing the position of the representative trajectories that were tracked throughout the flames, namely the height where soot is first detected in (a) the steady and (b) time-varying laminar flames at  $\phi = 0$  using the LII technique. The calculated isopleths of the stoichiometric mixture fraction,  $Z_{stoic} = 0.142$ , are presented in black solid lines. The red circular markers correspond to the locations where minimum soot volume fractions were first detected along the trajectories. . . . . 207
- 7.13 Calculated mixture fraction,  $Z$ , and mole fractions of ethylene,  $X_{C_2H_4,C}$ , vinyl,  $X_{C_2H_3,C}$ , acetylene,  $X_{C_2H_2,C}$ , carbon monoxide,  $X_{CO,C}$ , hydrogen atoms,  $X_{H,C}$ , and hydroxyl radicals,  $X_{OH,C}$ , as functions of dimensionless residence time,  $\hat{\tau}$  (normalised by the time particles require to reach the peak of  $X_{OH,C}$ ), along trajectories described in Fig. 7.12 for (a) the steady-state and (b) time-varying laminar flames. The vertical dotted lines represent the residence time required for the virtual inert particles released at the jet exit plane to reach the locations marked by the red circular markers in Fig. 7.12. . . . . 209
- 7.14 Images of the measured soot volume fraction,  $f_{v,E}$ , showing the position of the representative trajectories that were tracked throughout the flames, namely the maximum sooting region in (a) the steady and (b) time-varying laminar flames at  $\phi = 3\pi/2$  using the LII technique. The calculated isopleths of the stoichiometric mixture fraction,  $Z_{stoic} = 0.142$ , are presented in black solid lines. The red circular markers correspond to the locations of maximum soot volume fractions. 211
- 7.15 Calculated mixture fraction,  $Z$  and mole fractions of ethylene,  $X_{C_2H_4,C}$ , vinyl,  $X_{C_2H_3,C}$ , acetylene,  $X_{C_2H_2,C}$ , carbon monoxide,  $X_{CO,C}$ , hydrogen atoms,  $X_{H,C}$ , and hydroxyl radicals,  $X_{OH,C}$  as functions of a dimensionless residence time,  $\hat{\tau}$  (normalised by the time particles require to reach the peak of  $X_{OH,C}$ ), along trajectories described in Fig. 7.14 for (a) the steady-state and (b) time-varying laminar flames. The vertical dotted lines represent the residence time required for the virtual inert particles released at the jet exit plane to reach the locations marked by the red circular markers in Fig. 7.14. . . . . 213
- 7.16 Pseudo-colour contours for the computed strain rate,  $S_{rx,C}$  for the normal- (left) and zero-gravity (right) time-varying laminar non-premixed flames. The fuel flow modulation is determined by a 10-Hz sum-of-sinusoidal function with an amplitude of 50%. Red and white isopleths represent the locations of the maximum calculated number density of OH,  $n_{OH,C}$ , and the stoichiometric mixture fraction,  $Z_{stoic}$ . . . . . 215

7.17	Pseudo-colour contours for the computed strain rate, $S_{rx,C}$ for the normal- (left) and zero-gravity (right) time-varying laminar non-premixed flames. The fuel flow modulation is determined by a 10-Hz pure sinusoidal function with an amplitude of 50%. Red and white isopleths represent the locations of the maximum calculated number density of OH, $n_{OH,C}$ , and the stoichiometric mixture fraction, $Z_{stoic}$ . . . . .	215
------	--	-----

## List of Tables

3.1	Summary of test conditions for the steady and 10-Hz time-varying flames. . . . .	41
4.1	Summary of the soot properties measured in the steady and forced flames. . . . .	90
4.2	Summary of the flame properties measured in steady and forced flames. . . . .	98
5.1	Summary of test conditions . . . . .	113
6.1	Summary of test conditions . . . . .	145
6.2	Soot measurements in steady and forced flames of different burners at various forcing amplitudes . . . . .	168
7.1	Measurements reported with different kinds of time-varying laminar flames. . . . .	189
7.2	Key reactions that involved in the ethylene $\rightarrow$ vinyl $\rightarrow$ acetylene processes and key heat release reactions. . . . .	195

[This page is intentionally left blank]



# Chapter 1

## Introduction

The quest for achieving a comprehensive understanding of soot formation and oxidation stems from the critical role which soot plays in nearly all practical combustion devices that are fuelled by hydrocarbons. Interest in soot formation and oxidation spans a diverse spectrum of problems and can involve flow conditions as simple as a laboratory-scale laminar jet flame [1] or as complex as a gas turbine engine [2]. The development of advanced combustion technologies that produce low soot emission requires the knowledge of soot evolution in a wide range of conditions. The availability of robust and reliable computational soot models can help accelerate the progress of such developments. However, validation of numerical soot models requires experimental data sets that include measurements of multiple relevant parameters and cover a wide range of operational conditions. In this context, the present thesis contributes not only to the understanding of soot evolution but also to the development of soot models by providing a comprehensive experimental data set serving as validation cases.

### 1.1 Background

In 2017, the U.S. Energy Information Administration (EIA) released a report [3] presenting the assessment of global energy market and modelled projections of world's energy demand. Figure 1.1 presents the world energy production by source, based on statistics provided by EIA [3]. It suggests that almost 80% of global energy is supplied by burning fossil fuels, *i.e.* coal, natural gas, crude oil and natural gas liquids (NGLs). Despite the rapid growth of renewable energy and nuclear power, fossil fuels are predicted to continue to meet at least 70% of the world's energy demand until 2040. The growing consumption of fossil fuels is mainly driven by the economic growth in developing countries, particularly China and India [4]. These two countries are home to approximately 36% of the world's population [5] and are responsible for more than a quarter of the world's energy consumption [3].

The human-nature relationship is shaped, to a great extent, by our choice of energy generation technologies. Historically, our primary means of energy production has brought destructive impacts onto the natural environment, most notably the upward temperature trend observed across the entire Earth since

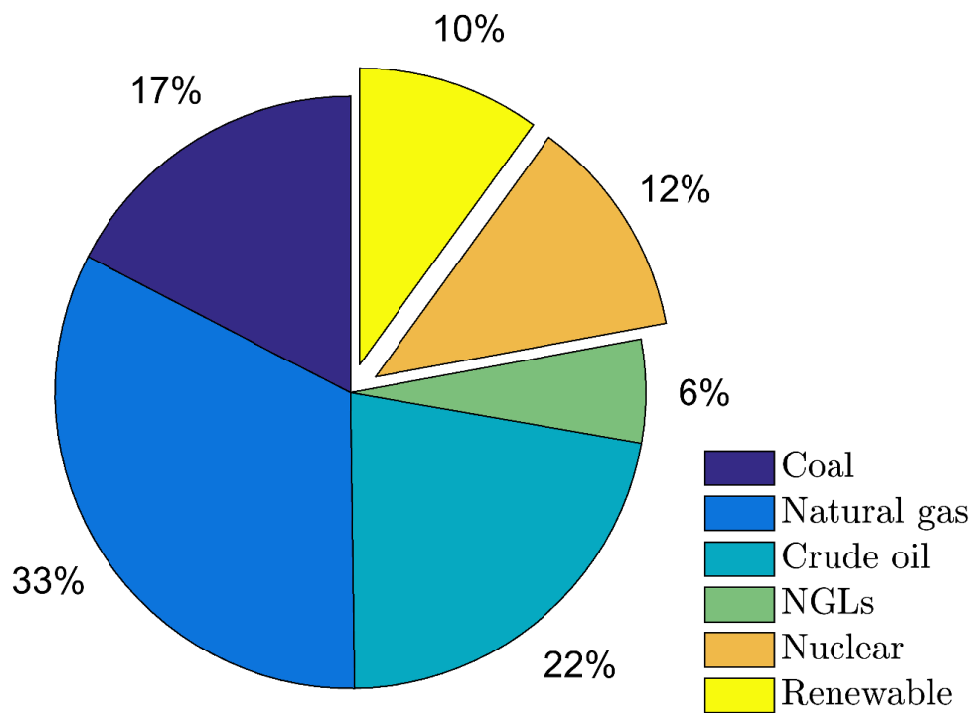


**Figure 1.1** Global primary energy production by source, regenerated using data provided by U.S. Energy Information Administration [3].

the industrial revolution, which took place from the 18th to 19th centuries [6, 7]. While anthropogenic global warming is mainly driven by emissions of a variety of greenhouse gases, which include carbon dioxide, methane, nitrous oxide, ozone, chlorofluorocarbons (CFCs) and hydrofluorocarbons (HFCs), particulate matter, such as soot, also plays a critical role in Earth’s climate system. A four-year study [8] suggests that the significance of soot in previous climate modelling analyses has been underestimated. In fact, soot is estimated to have a greater impact on the climate than that of methane [8], second only to the predominant climate forcer, carbon dioxide. Even though soot has a short atmospheric lifetime (from a few days to weeks) unlike the centuries-long atmospheric lifetime of carbon dioxide, reducing the soot emission has the potential to slow the climate change. The reason behind this is the wet removal of soot via snow and rain often leads to the soot deposition on glaciers or snowpack, which causes an albedo effect that accelerates melting [9].

Prior to the recognition of the crucial role played by the soot in Arctic melting, its emission was originally regulated to improve human health. A growing number of epidemiological studies [10–14] have reported evidence that supports the link between human exposure to soot and respiratory and cardiovascular diseases. The World Health Organization (WHO) estimated that fine particulate air pollution (PM<sub>2.5</sub>) of which soot is the major constituent, is responsible for ~3% of mortality from cardiopulmonary disease, ~5% of mortality from respiratory cancers, and ~1% of mortality from acute respiratory infections in children under-5 years,

globally [13]. Thus, a set of stringent regulations regarding the soot emission are highly desirable, regardless of whether those reductions actually have an effect on slowing climate change. For example, Australia has established national ambient air quality standards of which one of the goals is to reduce the 1-year and 24-hour maximum allowable concentrations of  $\text{PM}_{2.5}$  from  $8$  to  $7 \mu\text{g}/\text{m}^3$  and  $25$  to  $20 \mu\text{g}/\text{m}^3$ , respectively, by 2025 [15].

## 1.2 Overview of soot particles

Soot is a by-product of incomplete hydrocarbon combustion. Figure 1.2 shows an example of a scanning electron microscopy image of soot extracted from a diesel engine. Visible macroscopic soot flocculates are composed of fine primary particles, whose main constituents are carbon atoms, that aggregate to form irregularly shaped clusters [16]. Soot formation can take place in a huge variety of practical combustion systems, especially in systems associated with non-premixed flames. Within the flame environment, soot emits thermal radiation in a continuous spectrum over the visible and infra-red regions. While the ability to radiate is often considered as thermal efficiency loss in most practical combustion systems such as diesel engines and gas turbines, it is highly desirable in combustion devices that require efficient heat transfer from the flame, for instance, kilns, furnaces and boilers. Under these circumstances, the technical challenge is to produce soot particles in such a way that they can be oxidised before being released into the atmosphere.

Soot formation is a complex process involving the physical interaction between soot particles and fluid dynamics together with the chemistry of fuel pyrolysis under fuel-rich conditions where hundreds of aromatics are formed [17]. Even though the flame conditions may differ due to the configuration of the device and the type of fuel utilised, the processes of soot formation are rather similar. Most studies agree that the soot evolution can be qualitatively summarised into four stages: (1) particle inception; (2) surface growth and coalescence; (3) agglomeration and (4) soot oxidation. The time required for all these processes are typically on the order of a few milliseconds.

There is a non-linear relationship between the soot particle, gas-phase species, temperature and flow field [18]. These variables have influences on not only the rates of soot inception, growth and oxidation but also the spatial distribution of soot particles in flames. Therefore, in time-varying flames, simultaneous measurements of these quantities are essential for achieving a deeper understanding of the soot evolution in a comprehensive manner. In addition, existing soot models can be verified by the experimental data or new models can be developed based on the new theories derived from the dataset.

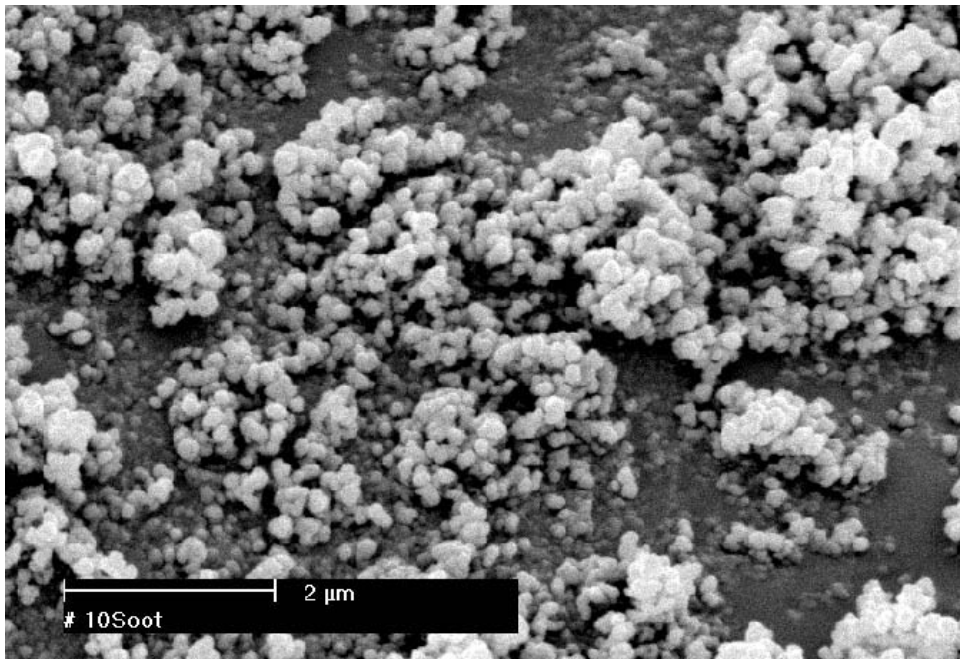


**Figure 1.2** Picture of soot particles extracted from a diesel engine taken with a scanning electron microscope. (SOURCE: JPM ©2017 The Pennsylvania State University.)

### 1.3 Soot particle studies

Laser-based techniques have been developed to provide an unrivalled edge over traditional intrusive probes in terms of spatial and temporal resolution. Physical probing methods may interrupt the combustion processes during an investigation. Although three-dimensional measurements are not widely implemented in practice due to the complexity of such experimental arrangements, laser-based diagnostic techniques are capable of delivering multi-dimensional measurements whereas probing methods are typically limited to point-wise measurement. Moreover, different laser diagnostic techniques can be applied simultaneously to measure a multitude of quantities.

Steady laminar non-premixed flames are frequently employed as a controllable system to study the soot evolution in both the temporal and spatial coordinates [1, 19–22]. Much of the current understanding of soot formation is developed from studying laboratory-scale laminar flames. However, vortex-flame interaction constitutes one of the fundamental problems in practical combustion systems due to the wide existence of vortices in many practical, mostly turbulent, flames. In most reacting flows, vortices are generated either naturally due to flow instability or externally excited to increase the mixing rate. Furthermore, vortex-flame interaction is also a key component in turbulent combustion problem since much experimental evidence indicates that turbulence may be described as a large-scale coherent structure superposed on a fine-grained background oscillations [23].

One of the effective and controllable methods to conjoin a laminar non-premixed jet flame and a time-dependent flow field is to impose a periodic pressure perturbations to the fuel stream of the flame using a loud-speaker. The coupling is most intensified when the fuel jet is forced in a range of excitation frequencies encompassing its unforced natural frequency [24]. The periodic nature of forced laminar flames allows basic studies of dynamic interactions between the flame structure, time-varying flow field and soot evolution. Such flames represent a controllable system which provide a broader range of temperature histories, stoichiometry, strain rate and residence time than are commonly found in steady flames. This type of flame is valuable as it typifies the more complex conditions found in turbulent combustion environments. This thesis achieves a better understanding of soot evolution in unsteady combustion environments by assessing a series of time-dependent flames spanning a wide range of operational conditions. Additionally, an experimental data set that includes measurements of multiple parameters in diverse flame conditions is potentially beneficial to the development and validation of soot models.

## 1.4 Thesis outline

The current research is presented in a thesis by publication, consisting of two published and two submitted journal papers. Chapter 2 contains a review of the current understanding and recent research concerning soot formation in time-varying laminar flames. Additionally, it also provides a background literature regarding various state-of-the-art techniques that are widely used in combustion research, particularly in soot-laden environments. The chapter concludes by identifying the research gaps and formulating scientific aims.

In Chapter 3, a description of the optical-based diagnostic techniques and computational simulations employed in this thesis is provided. Those techniques include Two-Line Atomic Fluorescence (TLAF) thermometry, Laser-Induced Incandescence (LII), Time-Resolved LII (TiRe-LII), Planar Laser-Induced Fluorescence of OH (OH-PLIF) and Particle Imaging Velocimetry (PIV).

Chapters 4–7 present results from a systematic study of the soot formation in a series of time-varying laminar non-premixed flames. In Chapter 4, the effects of forcing frequency on the soot formation and flame structure are investigated through examining a steady laminar jet flame forced at 20 and 40 Hz.

Chapter 5 presents the experimental findings concerning the influence of burner geometry (*i.e.*, fuel tube diameter) on the flame structure, in turn, has a great impact on the soot formation. The experiment compares three forced flames established using three burners under the same flow and forcing conditions. The measurements of temperature, soot and velocity are presented and discussed.

Chapter 6 investigates the impact of the acoustic forcing amplitude on the time-varying laminar flames. While keeping the flow conditions and forcing frequency constant, the oscillation amplitude and burner diameter are varied independently. Differences in the soot field and flame structure are discussed. Additionally, the spatial correlations between the controlling parameters under a variety of flame conditions are examined in detail.

Chapter 7 extends the investigation by including a numerical model of a time-varying laminar flame to study the distributions of the mixture fraction and soot precursors in the flame. The ability to acquire this information is limited by the experimental techniques employed in the current study.

Chapter 8 summarizes the results and concludes the thesis by answering the scientific research questions, with a list of possible future research suggested.

---

## References

- [1] M. D. Smooke, M. B. Long, B. C. Connelly, M. B. Colket, and R. J. Hall, “Soot formation in laminar diffusion flames”, *Combustion and Flame* **143** (2005), pp. 613–628.
- [2] M. Stöhr, K. Geigle, R. Hedef, I. Boxx, C. Carter, M. Grader, and P. Gerlinger, “Time-resolved study of transient soot formation in an aero-engine model combustor at elevated pressure”, *Proceedings of the Combustion Institute* (2018).
- [3] U. S. Department of Energy, “International Energy Outlook 2017”, Independent Statistics & Analysis, Energy Information Administration, 2017.
- [4] S. Kedia, “Approaches to low carbon development in China and India”, *Advances in Climate Change Research* **7** (2016), pp. 213–221.
- [5] U.S. Census Bureau, “World Population”, 2017, URL: <https://www.census.gov/popclock/>.
- [6] J. T. Hardy, “Climate change: causes, effects, and solutions”, John Wiley & Sons, 2003.
- [7] O. Hoegh-Guldberg, P. J. Mumby, A. J. Hooten, R. S. Steneck, P. Greenfield, E. Gomez, C. D. Harvell, P. F. Sale, A. J. Edwards, K. Caldeira, et al., “Coral reefs under rapid climate change and ocean acidification”, *Science* **318** (2007), pp. 1737–1742.
- [8] T. C. Bond et al., “Bounding the role of black carbon in the climate system: A scientific assessment”, *Journal of Geophysical Research: Atmosphere* **118** (2013), pp. 5380–5552.
- [9] J. Hansen and L. Nazarenko, “Soot climate forcing via snow and ice albedo”, *Proceedings of the National Academy of Sciences of the United States of America* **101** (2004), pp. 423–428.
- [10] D. Dockery, C. Pope, X. Xu, J. Spengler, J. Ware, M. Fay, B. F. Jr., and F. Speizer, “An association between air pollution and mortality in six U.S. cities”, *The New England Journal of Medicine* **329** (1993), pp. 1753–1759.
- [11] D. Dockery, “Epidemiologic evidence of cardiovascular effects of particulate air pollution”, *Environmental Health Perspectives* **109** (2001).
- [12] C. P. III, R. Burnett, M. Thun, E. Calle, D. Krewski, K. Ito, and G. Thurston, “Lung cancer, cardiopulmonary mortality, and long-term exposure to fine particulate air pollution”, *The Journal of the American Medical Association* **287** (2002), pp. 1132–1141.
- [13] A. J. Cohen, H. R. Anderson, B. Ostro, K. D. Pandey, M. Krzyzanowski, N. Künzli, K. Gutschmidt, A. Pope, I. Romieu, J. M. Samet, and K. Smith, “The Global Burden of Disease Due to Outdoor Air Pollution”, *Journal of Toxicology and Environmental Health, Part A* **68** (2005), pp. 1301–1307.
- [14] F. Caiazzo, A. Ashok, I. A. Waitz, S. H. Yim, and S. R. Barrett, “Air pollution and early deaths in the United States. Part I: Quantifying the impact of major sectors in 2005”, *Atmospheric Environment* **79** (2013), pp. 198–208.

## REFERENCES

---

- [15] M. Keywood, K. Emmerson, and M. Hibberd, “Ambient air quality: National air quality standards”, Australia state of the environment 2016, Australian Government Department of the Environment and Energy, Canberra, 2016, URL: <https://soe.environment.gov.au/theme/ambient-air-quality/topic/2016/national-air-quality-standards>.
- [16] B. S. Haynes and H. G. Wagner, “Soot formation”, *Progress in Energy and Combustion Science* **7** (1981), pp. 229–273.
- [17] N. R. Council et al., “Frontiers in chemical engineering: research needs and opportunities”, National Academies Press, 1988.
- [18] I. Glassman and P. Yaccarino, “The temperature effect in sooting diffusion flames”, *Proceedings of the Combustion Institute* **18** (1981), pp. 1175–1183.
- [19] A. Gomez, M. G. Littman, and I. Glassman, “Comparative study of soot formation on the centerline of axisymmetric laminar diffusion flames: fuel and temperature effects”, *Combustion and Flame* **70** (1987), pp. 225–241.
- [20] R. Santoro, T. Yeh, J. Horvath, and H. Semerjian, “The transport and growth of soot particles in laminar diffusion flames”, *Combustion Science and Technology* **53** (1987), pp. 89–115.
- [21] R. J. Santoro, T. T. Yah, J. J. Horvath, and H. G. Semerjian, “The Transport and Growth of Soot Particles in Laminar Diffusion Flames”, *Combustion Science and Technology* **53** (2007), pp. 89–115.
- [22] M. D. Smooke, C. S. McEnally, J. Fielding, M. B. Long, L. D. Pfefferle, R. J. Hall, and M. B. Colket, “Investigation of the Transition from Lightly Sooting towards Heavily Sooting Coflow Ethylene Diffusion Flames”, *Combustion Theory and Modelling* **8** (2004), pp. 593–606.
- [23] P. H. Renard, D. Thévenin, J. C. Rolon, and S. Candel, “Dynamics of flame/vortex interactions”, *Progress in Energy and Combustion Science* **26** (2000), pp. 225–282.
- [24] A. W. Strawa and B. J. Cantwell, “Investigation of an excited jet diffusion flame at elevated pressure”, *Journal of Fluid Mechanics* **200** (1989), pp. 309–336.



# Chapter 2

## Background literature

### 2.1 Mechanisms of soot formation and destruction

The evolution of soot within flames has become one of the central themes of research activities in the combustion field. The interest in this subject has inspired a diverse spectrum of experimental conditions, such as shock-tube pyrolysis [1, 2], laminar premixed [3, 4] or non-premixed flames [5, 6], externally-forced flames [7–11], spray flames [6, 12], bluff-body flames [13] and turbulent jet flames [14–17]. Reviews of experimental studies on soot formation have been done in the past, particularly the thorough review provided by Bockhorn [18]. Additionally, Michelsen [19] has also provided an exhaustive review of soot formation in combustion highlighting the different mechanisms involved. There is a large body of evidence indicates that soot evolution comprises four major processes, namely soot nucleation, particle surface growth, coagulation and agglomeration [20]. Parallel to the formation and growth of soot particles is the oxidation by  $O_2$  molecules and OH radicals.

Figure 2.1 presents a conceptual schematic of soot evolution. It starts by fuel pyrolysis, followed by the growth of polycyclic aromatic hydrocarbon (PAH). Soot inception is described using the resonance-stabilised radical (RSR) growth mechanism proposed by Johansson et al. [21] which is explained in the following section. The growth of soot particles includes coagulation, surface growth, and agglomeration. Soot destruction, which comprises oxidation and fragmentation, occurs either simultaneously in premixed combustion or consequently in non-premixed flames.

Extensive experimental and computational studies [22–26] have well-established that PAH species are the precursor of soot. There are two principal pathways for the formation of the first aromatic ring, *i.e.*, benzene and phenyl radical. Previous studies [27–30] have linked the formation of benzene to the reactions of small aliphatic species, such as  $C_2$  (acetylene),  $C_3$  (propargyl radical) or unsaturated  $C_4$  molecules. Additionally, a few studies [31–34] have suggested that heavier species (*e.g.*, cyclopentadienyl radical) also play an important role in the formation of PAH.

Frenklach and Wang [35] demonstrated that the mass growth of PAH species up to

4-rings (e.g. pyrene or acepyrene) can be modelled using the hydrogen-abstraction- $C_2H_2$ -addition (HACA) mechanism. It is a repetitive reaction sequence which comprises two principal steps: (i) first part of the mechanism is an abstraction of a hydrogen atom from the aromatic by a gaseous hydrogen atom



(ii) followed by an addition of a gaseous acetylene molecule to the radical site formed



Here,  $A_i$  is an aromatic molecule consists of  $i$  rings, while  $A_{i\cdot}$  is its radical. However, the growth of large PAH solely via HACA route is too slow to agree with experimental data [36]. A kinetic study conducted by Böhm et al. [22] showed that ring-ring condensation is more efficient than HACA in producing heavy aromatics at short reaction times.

Frenklach and Wang [35] considered the PAH growth beyond 4-rings (starting from pyrene) to occur through an irreversible coagulation process in the free molecular regime. The numerical work conducted by Howard [37] supported the idea that radical sites in the peripheries of PAH molecules (form as a result of H-abstraction) provide a reactive site for coagulation of PAH with each other and with small radicals. In addition to the standard HACA mechanism, D'Anna and co-workers [38–40] have developed a kinetic mechanism to predict the formation of heavy aromatics in a variety of combustion environment, such as shock-tubes, rich premixed flames and opposed-flow non-premixed flames. Parallel to the standard acetylene addition mechanism, D'Anna et al. [41] suggested that high-molecular-mass aromatic compounds are formed via the polymerisation of RSRs, including cyclopentadienyl self-combinations, propargyl addition to benzyl radicals, and the sequential addition of propargyl radicals to aromatic rings.

Soot inception (*i.e.*, the production of hydrocarbon clusters that indicates the transition of gas-phase species to solid particles) is one of the key steps in the understanding of soot formation. Arguments revolve between two mechanisms for soot inception [30]: (a) physical coalescence of moderate-sized PAHs by van der Waals forces into stacked clusters and (b) formation of covalently bound clusters. However, soot inception temperatures ( $\geq 1450 \pm 250$  K) are too volatile to bind PAHs simply by van der Waals forces [30]. Since Stein's stabilomers as large as coronene have boiling/sublimation temperatures well below 1000 K, they should evaporate, rather than cluster into particles at soot inception temperatures [30].

A molecular dynamics simulation carried out by Schuetz and Frenklach [43] demonstrated that the collision of a pair of PAH molecules can produce a ro-vibrationally excited dimer with a lifetime much longer than the collision

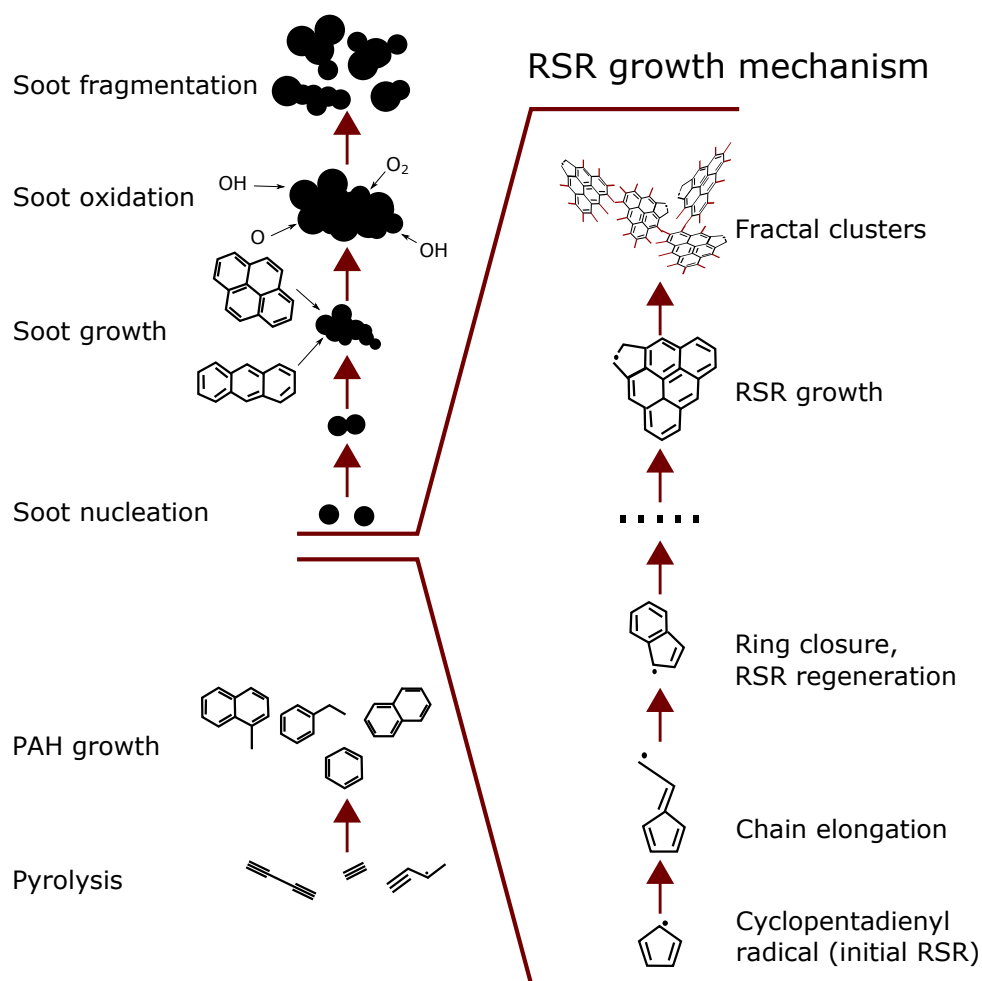


**Figure 2.1** A conceptual schematic of soot evolution. Cyclopentadienyl radical is used as an example of the initial resonance-stabilised radical (RSR). Concept adapted from [42].

timescale. It suggested that the relatively long lifetimes of dimers (as small as pyrene) that allow them to evolve into soot nuclei are attributed to the activation of internal rotors, which increases the stability of dimers [43]. However, while Wang [30] acknowledged the plausibility of such hypothesis, he pointed out that the simulation is not a concrete proof that a dimer would survive this long, as most of the collisions simulated are non-reactive.

Johansson et al. [21] proposed a radical-driven hydrocarbon-clustering mechanism that provides pathways to particle formation and growth that fully comply with fundamental scientific principles. The CHRCR (clustering of hydrocarbons by radical-chain reactions) mechanism involves polymerisation of RSR with hydrocarbons species to form covalently bound products with RSR character. The CHRCR mechanism can be described in three stages: (i) growth of an RSR through acetylene or vinyl addition, (ii) clustering of available hydrocarbons via radical-chain reactions, (iii) particle surface growth by RSR-driven radical-chain reactions

at surface-radical sites on larger carbonaceous particles that possess chemical properties similar to those of RSRs. For example, the chain reaction can begin with cyclopentadienyl (see Fig 2.1). It polymerises via radical-chain reactions. The high reactivity of RSR ensures the rapid species growth rate. Furthermore, there is no need for additional H-abstraction reactions that have high energy barrier. The resultant large resonance-stabilised  $\pi$ -radical<sup>1</sup> (e.g., indenyl) then undergoes partial loss of conjugation during  $\sigma$ -dimerisation to form a molecular cluster [21, 42].

Electron microscopic studies of soot particles [44–47] revealed that mature soot typically exhibit a collection of complex aggregate structures that comprise nearly-spherical primary particles that range from 15–60 nm in diameter. Primary soot particles are typically spheroidal due to the combined effect of coagulation and surface growth. The coagulation process between a pair of large and small particles usually produce simple aggregated structures. Simultaneously, surface reactions act on these aggregated structures promotes a spherical shape by countering the geometric randomness introduced by aggregation [30, 48]. It is generally presumed that soot aggregates begin to present fractal-like morphology when they are significantly larger than the primary particles [49].

Oxidation and fragmentation are two main pathways for soot destruction. Oxidation is a process by which gas-phase oxidising species (e.g., O<sub>2</sub> and OH) attack the surface of soot particles, removing carbon. Oxidation continuously competes with the processes of soot formation. Thus, the emission of soot from a combustion system is determined by the competition between soot formation and oxidation. In premixed combustion, soot oxidation occurs simultaneously with the formation, whereas it happens subsequent to soot formation in non-premixed flames. The dominant oxidising agent is OH under fuel-rich conditions and O<sub>2</sub> under fuel-lean conditions [50–52]. Wal and Tomasek [53] suggested that the oxidation rate is dependent on the nanostructure of soot, which is governed by fuel type and soot growth conditions. Fragmentation is the process by which aggregated soot particles break apart into small fragments during oxidation under fuel-lean conditions [54]. Neoh et al. [54] proposed that soot fragmentation is a consequence of the combined effect of internal burning in soot by O<sub>2</sub> and surface regression due to external oxidation. However, a numerical study conducted by Ghiassi et al. [55] demonstrated that while internal burning is possible for particles up to 10 nm, O<sub>2</sub> diffusion within soot would be ineffective for particles larger than 10 nm. The same study proposed that the occurrence of fragmentation is due to the burning of bridges between aggregates [55, 56]. Furthermore, Ghiassi et al. [57] revealed that the extent of fragmentation is inversely proportional to the peak temperature. It is presumably because soot burnout occurs rapidly at higher flame temperatures, consuming soot aggregates before they could fragment.

---

<sup>1</sup>A radical whose extended conjugation depends on maintaining an unpaired  $\pi$  electron.

## 2.2 Physical parameters affecting soot evolution

Soot evolution in combustion environments involves a series of complex chemical and physical interactions which are, to a great extent, controlled by a multitude of quantities including **temperature, pressure, mixture fraction, strain rate and residence time**. Thus, there is particular value in combining experimental techniques that are both temporally and spatially resolved and allow simultaneous measurement of multiple quantities [58].

### 2.2.1 Temperature

Temperature is one of the governing parameters in a combustion process as the rate of chemical reaction has a strong exponential dependence on it. The rate coefficient,  $k$ , can be expressed with a modified Arrhenius equation,

$$k(T) = A \cdot T^n \cdot e^{-E_a/(R_u \cdot T)}, \quad (2.3)$$

where  $A$  is the pre-exponential factor,  $n$  is a rate constant that typically lies in the range  $-1 < n < 1$ ,  $E_a$  is the activation energy and  $R_u$  is the universal gas constant, 8.314 J/mol·K. Values of  $n$  and  $E_a$  determine the dependence of a reaction rate on temperature. Due to the exponential nature of the latter, even a slight change in temperature often results in a significant change of the rate coefficient.

Many early studies [59–61] have noted the temperature dependence of soot formation. For example, by studying shock-tube pyrolysis of a variety of aromatic hydrocarbons (benzene, toluene, ethylbenzene and indene, highly diluted with argon), Graham et al. [62] reported that after reaching its maximum at 1750–1800 K, the soot yield falls rapidly with increasing temperature from near 100% to less than 5% at 2300 K. It showed a bell-shaped dependence of soot yield on temperature. This behaviour was reported by several studies [63–66].

Figure 2.2 shows an example of the bell-shaped curve observed at different time in argon-diluted (4.68% vol.) acetylene pyrolysis over a pressure range of 1.27–2.33 bar [64]. The position of the maximum is not universal but is dependent on observation time, pressure and extinction mode [64].

Sooting tendencies in premixed and non-premixed flames tend to react differently to the increase in temperature. In premixed flames, an increase in the flame temperature often leads to a decrease in soot production because the rate of oxidation reaction dominates over the formation rate. Conversely, in non-premixed flames, no oxidation occurs prior to the reaction zone, leaving only the pyrolysis, which leads to an increase in soot with temperature. Early soot formation is observed at a region where the temperature is near to 1300 K [67]. The particles are then transported to a higher temperature region where particle growth continues. Additionally, higher temperatures also lead to a more rapid oxidation of the soot particles.

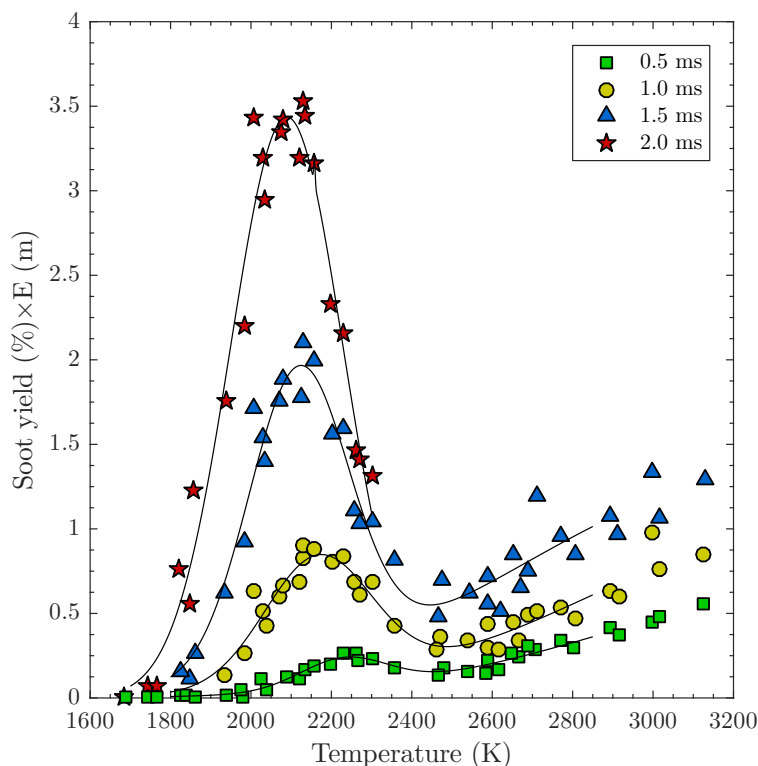


**Figure 2.2** Soot yield versus temperature in acetylene pyrolysis [64].

Since temperature is a dominant parameter in combustion processes, a variety of optical thermometry techniques have been developed to measure the temperature of flames. However, most of these techniques are highly susceptible to interference from soot particles, thus limiting the applications to clean combustion environments. A relatively simple optical thermometry technique is Rayleigh scattering. The major limitation of this method is to determine the Rayleigh cross section which requires knowledge of all major species concentrations, which can be challenging. Additionally, Rayleigh scattering is vulnerable to interference from Mie scattering which makes it an unsuitable technique for thermometry in particle-laden flows. In contrast, the Coherent anti-Stokes Raman Spectroscopy (CARS) technique is more applicable to thermometry in harsh combustion environment and benefits from its strong coherent signal [68]. Despite the effort invested in expanding CARS into planar measurement [69], its application is typically limited to point measurement [70–72]. Of the optical thermometry techniques, Two-Line Atomic Fluorescence (TLAF) is emerging as a promising robust technique in soot-laden combustion environments, especially where planar imaging is preferable. Therefore, the present thesis utilises the TLAF technique to characterise the gas temperature of flames in a two-dimensional manner. More details of this technique are discussed in the following chapter.

### 2.2.2 Pressure

In practical combustion systems, operational pressure spans a wide range and varies from atmospheric to above 200 bar. At elevated pressure, the density of carbon atoms increases and so does the collision frequency, which both contribute to a higher soot yield [73–76]. Furthermore, experimental investigation [76] suggests that increasing the pressure accelerates the rate of fuel pyrolysis which in turn leads to higher rates of soot nucleation and surface growth. However, despite the frequent use of high-pressure combustion in a wide range of practical devices, the majority of laboratory-scale flames are operated under atmospheric pressure due to technical challenges and cost [77]. The present thesis focuses on atmospheric flames, no attempt has been made to investigate the effect of pressure on soot evolution.

### 2.2.3 Mixture fraction

In a reacting flow system, the mixture fraction,  $Z$ , is a conserved scalar commonly defined as the ratio of the total mass of materials that originate from the fuel stream,  $m_{fuel}$ , to the total mass of the mixture of fuel and oxidiser,  $m_{mix} = m_{fuel} + m_{ox}$ , expressed as:

$$Z = \frac{m_{fuel}}{m_{mix}} = \frac{m_{fuel}}{m_{fuel} + m_{ox}} = \frac{\Phi}{\Phi + (A/F)_{stoic}}, \quad (2.4)$$

where  $\Phi$  is the equivalence ratio, commonly treated as a quantitative indicator of whether a fuel-oxidiser mixture is rich, lean or stoichiometric. It is defined as

$$\Phi = \frac{(A/F)_{stoic}}{(A/F)} = \frac{(F/A)}{(F/A)_{stoic}}. \quad (2.5)$$

Additionally,  $(A/F)_{stoic}$  is the stoichiometric air-fuel ratio,

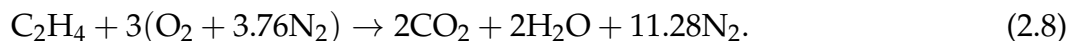
$$(A/F) = \frac{m_{ox}}{m_{fuel}} = \frac{n_{ox} \cdot MW_{ox}}{n_{fuel} \cdot MW_{fuel}}, \quad (2.6)$$

where  $n$  and  $MW$  represent the number of moles and molecular weights, respectively.

Stoichiometry is used to quantify the amount of air (or oxidiser) <sup>2</sup> required to completely react with a quantity of fuel. By definition [78], the flame surface of a non-premixed flame is where the fuel and oxidiser meet in stoichiometric proportion,  $\Phi = 1$ , or

$$Z_{stoic} = \frac{1}{1 + (A/F)_{stoic}}. \quad (2.7)$$

Since the only fuel investigated in this thesis is ethylene,  $C_2H_4$ , it is used as an example. Given the stoichiometric reaction of  $C_2H_4$ ,



The value of  $(A/F)_{stoic}$  is equal to 14.75. Therefore,  $Z_{stoic} = 0.064$ . If the distribution of  $Z$  is available, it can be used to identify the fuel-rich ( $Z > Z_{stoic}$ ) and fuel-lean ( $Z < Z_{stoic}$ ) sides of the flame. However, it is technically challenging to resolve the distribution of  $Z$  as it requires measurements of all major species in the combustion environment [79], which is especially challenging in flames containing soot. While it is possible to measure the concentrations of all of the major species by using simultaneous Raman and Rayleigh imaging [68, 80, 81], such measurements are often restricted to zero- and one-dimensional. It is because two-dimensional imaging of the fuel encounters two major challenges, which are the early dissociation of the fuel and the effect of differential diffusion on the rich side of stoichiometric [79]. Early fuel dissociation results in very low concentrations of the probed species which in turn leads to a poor signal quality. Furthermore, differential diffusion, which is particularly significant for multi-component fuels containing  $H_2$ , often leads to a misrepresentation of the mixing when only one part of the fuel composition is measured. An alternative to the direct measurement of all of the fuel species is to use a fuel tracer, such as acetone [82], 3-pentanone [83], toluene [84] and krypton [85]. However, these fuel-based tracers also suffer from a range of systematic errors which limit their applicability [86]. Therefore, the present thesis calculates the mixture fraction of flames via computational approaches, following experimental validations.

---

<sup>2</sup>For simplicity, throughout this thesis it is assumed that the composition of air is 21%  $O_2$  and 79%  $N_2$ , by volume.



### 2.2.4 Strain rate

The interaction between the flame and the fluid dynamics constitutes one of the principal governing mechanisms in non-premixed flames. In fluid dynamics, the strain rate indicates the local rate of deformation of the fluid elements [87] in the presence of velocity gradients across a distance unit. Strain rate plays a major role in the distribution of mixture fraction [88, 89], which in turn has a significant influence on the temperature [90] and the formation of soot [91].

Since the strain rate field cannot be measured directly, differentiation schemes are used to derive the quantity [92]. Although tomographic Particle Image Velocimetry (PIV) is continuing to be developed [93, 94], the majority of PIV measurements are planar. Three derivatives can be derived from the two available velocity components, axial ( $u_x$ ) and radial ( $u_r$ ), namely **axial**, **normal** and **shear**-strain rate:

$$S_{xx} = \frac{\partial u_x}{\partial x}, \quad (2.9)$$

$$S_{rr} = \frac{\partial u_r}{\partial r} \quad (2.10)$$

and

$$S_{rx} = \frac{1}{2} \left( \frac{\partial u_r}{\partial x} + \frac{\partial u_x}{\partial r} \right). \quad (2.11)$$

Another important differentiable quantity is the vorticity:

$$\omega = \frac{\partial u_x}{\partial r} - \frac{\partial u_r}{\partial x}. \quad (2.12)$$

For jet flames, it is common that the axial-velocity-gradient term,  $\partial u_x / \partial r$ , is dominant in Eqs. 2.11 and 2.12. As a result, the vorticity field often appears similar to the corresponding strain rate field. However, since vorticity alone has no effect on the deformation of fluid elements, it is not expected to affect the reaction [95].

Due to its significant role in the flame chemistry and the soot formation, the effects of strain rate on these aspects have been investigated extensively [14, 96–100]. Counterflow diffusion flames have been the flame of choice to many

of these studies since they have a well-defined, one-dimensional axisymmetric reacting field and, more importantly, they offer a direct control of the strain rate. In contrast, a turbulent flame has a three-dimensional flow field and that varies with time. Thus, it is extremely challenging, if not impossible, to resolve all the local instantaneous strain rates over the entire turbulent flow field. An alternative approach is to characterise the turbulent flame with a bulk exit strain rate [101]. The majority of opinion at present is that the soot production has an inverse relationship with the strain rate, as evidenced by numerous studies [97, 102, 103]. Figure 2.3 shows the maximum soot volume fraction in counterflow flames of different fuel types, which scales inversely with the strain rate. The findings reported by Böhm et al. [104] suggested that high strain rate-induced PAH suppression might contribute to the decrease in the soot production. Additionally, Decroix and Roberts [98] revealed that the thickness of soot field, defined as the full width at half maximum (FWHM), is inversely proportional to the square root of the strain rate in counterflow flames, as shown in Figure 2.4. Furthermore, Du et al. [105] demonstrated the controllability of strain rate in counterflow flames by identifying four critical strain rates based on the extinctions of soot luminosity, soot particle light-scattering, PAH fluorescence and flame. Therefore, the present thesis performs the PIV technique not only to characterise the two-dimensional velocity field but also to derive the strain components. Quantifying the strain field provides insights into the interaction between soot field and local strain in time-varying flames.

### 2.2.5 Residence time

Residence time is defined as the average duration of a fluid element or a particle resides in a given region or condition. It is well established that the soot production scales with the residence time at conditions that favour soot formation, as evidenced by previous studies [67, 106, 107]. A longer residence time results in more soot precursors form in the fuel pyrolysis region, which in turn increases the soot volume fraction. Experiments involving counterflow flames [108–110] have discovered that the characteristic residence time is proportional to the inverse of strain rate. It is because the reaction zone is compressed as the strain rate is increased, which leads to the decrease in residence time. Some studies [111, 112] simply defined the flame characteristic residence time to be the inverse of strain rate or vice versa. Additionally, residence time analyses can be done in numerical simulations by releasing virtual inert particles at the jet exit plane and by tracking their trajectories as they are convected through the flame [113]. The present thesis adapts a similar method to perform residence time analyses on soot evolution.

## 2.3 Vortex–flame interactions

Vortices can be found in many combustion systems associated with reacting flows (*e.g.*, turbine engines, internal combustion engines, rocket engines, boilers

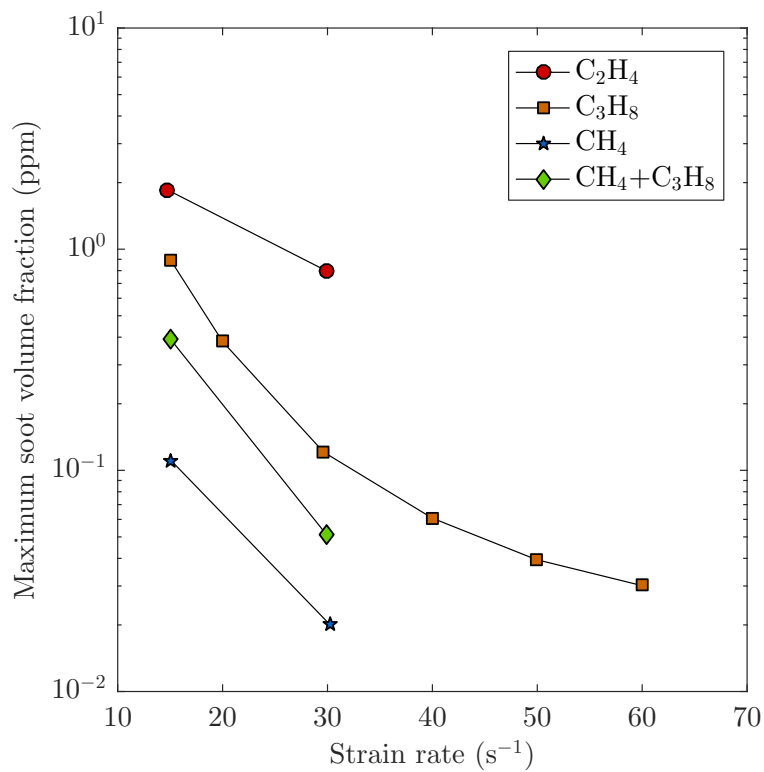


**Figure 2.3** Maximum soot volume fraction as a function of strain rate for different fuels: ethylene ( $C_2H_4$ ), propane ( $C_3H_8$ ), methane ( $CH_4$ ) and blended propane/methane ( $CH_4+C_3H_8$ ). Reproduced from [98].

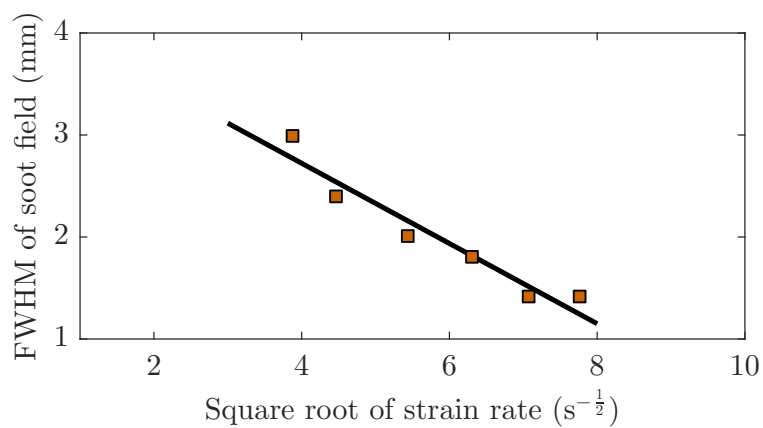


**Figure 2.4** Full width at half maximum (FWHM) of axial soot volume fraction profiles for a propane-air counterflow non-premixed flame at various strain rates, presented as a function of the square root of strain rate. Reproduced from [98].

and furnaces), either artificially embedded to enhance the mixing rate [114] or naturally occurring due to intrinsic fluid dynamic instability [115]. The laminar flamelet concept proposed by Peters [116] views a turbulent non-premixed flame as an ensemble of laminar flamelets that are distorted, extended, produced and dissipated by a multitude of vortices with a wide range of length scales. In the light of the laminar flamelet concept, understanding the fundamental interaction between a vortex and a flame appears as a pivotal process in the description of turbulent flames [117].

The low-frequency buoyancy-induced flame fluctuation, also known as the flicker, is a familiar phenomenon observable in free laminar non-premixed flames. The oscillation frequency observed is typically in the range of 10 to 20 Hz which are independent of the flow rate or fuel type [114, 118, 119]. Buckmaster and Peters [115] suggested that the flickering is a consequence of a modified Kelvin-Helmholtz type of instability of the buoyancy-induced flow field. Sato et al. [120] suggested that a different mode of oscillation occurs when the peak velocity is sited on the centreline of the flame. The vortical scale for the buoyancy-driven oscillation is larger than the momentum-driven flickering. Consequently, buoyancy-driven oscillation often results in a flame pinch-off (a parcel of flame separated from the attached flame), whereas the momentum-driven flickering only exhibited at the flame tip. A computational study conducted by Sánchez-Sanz et al. [121] suggested that flame oscillation frequencies larger than the natural flickering frequency lead to a regime in which the oscillations are confined to a region near to the jet exit. The extent of alteration on the structure of the flickering flame with respect to the steady counterpart decreases as the forcing frequency increases. However, the effect of oscillation frequency on soot evolution remains unclear. Therefore, the present thesis examines the behaviour of soot evolution in flames acoustically forced at different frequencies.

Figure 2.5 presents the effect of fuel jet velocity,  $u_f$ , on the flame flickering frequency,  $f$ . The results of Chen et al. [114], Sato et al. [120], and Durox et al. [122] show a consistent trend in three levels of gravity ( $G = 1, 2$  and  $5$ ). While the flickering frequencies increase with gravity, they are relatively independent of the variation in  $u_f$  for low-velocity conditions ( $u_f < 1.0 \text{ m}\cdot\text{s}^{-1}$ ). Beyond  $u_f = 1.0 \text{ m}\cdot\text{s}^{-1}$ , the flame oscillation frequency increases with  $u_f$ . However, the result of Hamins et al. [123] shows a broader spread of flickering frequency as compared with the others. This discrepancy is probably due to the large burner diameters ( $25 \text{ mm} \leq d \leq 100 \text{ mm}$ ) utilised in the study [123]. However, the effects of burner diameter on the flame structure and the soot field of time-varying laminar flames is unclear and have not been investigated before. Nevertheless, the burner diameter is commonly regarded as the characteristic length that defines the scale of a combustion system. For example, the transition from laminar to

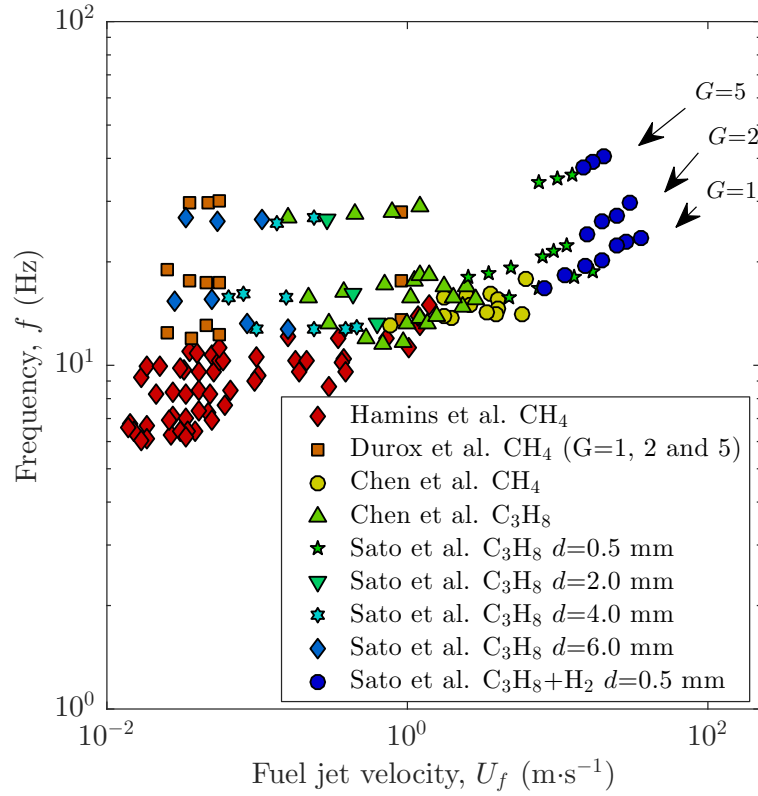


**Figure 2.5** Flame flickering frequency as a function of fuel jet velocity. Results are collected from several studies [114, 120, 122, 123].  $G$  represents the dimensionless gravity level relative to the gravity of earth, while the burner diameter is denoted as  $d$ .

turbulent flow is characterised by the Reynolds number,

$$Re = \frac{\rho \cdot u_f \cdot D}{\mu} = \frac{u_f \cdot D}{\nu}, \quad (2.13)$$

where  $\rho$  is the fuel density,  $D$  is the burner diameter (characteristic length),  $\mu$  and  $\nu$  are the dynamic and kinematic viscosities of the fluid, respectively. In the vast majority of combustion systems, the Reynolds number is defined based on the mean fluid conditions at the nozzle exit. In a dimensional analysis of the pulsation frequency of pool fires, Emori and Saito [124] suggested a strong dependence between the Strouhal (dimensionless frequency) and Froude (ratio of the flow inertia to the buoyant force) numbers:

$$St = \frac{f \cdot D}{u_f} \quad (2.14)$$

and

$$Fr = \frac{u_f^2}{D \cdot g} \quad (2.15)$$

where  $g$  is the earth normal gravitational acceleration,  $9.81 \text{ m}\cdot\text{s}^{-2}$ . Since the flame oscillations observed in both pool fires and naturally flickering flames are induced by buoyancy, it is reasonable to assume that the dependence developed from pool fires can be extended to freely flickering flames.

Figure 2.6 presents the Strouhal number as a function of the inverse Froude number obtained at a wide range of experimental conditions [120, 122, 123, 125]. Sato et al. [120] suggested that the Strouhal-Froude number relationship exhibits two regions that can be characterised by the following formulae:

$$St = 0.056Fr^{-0.41} \quad (\text{Region I}) \quad (2.16)$$

and

$$St = 0.29Fr^{-0.50} \quad (\text{Region II}). \quad (2.17)$$

However, the Strouhal-Froude number relationships differ from those proposed by Hamins et al. [123], which are determined between reacting and non-reacting flow cases:

$$St \propto Fr^{-0.57} \quad (\text{Reacting flow}) \quad (2.18)$$

and

$$St \propto Fr^{-0.38} \quad (\text{Non-reacting flow}). \quad (2.19)$$

Since the reacting and non-reacting flow cases each has different power-law dependence, it indicates that the vortex-flame interactions in flames with a low Froude number cannot be modelled through studies of isothermal buoyant flows.

An observation concerning the wide variation in the brightness of the luminous core of the forced flames made by Strawa and Cantwell [126] has sparked the combustion research community's interest in studying the formation and oxidation of soot in time-varying flames. Consequently, a number of experimental [7, 8, 127–130] and computational [11, 113, 121] studies have revolved around time-varying laminar sooting flames. The interest in this subject stems from the fact that time-varying laminar flames provide not only a broader range of flame conditions than steady-state flames, but also an opportunity to resolve the flame development and the soot evolution in a time-discrete manner via phase-locked measurements. However, the majority of experimental studies [7, 129, 130] in the literature report on measurements of only one or two quantities. Therefore, the present thesis aims to quantitatively characterise the time-varying flames in an increasingly comprehensive manner.

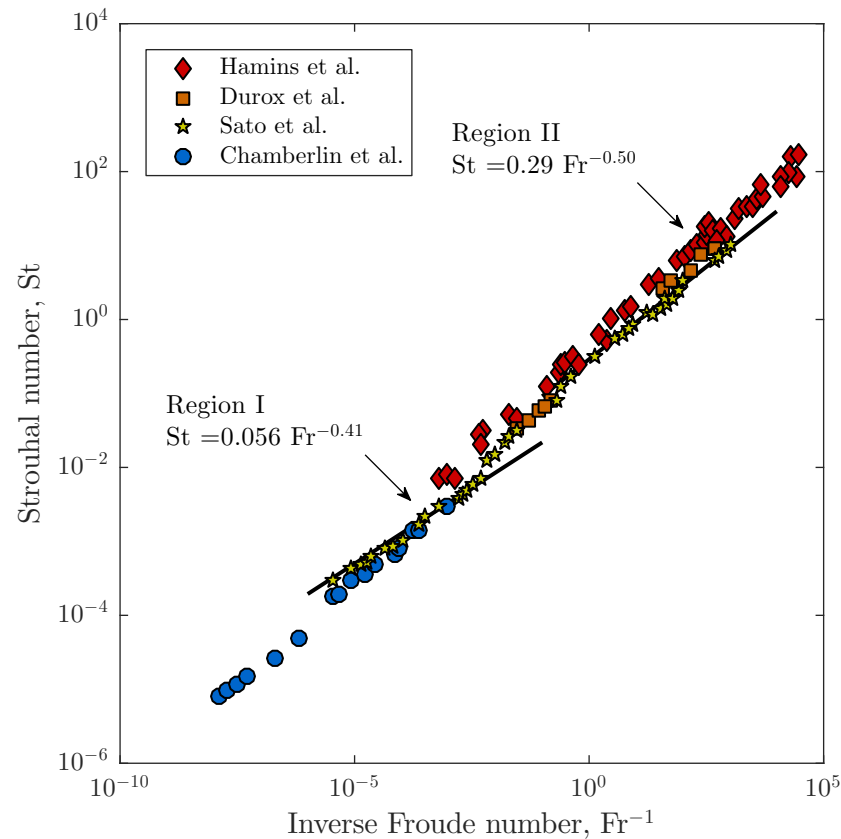


**Figure 2.6** Relation between the Strouhal number and the inverse Froude number for a wide range of experimental studies involving flickering flames. Image adapted from [120].

Laser-Induced Incandescence (LII) measurement has quantified the extent of the enhancement in soot production by measuring the soot volume fraction in both steady and flickering laminar non-premixed methane flames [7]. The maximum soot concentration measured in the flickering methane flame, forced with a 10 Hz sinusoidal acoustic wave, is four times greater than that in the corresponding steady flame [7]. Furthermore, the maximum primary particle size in the flickering flame is about 60% larger than those measured in the steady counterpart [127]. While the extent of the soot production enhancement achieved by the acoustic forcing varies with the fuel type (methane, ethylene and propane), Shaddix and Smyth [8] suggested that the intensity of the flame flickering has only a limited influence on the soot production augmentation. However, the computational study conducted by Kaplan et al. [113] clearly shows that the peak soot concentration in laminar methane flames flickering at 10 Hz increases with the forcing amplitude. However, other than methane flames, Shaddix and Smyth [8] also investigated ethylene and propane flames, in which they measured a lower peak soot concentration in the strongly forced flames for both the fuels as compared with the moderately flickering flames. This appears to contradict the trend established in [113]. Furthermore, Connelly [10] also reported that the peak

soot concentration in laminar ethylene flames, forced at 20 Hz, increases with the forcing amplitude. It is worth mentioning that the burners utilised in [10] and [8] have different diameters, 4.0 and 11.0 mm, respectively. It is unclear how the jet diameter and the forcing frequency affect these processes. Nevertheless, it shows the necessity of understanding the non-linear relationship between the forcing conditions and soot evolution.

While the majority studies agree that the extended residence time is the principal factor that promotes the peak soot concentration in a forced flame as compared with its steady equivalent [11, 113, 127, 130], the mechanisms that benefit from the prolonged residence time are still the subject of debate. Kaplan et al. [113] reported that the experimental and computational studies came to contradictory conclusions concerning the factor responsible for the enhanced soot production in the time-varying flames. The numerical models predict that the combined effects of soot inception and surface growth during the extended residence time in fuel-rich regions are the main contributors to the enhanced soot production in the time-varying flame. Conversely, the experimental measurements suggest that the increased soot concentration in the time-varying flame relative to that of the steady counterpart is primarily attributable to the extended soot surface growth on existing particles, where the effect of soot inception is relatively insignificant. However, Zhang and Megaridis [127] suggested that the specific surface growth rates under forcing conditions can be similar or even lower than those in the steady case. The study also implied that stronger soot inception mechanisms in the forced flame are responsible for generating a larger population of incipient particles in the forced flame, ultimately results in a higher peak soot concentration relative to its steady counterpart. Mohammed et al. [131] reported additional acetylene production in the downstream region of the time-varying flame at certain times during the forcing cycle, which supported the notion that the augmented soot surface growth contributes to the enhanced soot production. However, the study did not include any soot measurements. Another computational study conducted by Dworkin et al. [11] showed higher rates of both inception and surface growth in the time-varying flames. However, the study only qualitatively compared the numerical results with the experimental measurements. Additionally, there was a significant discrepancy in the amplitude of the jet exit velocity between the experimental ( $\alpha = 50\%$ ) and computational ( $\alpha = 90\%$ ) cases. There remains a necessity to improve the understanding of the influences of time-varying flow field on soot inception and surface growth.



## 2.4 Research gaps and aims

Despite the enormous efforts devoted to unravelling the underlying mechanisms of soot production in time-dependent reacting flows, there remains a gap between the understanding of soot evolution in steady laminar and unsteady non-premixed combustion. A steady laminar non-premixed jet flame acoustically driven by a well-defined pressure perturbation helps bridge the gap by providing an environment to study soot evolution in a discrete time manner. Before interpreting the phenomena observed in an acoustically forced laminar flame, however, it is important to understand the non-linear relationship between forcing conditions and flame responses. Based on the literature reviewed in this chapter, five important research gaps are identified as follows:

- It is well established that the flame structure decoupled from the incident pressure perturbations when the external forcing frequency is larger than that of the natural flame flickering, 10-20 Hz. However, no experimental study in the literature has examined the behaviour of soot evolution in time-varying flames for multiple forcing frequencies.
- In scaling studies, the burner diameter plays a significant role in characteristic principal dimensionless parameters (*e.g.*, Reynolds, Strouhal and Froude numbers). However, burners used in previous experiments that study unsteady laminar flames ( $Re < 1000$ ) had diameters ranging from 4 to 100 mm. This wide range of burner diameters would inevitably affect the flame structure and soot evolution. However, the influences of burner diameter on the vortex–flame interactions and the underlying mechanisms that promote soot production in time-varying flames remain unclear.
- In the literature, a previous study [8] shows that the intensity of the forcing has a limited effect on the soot production in the time-varying ethylene flames relative to the steady counterpart. Moreover, the strongly forced ethylene flame exhibits a lower peak soot concentration than the moderately forced one. Conversely, another experimental study [10] shows that the peak soot concentration in the time-varying ethylene flames increases as the amplitude of the fuel flow modulation increases. These previous findings seem to contradict each other. There is a necessity to resolve the contradiction in the literature.
- It is clear that an acoustically forced flame exhibits a prolonged residence time, thus has higher values of peak soot concentration and maximum primary particles diameter as compared with its steady equivalent. However, the passage of the forcing-induced vortex affects various flame regions differently. Furthermore, different stages of soot evolution, notably inception, growth/aggregation and oxidation, occur in different flame regions. Hence, to advance the understanding of enhanced soot production in time-varying

flame relative to the steady case, there is a need to identify the principal contributing parameter and mechanism in different flame regions, such as the neck zone and the detached flamelet.

- Soot evolution is dependent on a multitude of parameters. However, most studies in the literature correlate the enhanced soot production in time-varying flames with only one or two parameters. This limits the full understanding of the complex interactions between flame structure, flow field and soot evolution. Several studies [11, 113] have combined experimental data with numerical analysis, in an attempt to deepen the understanding of soot evolution in time-varying flames. Unfortunately, in those studies, the numerical results were not quantitatively validated against measurements, which highlights the need for a comprehensive experimental data set for the validation of reliable models. How do the interactions between properties of flame and flow field affect soot evolution?

The present thesis aims to address the gaps in the literature on soot evolution in time-varying non-premixed flames and answer the research questions posed above. The specific aims of the thesis are:

- To understand and quantify the effects of physical parameters, including the characteristics of external forcing and the diameter of the fuel nozzle, on the flame structure and soot evolution. The knowledge can be used to systematically generate a series of time-varying flames spanning a wide range of conditions, in which general trends regarding soot production can be identified.
- To expand the understanding of soot evolution in time-varying laminar flames by quantifying the soot formation and oxidation along a series of trajectories through the time-varying flame, in terms of histories of mixture fraction, temperature, soot volume fraction and primary soot particle diameter. Additionally, the quantitative experimental data set can serve as validation cases for numerical models that predict quantities that are inaccessible via experimental approaches due to technical challenges, such as mixture fraction and species concentrations.

---

## References

- [1] S. A. Skeen and K. Yasutomi, “Measuring the soot onset temperature in high-pressure *n*-dodecane spray pyrolysis”, *Combustion and Flame* **188** (2018), pp. 483–487.
- [2] A. Drakon, A. Eremin, E. Mikheyeva, B. Shu, M. Fikri, and C. Schulz, “Soot formation in shock-wave-induced pyrolysis of acetylene and benzene with H<sub>2</sub>, O<sub>2</sub>, and CH<sub>4</sub> addition”, *Combustion and Flame* **198** (2018), pp. 158–168.
- [3] M. Sirignano, D. Bartos, M. Conturso, M. Dunn, A. D’Anna, and A. R. Masri, “Detection of nanostructures and soot in laminar premixed flames”, *Combustion and Flame* **176** (2017), pp. 299–308.
- [4] M. Commodo, G. D. Falco, P. Minutolo, and A. D’Anna, “Structure and size of soot nanoparticles in laminar premixed flames at different equivalence ratios”, *Fuel* **216** (2018), pp. 456–462.
- [5] R. J. Santoro, T. T. Yah, J. J. Horvath, and H. G. Semerjian, “The Transport and Growth of Soot Particles in Laminar Diffusion Flames”, *Combustion Science and Technology* **53** (2007), pp. 89–115.
- [6] Y. Wang, A. Makwana, S. Iyer, M. Linevsky, R. J. Santoro, T. A. Litzinger, and J. O’Connor, “Effect of fuel composition on soot and aromatic species distributions in laminar, co-flow flames. Part 1. Non-premixed fuel”, *Combustion and Flame* **189** (2018), pp. 443–455.
- [7] C. R. Shaddix, J. E. Harrington, and K. C. Smyth, “Quantitative Measurements of Enhanced Soot Production in a Flickering Methane/Air Diffusion Flame”, *Combustion and Flame* **99** (1994), pp. 723–732.
- [8] C. R. Shaddix and K. C. Smyth, “Laser-Induced Incandescence Measurements of Soot Production in Steady and Flickering Methane, Propane, and Ethylene Diffusion Flames”, *Combustion and Flame* **107** (1996), pp. 418–452.
- [9] A. Cuoci, A. Frassoldati, T. Faravelli, and E. Ranzi, “Formation of Soot and nitrogen oxides in unsteady counterflow diffusion flames”, *Combustion and Flame* **156** (2009), pp. 2010–2022.
- [10] B. C. Connelly, “Quantitative Characterization of Steady and Time-Varying, Sooting, Laminar Diffusion Flames using Optical Techniques”, Ph.D. dissertation, Yale University, 2009.
- [11] S. B. Dworkin, J. A. Cooke, B. A. V. Bennett, B. C. Connelly, M. B. Long, M. D. Smooke, R. J. Hall, and M. B. Colket, “Distributed-memory parallel computation of a forced, time-dependent, sooting, ethylene/air coflow diffusion flame”, *Combustion Theory and Modelling* **13** (2009), pp. 795–822.
- [12] W. Park, S. Park, R. D. Reitz, and E. Kurtz, “The effect of oxygenated fuel properties on diesel spray combustion and soot formation”, *Combustion and Flame* **180** (2017), pp. 276–283.
- [13] S. Deng, M. E. Mueller, Q. N. Chan, N. H. Qamar, B. B. Dally, Z. T. Alwahabi, and G. J. Nathan, “Hydrodynamic and chemical effects of hydrogen addition on soot evolution in turbulent nonpremixed bluff body ethylene flames”, *Proceedings of the Combustion Institute* **36** (2017), pp. 807–814.

## REFERENCES

---

- [14] N. Qamar, G. J. Nathan, Z. T. Alwahabi, and K. D. King, “The effect of global mixing on soot volume fraction: measurements in simple jet, precessing jet and bluff body flames”, *Proceedings of the Combustion Institute* **30** (2005), pp. 1493–1500.
- [15] M. Köhler, K. P. Geigle, W. Meier, B. M. Crosland, K. A. Thomson, and G. J. Smallwood, “Sooting turbulent jet flame: characterization and quantitative soot measurements”, *Applied Physics B* **104** (2011), pp. 409–425.
- [16] I. Boxx, O. Henold, and K. Geigle, “Laser-induced incandescence measurements in a fired diesel engine at 3 kHz”, *Experiments in Fluids* **56** (2015).
- [17] T. R. Meyer, B. R. Halls, N. Jiang, M. N. Slipchenko, S. Roy, and J. R. Gord, “High-speed, three-dimensional tomographic laser-induced incandescence imaging of soot volume fraction in turbulent flames”, *Optics Express* **24** (2016), pp. 29547–29555.
- [18] H. Bockhorn, “Soot formation in combustion: mechanisms and models”, vol. 59, Springer Science & Business Media, 2013.
- [19] H. Michelsen, “Probing soot formation, chemical and physical evolution, and oxidation: A review of *in situ* diagnostic techniques and needs”, *Proceedings of the Combustion Institute* **36** (2017), pp. 717–735.
- [20] M. Frenklach, “Reaction mechanism of soot formation in flames”, *Physical Chemistry Chemical Physics* **4** (2005), pp. 2028–2037.
- [21] K. Johansson, M. Head-Gordon, P. Schrader, K. Wilson, and H. Michelsen, “Resonance-stabilized hydrocarbon-radical chain reactions may explain soot inception and growth”, *Science* **361** (2018), pp. 997–1000.
- [22] H. Böhm, H. Jander, and D. Tanke, “PAH growth and soot formation in the pyrolysis of acetylene and benzene at high temperatures and pressures: Modeling and experiment”, *Proceedings of the Combustion Institute* **27** (1998), pp. 1605–1612.
- [23] H. Richter, S. Granata, W. H. Green, and J. B. Howard, “Detailed modeling of PAH and soot formation in a laminar premixed benzene/oxygen/argon low-pressure flame”, *Proceedings of the Combustion Institute* **30** (2005), pp. 1397–1405.
- [24] V. Chernov, M. J. Thomson, S. B. Dworkin, N. A. Slavinskaya, and U. Riedel, “Soot formation with C<sub>1</sub> and C<sub>2</sub> fuels using an improved chemical mechanism for PAH growth”, *Combustion and Flame* **161** (2014), pp. 592–601.
- [25] Y. Xuan and G. Blanquart, “Effects of aromatic chemistry-turbulence interactions on soot formation in a turbulent non-premixed flame”, *Proceedings of the Combustion Institute* **35** (2015), pp. 1911–1919.
- [26] S. Park, Y. Wang, S. H. Chung, and M. S. Sarathy, “Compositional effects on PAH and soot formation in counterflow diffusion flames of gasoline surrogate fuels”, *Combustion and Flame* **178** (2017), pp. 46–60.
- [27] C. F. Melius, J. A. Miller, and E. M. Evleth, “Unimolecular reaction mechanisms involving C<sub>3</sub>H<sub>4</sub>, C<sub>4</sub>H<sub>4</sub> and C<sub>6</sub>H<sub>6</sub> hydrocarbon species”, *Proceedings of the Combustion Institute* **24** (1992), pp. 621–628.

- [28] H. Wang and M. Frenklach, “A detailed kinetic modeling study of aromatics formation in laminar premixed acetylene and ethylene flames”, *Combustion and Flame* **110** (1997), pp. 173–221.
- [29] C. S. McEnally, L. D. Pfefferle, B. Atakan, and K. Kohse-Höinghaus, “Studies of aromatic hydrocarbon formation mechanisms in flames: Progress towards closing the fuel gap”, *Progress in Energy and Combustion Science* **32** (2006), pp. 247–294.
- [30] H. Wang, “Formation of nascent soot and other condensed-phase materials in flames”, *Proceedings of the Combustion Institute* **33** (2011), pp. 41–67.
- [31] C. F. Melius, M. E. Colvin, N. M. Marinov, W. J. Pit, and S. M. Senkan, “Reaction mechanism in aromatic hydrocarbon formation involving the C<sub>5</sub>H<sub>5</sub> cyclopentadienyl moiety”, *Proceedings of the Combustion Institute* **26** (1996), pp. 685–692.
- [32] N. Slavinskaya and P. Frank, “A modelling study of aromatic soot precursors formation in laminar methane and ethene flames”, *Combustion and Flame* **156** (2009), pp. 1705–1722.
- [33] S. B. Dworkin, Q. Zhang, M. J. Thomson, N. A. Slavinskaya, and U. Riedel, “Application of an enhanced PAH growth model to soot formation in a laminar coflow ethylene/air diffusion flame”, *Combustion and Flame* **158** (2011), pp. 1682–1695.
- [34] N. A. Slavinskaya, U. Riedel, S. B. Dworkin, and M. J. Thomson, “Detailed numerical modeling of PAH formation and growth in non-premixed ethylene and ethane flames”, *Combustion and Flame* **159** (2012), pp. 979–995.
- [35] M. Frenklach and H. Wang, “Detailed Modeling of Soot Particle Nucleation and Growth”, *Proceedings of the Combustion Institute* **23** (1991), pp. 1559–1566.
- [36] J. T. Mckinnon and J. B. Howard, “The roles of PAH and acetylene in soot nucleation and growth”, *Proceedings of the Combustion Institute* **24** (1992), pp. 965–971.
- [37] J. B. Howard, “Carbon addition and oxidation reactions in heterogeneous combustion and soot formation”, *Proceedings of the Combustion Institute* **23** (1990), pp. 1107–1127.
- [38] A. D’Anna and A. Violi, “A kinetic model for the formation of aromatic hydrocarbons in premixed laminar flames”, *Proceedings of the Combustion Institute* **27** (1998), pp. 425–433.
- [39] A. Violi, A. D’Anna, and A. D’Alessio, “Modeling of particulate formation in combustion and pyrolysis”, *Chemical Engineering Science* **54** (1999), pp. 3433–3442.
- [40] A. D’Anna, A. Violi, and A. D’Alessio, “Modeling the rich combustion of aliphatic hydrocarbons”, *Combustion and Flame* **121** (2000), pp. 418–429.
- [41] A. D’Anna, M. Sirignano, and J. Kent, “A model of particle nucleation in premixed ethylene flames”, *Combustion and Flame* **157** (2010), pp. 2106–2115.
- [42] M. Thomson and T. Mitra, “A radical approach to soot formation”, *Science* **361** (2018), pp. 978–979.
- [43] C. A. Schuetz and M. Frenklach, “Nucleation of soot: molecular dynamics simulations of pyrene dimerization”, *Proceedings of the Combustion Institute* **29** (2002), pp. 2307–2314.

## REFERENCES

---

- [44] Ü. Köylü, G. Faeth, T. Farias, and M. Carvalho, “Fractal and projected structure properties of soot aggregates”, *Combustion and Flame* **100** (1995), pp. 621–633.
- [45] A. Liati, B. T. Brem, L. Durdina, M. Vögtli, Y. A. R. Dasilva, P. D. Eggenschwiler, and J. Wang, “Electron microscopic study of soot particulate matter emissions from aircraft turbine engines”, *Environmental Science and Technology* **48** (), pp. 10975–10983.
- [46] P. Parent, C. Laffon, I. Marhaba, D. Ferry, T. Regier, I. Ortega, B. Chazallon, Y. Carpentier, and C. Focsa, “Nanoscale characterization of aircraft soot: A high-resolution transmission electron microscopy, Raman spectroscopy, X-ray photoelectron and near-edge X-ray absorption spectroscopy study”, *Carbon* **101** (2016), pp. 86–100.
- [47] A. D. Sediako, C. Soong, J. Y. Howe, M. R. Kholghy, and M. J. Thomson, “Real-time observation of soot aggregate oxidation in an Environmental Transmission Electron Microscope”, *Proceedings of the Combustion Institute* **36** (2017), pp. 841–851.
- [48] P. Mitchell and M. Frenklach, “Monte Carlo Simulation of Soot Aggregation with Simultaneous Surface Growth—Why Primary Particles Appear Spherical”, *Proceedings of the Combustion Institute* **27** (1998), pp. 1507–1514.
- [49] P. Mitchell and M. Frenklach, “Particle aggregation with simultaneous surface growth”, *Physical Review E* **67** (2003), p. 061407.
- [50] P. Roth, O. Brandt, and S. Von Gersum, “High temperature oxidation of suspended soot particles verified by CO and CO<sub>2</sub> measurements”, *Proceedings of the Combustion Institute* **23** (1990), pp. 1485–1491.
- [51] A. Cavaliere, R. Barbella, A. Ciajolo, A. D’Anna, and R. Ragucci, “Fuel and soot oxidation in diesel-like conditions”, *Proceedings of the Combustion Institute* **25** (1994), pp. 167–174.
- [52] H. Richter and J. B. Howard, “Formation of polycyclic aromatic hydrocarbons and their growth of soot – a review of chemical reaction pathways”, *Progress in Energy and Combustion Science* **26** (2000), pp. 565–608.
- [53] R. L. V. Wal and A. J. Tomasek, “Soot oxidation: dependence upon initial nanostructure”, *Combustion and Flame* **134** (2003), pp. 1–9.
- [54] K. Neoh, J. Howard, and A. Sarofim, “Effect of oxidation on the physical structure of soot”, *Proceedings of the Combustion Institute* **20** (1984), pp. 951–957.
- [55] H. Ghiassi, P. Toth, I. c. Jaramillo, and J. S. Lighty, “Soot oxidation-induced fragmentation: Part 1: The relationship between soot nanostructure and oxidation-induced fragmentation”, *Combustion and Flame* **163** (2016), pp. 179–187.
- [56] C. A. Echavarria, I. C. Jaramillo, A. F. Sarofim, and J. S. Lighty, “Burnout of soot particles in a two-stage burner with a JP-8 surrogate fuel”, *Combustion and Flame* **159** (2012), pp. 2441–2448.
- [57] H. Ghiassi, I. c. Jaramillo, P. Toth, and J. S. Lighty, “Soot oxidation-induced fragmentation: Part 2: Experimental investigation of the mechanism of fragmentation”, *Combustion and Flame* **163** (2016), pp. 170–178.

- [58] R. S. Barlow, “Laser diagnostics and their interplay with computations to understand turbulent combustion”, *Proceedings of the Combustion Institute* **31** (2007), pp. 49–75.
- [59] I. Glassman and P. Yaccarino, “The temperature effect in sooting diffusion flames”, *Proceedings of the Combustion Institute* **18** (1981), pp. 1175–1183.
- [60] I. Glassman, K. Brezinsky, A. Gomez, and F. Takahashi, “Physical and Chemical Kinetic Effects in Soot Formation”, *Recent Advances in the Aerospace Sciences: In Honor of Luigi Crocco on His Seventy-fifth Birthday*, ed. by C. Casci and C. Bruno, Boston, MA: Springer US, 1985, pp. 345–370.
- [61] R. J. Santoro and T. F. Richardson, “Concentration and Temperature Effects on Soot Formation in Diffusion Flames”, *Soot Formation in Combustion: Mechanisms and Models*, ed. by H. Bockhorn, Berlin, Heidelberg: Springer Berlin Heidelberg, 1994, pp. 221–238.
- [62] S. Graham, J. Homer, and J. Rosenfeld, “The formation and coagulation of soot aerosols generated by the pyrolysis of aromatic hydrocarbons”, *Proceedings of the Royal Society A* **344** (1975), pp. 259–285.
- [63] T. Wang and R. M. nad R.C. Farmer, “Combustion kinetics of soot formation from toluene”, *Proceedings of the Combustion Institute* **18** (1981), pp. 1149–1158.
- [64] M. Frenklach, S. Taki, M. B. Durgaprasad, and R. A. Matula, “Soot formation in shock-tube pyrolysis of acetylene, allene, and 1,3-Butadiene”, *Combustion and Flame* **54** (1983), pp. 81–101.
- [65] M. Frenklach, S. Taki, and R. Matula, “A conceptual model for soot formation in pyrolysis of aromatic hydrocarbons”, *Combustion and Flame* **49** (1983), pp. 275–282.
- [66] G. Blanquart and H. Pitsch, “Analyzing the effects of temperature on soot formation with a joint volume-surface-hydrogen model”, *Combustion and Flame* **156** (2009), pp. 1614–1626.
- [67] R. Santoro, T. Yeh, J. Horvath, and H. Semerjian, “The transport and growth of soot particles in laminar diffusion flames”, *Combustion Science and Technology* **53** (1987), pp. 89–115.
- [68] A. C. Eckbreth, “Laser diagnostics for combustion temperature and species”, vol. 3, CRC Press, 1996.
- [69] J. D. Miller, M. N. Slipchenko, J. G. Mance, S. Roy, and J. R. Gord, “1-kHz two-dimensional coherent anti-Stokes Raman scattering (2D-CARS) for gas-phase thermometry”, *Optics Express* **24** (2016), pp. 24971–24979.
- [70] S. Kampmann, T. Seeger, and A. Leipertz, “Simultaneous coherent anti-Stokes Raman scattering and two-dimensional laser Rayleigh thermometry in a contained technical swirl combustor”, *Applied Optics* **34** (1997), pp. 2780–2786.
- [71] J. Jonuscheit, A. Thumann, M. Schenk, T. Seeger, and A. Leipertz, *Applied Optics* **36** (1997), pp. 3253–3260.

## REFERENCES

---

- [72] S. Roy, J. R. Gord, and A. K. Patnaik, “Recent advances in coherent anti-Stokes Raman scattering spectroscopy: Fundamental developments and applications in reacting flows”, *Progress in Energy and Combustion Science* **36** (2010), pp. 280–306.
- [73] Z. A. Mansurov, “Soot formation in combustion processes (review)”, *Combustion, Explosion, and Shock Waves* **41** (2005), pp. 727–744.
- [74] J. Macfarlane, F. Holderness, and F. Witcher, “Soot Formation Rates in Premixed C<sub>5</sub> and C<sub>6</sub> Hydrocarbon-Air Flames at Pressures up to 20 Atmospheres”, *Combustion and Flame* **8** (1964), pp. 215–229.
- [75] M. Bönig, C. Feldermann, H. Jander, B. Lüers, G. Rudolph, and H. G. Wagner, “Soot formation in premixed C<sub>2</sub>H<sub>4</sub> flat flames at elevated pressure”, *Proceedings of the Combustion Institute* **23** (1991), pp. 1581–1587.
- [76] H. I. Joo and Ö. L. Gülder, “Soot formation and temperature field structure in co-flow laminar methane-air diffusion flames at pressures from 10 to 60 atm”, *Proceedings of the Combustion Institute* **32** (2009), pp. 769–775.
- [77] L. Figura, F. Carbone, and A. Gomez, “Challenges and artifacts of probing high-pressure counterflow laminar diffusion flames”, *Proceedings of the Combustion Institute* **35** (2015), pp. 1871–1878.
- [78] S. R. Turns, “An introduction to combustion: concepts and applications”, 3rd ed., New York, United States: McGraw-Hill, 2012.
- [79] G. Nathan, P. Kalt, Z. Alwahabi, B. Dally, P. Medwell, and Q. Chan, “Recent advances in the measurement of strongly radiating, turbulent reacting flows”, *Progress in Energy and Combustion Science* **38** (2012), pp. 41–61.
- [80] J. H. Frank, K. M. Lyons, D. F. Marran, M. B. Long, S. H. Stråner, and R. W. Bilger, “Mixture fraction imaging in turbulent nonpremixed hydrocarbon flames”, *Proceedings of the Combustion Institute* **25** (1994), pp. 1159–1166.
- [81] R. Barlow, A. Karpetis, J. Frank, and J.-Y. Chen, “Scalar profiles and NO formation in laminar opposed-flow partially premixed methane/air flames”, *Combustion and Flame* **127** (2001), pp. 2102–2118.
- [82] A. Lakshmanarao, M. Renfro, G. King, and N. Laurendeau, “Acetone as a tracer for mixture fraction time-series measurements in turbulent non-reacting jets”, *Experiments in Fluids* **30** (2001), pp. 595–596.
- [83] J. Koch and R. Hanson, “Temperature and excitation wavelength dependencies of 3-pentanone absorption and fluorescence for PLIF applications”, *Applied Physics B* **76** (2003), pp. 319–324.
- [84] W. Koban and J. Koch, “Toluene as a tracer for fuel, temperature and oxygen concentrations”, Technical paper series 2005-01-2091, SAE, 2005.
- [85] A. H. amd V. Narayanaswamy, N. Clemens, and J. Frank, “Mixture fraction imaging in turbulent non-premixed flames with two-photon LIF of krypton”, *Proceedings of the Combustion Institute* **33** (2010), pp. 759–766.
- [86] C. Schulz and V. Sick, “Tracer-LIF diagnostics: quantitative measurement of fuel concentration, temperature and fuel/air ratio in practical combustion systems”, *Progress in Energy and Combustion Science* **31** (2005), pp. 75–121.



- 
- [87] F. Irgens, “Continuum mechanics”, Springer Science & Business Media, 2008.
- [88] G. F. Carrier, F. E. Fendell, and F. E. Marble, “The effect of strain rate on diffusion flames”, *SIAM Journal on Applied Mathematics* **28** (1975), pp. 463–500.
- [89] R. S. Barlow and J. H. Frank, “Effects of turbulence on species mass fractions in methane/air jet flames”, *Proceedings of the Combustion Institute* **27** (1998), pp. 1087–1095.
- [90] J. H. Frank, S. A. Kaiser, and M. B. Long, “Reaction-rate, mixture-fraction, and temperature imaging in turbulent methane/air jet flames”, *Proceedings of the Combustion Institute* **29** (2002), pp. 2687–2694.
- [91] K.-C. Lin and G. M. Faeth, “Effects of hydrodynamics on soot formation in laminar opposed-jet diffusion flames”, *Journal of Propulsion and power* **12** (1996), pp. 691–698.
- [92] D. Dabiri, “Digital particle image thermometry/velocimetry: a review”, *Experiments in Fluids* **46** (2009), pp. 191–241.
- [93] J. Weinkauff, D. Michaelis, A. Dreizler, and B. Böhm, “Tomographic PIV measurements in a turbulent lifted jet flame”, *Experiments in Fluids* **54** (2013), pp. 1624–1628.
- [94] B. Coriton and J. H. Frank, “High-speed tomographic PIV measurements of strain rate intermittency and clustering in turbulent partially-premixed jet flames”, *Proceedings of the Combustion Institute* **35** (2015), pp. 1243–1250.
- [95] D. Han and M. G. Mungal, “Simultaneous measurements of velocity and CH distributions. Part 1: jet flames in co-flow”, *Combustion and Flame* **132** (2003), pp. 565–590.
- [96] D. X. Du, R. L. Axelbaum, and C. K. Law, “Soot formation in strained diffusion flames with gaseous additives”, *Combustion and Flame* **102** (1995), pp. 11–20.
- [97] H. Wang, D. X. Du, C. J. sung, and C. K. Law, “Experiments and numerical simulation on soot formation in opposed-jet ethylene diffusion flames”, *Proceedings of the Combustion Institute* **26** (1996), pp. 2359–2368.
- [98] M. E. Decroix and W. L. Roberts, “Transient flow field effects on soot volume fraction in diffusion flames”, *Combustion Science and Technology* **160** (2000), pp. 165–189.
- [99] M. Bundy, A. Hamins, and K. Y. Lee, “Suppression limits of low strain rate non-premixed methane flames”, *Combustion and Flame* **133** (2003), pp. 299–310.
- [100] V. Huijnen, A. Evlampiev, L. Somers, R. Baert, and L. de Goey, “The effect of the strain rate on PAH/soot formation in laminar counterflow diffusion flames”, *Combustion Science and Technology* **182** (2010), pp. 103–123.
- [101] S. M. Mahmoud, G. J. Nathan, Z. T. Alwahabi, Z. W. Sun, P. R. Medwell, and B. B. Dally, “The effect of exit strain rate on soot volume fraction in turbulent non-premixed jet flames”, *Proceedings of the Combustion Institute* **36** (2017), pp. 889–897.
- [102] U. Vandsburger, I. M. Kennedy, and I. Glassman, “Sooting counter-flow diffusion flames with varying velocity gradients”, *Proceedings of the Combustion Institute* **20** (1984), pp. 1103–1112.

## REFERENCES

---

- [103] A. Beltrame, P. Porshnev, W. Merchan-Merchan, A. Saveliev, A. Fridman, L. A. Kennedy, O. Petrova, S. Zhdanok, F. Amouri, and O. Charon, “Soot and NO formation in methane-oxygen enriched diffusion flames”, *Combustion and Flame* **124** (2001), pp. 295–310.
- [104] H. Böhm, K. Kohse-Höinghaus, F. Lacas, C. Rolon, N. Darabiha, and S. Candel, “On PAH formation in strained counterflow diffusion flames”, *Combustion and Flame* **124** (2001), pp. 127–136.
- [105] D. X. Du, R. L. Axelbaum, and C. K. Law, “Experiments on the sooting limits of aerodynamically-strained diffusion flames”, *Proceedings of the Combustion Institute* **22** (1988), pp. 387–394.
- [106] F. Xu, P. B. Sunderland, and G. M. Faeth, “Soot formation in laminar premixed ethylene/air flames at atmospheric pressure”, *Combustion and Flame* **108** (1997), pp. 471–493.
- [107] M. D. Smooke, M. B. Long, B. C. Connelly, M. B. Colket, and R. J. Hall, “Soot formation in laminar diffusion flames”, *Combustion and Flame* **143** (2005), pp. 613–628.
- [108] M. C. Drake and R. J. Blint, “Thermal NO<sub>x</sub> in stretch laminar opposed-flow diffusion flames with CO/H<sub>2</sub>/N<sub>2</sub> fuel”, *Combustion and Flame* **76** (1989), pp. 151–167.
- [109] S. R. Turns and F. H. Myhr, “Oxides of nitrogen emissions from turbulent jet flames: Part I – fuel effects and flame radiation”, *Combustion and Flame* **87** (1991), pp. 319–335.
- [110] M. C. Drake and R. J. Blint, “Relative importance of nitric oxide formation mechanisms in laminar opposed-flow diffusion flames”, *Combustion and Flame* **83** (1991), pp. 185–203.
- [111] A. Vranos and R. J. Hall, “Influence of radiative loss on nitric oxide formation in counterflow diffusion flames at high pressure”, *Combustion and Flame* **93** (1993), pp. 230–238.
- [112] A. Grudno and K. Seshadri, “Characteristic residence times of laminar non-premixed flames at extinction”, *Combustion Science and Technology* **112** (1996), pp. 199–210.
- [113] C. R. Kaplan, C. R. Shaddix, and K. C. Smyth, “Computations of enhanced soot production in time-varying ethylene/ air diffusion flames”, *Combustion and Flame* **106** (1996), pp. 89–115.
- [114] L. D. Chen, J. P. Seaba, W. M. Roquemore, and L. P. Goss, “Buoyant diffusion flames”, *Proceedings of the Combustion Institute* **22** (1988), pp. 677–684.
- [115] J. Buckmaster and N. Peters, “The infinite candle and its stability – a paradigm for flickering diffusion flame”, *Proceedings of the Combustion Institute* **21** (1988), pp. 1829–1836.
- [116] N. Peters, “Laminar diffusion flamelet models in non-premixed turbulent combustion”, *Progress in Energy and Combustion Science* **10** (1984), pp. 319–339.
- [117] P. H. Renard, D. Thévenin, J. C. Rolon, and S. Candel, “Dynamics of flame/vortex interactions”, *Progress in Energy and Combustion Science* **26** (2000), pp. 225–282.

- 
- [118] D. S. Chamberlin and A. Rose, “The flicker of luminous flames”, *Industrial & Engineering Chemistry Research* **20** (1928), pp. 1013–1016.
- [119] A. J. Grant and J. M. Jones, “Low-frequency diffusion flame oscillations”, *Combustion and Flame* **25** (1975), pp. 153–160.
- [120] H. Sato, K. Amagai, and M. Arai, “Diffusion flames and their flickering motions related with Froude numbers under various gravity levels”, *Combustion and Flame* **123** (2000), pp. 107–118.
- [121] M. Sánchez-Sanz, B. A. V. Bennett, M. D. Smooke, and A. Liñán, “Influence of Strouhal number on pulsating methane-air coflow jet diffusion flames”, *Combustion Theory and Modelling* **14** (2010), pp. 453–478.
- [122] D. Durox, T. Yuan, F. Baillot, and J. M. Most, “Premixed and diffusion flames in a centrifuge”, *Combustion and Flame* **102** (1995), pp. 501–511.
- [123] A. Hamins, J. C. Yang, and T. Kashiwagi, “An experimental investigation of the pulsation frequency of flames”, *Proceedings of the Combustion Institute* **24** (1992), pp. 1695–1702.
- [124] R. I. Emori and K. Saito, “A study of scaling laws in pool and crib fires”, *Combustion Science and Technology* **31** (1983), pp. 217–231.
- [125] D. Chamberlin and A. Rose, “The flicker of luminous flames”, *Proceedings of the Combustion Institute* **1** (1948), pp. 27–32.
- [126] A. W. Strawa and B. J. Cantwell, “Visualization of the structure of a pulsed methane-air diffusion flame”, *Phys. Fluids* **28** (1985), pp. 2317–2320.
- [127] J. Zhang and C. M. Megaridis, “Soot microstructure in steady and flickering laminar methane/air diffusion flames”, *Combustion and Flame* **112** (1998), pp. 473–484.
- [128] O. A. Ezekoye, K. M. Martin, and F. Bisetti, “Pulsed flow modulation of soot production in a laminar jet-diffusion flame”, *Proceedings of the Combustion Institute* **30** (2005), pp. 1485–1492.
- [129] J. Hentschel, R. Suntz, and H. Bockhorn, “Soot formation and oxidation in oscillating methane-air diffusion flames at elevated pressure”, *Applied Optics* **44** (2005), pp. 6673–6681.
- [130] H. S. Sapmaz, “Soot measurements in steady and pulsed ethylene/air diffusion flames using laser-induced incandescence”, Ph.D. dissertation, Florida International University, 2006.
- [131] R. K. Mohammed, M. A. Tanoff, M. D. Smooke, A. M. Schaffer, and M. B. Long, “Computational and experimental study of a forced, time-varying, axisymmetric, laminar diffusion flame”, *Proceedings of the Combustion Institute* **27** (1998), pp. 693–702.

[This page is intentionally left blank]

# Chapter 3

## Methodology

This chapter provides details of the apparatus and diagnostic techniques employed in this thesis. To adequately describe the steady and time-varying flames, multiple optical-based techniques were used to characterise the soot, reaction zone, temperature and flow fields. Computational analysis was performed to complement the experimental studies, focused on the distribution of key species concentrations.

### 3.1 Co-flow burner

Figure 3.1 presents the cross-sectional diagram of the co-flow burner used in the thesis. The burner was a replica of the Yale Co-flow Burner, used in the work of Connelly [1]. In addition to the original 4.0-mm-inner-diameter fuel tube (wall thickness,  $\delta = 0.38$  mm), two interchangeable fuel tubes, with inner diameters of 5.6 and 8.0 mm ( $\delta = 1.2$  and 1 mm, respectively) were built to meet one of the objectives. The fuel issues from a cylindrical tube into a concentric 74-mm-diameter air co-flow. A loudspeaker at the bottom of the fuel plenum was driven to impose pressure perturbations onto the fuel stream. The co-flow was conditioned with the use of glass beads sandwiched between a pair of Hastelloy-X (a nickel–chromium–iron–molybdenum alloy) honeycombs. All the flames studied in this thesis are fuelled with nitrogen-diluted ethylene. Fuel dilution is necessary for altering the soot production of flames to prevent smoking.

[This page is intentionally left blank]

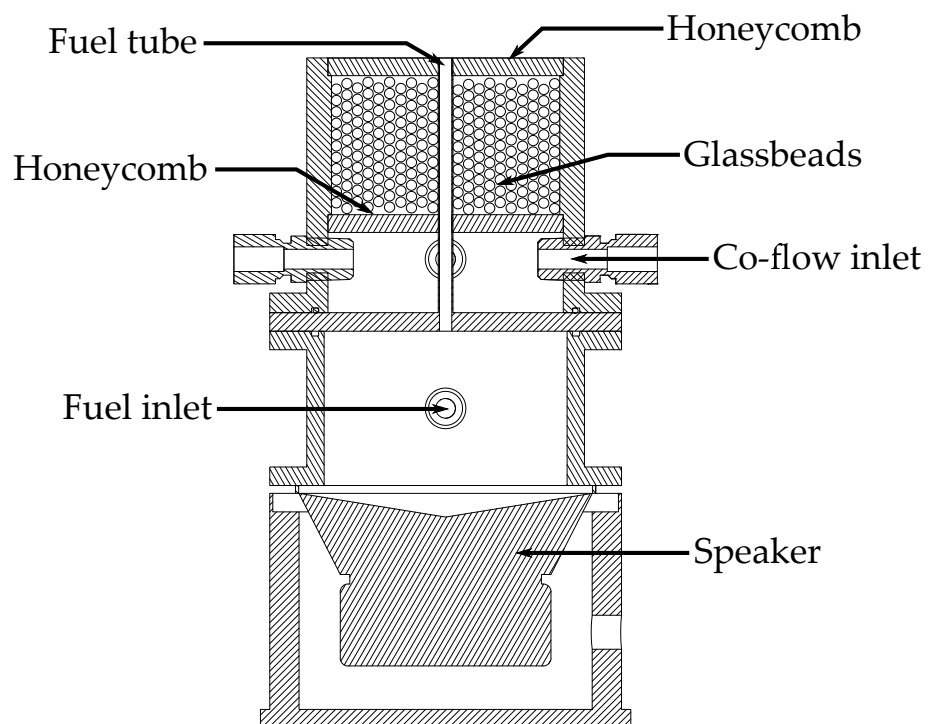


**Figure 3.1** Cross-sectional diagram of the co-flow burner.

## 3.2 Studied flame conditions

Yale University [2] has experimentally investigated a series of steady and time-varying laminar flames, and the measurements are publicly accessible. All the time-varying flames (both ethylene and methane) were operated with a 4.0-mm-inner-diameter nozzle and acoustically forced at 20 Hz. The first step of the experiments was to reproduce one of those flames. An ethylene non-premixed flames with 32% of fuel diluted with nitrogen, by volume, was chosen to be the first test case. The fuel dilution was necessary to avoid smoking. In addition to 20 Hz forcing, the laminar flame was acoustically forced at 40 Hz, with the same amplitude, to investigate the influence of frequency on time-varying flames. The bulk exit velocities of the fuel and air co-flow were maintained at  $0.35 \text{ m}\cdot\text{s}^{-1}$  for both cases.

The second part of the experiments involved three steady (with nozzle diameters of 4.0, 5.6 and 8.0 mm) and six time-varying laminar flames (two forcing amplitudes for each nozzle diameter). The fuel concentration was 41.7% ethylene and 58.3% nitrogen, slightly different from the 20- and 40-Hz time-varying flames. The volumetric flow rates of fuel and air co-flow were remained the same, 0.31 and 60.0 standard litres per minute (SLPM), respectively. Table 3.1 summaries the test conditions. The Reynolds numbers were selected to obtain a similar natural flickering frequency for all cases. Sato et al. [3] reported that the natural flickering frequency is approximately 10 Hz for laminar reacting flows in the region of  $Re \leq 700$ , regardless of the nozzle diameter.

The experiments also studied the effects of the forcing amplitude on the flame response and soot evolution. However, the relationship between the flow response and acoustic forcing is non-linear, which makes it challenging to determine the amplitude of the system. In the thesis, the forcing amplitude is defined as

$$\alpha = \frac{U_{cl,max} - \bar{U}_{cl}}{\bar{U}_{cl}} \quad (3.1)$$

where  $U_{cl,max}$  is the maximum centreline velocity and  $\bar{U}_{cl}$  is the mean centreline velocity. Two different forcing amplitude were applied to each forced flame: 25% and 50% for the 4.0- and 8.0-mm-diameter burners, while 50% and 75% for the 5.6-mm-diameter burner. The flame with 4.0-mm-diameter could not be forced by a forcing amplitude larger than 50% as it led to blow-off. Furthermore, the magnitudes of the positive and negative phases of the oscillation are asymmetric. As a result, a forcing amplitude larger than 50% is also unsuitable for the forced flames with 8.0-mm-diameter burner since it can lead to a negative flow during part of the cycle, which is undesired.



**Table 3.1** Summary of test conditions for the steady and 10-Hz time-varying flames.

	Cases	$D$ (mm)	$U_f$ (m/s)	$U_c$ (m/s)	$\alpha$ (-)	$f$ (Hz)	$St$ (-)	$Fr$ (-)	$Re$ (-)
Steady	S-1	4.0	0.41	0.83	-	0	0	4.28	147
	S-2	5.6	0.21	0.36	-	0	0	0.80	104
	S-3	8.0	0.10	0.21	-	0	0	0.13	72
Forced	F-1	4.0	0.41	1.25	50%	10	0.10	4.28	147
	F-2	5.6	0.21	0.53	50%	10	0.27	0.80	104
	F-3	8.0	0.10	0.31	50%	10	0.80	0.13	72
	F-4	4.0	0.41	1.04	25%	10	0.10	4.28	147
	F-5	5.6	0.21	0.62	75%	10	0.27	0.80	104
	F-6	8.0	0.10	0.27	25%	10	0.80	0.13	72

### 3.3 Optical diagnostic techniques

Figure 3.2 shows the layout of lasers and cameras utilised in the simultaneous measurements of soot volume fraction, primary particle diameter, OH concentration distribution and temperature profile. Additionally, velocity measurement was performed independent of all these measurements.

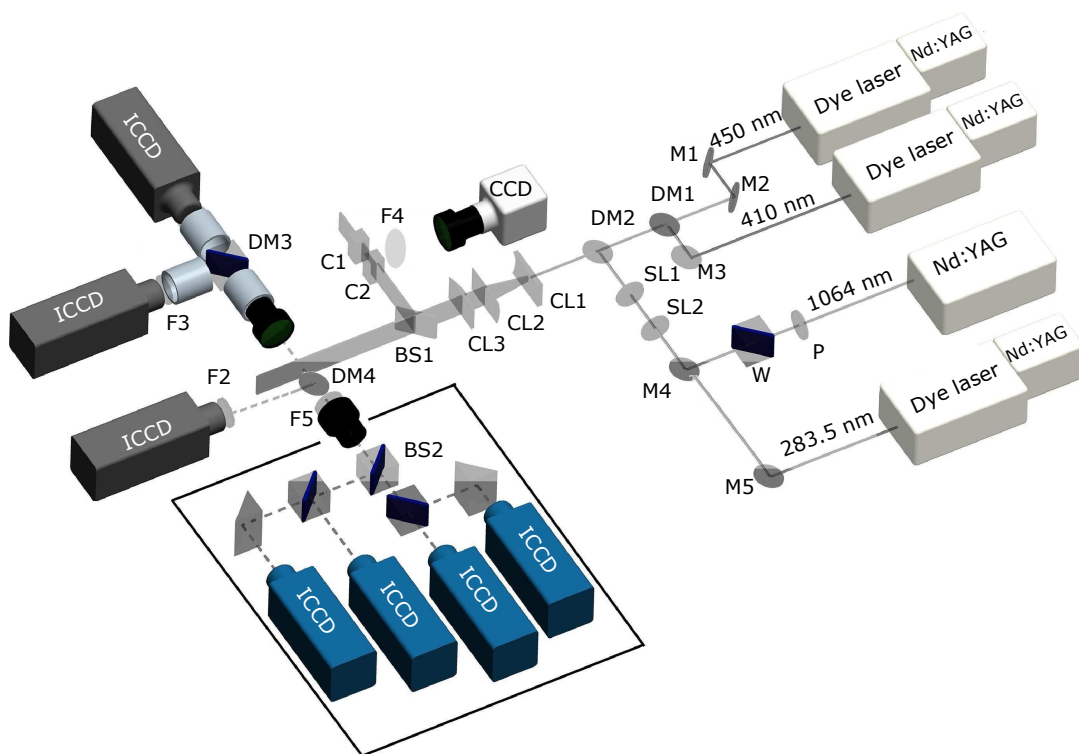


**Figure 3.2** Experimental setup of burner and the simultaneous measurements of Laser-Induced Incandescence (LII), Time-Resolved LII (TiRe-LII), Non-Linear regime of Two-Line Atomic Fluorescence thermometry (NTLAF) and Planar Laser-Induced Fluorescence for hydroxyl radical (OH-PLIF). M: mirror; DM: dichroic beam-splitter; W: half-wave plate; P: Glan-laser polariser; CL: cylindrical lens; SL: spherical lens; C: cuvette; F: band-pass filter; BS: prism beam splitter.

### 3.3.1 Laser-Induced Incandescence

Within the flame environment, soot can be characterised by the total amount of the condensed phase, often expressed as the soot volume fraction,  $f_v$  (ppm); the diameter of the primary soot particles,  $d_p$  (nm); and the number density of the soot particles,  $N$  ( $\text{m}^{-3}$ ). The relationship between the quantities can be expressed as

$$f_v = \frac{\pi}{6} N \cdot d_p^3, \quad (3.2)$$

assuming the size distribution is mono-disperse and the soot particles are spherical.

Melton [4] demonstrated that it is possible to acquire the soot volume fraction and its size distribution in a sooting flame using an optical diagnostic technique, Laser-Induced Incandescence (LII). The principle of the LII technique involves heating of the soot particles to approximately 4000 K, a temperature far above the surrounding gas temperature (typically  $\sim 2500$  K) by introducing a laser beam with sufficient energy flux into the soot field. Subsequently, the soot particles at elevated temperature emit incandescence which is detected and used to determine the local  $f_v$ . The intensity of the detected LII signal  $S_{LII}$  can be expressed as a function of time and laser wavelength [5]:

$$S_{LII}(t, \lambda_i) = C \frac{8 \cdot \pi \cdot c^2 \cdot h}{\lambda_i^5} \left[ \exp \left( \frac{h \cdot c}{\lambda_i \cdot k_B \cdot T(t)} \right) - 1 \right]^{-1} \times \pi^2 \cdot d_p(t)^3 \cdot \frac{E(m, \lambda_i)}{\lambda_i} \quad (3.3)$$

where  $\lambda_i$  is the emission wavelength and  $E(m, \lambda_i)$  is the refractive-index function for absorption,  $m$  is the complex refractive index of soot considered at  $\lambda_i$ ,  $h$  is the Planck constant,  $c$  is the speed of light in vacuum,  $k_B$  is the Boltzmann constant and  $C$  is the empirical factor related to the optical arrangement. The symbols  $T(t)$  and  $d_p(t)$  represent the temporal profiles of temperature and primary particle diameter, respectively. The current work assumed the absorption function to be  $E(m) = 0.232 + 1.2546 \times 10^5 \cdot \lambda_i$ , where  $\lambda_i$  is in meters [6]. A considerable amount of work [7–10] has been dedicated to the measurement of the spectral dependence of  $E(m)$  by a combination of laser extinction (LE) and gravimetric determination of soot concentration. The magnitude of  $E(m)$  is sensitive to wavelength [11], particle composition [12] and particle temperature [11].

To obtain the  $f_v$  measurement, one must calibrate LII signals through comparison with extinction measurements, in which  $E(m)$  is of principal importance. The LE technique, performed in a well-defined laminar premixed flame, is most

commonly utilised to acquire the calibration factor. The dimensionless soot extinction coefficient,  $K_{ext}$ , can be described by Bouguer's Law:

$$K_{ext} = \frac{6\pi^2}{\lambda_i} \cdot N \cdot d_p^3 \cdot E(m) = -\frac{6\pi^2}{\lambda_i} \cdot N \cdot d_p^3 \cdot \text{Im} \left\{ \frac{m^2 - 1}{m^2 + 2} \right\}. \quad (3.4)$$

The calibration method relies on the assumption of negligible scattering, which is almost never true but is reasonable in the Rayleigh regime [13] where the soot particle diameters are expected to be in the range of  $d_p < 0.3\lambda/\pi$ . This limits the soot diameters to  $< 50$  nm,  $< 60$  nm and  $< 101$  nm, for incident laser wavelengths of 532, 632 and 1064 nm, respectively. Even though, in principle, any wavelength in the visible or infra-red (IR) regions can be utilised for the LII application, the Nd:YAG laser at fundamental wavelength, 1064 nm, is commonly employed rather than other harmonics to minimise interferences from a variety of sources.

The principal interference is the emissions from the C<sub>2</sub> Swan bands, especially when the wavelength of the excitation laser is located between the  $\Delta\nu = +1, 0, -1$  corresponding to wavelengths of 473.7, 516.5 and 563.6 nm, respectively. While emissions from C<sub>2</sub> Swan bands can be induced by 1064-nm excitation at high laser fluences, their intensity is significantly weaker than those emitted with 532-nm excitation. Another form of interference comes from Laser-Induced Fluorescence (LIF) of Polycyclic Aromatic Hydrocarbons (PAH) which is excited by visible or ultra-violet (UV) light. Fluorescence emitted from excited PAH extends over a broad spectral range in the visible region, thus it is challenging to filter it from the LII.

### 3.4 Time-Resolved Laser-Induced Incandescence

Subsequent to the laser heating of soot particles, the temperature of the soot particles gradually decreases due to conductive and radiative heat losses. The temporal variation in the LII signal intensity qualitatively follows the temperature of the soot particle in time, while the cooling rate is inversely proportional to the volume-to-surface area ratio. Thus, with an interpretation of the time-resolved detection of the LII signal as it decays can be used to determine the value of  $d_p$ . The ability to determine accurate  $d_p$  is principally limited by the accuracy of the model that describes the cooling process of the heated soot particles. The LII model numerically describes the rate of change of the internal energy stored by a soot particle ( $\dot{Q}_{int}$ ), which balances the rates of energy gain by laser absorption ( $\dot{Q}_{abs}$ ) and energy dissipation primarily by conduction ( $\dot{Q}_{cond}$ ), sublimation ( $\dot{Q}_{sub}$ )

and radiation ( $\dot{Q}_{\text{radiation}}$ ):

$$\dot{Q}_{\text{int}} = \dot{Q}_{\text{abs}} - \dot{Q}_{\text{cond}} - \dot{Q}_{\text{sub}} - \dot{Q}_{\text{rad}}. \quad (3.5)$$

In the following definition of each individual components of Eq. 3.5, two subscripts  $p$  and  $g$  are used to specify the properties of particle or gas, respectively. Firstly, the rate of change in the internal energy of the particle is defined as

$$\dot{Q}_{\text{int}} = \frac{d(m_p \cdot c_p \cdot T_p)}{dt}, \quad (3.6)$$

where  $m_p$ ,  $c_p$  and  $T_p$  are the mass, heat capacity and temperature of the soot particle, respectively. The rate of laser energy absorption is a function of the incident laser intensity,  $I(t)$  and the absorption cross section,  $C_{\text{abs}}$ :

$$\dot{Q}_{\text{abs}} = C_{\text{abs}} I(t) = \frac{\pi^2 \cdot d_p^3}{\lambda_i} \cdot E(m) \cdot I(t), \quad (3.7)$$

Equations 3.8, 3.10 and 3.11 describe the energy loss via three different ways: conduction, sublimation and radiation, respectively.

The rate of conductive heat loss can be described with the free molecular regime theory, which is expressed as

$$\dot{Q}_{\text{cond}} = \frac{1}{8} \alpha \cdot \pi \cdot d_p^2 \cdot P \cdot \sqrt{\frac{8k_B \cdot T_g}{\pi \cdot m_g} \frac{\gamma^* + 1}{\gamma^* - 1}} \left( \frac{T_p}{T_g} - 1 \right), \quad (3.8)$$

where  $\alpha$  is the thermal accommodation coefficient,  $k_B$  is the Boltzmann constant, ( $= 1.381 \times 10^{-23} \text{ J} \cdot \text{K}^{-1}$ ),  $P$  is the gaseous pressure and  $\gamma^*$  is the mean heat capacity ratio, which is defined as [14]

$$\frac{1}{\gamma^* - 1} = \frac{1}{T_p - T_g} \int_{T_g}^{T_p} \frac{1}{\gamma(T) - 1} \cdot dT, \quad (3.9)$$

in which  $\gamma(T)$  is the heat capacity ratio. The rate of energy loss through material sublimation can be expressed as

$$\dot{Q}_{\text{sub}} = \frac{\Delta H_v}{M_p} \frac{dm_p}{dt}, \quad (3.10)$$

where  $\Delta H_v$  is the enthalpy of sublimation of soot,  $M_p$  is the molar mass of the particle and  $dm_p/dt$  is the mass flux. Meanwhile, the rate of radiative heat loss can be described using the Stefan-Boltzmann law

$$\dot{Q}_{\text{rad}} = \pi \cdot d_p^2 \cdot \sigma_B \cdot (T_p^4 - T_g^4), \quad (3.11)$$

where  $\sigma_B$  is the Stefan-Boltzmann constant,  $= 5.67 \times 10^{-8} \text{ W} \cdot \text{m}^{-2} \cdot \text{K}^{-4}$ .

Equation 3.5 is then numerically solved by inserting Eqs. 3.7, 3.8, 3.10 and 3.11 to provide the time histories of  $d_p(t)$ ,  $m_p(t)$  and  $T(t)$  [6]. Then, the intensity of the LII signal can be determined from the particle temperature using various approaches [1, 15]. The value of  $d_p$  can be determined by comparing the decay curves of experimental and numerical LII signals. Liu et al. [16] suggested that the poly-dispersity in aggregate size is minor to the particle temperature decay after the laser pulse. In this case, the heat conduction between soot particles and the surrounding gas takes place in the free-molecular regime. However, the knowledge of the poly-disperse aggregate size is critical when heat conduction occurs in the near transition regime. In this case, the temporal evolution of the soot particle temperature alone is insufficient to determine the primary particle diameter. Nevertheless, poly-disperse in particle size is important in the measurement of  $d_p$ . Evaluating the primary particle size with a mono-disperse assumption results in a mono-disperse equivalent mean particle size that is biased towards larger sizes [17]. However, determining the aggregate number and poly-disperse distribution experiment are difficult to achieve in the current experimental setup. Hence, in the present work, the primary particles were assumed to be non-aggregated with a mono-disperse size distribution [6]. Furthermore, the maximum temperature that soot particles reach also has an influence on the  $d_p$  measurement. The thermal radiation emitted by the hottest particles contributes most to the incandescence signal because of the non-linear temperature dependence of Planck's law [18]. As a result, the TiRe-LII technique employed in this work tends to overestimate the magnitude of  $d_p$  by a factor of two. Additionally, the minimum detection threshold for  $d_p$  is limited to 5 nm.

### 3.5 Two-Line Atomic Fluorescence

Alkemade [19] was the first to theoretically confirm the feasibility of evaluating the flame temperature through Two-Line Atomic Fluorescence (TLAF). The theory was subsequently applied to thermometry in combustion environments by Omenetto et al. [20] and Haraguchi et al. [21]. The fundamental principle of the TLAF technique involves optical excitation of the two electronic transitional states of the atomic species and the subsequent detection of the resultant fluorescence emissions. Of the available atomic species, indium has been identified as a suitable thermometry species for TLAF [21]. Figure 3.3 schematically illustrates the two optically accessible transitions of indium, dubbed Stokes and anti-Stokes transitions, corresponding to the  $5^2P_{1/2} \rightarrow 6^2S_{1/2}$  and  $5^2P_{3/2} \rightarrow 6^2S_{1/2}$  transitions, respectively. Three electronic energy levels are depicted in Fig. 3.3 where the first excited level state (level 1) is close to the ground state (level 0) so both are populated at the temperatures of interest while the second excited state (level 2) is sufficiently high so that its natural population is virtually zero.

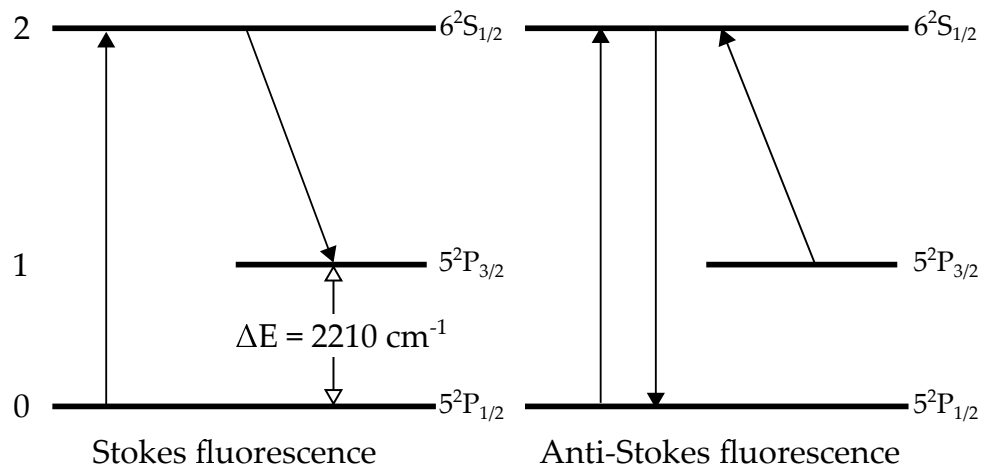


**Figure 3.3** Schematic diagram of the fluorescence processes for indium: Stokes and Anti-Stokes fluorescences. Adapted from Omenetto et al. [20]

The Stokes transition requires an excitation laser at 410.18 nm and the subsequent fluorescence is detected at 451.13 nm. Conversely, the anti-Stokes transition is excited at 451.13 nm and emits a fluorescence at 410.18 nm. Consequently, the relative populations in the two lower states when in a thermal equilibrium can be estimated based on the ratio of the fluorescence signals, which results in the local temperature. By applying the rate equations for the optical excitations and the fluorescent emissions while incorporating the Boltzmann distribution, in the linear excitation regime, the temperature expression is given by [22]

$$T = \frac{\Delta E_{10}/k}{\ln\left(\frac{F_{21}}{I_{02}}\right) - \ln\left(\frac{F_{20}}{I_{12}}\right) + 4\ln\left(\frac{\lambda_{21}}{\lambda_{20}}\right) + C_t} \quad (3.12)$$

Here  $\Delta E$  is the energy difference between the energy levels,  $k$  is the Boltzmann constant,  $F$  is the fluorescence,  $I$  is the laser spectral irradiance,  $\lambda$  is the wavelength and  $C_t$  is a constant dependent on a number of experimental factors. Dual subscripts (0, 1 and 2 represent ground state, the first excited level and the second excited state, respectively) indicate a transition from the first energy level to the second. For example,  $F_{20}$  represents the fluorescence emitted when the energy level of indium transits from level 2 to ground state (refer to Fig. 3.3). Equation 3.12 relies on the linear relationship between the excitation fluence and the resulting fluorescence signal. Within the linear regime, the optical excitation is limited to a low laser fluence which resulting in a low signal-to-noise ratio (SNR) fluorescence signal. Nonetheless, the fluorescence signal can be improved by extending the excitation fluence beyond the linear limitation. As a result, the derivations developed in the linear excitation regime (Eq 3.12) are no longer fit to describe the non-linear relationship between the excitation fluence and the resultant fluorescence signal. Without any simplifications arising from the linearity assumption, the derivation of the temperature follows a similar approach but includes two additional parameters that allow the equation to be independent of the fluence regime [22]. The equation for the Non-linear excitation regime of TLAF (NTLAF) can be expressed as

$$T = \frac{\Delta E_{10}/k}{\ln\left(F_{21} \times \left(1 + \frac{C_S}{I_{20}}\right)\right) - \ln\left(F_{20} \times \left(1 + \frac{C_A}{I_{21}}\right)\right) + C_t}, \quad (3.13)$$

where the parameters  $C_S$ ,  $C_A$  and  $C_T$  are defined as

$$C_S = \frac{Q + A}{B_{20}}, \quad (3.14)$$



$$C_A = \frac{Q + A}{B_{21}} \quad (3.15)$$

and

$$C_T = \ln \left( \frac{\nu_{20}}{\nu_{21}} \right) + \ln \left( \frac{\Omega_{20}}{\Omega_{21}} \right) + \ln \left( \frac{\epsilon_{20}}{\epsilon_{21}} \right) + \ln \left( \frac{A_{20}}{A_{21}} \right). \quad (3.16)$$

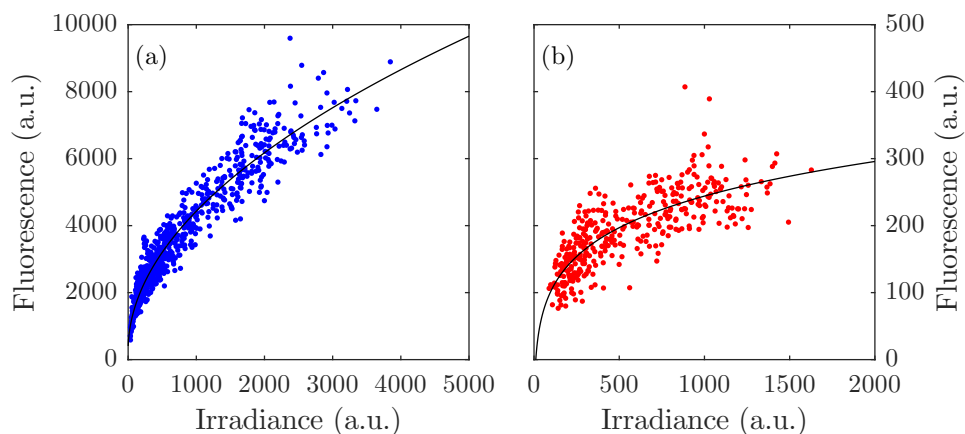
Here,  $Q$  is the non-radiative rate constant,  $A$  is the transition probability coefficient for spontaneous absorption or emission,  $B$  is the transition probability coefficient for stimulated absorption or emission,  $\nu$  is the frequency of fluorescence signals,  $\Omega$  is the collection solid angle,  $\epsilon$  represents the collection efficiency and  $A = A_{20} + A_{21}$ .

Since the TLAF technique requires tracer species, the seeding of indium constitutes an essential part of the diagnostic system. Indium can be introduced into the flame via feeding the fuel stream with indium chloride ( $\text{InCl}_3$ ) dissolved in a solvent using an ultrasonic nebuliser [22]. Unfortunately, the presence of solvent required to transport the  $\text{InCl}_3$  droplets inevitably decreases (except when the solvent is also fuel) the local flame temperature through evaporation [23]. Furthermore, the addition of solvents tends to influence the local stoichiometry which in turn affects the sooting propensity [24]. Consequently, these disadvantages have prompted the development of alternative seeding techniques. Of major approaches, ablation seeding of nanoparticles emerges as an attractive option as it offers the potential to deliver pure indium nanoparticles [25]. Additionally, nanoparticles have a lower melting point [26], a larger absorption cross-section [27] and a higher reactivity [28] than macroparticles.

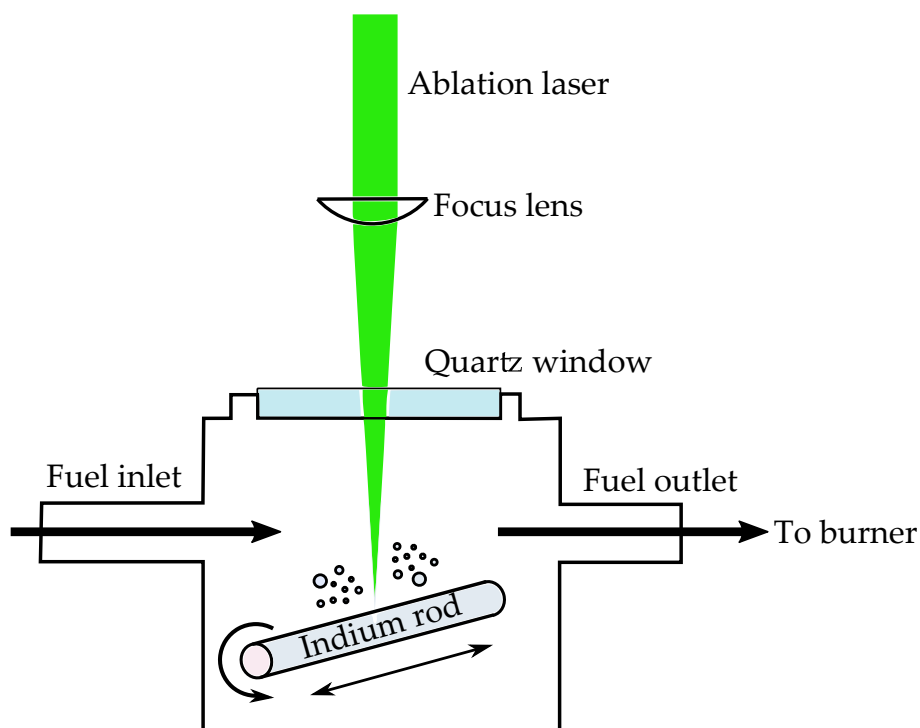
Figure 3.4 (a) and (b) are examples of the intensity of indium fluorescence signals as a function of the laser irradiance for Stokes and anti-Stokes excitations, respectively, collected in a flat-flame. The adiabatic temperature for the steady premixed flame is calculated to be 2234 K using the OPPDIF routine of CHEMKIN, with the GRI-Mech 3.0 mechanism [29]. This is 260 K higher than the thermocouple measurement, which is consistent with the enhanced heat loss through the burner. The parameters  $C_S$  and  $C_A$  are derived from the curve fits of the plots, over a range of laser intensity. The  $C_T$  is determined via a calibration with the use of temperature measurements from an alternative thermometry technique (*e.g.*, thermocouple) as a reference point, after  $C_S$  and  $C_A$  are determined.

Figure 3.5 shows a schematic diagram of the in-house built indium seeding device [25, 30, 31]. The seeding of indium was achieved by the laser ablation method which employed a pulsed laser beam to remove indium nanoparticles from the surface of an indium rod that was placed within a mounting device. Its main purpose was to mount an indium rod on a motorised rotating shaft

to provide a combined rotational and translational motion that allowed each ablating pulse to focus on a “fresh” region of the rod. The fuel supply system was arranged so that the fuel passed through the mounting device, carrying the indium nanoparticles into the fuel.



**Figure 3.4** Fluorescence versus irradiance for (a) Stokes and (b) anti-Stokes transitions. Solid line represents the curve fit.



**Figure 3.5** Schematic of a laser ablation indium seeding system.

### 3.6 OH Planar Laser-Induced Fluorescence

The distribution of OH is often used as an indicator of flame position because of its relatively high concentration in the reaction zone [32–34]. Laser-Induced Fluorescence (LIF) is the main technique for OH detection in reacting flows. It can be extended into planar imaging by transforming the excitation laser into a sheet, known as OH Planar Laser-Induced Fluorescence (OH-PLIF).

The hydroxyl (OH) radical is an important intermediate species in combustion chemistry since it plays a vital role in the oxidation of hydrocarbon fuels. The principal reactions producing OH are



and

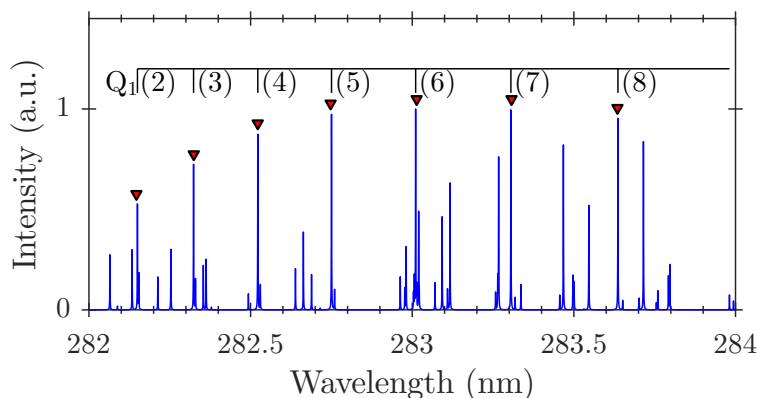


Additionally, a small fraction of hydroxyl in the electronic excited state (OH\*) is produced primarily through the reaction [35]

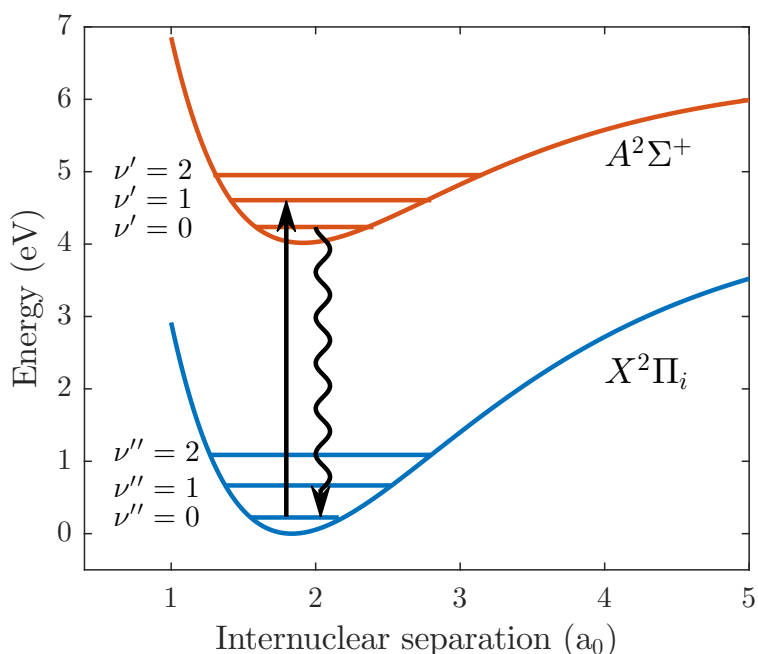


Figure 3.6 shows a simulation of LIF excitation spectra modelled by LIFBASE [36]. The Q<sub>1</sub>(8) line was chosen to excite OH molecules due to its relative insensitivity to changes in temperature over the range of interest [37, 38]. Figure 3.7 presents the electronic transition  $A^2\Sigma^+ \leftarrow X^2\Pi (1,0)$  on which the experimental OH measurements in this thesis was based. Absorption of photons at a wavelength of approximately 283.6 nm raises the OH molecules from its electronic ground state ( $X^2\Pi_i$ ) to the first excited electronic state ( $A^2\Sigma^+$ ). Subsequently, the Q<sub>1</sub>(8) transition emits fluorescence at approximately 308 nm.

[This page is intentionally left blank]



**Figure 3.6** Simulation of LIF excitation spectra by LIFBASE [36] (assumed a resolution of 0.01 nm, Gaussian line shape), showing the Q-branch transitions of the  $A^2\Sigma^+(\nu' = 1) \leftarrow X^2\Pi_i(\nu'' = 0)$  OH band. The line  $Q_1(8)$  at 283.6 nm was used to excite OH.



**Figure 3.7** Potential energy curves for the ground state ( $X^2\Pi_i$ ) and the first excitation state ( $A^2\Sigma^+$ ) of OH. The upward arrow represents the absorption of a photon near 283.6 nm,  $A^2\Sigma^+(\nu' = 1) \leftarrow X^2\Pi_i(\nu'' = 0)$ , while the downward arrow represents the subsequent fluorescence emission near 308 nm. The internuclear separation is given in the unit of Bohr radius,  $1 a_0 \approx 5.29 \times 10^{-11}$  m. Molecular constant used for the Morse potential curves were taken from [39].

### 3.7 Particle Image Velocimetry

Particle Image Velocimetry (PIV) is a well-established flow visualisation technique. Excellent sources of information on the fundamental aspects of PIV can be found in the literature [40, 41]. The PIV technique provides global planar velocity measurements in a cross-section of a flow and it is capable of mapping the evolution of coherent structure through time. The principle of PIV technique based on successively recording images of the fluid seeded with particles with a size sufficiently small to faithfully trace the flow dynamics. The fidelity of the flow tracers can be evaluated by calculating the Stokes number ( $Stk$ ):

$$Stk = \frac{\rho_p \cdot d_p^2 \cdot u_f}{18 \cdot \mu \cdot L}, \quad (3.20)$$

where  $\rho_p$  is the particle density,  $d_p$  is the particle diameter,  $u_f$  is the fluid velocity,  $\mu$  is the fluid dynamic viscosity and  $L$  is the characteristic length. A smaller Stokes number indicates a better tracing accuracy. Typically, a  $Stk < 0.1$  is required to achieve an acceptable tracing accuracy, of which the error is below 1% [42]. To fit the criteria, minimising the particle size is the most convenient approach, but it also decreases the amount of light scattered which leads to a poorer signal-to-noise ratio (SNR) of the recorded images [43].

Successive laser pulses, temporally separated by  $\Delta t$ , are used to illuminate the cross-section of the seeded fluid. Sequential images that contain the information of particles location at  $t$  and  $t + \Delta t$  are then captured by a CCD camera synchronised to the laser pulsing. Cross-correlation of PIV image pairs yields the particles displacements, which are then divided by  $\Delta t$  to produce a velocity field. The cross-correlation procedure is performed on sub-regions, specified by the interrogation window sizes (e.g.,  $16 \times 16$ ,  $32 \times 32$  or  $64 \times 64$  pixels), extracted from the PIV image pairs. Owing to the nature of a CCD camera, the PIV images are inherently pixelated and discrete. The discrete cross-covariance can therefore be mathematically described as [44],

$$C(r, s) = \frac{1}{M * N} \sum_{m=1}^M \sum_{n=1}^N [A(m, n) - \bar{A}] [B(m + r, n + s) - \bar{B}], \quad (3.21)$$

where  $*$  denotes a convolution operation,  $M$  and  $N$  represent the number of rows and columns within the window,  $(r, s)$  represents the location at which the correlation is evaluated, while  $\bar{A}$  and  $\bar{B}$  represent the mean image intensity of the interrogation areas,  $A$  and  $B$ , respectively. Equation 3.21 can be solved either directly in the spatial domain (Direct Cross-Correlation, DCC) [45] or in the frequency domain using Discrete Fourier Transform (DFT) [46]. An analysis done by Huang et al. [47] has shown that the DCC method produces results with reduced systematic errors. However, the drawback of using DCC is the increased

computational time, compared with a standard DFT approach, especially with large images [41]. Moreover, even though DFT produces low SNR results, this disadvantages can be offset by implementing multi-pass routines: starting with a large interrogation area and refines it with every pass. Consequently, it yields high spatial resolution and high SNR velocity fields.

### 3.8 CCD and ICCD cameras

All signals of interest in this thesis (*i.e.*, Mie scattering, incandescence and fluorescence) were recorded using charge-coupled device (CCD) and intensified CCD (ICCD) cameras. A CCD is a photosensitive analogue device comprising semiconductors that are arranged in a two-dimensional array that represents pixels [48]. When a photon interacts with the semiconductor, it emits free electrons by a phenomenon known as the photoelectric effect [49]. The number of electrons collected is directly proportional to the incident light intensity on each pixel. At the end of the collection time, the number of electrons in each pixel are measured and the information is used to reconstruct the image. An ICCD camera is a CCD camera with an image intensifier mounted in front of it, which amplifies the incident light intensity before the photons hit the CCD detector.

The experiment employed two PI-MAX4 (Princeton Instruments) ICCD cameras to perform the NTLAF technique. The ICCD camera has the highest possible sensitivity in the visible and near-infrared wavelengths. It operates at  $-25^{\circ}\text{C}$  to minimise the dark current. Both LII and TiRe-LII techniques used HSFC Pro (pco). It is an ultra speed camera system comprises an image splitter unit, four intensified CCD camera modules with fast switchable intensifiers and high resolution CCD image sensors. It also allows single photon detection. Additionally, the exposure time can be set as low as 3 ns. The second part of the experiment has included OH-PLIF, which utilised an ICCD-576 (Princeton Instruments). It was equipped with a 105mm UV lens and a UV filter centred at 310 nm with an full-width at half maximum of 10 nm. The MegaPlus ES4020 (Princeton Instruments) was utilised to record the variation in the beam profile of the lasers used in the NTLAF technique. Furthermore, the PIV measurement used two of the same CCD camera. These cameras allow the acquisition of two consecutive images over a short time interval. However, there are significant differences in the exposure time between the first and second frames (sub-microsecond vs. more than 30 milliseconds). This becomes a problem for PIV in highly luminous sooting flames because the second frame may record orders of magnitude greater soot luminosity than the first frame. Since the PIV technique relies on the cross-correlation of two consecutive particle images, it is challenging to obtain vectors from two images that have different intensities.

## 3.9 Image pre-processing

Image pre-processing is a generic term for operations that prepare image data for further analysis. The purpose of pre-processing is to enhance the image quality by suppressing pixel brightness distortions due to dark-charge, background noise and detector attenuation. Ideally, the laser beam should have a uniform intensity profile and a constant power output, but this assumption is almost impossible in many practical cases. Therefore, it is also necessary to correct the image data for the spatial and temporal variations in the laser beam. Furthermore, since multiple optical based techniques were employed in this thesis, geometric transformations of images (*e.g.*, translation, scaling and rotation) are also mandatory for spatially matching images produced by different techniques.

### 3.9.1 Dark charge and background corrections

Dark charge is a product of thermal excited vibrations of silicon atoms in the ICCD even when the device is not exposed to light, hence the name. Since the generation of dark charge is thermally activated, it is highly temperature dependent [50]. If the temperature of the CCD is near constant, the average dark charge in a pixel is approximately consistent, but varies spatially across the image, leading to a fixed offset added to each pixel value. Hence, simply subtracting a time-averaged dark charge image (taken while the aperture of the ICCD camera is completely closed) from all the raw image data can virtually remove the influence of dark charge.

Background noise is any signals detected by the camera that are unrelated to the measurements. Similar with the dark charge correction, background noise can be effectively removed from the image data by subtracting a mean background image (an averaged of a series of images consist of both the flame running without lasers pulsing and lasers firing with no flame).

### 3.9.2 Detector attenuation correction

Vignetting is a phenomenon of brightness attenuation away from the image centre, mainly due to the optical properties of camera lenses or off-axis illumination falloff [51]. The photosensitive part of the detector array is not of identical sensitivity and the mounted lens attenuates more light if it passes further from the optical axis [52]. Vignetting distortion becomes more severe as the camera aperture increases [53]. To counter the vignetting effect, images of a uniformly illuminated white background were recorded to reflect the intensity attenuation. The image data, after dark charge and background corrections, were normalised by the uniformity image.



### 3.9.3 Laser energy profile correction

The intensity of a laser beam varies across its radial profile while the laser power fluctuates between pulses [54]. The spatial and temporal variations in the laser energy have a great influence on the resultant signal, for example, the intensity of the fluorescence signals in the TLAF measurement is a function of laser pulse energy. To evaluate its radial profile, the laser beam was reflected through a cuvette filled with distilled water, into which titanium oxide nanoparticles were suspended. The Mie scattering from titanium oxide nanoparticles was recorded simultaneously as the fluorescence images and was averaged along the laser propagation direction. Subsequently, an instantaneous laser energy profile was acquired to correct the radial fluctuation in the laser beam profile as well as the shot-by-shot laser power variation.

### 3.9.4 Image matching

Ten cameras in total were utilised for simultaneous TiRe-LII (four ICCD cameras), TLAF (one CCD camera for recording the Mie scattering and two ICCD cameras for imaging the fluorescence signals) and OH-PLIF (an ICCD camera) measurements, while PIV measurement (two CCD cameras) was conducted consecutively. All these image data must be spatially matched such that each pixel in them corresponds to the same physical location, so that a meaningful spatial-correlated dataset can be constructed.

A transparent target with letters and a equispaced grid printed on it was recorded by all cameras (except for CCD cameras as the PIV was not performed simultaneously with the others) to provide a set of common reference points in each image. The letters were printed to identify the orientation and particular sections of the target. By identifying a set of shared intersection points (a minimum of four ) on the target grid, an image transformation algorithm in MATLAB<sup>®</sup>2016 was used to perform the necessary translation, scaling and rotation to the images. Images were locally morphed using an in-house image processing algorithm to ensure sub-pixel spatial matching. The image with the lowest spatial resolution was selected as the “base” image, while the others were “input” images subjected to the transformation.

### 3.10 Computational approach

Numerical modelling can complement and corroborate experimental measurements, especially shedding light on properties that are challenging for practical techniques to measure. Once validated with experimental data, the numerical models can be used effectively to predict combustion under different conditions.

In this thesis, numerical models were used as a first attempt to model the fluid-chemistry interactions that were observed experimentally. The simulations of steady and time-varying laminar flames were computed in ANSYS 17.2 Fluent [55]. The numerical model solved the time-dependent Navier-Stokes equations using the SIMPLEC (Semi-implicit Method for Pressure Linked Equations-Consistent) algorithm. All variables were spatially discretised with a second-order scheme [56]. To simulate the acoustic forcing in the computation, a sum of sinusoids fitted to the experimental jet exit velocity at the centreline was assigned to the time-varying fuel inlet via the User Define Function provided by ANSYS 17.2 Fluent.

The model predicted the ethylene-air combustion using a 32-species and 206-reaction skeletal mechanism, developed by Lu and co-workers [57] based on USC-Mech II [58], coupled with an *in-situ* adaptive tabulation algorithm. The simulation used the Discrete Ordinates Method of Liu and Kurokawa [59] to account for gas phase and soot radiation. To include the formation of soot as part of the combustion solution, ANSYS 17.2 Fluent provides users with four options: the one-step Khan and Greeves model [60], the two-step Tesner model [61, 62], the Moss-Brookes model [63] (for higher hydrocarbon fuels such as kerosene, there is an extended version known as the Moss-Brookes-Hall model [64, 65]) and the method of moments (MOM) model [66].

In the one-step model, as its name suggests, there is only a single transport equation for the soot mass fraction that need to be solved. The two-step model, however, computes the rate of soot formation based on the earlier predictions of the radical nuclei concentration. Although it seems to be particularly useful for the combustion of acetylene, the constants in the model require modifications before applying to other fuels [67]. Additionally, the Moss-Brookes model also solves transport equations for two scalar quantities: the normalised radical nuclei concentration and the soot mass fraction. However, due to the aforementioned limitation, the Moss-Brookes model is superior than the standard Tenser model in term of predicting the soot formation within methane flames.

In addition to a detailed kinetic modelling of soot formation, it also requires a fine resolution of the particle distribution to accurately predict the soot formation. The time evolution of the number density of soot particles as they coagulate can

be described by the Smoluchowski master equations [68]:

$$\frac{dN_1}{dt} = - \sum_{j=1}^{\infty} \beta_{1,j} \cdot N_1 \cdot N_j \quad (3.22)$$

and

$$\frac{dN_i}{dt} = \frac{1}{2} \sum_{j=1}^{i-1} \beta_{j,i-j} \cdot N_{i-j} \cdot N_j - \sum_{j=1}^{\infty} \beta_{i,j} \cdot N_i \cdot N_j \quad i = 2, \dots, \infty$$

where  $N_i$  is the particles number density function (the population of soot particles of the  $i^{\text{th}}$  size class per unit volume) and  $\beta_{i,j}$  is the collision coefficient between particles of size classes  $i$  and  $j$ . Instead of solving all the equations, the MOM model solves only a small number of equations for the first few moments,  $M_i$  [66]:

$$\frac{dM_0}{dt} = - \frac{1}{2} \sum_{i=1}^{\infty} \sum_{j=1}^{\infty} \beta_{i,j} \cdot N_i \cdot N_j, \quad (3.23)$$

$$\frac{dM_1}{dt} = 0, \quad (3.24)$$

$$\frac{dM_2}{dt} = \sum_{i=1}^{\infty} \sum_{j=1}^{\infty} i \cdot j \cdot \beta_{i,j} \cdot N_i \cdot N_j, \quad (3.25)$$

$$\frac{dM_3}{dt} = 3 \sum_{i=1}^{\infty} \sum_{j=1}^{\infty} i \cdot j^2 \cdot \beta_{i,j} \cdot N_i \cdot N_j, \dots, \quad (3.26)$$

where

$$M_r = \sum_{i=1}^{\infty} m_i^r \cdot N_i. \quad (3.27)$$

In most practical applications, the properties are determined by just the first few moments. As a result, the MOM model becomes numerically economic, to an extent that it is feasible to couple particle dynamics with realistic flow simulations [69]. However, while the equations solved in MOM yield mean quantities of interest, the information about the exact distribution of particle sizes is lost [70]. Furthermore, the formulation of MOM does not include particle fragmentation. Likewise, it cannot handle complete particle oxidation [66]. Mueller et al. [71] also found that the primary particle diameter predicted by MOM is bias towards larger particles size.

### 3.11 Summary

In summary, the experimental study employed LII to evaluate the volume fraction of soot within flames, TiRe-LII to resolve the primary soot particle-size distribution, NTLAF to measure the gas temperature, OH-PLIF to determine the location of the reaction zone and PIV to characterise the time-varying flow fields. Computationally, steady and acoustically forced laminar flames were simulated using ANSYS 17.2 Fluent. The main purpose of the simulation is to provide the mixture fraction and distribution of major species concentrations.

### References

- [1] B. C. Connelly, “Quantitative Characterization of Steady and Time-Varying, Sooting, Laminar Diffusion Flames using Optical Techniques”, Ph.D. dissertation, Yale University, 2009.
- [2] Y. University, “<http://guilford.eng.yale.edu/yalecoflowflames/flames.html>”, 2014.
- [3] H. Sato, K. Amagai, and M. Arai, “Flickering frequencies of diffusion flames observed under various gravity fields”, *Proceedings of the Combustion Institute* **28** (2000), pp. 1981–1987.
- [4] L. A. Melton, “Soot diagnostics based on laser heating”, *Applied Optics* **23** (1984), pp. 2201–2208.
- [5] E. Therssen, Y. Bouvier, C. Schoemaeker-Moreau, X. Mercier, P. Descroux, M. Ziskind, and C. Focsa, “Determination of the ratio of soot refractive index function  $E(m)$  at the two wavelengths 532 and 1064 nm by laser induced incandescence”, *Applied Physics B* **89** (2007), pp. 417–427.
- [6] Z. W. Sun, D. H. Gu, G. J. Nathan, Z. T. Alwahabi, and B. B. Dally, “Single-shot, Time-Resolved planar Laser-induced Incandescence for soot primary particle sizing in flames”, *Proceedings of the Combustion Institute* **35** (2015), pp. 3673–3680.
- [7] S. Krishnan, K.-C. Lin, and G. Faeth, “Extinction and scattering properties of soot emitted from buoyant turbulent diffusion flames”, *Journal of Heat Transfer* **123** (2001), pp. 331–339.
- [8] M. Schnaiter, J. Horvath, O. Möhler, K.-H. Naumann, H. Saathoff, and O. Schöck, “UV-VIS-NIR spectral optical properties of soot and soot-containing aerosols”, *Journal of Aerosol Science* **34** (2003), pp. 1421–1444.
- [9] N.-E. Olofsson, J. Simonsson, S. Török, H. Bladh, and P.-E. Bengtsson, “Evolution of properties for aging soot in premixed flat flames studied by laser-induced incandescence and elastic light scattering”, *Applied Physics B* **119** (2015), pp. 669–683.
- [10] G. A. Kelesidis and S. E. Pratsinis, “Soot light absorption and refractive index during agglomeration and surface growth”, *Proceedings of the Combustion Institute* (2018).

- 
- [11] H. A. Michelsen, P. E. Schrader, and F. Goulay, “Wavelength and temperature dependences of the absorption and scattering cross sections of soot”, *Carbon* **48** (2010), pp. 2175–2191.
- [12] R. P. Bambha, M. A. Dansson, P. E. Schrader, and H. A. Michelsen, “Effects of volatile coatings on the laser-induced incandescence of soot”, *Applied Physics B* **112** (), pp. 343–358.
- [13] K. Smyth and C. Shaddix, “The elusive history of  $\tilde{m} = 1.57 - 0.56i$  for the refractive index of soot”, *Combustion and Flame* **107** (1996), pp. 314–320.
- [14] F. Liu, K. Daun, D. Snelling, and G. Smallwood, “Heat conduction from a spherical nano-particle: status of modeling heat conduction in laser-induced incandescence”, *Applied Physics B* **83** (2006), pp. 355–382.
- [15] C. Schulz, B. F. Kock, M. Hofmann, H. Michelsen, S. Will, B. Bougie, R. Suntz, and G. Smallwood, “Laser-induced incandescence: recent trends and current questions”, *Applied Physics B* **83** (2006), pp. 333–354.
- [16] F. Liu, M. Yang, F. Hill, D. Snelling, and G. Smallwood, “Influence of polydisperse distributions of both primary particle and aggregate size on soot temperature in low-fluence LII”, *Applied Physics B* **83** (2006), pp. 383–395.
- [17] E. Cenker, G. Bruneaux, T. Dreier, and C. Schulz, “Determination of small soot particles in the presence of large ones from time-resolved laser-induced incandescence”, *Applied Physics B* **118** (2015), pp. 169–183.
- [18] T. Lehre, B. Jungfleisch, R. Suntz, and H. Bockhorn, “Size distributions of nanoscaled particles and gas temperatures from time-resolved laser-induced-incandescence measurements”, *Applied Optics* **42** (2003), pp. 2021–2030.
- [19] C. T. J. Alkemade, “A theoretical discussion on some aspects of atomic fluorescence spectroscopy in flames”, *Pure and Applied Chemistry* **23** (1969), pp. 73–98.
- [20] N. Omenetto, P. Benetti, and G. Rossi, “Flame temperature measurements by means of atomic fluorescence spectrometry”, *Spectrochimica Acta Part B: Atomic Spectroscopy* **27** (1972), pp. 453–461.
- [21] H. Haraguchi, B. Smith, S. Weeks, D. J. Johnson, and J. D. Winefordner, “Flame Diagnostics: Local Temperature Profiles and Atomic Fluorescence Intensity Profiles in Air-Acetylene Flames”, *Applied Spectroscopy* **31** (1977), pp. 195–200.
- [22] Q. N. Chan, “Development of Instantaneous Temperature Imaging in Sooty Flames”, PhD thesis, The University of Adelaide, 2011.
- [23] J. Engström, J. Nygren, M. Aldén, and C. F. Kaminski, “Two-line atomic fluorescence as a temperature probe for highly sooting flames”, *Optics Letters* **25** (2000), pp. 1469–1471.
- [24] B. Chakraborty and R. Long, “The formation of soot and polycyclic aromatic hydrocarbons in diffusion flames III—Effect of additions of oxygen to ethylene and ethane respectively as fuels”, *Combustion and Flame* **12** (1968), pp. 469–476.
- [25] D. H. Gu, Z. W. Sun, P. R. Medwell, Z. T. Alwahabi, B. B. Dally, and G. J. Nathan, “Mechanism for laser-induced fluorescence signal generation in a nanoparticle-seeded flow for planar flame thermometry”, *Applied Physics B* **118** (2015), pp. 209–218.

## REFERENCES

---

- [26] S. Lai, J. Guo, V. Petrova, G. Ramanath, and I.H. Allen, “Size-Dependent Melting Properties of Small Tin Particles: Nanocalorimetric Measurements”, *Physical Review Letters* **77** (1996), pp. 99–102.
- [27] R. A. Yetter, G. A. Risha, and S. F. Son, “Metal particle combustion and nanotechnology”, *Proceedings of the Combustion Institute* **32** (2009), pp. 1819–1838.
- [28] Y. S. Kwon, A. A. Gromov, A. P. Ilyin, E. M. Popenko, and G. H. Rim, “The mechanism of combustion of superfine aluminum powders”, *Combustion and Flame* **133** (2003), pp. 385–391.
- [29] G. P. Smith, D. M. Golden, M. Frenklach, N. W. Moriarty, B. Eiteneer, M. Goldenberg, C. T. Bowman, R. K. Hanson, S. Song, W. C. Gardiner, V. V. Lissianski, and Z. W. Qin, 2016.
- [30] P. R. Medwell, Q. N. Chan, B. B. Dally, Z. T. Alwahabi, G. F. Metha, and G. J. Nathan, “Flow seeding with elemental metal species via an optical method”, *Applied Physics B* **107** (2012), pp. 665–668.
- [31] P. R. Medwell, Q. N. Chan, B. B. Dally, S. Mahmoud, Z. T. Alwahabi, and G. J. Nathan, “Temperature measurements in turbulent non-premixed flames by two-line atomic fluorescence”, *Proceedings of the Combustion Institute* **34** (2013), pp. 3619–3627.
- [32] J. Bechtel and R. Teets, “Hydroxyl and its concentration profile in methane-air flames”, *Applied Optics* **18** (1979), pp. 4138–4144.
- [33] C. F. Kaminski, J. Engström, and M. Aldén, “Quasi-instantaneous two-dimensional temperature measurements in spark ignition engine using 2-line atomic fluorescence”, *Proceedings of the Combustion Institute* **27** (1998), pp. 82–93.
- [34] P. Medwell, P. Kalt, and B. Dally, “Imaging of diluted turbulent ethylene flames stabilized on a jet in hot coflow (JHC) burner”, *Combustion and Flame* **152** (2008), pp. 100–113.
- [35] S. Carl, M. V. Poppel, and J. Peeters, “Identification of the  $\text{CH} + \text{O}_2 \rightarrow \text{OH}(\text{A}) + \text{CO}$  reaction as the source of  $\text{OH}(\text{A-X})$  chemiluminescence in  $\text{C}_2\text{H}_2/\text{O}/\text{O}_2$  atomic flames and determination of its absolute rate constant over the range  $T=296$  to  $511\text{ K}$ ”, *The Journal of Physical Chemistry A* **107** (2003), pp. 11001–11007.
- [36] J. Luque and D. R. Crosley, “LIFBASE: Database and spectral simulation program (Version 1.5)”, Report MP 99-009, SRI International, 1999.
- [37] S. O’Byrne, I. Stotz, A. Neely, R. Boyce, N. Mudford, and F. Houwing, “OH PLIF imaging of supersonic combustion using cavity injection”, *AIAA/CIRA 13th International Space Planes and Hypersonics Systems and Technologies Conference* (2005), pp. 3357–3368.
- [38] C. T. Johansen, C. D. McRae, P. M. Danehy, E. C. Gallo, L. M. Cantu, G. Magnotti, A. D. Cutler, R. D. Rockwell, C. P. Goyne, and J. C. McDaniel, “OH PLIF visualization of the UVa supersonic combustion experiment: configuration A”, *Journal of Visualization* **17** (2014), pp. 131–141.
- [39] D. R. Crosley and I. L. Chidsey, “Tables of calculated transition probabilities for the A–X system of OH”, Technical report ARBRL-TR-02326, Molecular Physics Laboratory, SRI International, 1981.

- 
- [40] J. Westerweel, “Fundamentals of digital particle image velocimetry”, *Measurement Science and Technology* **8** (1997), pp. 1379–1392.
- [41] M. Raffel, C. Willert, S. Wereley, and J. Kompenhans, “Particle Image Velocimetry - A Practical Guide”, Springer, 2007.
- [42] B. J. McKeon, G. Comte-Bellot, J. F. Foss, F. S. J. Westerwell, C. Tropea, J. F. Meyers, J. W. Lee, A. A. Cavone, R. Schodl, M. M. Koochesfahani, D. G. Nocera, Y. Andreopoulos, W. J. A. Dahm, J. A. Mullin, J. M. Wallace, P. V. Vukoslavčević, S. C. Morris, E. R. Pardyjak, and A. Cuerva, “Velocity, Vorticity and Mach Number”, *Springer Handbook of Experimental Fluid Mechanics*, ed. by C. Tropea, A. L. Yarin, and J. F. Foss, Springer, Heidelberg, Germany, 2007.
- [43] A. Melling, “Tracer particles and seeding for particle image velocimetry”, *Measurement Science and Technology* **8** (1997), pp. 1406–1416.
- [44] D. Dabiri, “Digital particle image thermometry/velocimetry: a review”, *Experiments in Fluids* **46** (2009), pp. 191–241.
- [45] K. Okamoto, S. Nishio, T. Saga, and T. Kobayashi, “Standard images for particle-image velocimetry”, *Measurement Science and Technology* **11** (2000), pp. 685–691.
- [46] R. Gilbert and D. Johnson, “Evaluation of FFT-based cross-correlation algorithms for PIV in a periodic grooved channel”, *Experiments in Fluids* **34** (2003), pp. 473–483.
- [47] H. Huang, D. Dabiri, and M. Gharib, “On errors of digital particle image velocimetry”, *Measurement Science and Technology* **8** (1997), pp. 1427–1440.
- [48] J. R. Janesick, “Scientific charge-coupled devices”, vol. 83, SPIE press, 2001.
- [49] S. Donati, “Photodetectors”, vol. 1, Prentice Hall PTR, 1999.
- [50] R. Widenhorn, M. M. Blouke, A. Weber, A. Rest, and E. Bodegom, “Temperature dependence of dark current in a CCD”, *Sensors and Camera Systems for Scientific, Industrial, and Digital Photography Applications III*, vol. 4669, International Society for Optics and Photonics, 2002, pp. 193–202.
- [51] Y. Zheng, S. Lin, C. Kambhamettu, J. Yu, and S. B. Kang, “Single-image vignetting correction”, *IEEE Transactions on Pattern Analysis and Machine Intelligence* **31** (2009), pp. 2243–2256.
- [52] M. Sonka, V. Hlavac, and R. Boyle, “Image pre-processing”, *Image Processing, Analysis and Machine Vision*, Springer, 1993.
- [53] N. Asada, A. Amano, and M. Baba, “Photometric calibration of zoom lens systems”, *Proceedings of International Conference on Pattern Recognition* **13** (1996), pp. 186–190.
- [54] J. Armstrong and A. Smith, “VI Experimental Studies of Intensity Fluctuations in Lasers”, *Progress in optics*, vol. 6, Elsevier, 1967, pp. 211–257.
- [55] ANSYS, “ANSYS 17.2 Fluent”, 2016.
- [56] O. Desjardins, G. Blanquart, G. Balarac, and H. Pitsch, “High order conservative finite difference scheme for variable density low Mach number turbulent flows”, *Journal of Computational Physics* **227** (2008), pp. 7125–7159.

## REFERENCES

---

- [57] Z. Luo, C. Yoo, E. S. Richardson, J. Chen, C. Law, and T. Lu, “Chemical explosive mode analysis for a turbulent lifted ethylene jet flame in highly-heated coflow”, *Combustion and Flame* **159** (2012), pp. 265–274.
- [58] H. Wang, X. You, A. V. Joshi, S. G. Davis, A. Laskin, F. Egolfopoulos, and C. K. Law, “USC Mech Version II. High-Temperature Combustion Reaction Model of H<sub>2</sub>/CO/C<sub>1</sub>-C<sub>4</sub> Compounds”, 2007, URL: [http://ignis.usc.edu/USC\\_Mech\\_II.htm](http://ignis.usc.edu/USC_Mech_II.htm).
- [59] Y. Liu and H. Kurokawa, “On a surge: properties of an emerging flux region”, *The Astrophysical Journal* **610** (2004), pp. 1136–1147.
- [60] I. M. Khan and G. Greeves, “A method for calculating the formation and combustion of soot in diesel engines”, *Heat Transfer in Flames*, ed. by N. H. Afgan and J. M. Beer, Scripta, Washington DC., 1974.
- [61] P. Tesner, T. Snegirova, and V. Knorre, “Kinetics of dispersed carbon formation”, *Combustion and Flame* **17** (1971), pp. 253–260.
- [62] B. F. Magnussen and B. H. Hjertager, “On mathematical models of turbulent combustion with special emphasis on soot formation and combustion”, *Proceedings of the Combustion Institute* **16** (1977), pp. 719–729.
- [63] S. Brookes and J. Moss, “Prediction of soot and thermal radiation in confined turbulent jet diffusion flames”, *Combustion and Flame* **116** (1999), pp. 486–503.
- [64] R. Hall, M. Smooke, and M. Colket, “Predictions of soot dynamics in opposed jet diffusion flames”, *Physical and Chemical Aspects of Combustion: A Tribute to Irvin Glassman*, ed. by F. L. Dryer and R. F. Sawyer, Gordon and Breach Science Publishers, Amsterdam, Netherlands, 1997.
- [65] Z. Wen, S. Yun, M. Thomson, and M. Lightstone, “Modeling soot formation in turbulent kerosene/air jet diffusion flames”, *Combustion and Flame* **135** (2003), pp. 323–340.
- [66] M. Frenklach, “Method of moments with interpolative closure”, *Chemical Engineering Science* **57** (2002), pp. 2229–2239.
- [67] T. Ahmad, S. L. Plee, and J. P. Myers, “Computation of nitric oxide and soot emissions from turbulent diffusion flames”, *Journal of Engineering for Gas Turbines and Power* **107** (1985), pp. 48–53.
- [68] M. V. Smoluchowski, “Versucheiner Mathematischen Theorie der Koagulations Kinetik Kolloider Lousungen”, *Zeitschrift für Physikalische Chemie* **92** (1917), pp. 129–168.
- [69] X. Bai, M. Balthasar, F. Mauss, and L. Fuchs, “Detailed soot modeling in turbulent jet diffusion flames”, *Proceedings of the Combustion Institute* **27** (1998), pp. 1623–1630.
- [70] M. Mueller, G. Blanquart, and H. Pitsch, “Hybrid Method of Moments for modeling soot formation and growth”, *Combustion and Flame* **156** (2009), pp. 1143–1155.
- [71] M. Mueller, G. Blanquart, and H. Pitsch, “A joint volume-surface model of soot aggregation with the method of moments”, *Proceedings of the Combustion Institute* **32** (2009), pp. 785–792.



## Chapter 4

# Experimental investigation of acoustic forcing on temperature, soot volume fraction and primary particle diameter in non-premixed laminar flames

This chapter consists of the published journal article:

Kae Ken Foo, Zhiwei Sun, Paul R. Medwell, Zeyad T. Alwahabi, Bassam B. Dally and Graham J. Nathan, "Experimental investigation of acoustic forcing on temperature, soot volume fraction and primary particle diameter in non-premixed laminar flames", *Combustion and Flame* **181** (2017), pp. 270–282.

The content of this chapter is identical to that of the published article, with the following exceptions:

1. The typesetting and referencing style have been altered to maintain a consistent appearance within the thesis.
2. The numbering of tables, figures and equations has been changed to include the number of the chapter.

The article in its published format is available at:

<https://doi.org/10.1016/j.combustflame.2017.04.002>

## Statement of Authorship

Title of Paper	Experimental investigation of acoustic forcing on temperature, soot volume fraction and primary particle diameter in non-premixed laminar flames
Publication Status	<input checked="" type="checkbox"/> Published <input type="checkbox"/> Accepted for Publication <input type="checkbox"/> Submitted for Publication <input type="checkbox"/> Unpublished and Unsubmitted work written in manuscript style
Publication Details	K.K. Foo, Z.W. Sun, P.R. Medwell, Z.T. Alwahabi, B.B. Dally and G.J. Nathan, "Experimental investigation of acoustic forcing on temperature, soot volume fraction and primary particle diameter in non-premixed laminar flames", <i>Combustion and Flame</i> 181 (2017) 270—282.

### Principal Author

Name of Principal Author (Candidate)	Kae Ken Foo
Contribution to the Paper	<p>I planned and proposed the experimental design matrix to the co-authors after a thorough literature review. Together with all the co-authors, we decided the experimental cases.</p> <p>I set up the experiments with the assistance provided by the second co-author, Z.W. Sun. We collected the experimental results together.</p> <p>I processed, analysed and interpreted all the experimental data. After some discussion with the co-authors regarding my interpretation of the experimental data, I wrote the manuscript. Furthermore, as the corresponding author, I responded to the reviewers' comments and recommendations.</p>
Overall percentage (%)	65%
Certification:	This paper reports on original research I conducted during the period of my Higher Degree by Research candidature and is not subject to any obligations or contractual agreements with a third party that would constrain its inclusion in this thesis. I am the primary author of this paper.
Signature	Digitally signed by Kae Ken Foo Date: 2018.08.20 09:32:15 +09'30'

### Co-Author Contributions

By signing the Statement of Authorship, each author certifies that:

- i. the candidate's stated contribution to the publication is accurate (as detailed above);
- ii. permission is granted for the candidate to include the publication in the thesis; and
- iii. the sum of all co-author contributions is equal to 100% less the candidate's stated contribution.

Name of Co-Author	Zhi Wei Sun
Contribution to the Paper	This co-author co-designed the experiments and provided aid collecting data. He helped to edit the experimental details section of the manuscript.
Signature	Digitally signed by Zhiwei Sun Date: 2018.08.21 10:59:16 +09'30'

Name of Co-Author	Paul R. Medwell
Contribution to the Paper	This co-author provided suggestions for the experimental set-up and data post-processing. He also helped evaluate and edit the manuscript.
Signature	Paul Medwell 2018.08.23 11:11:30 +09'30'

Name of Co-Author	Zeyad T. Alwahabi
Contribution to the Paper	This co-author provided suggestions for the experimental set-up. He also helped to evaluate and edit the manuscript.
Signature	Digitally signed by Zeyad Alwahabi DN: cn=Zeyad Alwahabi, o=Chem Eng, ou, email=zeyad.alwahabi@adelaide.edu.au, c=AU Date: 2018.08.21 14:06:17 +09'30'

Name of Co-Author	Bassam B. Dally
Contribution to the Paper	This co-author co-supervised the development of the work. He also helped to evaluate and edit the manuscript.
Signature	Digitally signed by Bassam Dally Date: 2018.08.20 10:07:36 +09'30'

Name of Co-Author	Graham J. Nathan
Contribution to the Paper	This co-author co-supervised the development of the work. He also helped to evaluate and edit the manuscript.
Signature	Digitally signed by Graham J Nathan Date: 2018.08.23 12:46:57 +09'30'

# Experimental investigation of acoustic forcing on temperature, soot volume fraction and primary particle diameter in non-premixed laminar flames

Kae Ken Foo, Zhiwei Sun, Paul R. Medwell, Zeyad T. Alwahabi,  
Bassam B. Dally, Graham J. Nathan

## Abstract

The influence of the acoustic-driven oscillation frequency on the structure and the soot formation of a laminar non-premixed ethylene flame is presented. The flames were forced at either 20 and 40 Hz, corresponding to Strouhal numbers of 0.23 and 0.46. Two-dimensional phase-resolved measurements of gas temperature, soot volume fraction and the diameter of primary particles were measured simultaneously for one steady and two forced flames with non-linear excitation regime Two-Line Atomic Fluorescence, Laser-Induced Incandescence and Time-Resolved LII, respectively. Simultaneous measurements of gas temperature and soot volume fraction provide details of the difference between the flame structure and the soot distribution in the forced and unforced flames. The distinctive features of the forced flames are the occurrence of necking near to the fuel tube and the formation of hollow soot “shell”. Despite the distinctive structure, the soot region is confined to a restricted range of temperatures, 1700–1800 K. The spatial relationship between gas temperature and soot volume fraction for forced flames is reported for the first time, although it is well established for steady laminar flames. The present measurements also reveal the non-linear relationship between diameter of primary particles and soot volume fraction for these flames. Planar gas temperature images and OH\* chemiluminescence profiles show that the reaction zone extends periodically upstream from the exit plane of the fuel tube for the flame with  $St = 0.23$ . This phenomenon, which only occurs for some conditions, is an important consideration for the modelling of these flames because the boundaries of the computational domain typically starts at the fuel flow exit plane.

## 4.1 Introduction

The majority of practical combustion devices employ turbulent non-premixed flames to achieve intense mixing and heat release. However, careful design and control is needed to limit the emission of pollutants from turbulent non-premixed flames, such as soot particles, CO and NO<sub>x</sub>. With the trend of increasingly stringent limits being imposed on pollutant emissions, there is a growing need for

techniques to control the combustion process and achieve low emissions. More reliable predictive numerical design tools are among the techniques needed to enable optimisation of the combustion systems, which in turn requires sufficiently complete and systematic data sets. Furthermore, because of the coupled and non-linear relationships between temperature, strain rate, mixture fraction and soot properties (e.g., volume fraction, aggregate size and diameter of primary particles), simultaneous measurements of these parameters are needed to fully validate models. Unfortunately, practical constraints limit the number of parameters that can be measured simultaneously. While some simultaneous measurements of temperature and soot volume fraction are available [1–3], it will be many years before any one laboratory has sufficient capability to measure all controlling parameters simultaneously. In this context, time-varying laminar flames offer a means to reduce the need for simultaneous measurements by offering the potential to establish repeatable time-varying flames with a broader range of flame characteristics than is possible with steady laminar flames.

Time-varying laminar flames typically employ speakers to impose pressure fluctuations on the initial flow profile of fuel jets [4–9]. Other methods to force the fuel flow include mechanical forcing [10, 11] and magnetically-induced flow fluctuation [12]. The use of acoustic forcing imposes a periodic oscillation, typically on the fuel flow, which allows different parameters to be measured separately at the same phase and position. In addition, it enables a variety of measurement techniques from different laboratories to be combined. Thus, the need for simultaneous measurements is not as critical. Furthermore, the ability to repeat the measurement at different cycles offers the opportunity to resolve the evolution of a flame through the phase of the cycle without the need for high-speed laser diagnostics. Meanwhile, periodic flows allow the application of phase-average technique to measurements which enhances the signal-to-noise ratio (SNR), thus increasing the accuracy of the measurements. Nevertheless, simultaneous measurements are still desirable to reduce the uncertainties arising from slightly different conditions, such as in phase matching of two different data sets. For the above reasons, the present investigation was conducted with simultaneous measurements for one steady and two acoustically forced non-premixed laminar jet flames.

The literature is replete with experimental studies of acoustically forced laminar non-premixed flames [5–9, 13–15] that have been investigated with a variety of diagnostic techniques. From these, two distinct frequency regimes have been identified. One is a low frequency oscillation for which the forcing frequency is close to the natural flickering frequency, which typically range from 10 to 20 Hz [6, 14]. The other is a high frequency oscillation, which is typically more than one order of magnitude higher than the natural flickering frequency [8, 9, 13]. It is well established that the large-scale eddies in jet flames are amplified when the acoustic excitation produces a preferred-mode coupling between jet forcing and

the flame structure, which corresponds to a Strouhal number ( $St = fD/U_{jet}$ ) of approximately 0.3. Here,  $f$  is the frequency of the forcing,  $D$  is the diameter of the jet and  $U_{jet}$  is the bulk exit velocity of the jet. When a non-premixed jet flame is excited at the preferred-mode, this leads to a significant increase in the entrainment rate [16] and can result in a reduction in flame length and width relative to its steady counterpart. A reduced flame length and width implies a decrease in the global residence time [17], which typically also reduces the in-flame soot volume fraction. Furthermore, it has been reported that the soot volume fraction decreases when both the flame and the surrounding were forced [8, 13]. It has been hypothesised that the acoustic-driven oscillations lead to both enhanced air-fuel mixing and soot suppression [13]. However, strong acoustic excitation at the preferred-mode does not necessarily lead to enhanced mixing and soot suppression. Shaddix et al. [6] and Shaddix and Smyth [7] have reported that the peaks of the soot volume fraction and the size of primary soot particles in forced flames can increase by factors of two to four over their steady counterparts for cases in which the acoustic forcing was driven by a speaker. They concluded that an increase in global residence time is the dominant factor responsible for the measured increase in both the peak soot volume fraction and the diameter of primary particles [18, 19]. Consistent with this, Langman and Nathan [20] reported a case in which forcing of a highly turbulent non-premixed flame at the preferred-mode led to a strong increase in the flame brightness (implying more soot within the flame) but did not generate any measurable change to the global mixing rate. They attributed this apparent contradiction with earlier work to the acoustic forcing in their study being generated entirely naturally (by coupling with a resonance), in contrast to the previous cases in which the acoustic forcing was driven with a speaker, which also added energy to the flow. They concluded that the natural acoustic resonance led to an increase in the residence time of the sooting flow within the large eddies but did not change the overall mixing rate of the flame. Nevertheless, without an in-depth analysis of the local conditions of time-varying flames, together with systematic investigations of a range of conditions, it is difficult to isolate the different effects of alternative non-linear mechanisms that influence flame/vortex interactions.

In light of the incomplete understanding of acoustically forced sooting flames, the aim of the present investigation is to provide new insights into the coupling between combustion and time-varying flow field through assessing the spatial relationship between flame temperature, soot volume fraction and the diameter of primary particles in different regions of two acoustically forced flames of different Strouhal number. A further objective is to contribute to the development of improved understanding and predictive capability of these flames and, in turn, of the evolution of soot in turbulent flames.

## 4.2 Experimental details

### 4.2.1 Burner

The laminar non-premixed jet flame was generated above a co-flowing burner that replicates a previous design [21, 22]. A more detailed description of the burner has been provided by Dworkin et al. [21]. The fuel was introduced through a stainless steel tube with an inner diameter of 4 mm in a concentric 74-mm-diameter co-flow tube. The co-flow was homogenised with two layers of hexagonal honeycomb and 2-mm-diameter glass beads filled in between.

A speaker was placed in a plenum underneath the fuel tube to impose sinusoidal perturbations on the fuel flow. The speaker was driven by a function generator that provided exact reproducibility of the forcing amplitude and phase settings. The optical diagnostics systems presented in Sections 4.2.3, 4.2.4 and 4.2.5 were phase-locked to the sinusoidal signal produced by the function generator, permitting phase-specific measurements to be performed in the forced flames. Two frequencies were chosen to force the fuel flow, namely 20 and 40 Hz, corresponding to  $St = 0.23$  and  $0.46$ , respectively.

The fuel stream contained a mixture of 32% of ethylene diluted with 68% of nitrogen, by volume. Nitrogen was introduced to limit the maximum amount of soot in the forced flame so that the level of interference from soot to the laser diagnostic measurements was kept to a minimum. The volumetric flow rates of the fuel and co-flow for the steady and unsteady states were 0.264 and 80 litre per minute (LPM), respectively, which resulted in a bulk exit velocity of 0.35 m/s for both the fuel flow and co-flow.

### 4.2.2 Velocity measurement

The axial component of the centreline velocity of the non-reacting fuel jet was measured with a Constant Temperature Anemometer (CTA) at a height of  $\sim 2$  mm above the burner (HAB). The amplitude of the perturbation was defined as  $\alpha = \frac{v_c - \bar{v}_c}{\bar{v}_c}$ , where  $v_c$  is the centreline velocity, and  $\bar{v}_c$  is the time-averaged centreline velocity. As shown in Fig. 4.1, the amplitudes of the velocity perturbation for  $St = 0.23$  and  $St = 0.46$  cases were approximately 50%. The departure from a pure sinusoidal motion exhibited in both measured velocities indicates the presence of higher-order harmonics. Fourier-transformation of the measured velocities reveals that the measured signals can be decomposed into the fundamental and the first harmonic component, as is shown in Fig. 4.1. Further analysis identified the phase-lags of  $\sim 101^\circ$  and  $\sim 283^\circ$  between the input signals and the flow response at the nozzle exit for the  $St = 0.23$  and  $0.46$  cases, respectively. The time-series results presented in Sections 4.3.2 and 4.3.3 were phase-shifted to coincide with the measured flow perturbation profiles. Thus, all of the measured images for both  $St = 0.23$  and  $St = 0.46$  are phase-locked. Since the perturbations were

driven with a sine wave function, the first phase angle ( $\phi = 0^\circ$ ) in Section 4.3.2 and 4.3.3 was defined as the phase when  $v_c = \bar{v}_c + \alpha \sin(0^\circ)$ .

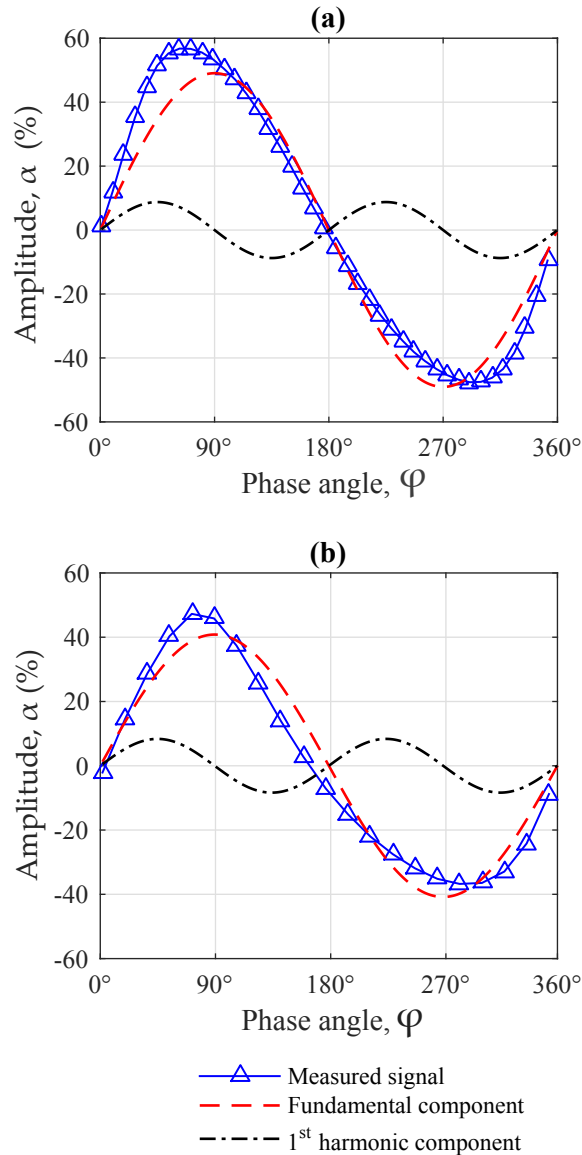


**Figure 4.1** Amplitude of the perturbation to the axial component of the centreline velocity for the non-reacting flow,  $\alpha = \frac{v_c - \bar{v}_c}{\bar{v}_c}$ , where  $v_c$  is the centreline velocity measured at 2 mm above the burner using a constant temperature anemometer, and  $\bar{v}_c$  is the time-averaged centreline velocity. The measured  $v_c$  is presented together with the components of the fundamental and the first harmonic derived using a Fourier-transformation analysis. The average centreline velocities,  $\bar{v}_c$  for (a)  $St = 0.23$  and (b)  $St = 0.46$  cases were both 0.7 m/s.



### 4.2.3 Temperature measurement

Gas temperature of the steady and forced flames was measured using the Non-linear excitation regime Two Line Atomic Fluorescence (NTLAF) technique, which has been described in detail previously [23–25]. This technique is based on the sequential excitation of indium atoms from two lower energy states [26] to generate fluorescence from each of the two transitions that is detected at the wavelength opposite to that of the excitation laser. These two processes are referred to as the Stokes (excited at 410 nm and detected at 450 nm) and anti-Stokes (excited at 450 nm and detected at 410 nm) processes, respectively. Two Nd:YAG-pumped dye lasers were tuned to 410.18 nm and 451.13 nm and fired with  $\sim 120$  ns separation. These two beams were merged together using a dichroic mirror (Thorlabs, DMLP425), and reshaped into a coplanar laser sheet with  $\sim 350$   $\mu\text{m}$  thickness. The laser sheet was directed through a thin glass plate before the flame and reflected into two cuvettes that were filled with distilled water, into which  $\sim 300$  nm titanium oxides particles were suspended. The laser scattering facilitated the correction of laser energy variation across the sheet height and between laser pulses [27].

The resultant Stokes and anti-Stokes fluorescences were recorded through two customised narrow band-pass filters (centred at 410.1 and 451.4 nm with a full-width at half maximum of 1.08 and 1.32 nm, respectively) using two intensified CCD cameras (ICCD, PI-Max4). To ease the spatial matching process for Stokes and anti-Stokes images, an image splitter (TwinCam) was placed in front of the ICCD cameras so that the images were collected at the same angle. The image splitter consisted of a 50 mm, f/1.2 lens, and a long-pass dichroic beam splitter (Thorlabs, DMLP425) to separate the Stokes and anti-Stokes fluorescence signals.

The flames were seeded with indium nanoparticles using an in-house built ablation device, described previously [23, 27, 28]. It is important to note that NTLAF technique with indium seeding provides a conditional measurement of gas temperature. The Boltzmann distribution estimates that at  $\sim 800$  K, the relative population of the anti-Stokes transition is  $< 3\%$  [29]. Hence, a minimum temperature of 800 K is needed to yield a sufficient population of the anti-Stokes signal. An indium rod was placed in a sealed ablation chamber, and constantly rotated and translated to provide a fresh surface for each ablation pulse. A 10 Hz (8 ns pulse width) 532 nm laser generated from an Nd:YAG laser was chosen for the ablation process. The ablation laser energy was chosen to be  $\sim 0.1$  J/pulse to yield sufficient indium nanoparticles for a good signal. No significant influence of indium seeding on the LII images was visually detectable. The SNR of the single-shot images is 9.1 : 1 for Stokes and 4.8 : 1 for anti-Stokes. Phase-averaging the images results in improved SNR of 21.4 : 1 for Stokes and 20.1 : 1 for anti-Stokes. Applying the NTLAF theory to the fluorescence images yields the images of gas temperature presented in Figs. 4.2, 4.4 and 4.7 which have a SNR of  $\sim 84.6$  : 1. The temperature uncertainty arises from the interpixel noise is  $\sim 139$  K.

The system-dependent parameters of NTLAF were calibrated in an ethylene premixed flame with an equivalence ratio of  $\Phi = 1.23$  with the same burner. A  $75\ \mu\text{m}$  R-type thermocouple was utilised to measure the radiation-corrected flame temperatures at the centreline of the premixed flame for calibration.

#### 4.2.4 Primary particles diameter measurement

A detailed description of the Time-Resolved Laser Induced Incandescence (TiRe-LII) system utilised in the current study has been provided previously [30]. The light source for the LII was the fundamental output (1064 nm) from an Nd:YAG laser. Four LII images were collected sequentially using an ultra-high speed camera (HSFC pro, PCO) to resolve the diameter of the primary soot particles. The four ICCD cameras were delayed by 0, 40, 80, and 120 ns relative to the prompt LII signal using an integration time of 40 ns for each camera. The diameter of primary particles,  $d_p$  was determined with a look-up table of theoretical intensity ratios of  $S_2/S_1$ ,  $S_3/S_1$ ,  $S_4/S_1$ ,  $S_3/S_2$ ,  $S_4/S_2$  and  $S_4/S_3$  (where  $S_i$  denotes the signal from the  $i$ th camera) at the four chosen delay times spanning  $d_p$  from 5 to 100 nm in increments of 5 nm. By comparing the ratios of measured LII against the theoretically calculated decay curve, each ratio provides an independent measurement of  $d_p$ . Averaging all six independent measurements gives the most representative of the mean value of  $d_p$  in the measured region. The theoretical model has also been described previously [30]. However, previous measurements assumed a constant initial temperature of 1700 K, while the current TiRe-LII data took the temperature results from the simultaneous NTLAF measurement.

#### 4.2.5 Soot volume fraction measurement

The in-flame soot volume fraction was evaluated from the prompt signal collected with the first camera, with the LII data calibrated against Connelly's published data sets [31]. The main difference from previous measurements, however, is that the present data were phase-averaged from 50 images to significantly enhance the SNR over the single-shot case. Phase-averaging the single-shot images increases the SNR from 7.3 : 1 to 21.4 : 1. This improved SNR is a feature of the present measurements, not only for the LII, but also for the TiRe-LII. The lower limit of detection for the soot volume fraction is 0.01 ppm.

#### 4.2.6 Chemiluminescence of OH\* measurement

The chemiluminescence of OH\* is a natural emission of radiation when chemically excited OH return to its lower electronic state. Previous studies have shown that the intensity of OH\* chemiluminescence can act as a flame marker to study the flame location [32, 33]. In order to investigate the flame structure near to the fuel tube for the  $St = 0.23$  case, a series of OH\* chemiluminescence images were taken using a ICCD camera coupled with a f/4.5 UV transmissive lens. To increase the

SNR, an exposure time of 3 ms was used and 50 images were accumulated to form one image which yields a SNR of 15.8 : 1.

## 4.3 Results

### 4.3.1 Steady flame

Figure 4.2 presents the planar images of gas temperature,  $T_g$ , soot volume fraction,  $f_v$  and diameter of primary particles,  $d_p$  for the steady flame. The white regions of the temperature image correspond to a condition in which the measurement is outside the range of NTLAF sensitivity, i.e. below 800 K, or in the oxidising region of the flame where the population of indium nanoparticles is insufficient. For example, the white cone shape region immediately above the burner in Fig. 4.2a is the "potential core" region in which the fuel is below the 800 K threshold. The adiabatic temperature for the soot-free steady premixed flame is calculated to be 2340 K using the OPPDIF routine of CHEMKIN, with the GRI-Mech 3.0 mechanism [34]. This is 366 K higher than the maximum  $T_g$  measured with NTLAF of 1974 K, consistent with the enhanced heat loss through the radiative heat transfer, particularly from the soot in the flame, but also to the burner.

Figure 4.2b shows that the mature soot first forms in the wings on the fuel-rich side of the high-temperature reaction zone, as is well known. However, the peak of  $f_v$  occurs on the jet centreline near to  $x/D = 5.5$ . In the region where soot is first measured, local  $T_g$  ranges from 1700–1800 K, which is consistent with previous literature [35]. However, this temperature is not the same as that of soot inception, because the LII technique only measures soot in the mature state, so that it does not respond to nascent soot. The inception of nascent soot typically starts at a temperature of approximately 1300 K [36]. Figure 4.2c shows that, although  $d_p$  scales loosely with  $f_v$ , there are nevertheless significant differences. That is, while  $d_p$  and  $f_v$  tend to increase and decrease together, the regions of uniform  $d_p$  are much broader, so that the peak values of  $d_p$  are found well into the wings, rather than only on the centreline, as is the case for  $f_v$ .

[This page is intentionally left blank]

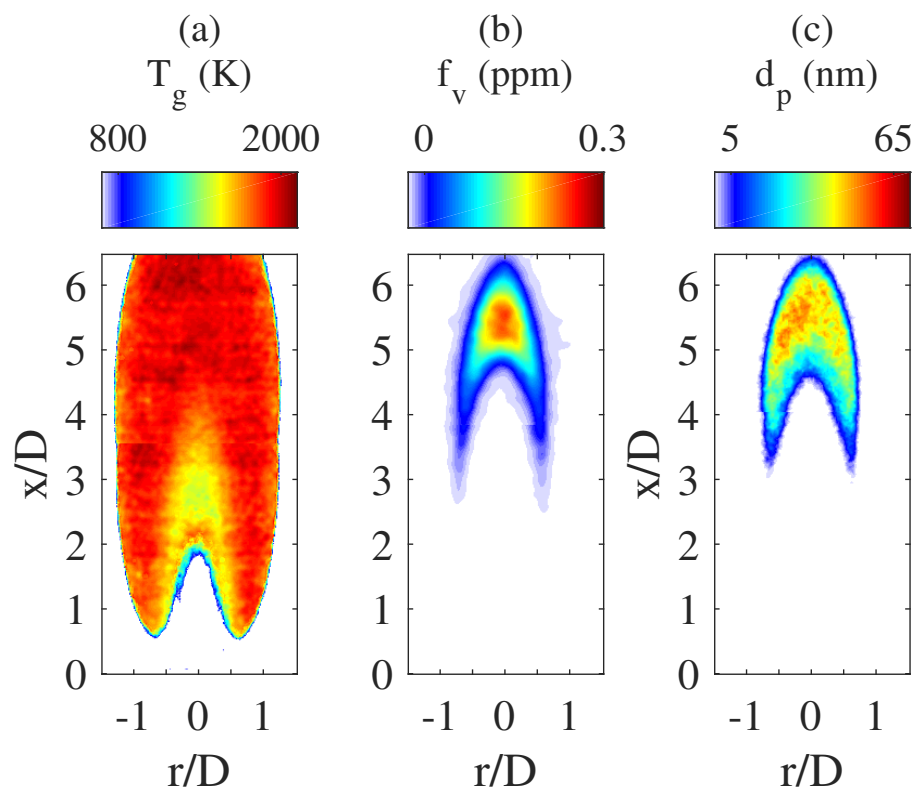


**Figure 4.2** Planar pseudo-colour images (each at the same spatial scale) of the steady laminar non-premixed flames (32% ethylene diluted by nitrogen), with showing (a) gas temperature,  $T_g$  measured with NTLAF; (b) soot volume fraction,  $f_v$  measured with LII; (c) diameter of primary soot particles,  $d_p$  measured with TiRe-LII.

Figure 4.3 presents a quantitative comparison of current temperature measurements with the data of Connolly [37], here referred to as the Connolly data, together with the measurements of  $f_v$ . It is important to note that Connolly reports the soot temperature,  $T_s$ , as obtained with two-colour pyrometry, while the current study reports gas temperature. All data are plotted along the flame's axis of symmetry. Both  $T_g$  and  $T_s$  exhibit a similar trend, although  $T_g$  is  $\sim 300$  K lower and also extends to a near-field peak of  $\sim 1700$  K, reducing again to  $\sim 1500$  K and then increasing approximately linearly with the HAB although with some notable departures. The reduction at  $x/D \simeq 2$  coincides with the onset of solid phase soot, so can be deduced to be associated with enhanced radiative cooling from soot. However, given that the actual values of  $f_v$  are very low at this point, it is possible that nascent soot may be primarily responsible for this cooling. More work is required to investigate this point. A second weaker reduction in temperature is found at  $x/D \simeq 3.5$ , which is more pronounced in the Connolly data and at a slightly different position, but present in both data. This coincides with a slight local peak in  $f_v$  as measured by Connolly, although the same peak is not found in the present measurement. A further local peak in  $T_g$  is found at  $x/D \simeq 5$ , which coincides with the peak in  $f_v$  in the present data. Still higher in the flame, the  $T_g$  increases slightly as the soot is consumed to peak in a region of near uniform temperature for  $x/D \geq 6$  to the end of the measurement range.

Figure 4.3 also shows the current  $f_v$  compared with the LII-measured and pyrometry-derived  $f_v$  of Connolly data. The maximum values of the three  $f_v$  data sets agree well with each other. Interestingly, the current LII measurement agrees much better with the previous pyrometry-derived result than the LII-measured  $f_v$  of Connolly data. The cause for this is presently unknown.

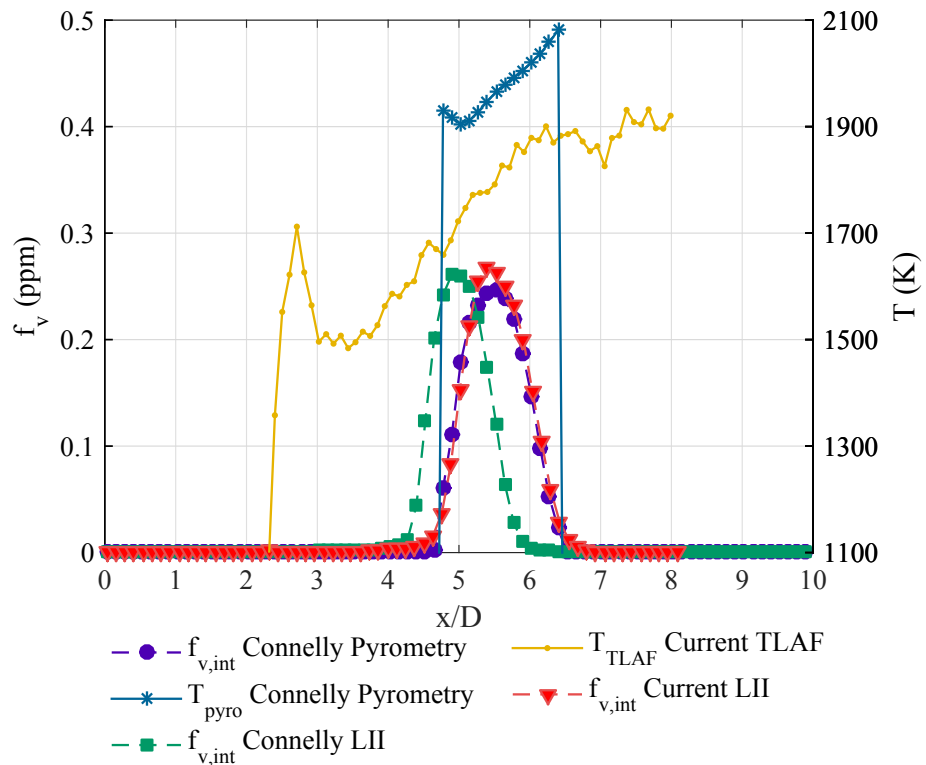


**Figure 4.3** Axial evolution of gas temperature along the centreline and soot volume fraction as a function of height above the burner ( $x/D$ ) for steady  $C_2H_4$ /air flame with a fuel bulk exit velocity of 0.35 m/s. Current measured gas temperature and soot volume fraction results are compared with Connelly's soot temperature and two sets of soot volume fractions measured with LII and derived from pyrometry. For clarity, only every fifth measurement point is shown.

### 4.3.2 Flame with $St = 0.23$

Figure 4.4 present the average of 50 phase-resolved planar images of  $T_g$ ,  $f_v$  and  $d_p$  for the flame with  $St = 0.23$ , correspondingly. The results are presented for a time interval between each panel of 5 ms, which is equivalent to a phase angle difference of  $36^\circ$ . The upper regions of the  $T_g$  images in the panels  $\phi = 36^\circ$  and  $288^\circ$  are cropped because they exceeded the height of laser sheet and result in poor SNR.

The planar images of  $T_g$  as shown in Fig. 4.4a serve as an indicator of the flame structure. The flame structure under acoustic forcing is dramatically different from that of the steady flame. The most noticeable differences are the neck region near to the burner exit and the cold region at the core of the forced flame. During  $\phi = 36^\circ$  to  $180^\circ$ , the regions presented as white colour at the centreline near to the jet exit surrounded by the high-temperature regions are deduced to result from the cold fuel that is injected into the reaction zone (i.e. to be at a temperature below that required to thermally decompose the indium). At  $\phi = 216^\circ$ , the white region shrinks as the flame starts to burn radially inward near to the jet exit because the centreline velocity decreases. The fuel-rich component, as denoted by the low temperature region at the core of the flame, travels downstream with time while the upstream region is gradually narrowed by the reaction zone. The tip of the flame is pinched off from the base at  $\phi = 324^\circ$ , as can be seen from the temperature images. The pinched-off flamelet travels downstream under the influence of buoyancy and the tip flamelet burns toward the rich core to be entirely consumed at  $\phi = 108^\circ$ . The values of both  $T_g$  and  $f_v$  for the tip flamelet are relatively uniform for the final phases from  $\phi = 36^\circ$  to  $108^\circ$ . It is also interesting to note that at  $\phi = 324^\circ$ , when the flamelet is fully detached, no high-temperature region is found on the burner axis. However, at  $\phi = 0^\circ$ , a dome-shaped high-temperature region can be found attached to the burner lip. More insight into this can be obtained from Figure 4.5, which presents the temporal evolution of the natural chemiluminescence of  $\text{OH}^*$  for the flame with  $St = 0.23$  from  $\phi = 288^\circ$  to  $\phi = 18^\circ$ , with phase angle interval of  $10^\circ$ . This clearly shows that combustion is found right on the axis and extends right across the base of the burner but does not extend downstream, providing strong evidence that the combustion extends further upstream into the fuel tube during this phase of the cycle. This phenomenon has not been reported previously.

Figure 4.4b shows the temporal evolution of  $f_v$  for the flame with  $St = 0.23$ . The maximum value of  $f_v$  is 0.45 ppm, which is higher than that of the steady flame by a factor of two. During  $\phi = 0^\circ$  to  $108^\circ$ , while the pinched-off flamelet exhibits high soot loading, the attached flame does not generate any soot until phase  $\phi = 144^\circ$ , at which point the soot in the flamelet is completely oxidised. There is a general trend of  $f_v$  increasing with the flame length. Also, different from the steady flame, the  $f_v$  tends to peak in the annular region of the tip flamelet, instead of on the centreline. The soot region forms a hollow soot "shell" at  $\phi = 288^\circ$ ,



and the value of  $f_v$  at  $x/D = 4$  increases significantly from about 0.05 ppm to above 0.2 ppm. However, the distribution of  $f_v$  is not uniform within the flamelet. Instead, it exhibits peaks both in the width and in the magnitude of  $f_v$  at three locations, one near to the base and in the other two at outer-extremities of the flamelet. More data are required to fully resolved the cause for these peaks.

Figure 4.4c presents the temporal evolution of  $d_p$  for the flame with  $St = 0.23$ . The value of  $d_p$  peaks only at the outer-extremities of the flamelet and not at its base, so that it coincides with only two of the three peaks of  $f_v$  described above. Similarly, the regions of large  $d_p$  are somewhat larger than those of peak  $f_v$ . That is, the evolution of  $d_p$  and  $f_v$  are different, suggesting a distinctive dependence on temperature and residence time.

Figure 4.6a and b show the contours of normalised  $f_v$  and  $d_p$  superimposed onto the planar  $T_g$  image for the flame with  $St = 0.23$  at  $\phi = 288^\circ$ , correspondingly. The values of  $f_v$  and  $d_p$  are normalised by the maximum values,  $f_{v,max} = 0.45$  ppm and  $d_{p,max} = 73.6$  nm. The absence of soot at the core of the flame suggests that  $T_g$  as low as 1500 K is unfavourable for the formation of graphitic soot, at least for the residence times associated with this flame. The values of  $f_v$  and  $d_p$  peak in the region where  $T_g$  is about 1700 K. At the neck region of the flame, however, even though the value of  $T_g$  is around 1700 K, no mature soot is measured. This is consistent with expectation that this region is associated with high strain, which inhibits soot.

[This page is intentionally left blank]

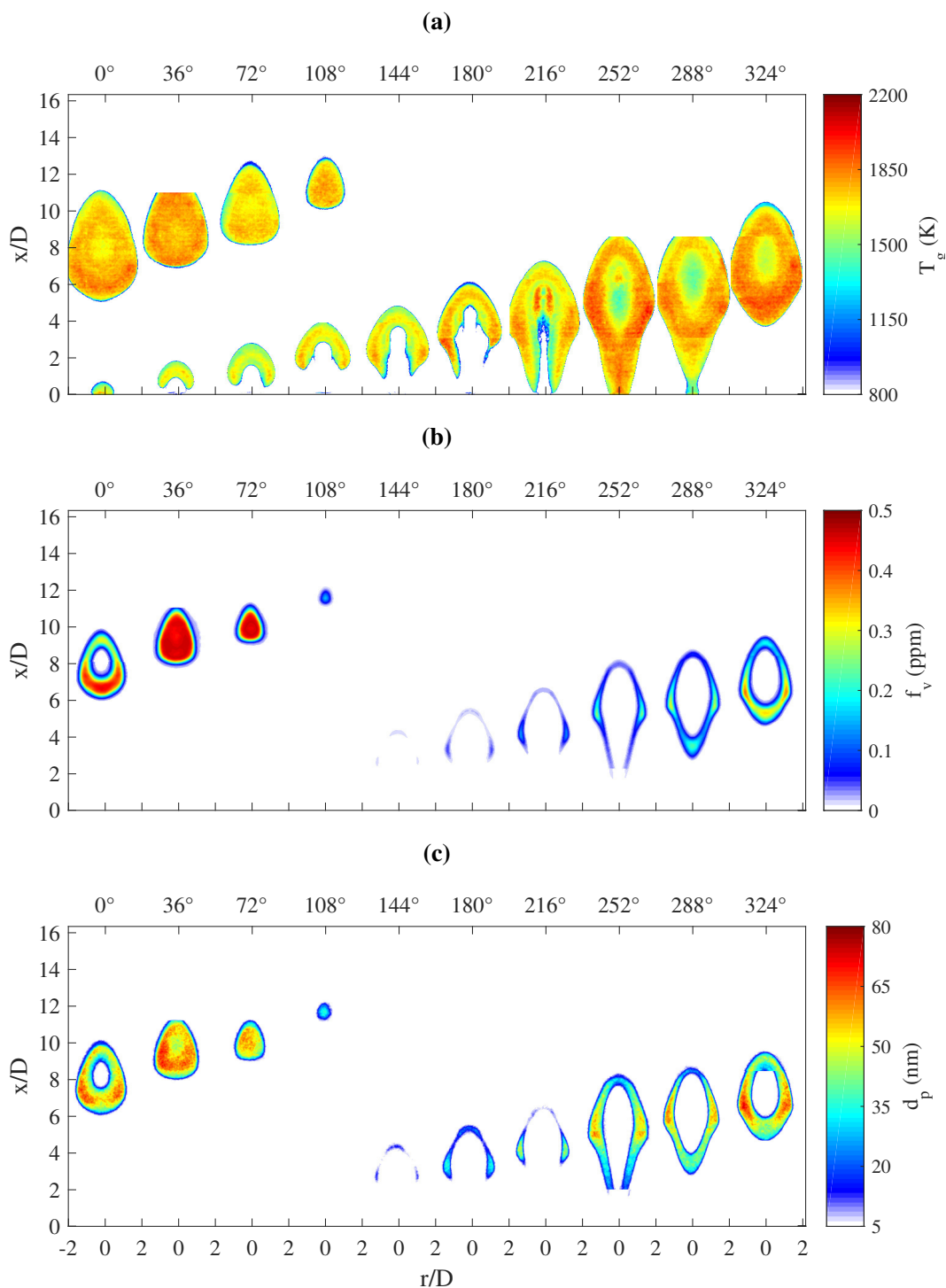


**Figure 4.4** Planar images of (a) gas temperature, (b) soot volume fraction and (c) diameter of primary soot particles for flame with  $St = 0.23$  at 50% modulation. The time interval between the panels is 5 ms, corresponding to phase angle of  $36^\circ$ . Panels  $\phi = 36^\circ$ ,  $252^\circ$  and  $288^\circ$  are cropped because these regions exhibit poor SNR.

[This page is intentionally left blank]

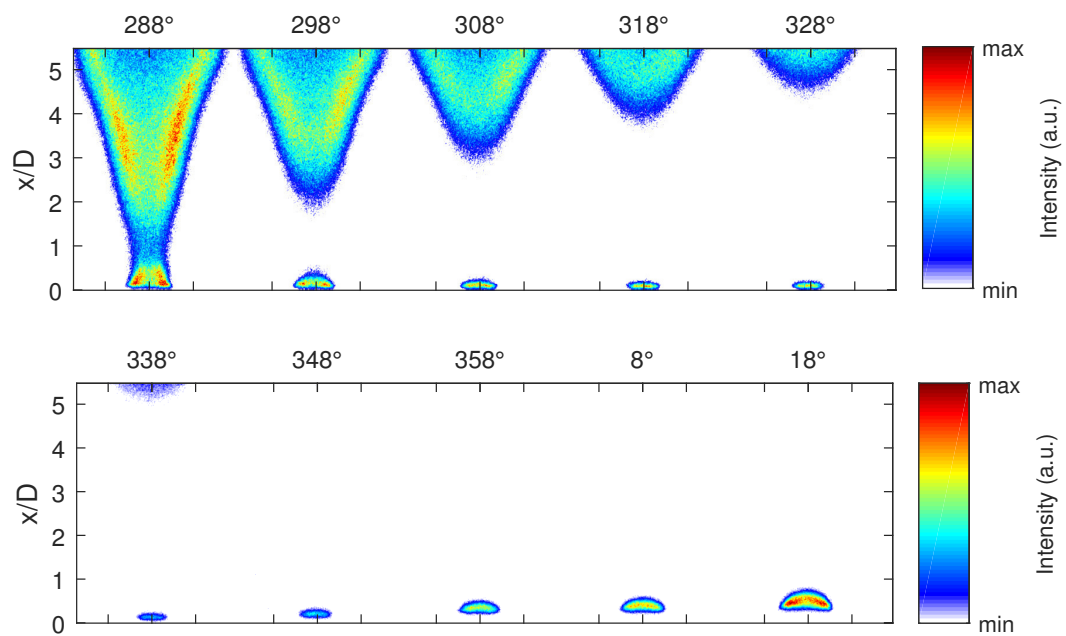


**Figure 4.5** Temporal evolution of the distribution of OH\* chemiluminescence for the flame with  $St = 0.23$ . The phase angle difference between panels is  $10^\circ$ , starts from  $\phi = 288^\circ$  to  $18^\circ$ .

[This page is intentionally left blank]

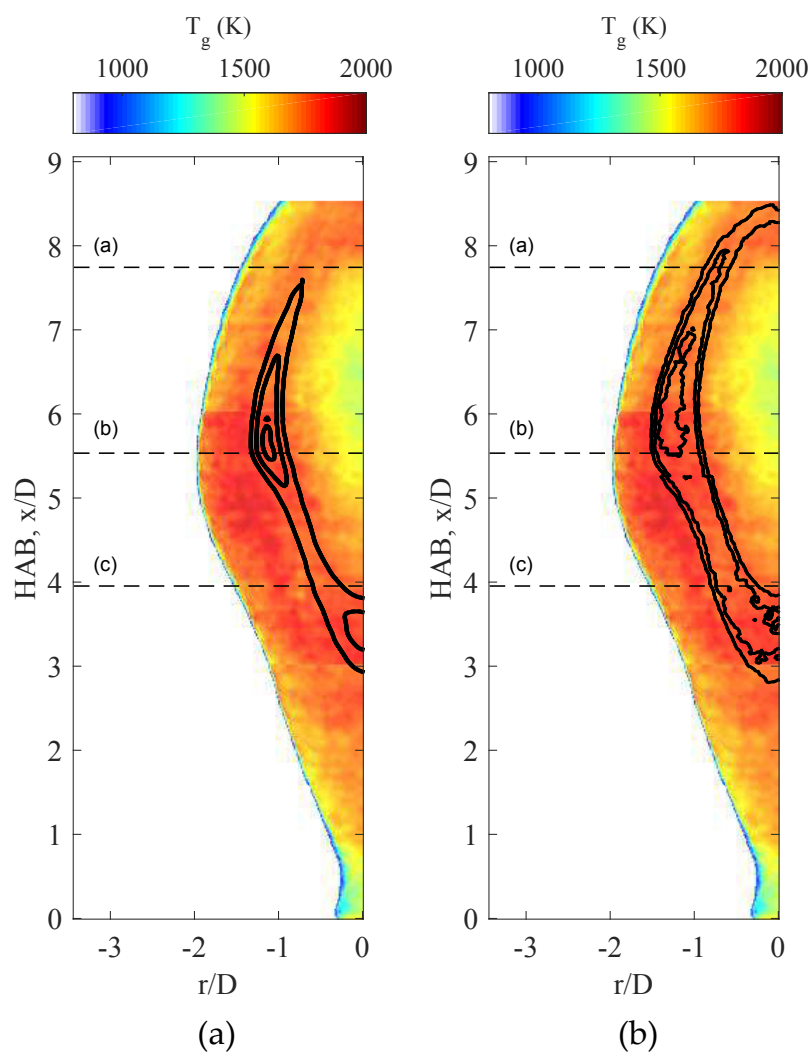


**Figure 4.6** Contours of (a) soot volume fraction and (b) diameter of primary particles superimposed onto the planar image of gas temperature for the flame with  $St = 0.23$  at  $\phi = 288^\circ$ . The soot volume fraction and diameter of primary soot particles are normalised by the maximum values,  $f_{v,max} = 0.45$  ppm and  $d_{p,max} = 73.6$  nm.

### 4.3.3 Flame with $St = 0.46$

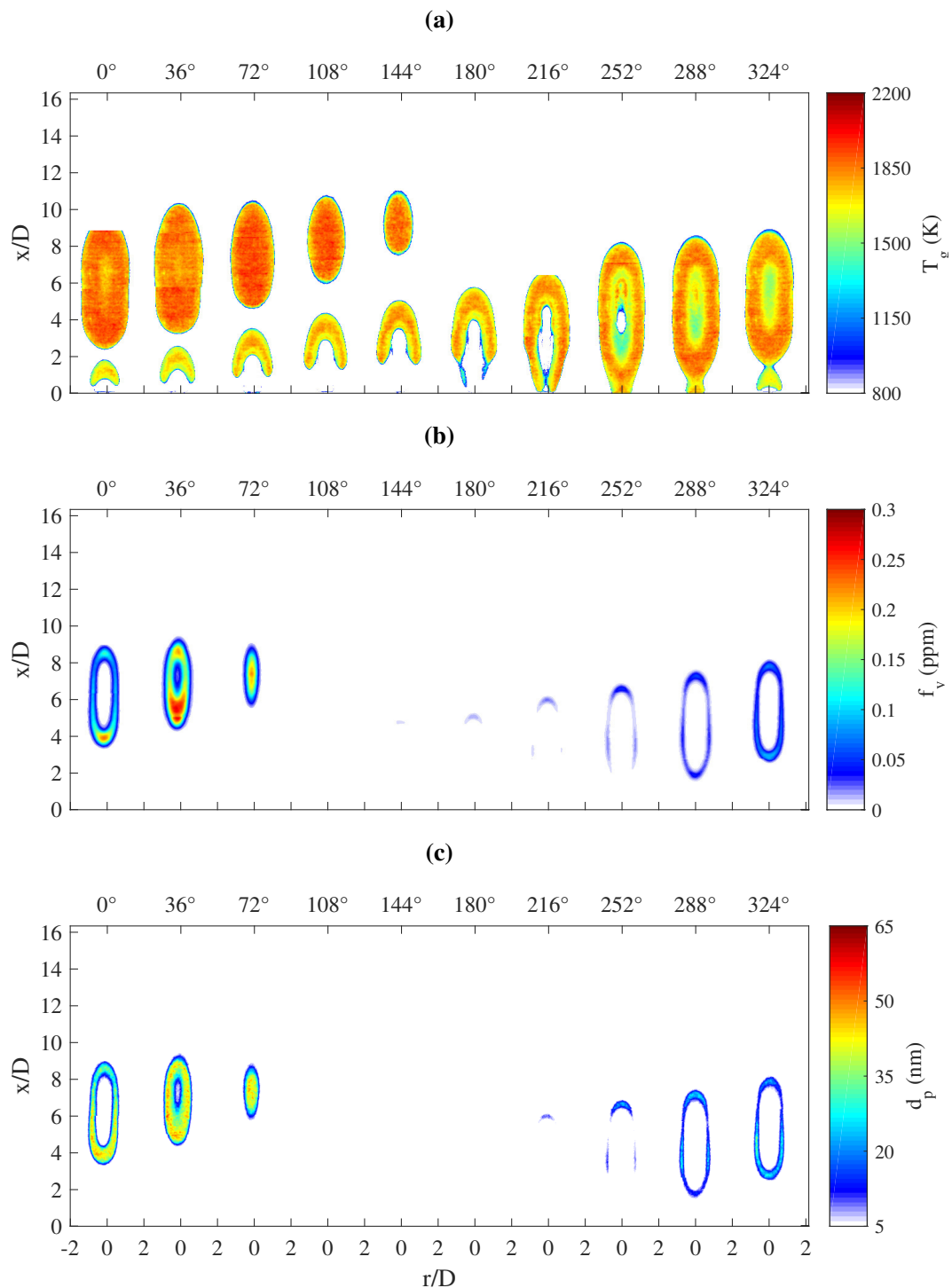
Figure 4.7 presents the average of 50 phase-resolved planar images of  $T_g$ ,  $f_v$  and  $d_p$  for the flame with  $St = 0.46$ . A series of images is presented, with a time interval of 2.5 ms between each panel, which is equivalent to a phase angle difference of  $36^\circ$ . The upper regions of the temperature images for  $\phi = 0^\circ$  and  $216^\circ$  are cropped because of the poor SNR exhibited there.

Figure 4.7a shows that the structure of the flame with  $St = 0.46$  is significantly different from that for the flame with  $St = 0.23$ . The temporal evolution of the shape of the attached flame is similar to the other forced flame, but the width and length of this flame are both relatively narrow and long. Different from the other forced flame, the cold fuel region at the centreline of this flame remains unburned at  $\phi = 252^\circ$ , although the fuel-rich core is completely surrounded by reaction zone. However, at  $\phi = 72^\circ$ , there are two distinct fuel-rich components at the core of the flame, one at the upper part with a higher  $T_g$ , and the other one at the lower part with a lower  $T_g$ . The planar image of  $T_g$  at  $\phi = 108^\circ$  shows the transition phase of these two components merging together. At phase  $\phi = 144^\circ$ , they are merged entirely so that only one low-temperature region is found at the core of the flame. The necking occurs at  $\phi = 324^\circ$  and the flamelet is pinched off at  $\phi = 0^\circ$ . Unlike the flame with  $St = 0.23$ , the attached flame for  $St = 0.46$  is always visible, whereas in the other forced flame, the attached flame disappears at  $\phi = 324^\circ$  when the pinching occurs. This implies that the attached flame for  $St = 0.46$  does not extend upstream from the burner exit plane.

Figure 4.7b presents the temporal evolution of  $f_v$  measured for the flame with  $St = 0.46$ . The peak value of  $f_v$  measured is 0.27 ppm, higher than the value of  $f_v$  (0.24 ppm) measured for the steady flame, but lower than the peak value of  $f_v$  (0.45 ppm) for the flame with  $St = 0.23$ . In contrast to the other forced flame, the maximum value of  $f_v$  is found at the centreline of the flame. Similar to the flame with  $St = 0.23$ , the soot does not mature in the cold region at the core of the flame, and at the neck region near to the burner exit. At  $\phi = 36^\circ$ , the value of  $f_v$  reaches a maximum and decreases with time in the following phases. For  $\phi = 108^\circ$ , all the soot is oxidised, so that no LII signal is detected in either the pinched-off flamelet or the attached flame.

Figure 4.7c presents the temporal evolution of  $d_p$  for the flame with  $St = 0.46$ . No data are presented for  $\phi = 108^\circ$ ,  $144^\circ$  and  $180^\circ$  (i.e. the regions are coloured white), although for different reasons. The phase  $\phi = 108^\circ$  is coloured white due to the absence of soot particles. However, the data of  $d_p$  at  $\phi = 144^\circ$  and  $180^\circ$  are discarded because the average  $d_p$  is below 5 nm and the SNR is too weak to be reliably separated from noise. The  $d_p$  reaches its maximum (56 nm) at  $\phi = 36^\circ$  at  $x/D = 4$ . All the soot is oxidised at  $\phi = 108^\circ$ .





**Figure 4.7** Planar images of (a) gas temperature, (b) soot volume fraction and (c) primary particles diameter for the flame with  $St = 0.46$  at 50% modulation. The time interval between the panels is 2.5 ms, corresponding to phase angle of  $36^\circ$ . Panels  $\phi = 36^\circ$  and  $180^\circ$  are cropped as these regions exhibit poor SNR.

Figure 4.8a and b present the contours of normalised  $f_v$  and  $d_p$  superimposed onto the planar image of  $T_g$  for the flame with  $St = 0.46$  at  $\phi = 288^\circ$ . The values of  $f_v$  and  $d_p$  are normalised by the maximum values,  $f_{v,max} = 0.27$  ppm and  $d_{p,max} = 56.4$  nm. The high-temperature region at the core of the flame is the result of two fuel-rich components merging together, as noted earlier. The soot region is located at the fuel-rich side of reaction zone, where  $T_g$  is around 1800 K. In contrast to the flame with  $St = 0.23$ , the values of  $f_v$  and  $d_p$  for this flame peak at the tip of the flamelet, whereas the corresponding values for the other forced flame peak at a height just above the neck region.

#### 4.3.4 Comparison of different flames

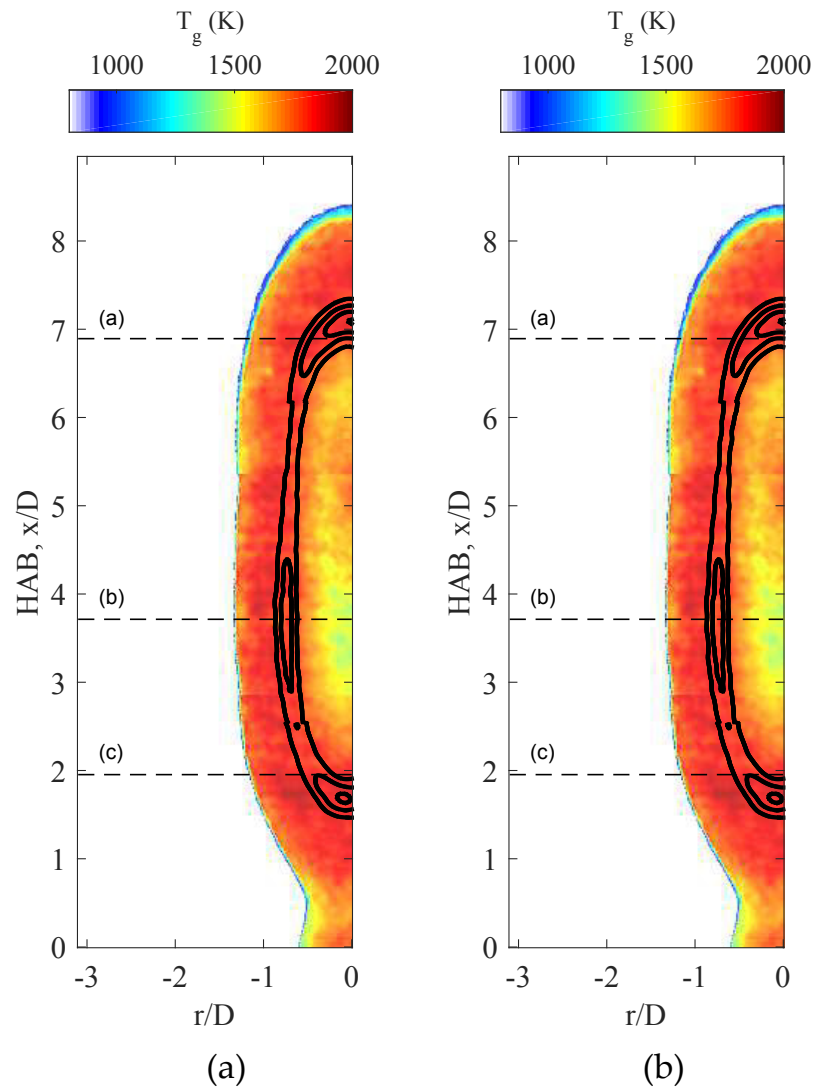
Table 4.1 compares the peak values of  $f_v$  with the time-averaged and volume-integrated soot volume fraction,  $\bar{f}_{v,total}$  for both the steady flame and the two forced flames. For an axisymmetric flame, the instantaneous total soot volume fraction can be expressed as

$$f_{v,total}(t) = 2\pi r \int_0^{x_{max}} \int_0^{r_{max}} f_v(r, x) dr \cdot dx \quad (4.1)$$

where  $f_v(r, x)$  is the local soot volume fraction at a given HAB,  $x$ , and a radial distance from the axis,  $r$ . For the two forced flames, the values of  $f_v$  are integrated at each HAB and then time-averaged over the entire cycle before integrated along the axis [7].

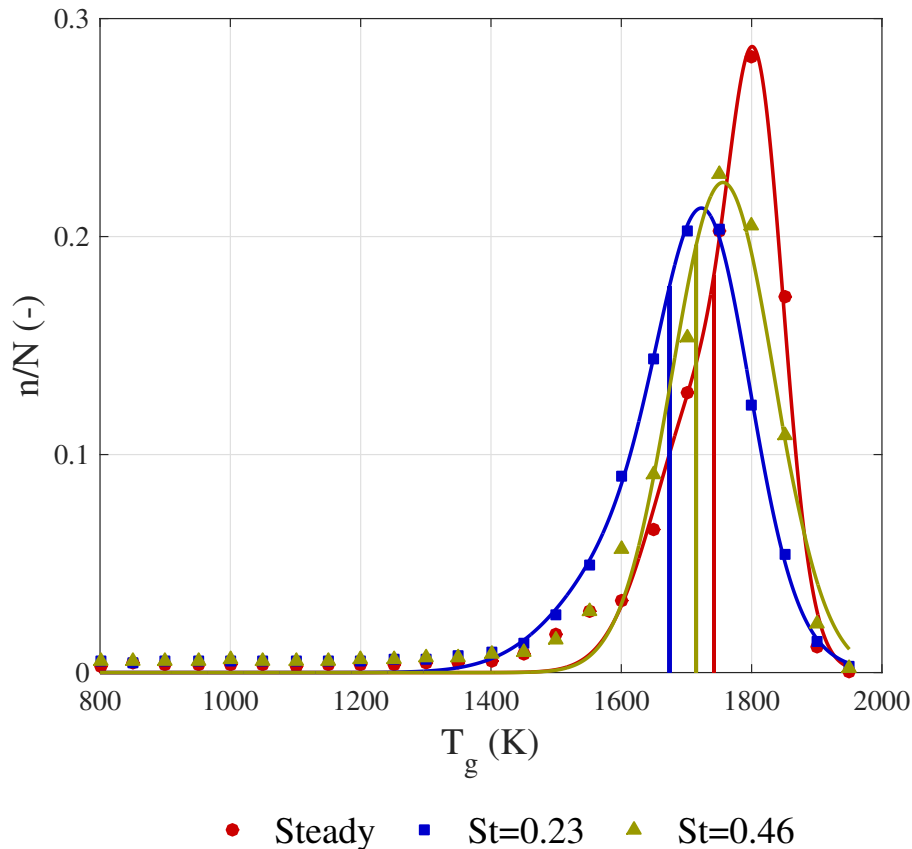
**Table 4.1** Summary of the soot properties measured in the steady and forced flames.

	Peak soot volume fraction, $f_{v,max}$ (ppm)	Time-averaged total soot volume fraction, $\bar{f}_{v,total}$ ( $m^3$ )	Maximum diameter of primary particles, $d_{p,max}$ (nm)
Steady	0.24	$1.22 \times 10^{-9}$	51.8
$St = 0.23$	0.45	$5.37 \times 10^{-9}$	73.6
$St = 0.46$	0.27	$1.65 \times 10^{-9}$	56.4



**Figure 4.8** Contours of (a) soot volume fraction and (b) diameter of primary particles superimposed onto the planar image of gas temperature for the flame with  $St = 0.46$  at  $\phi = 288^\circ$ . The soot volume fraction and diameter of primary soot particles are normalised by the maximum values,  $f_{v,max} = 0.27$  ppm and  $\bar{d}_{p,max} = 56.4$  nm.

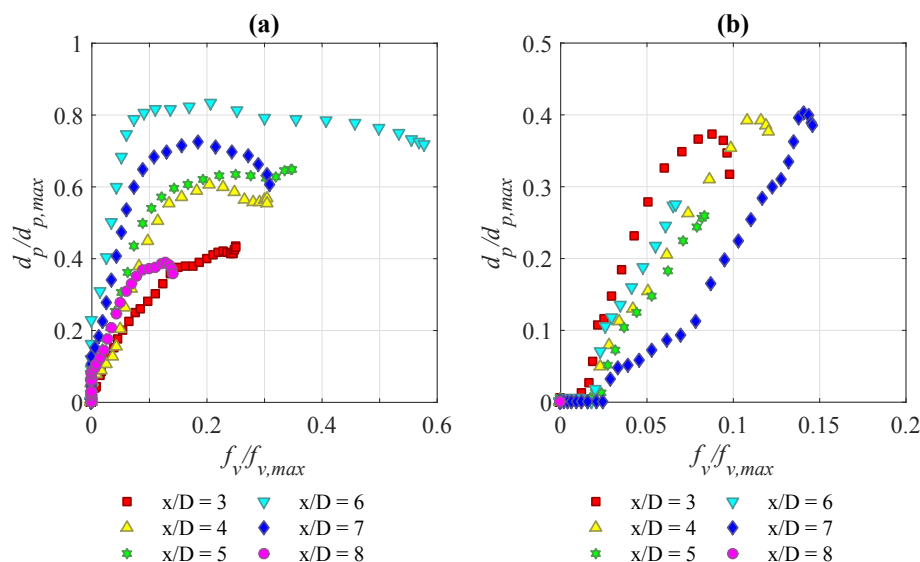
Figure 4.9 presents histograms of the distribution of  $T_g$  calculated from the three-dimensional revolution of the images of  $T_g$  shown in Figs. 4.2a, 4.4a and 4.7a. This is the fraction ( $n$ ) of the total flame volume ( $N$ ) that exhibits the temperatures range from 800-2000 K, in increments of 50 K. Here,  $n$  is calculated by performing a three-dimensional revolution around the axis for each pixel that falls into each bin, and the values of  $N$  is the sum of  $n$ . Each histograms is left-skewed (toward the temperatures favourable for graphitic soot formation, around 1700–1800 K). The mean of  $T_g$ , as denoted by the vertical lines in Fig. 4.9, is defined as the temperature at the 50th percentile ( $\sum \frac{n}{N} = 0.5$ ). The mean of  $T_g$  for the steady flame, the flame with  $St = 0.23$  and 0.46 is 1742, 1674 and 1715 K, respectively. The histogram for the steady flame exhibits the highest skewness, followed by the flame with  $St = 0.46$  and the flame with  $St = 0.23$ . That is, the most probable temperature is lower for the forced flames than the steady flame. This is consistent with the trends in  $f_{v,total}$ , in that an increase in the volume fraction of soot corresponds to a decrease in the flame temperature.



**Figure 4.9** Distribution of gas temperature calculated from the three-dimensional revolution of corresponding images of gas temperature. It presents the fraction ( $n$ ) of the total flame volume ( $N$ ) that exhibits the temperatures range from 800-2000 K, with an increment of 50 K. The vertical lines correspond to the mean temperature for each flame.

Figure 4.10a presents the values of  $d_p/d_{p,max}$  as a function of  $f_v/f_{v,max}$  at selected HABs. That is, the data span a radial traverse across the flamelet. Several important points can be made. Each data set typically exhibits two distinct regimes, a linear and a “plateau” regime with elbow point. However, this trend is not absolute, so that the case  $x/D = 7$  is more like an inverted hook than an elbow. Similarly, some cases exhibit extra points of inflection in the “linear” region at low values of  $f_v$ , notably at  $x/D = 4$  and 8. In addition, the slope of the linear region is not constant, but depends on the value of  $x/D$ . Furthermore, the value of the elbow point does not occur at either a constant value of  $f_v$  or  $d_p$ , although it is typically found in the range  $0.05 \leq f_v \leq 0.1$  ppm. This shows that it is not possible to accurately correlate  $f_v$  with  $d_p$  using a simple analytical function. Nevertheless, the elbow function is a significantly better approximation than a linear function.

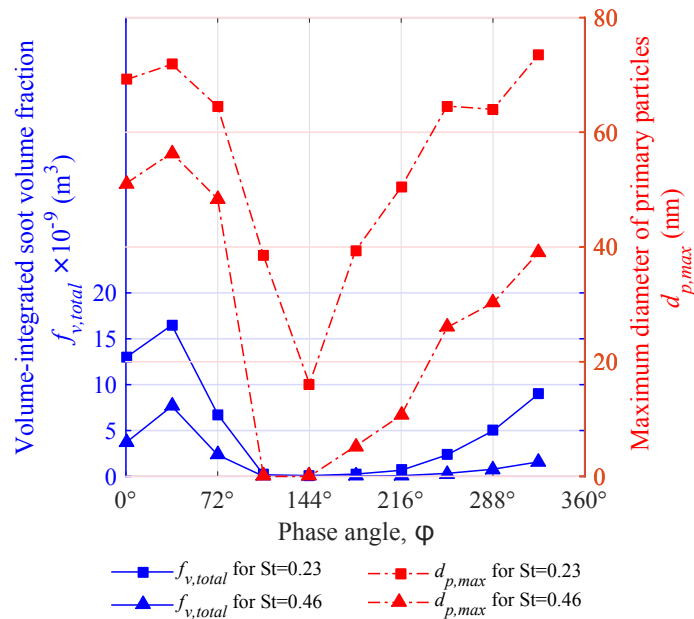
Figure 4.10b presents the values of  $d_p/d_{p,max}$  as a function of  $f_v/f_{v,max}$  at various values of HAB for the flame with  $St = 0.46$ . Similar to Fig. 4.10a, a linear regime is evident. However, unlike Fig. 4.10a, the constant of proportionality between  $d_p$  and  $f_v$  is almost the same at each HAB and there is almost no plateau regime. Furthermore, the linear region does not go through the origin and the linear regions are offset from each other by complex relationships at low values of  $f_v$ . Once again, these dependences are not easily presented by a simple function, which demonstrates that their interdependence is both highly complex and non-linear.



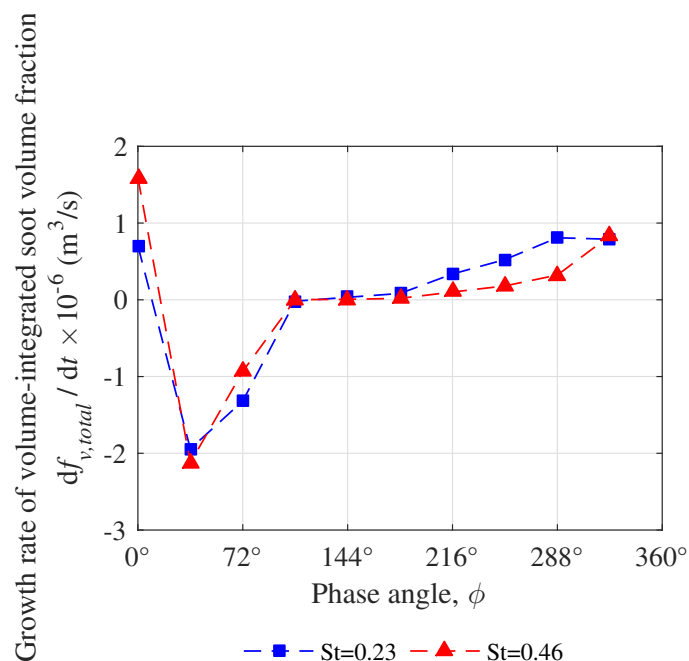
**Figure 4.10** The dependence of  $d_p/d_{p,max}$  upon  $f_v/f_{v,max}$  at selected HABs for the flames with (a)  $St = 0.23$  ( $f_{v,max} = 0.45$  ppm and  $d_{p,max} = 73.6$  nm), and (b)  $St = 0.46$  ( $f_{v,max} = 0.27$  ppm and  $d_{p,max} = 56.4$  nm) at  $\phi = 288^\circ$ . These data are obtained only from the left hand side of the flame.

Figure 4.11 presents the maximum values of  $d_p$  and  $f_{v,total}$  at each phase for the flames with  $St = 0.23$  and  $0.46$ . The maximum value of  $f_{v,total}$  and  $d_p$  for the flames with  $St = 0.23$  peaks at the same phase as the other forced flame, which is  $\phi = 36^\circ$ . The growth rates of the  $f_{v,total}$  for both flames share a similar trend, as shown in Fig. 4.12. The growth rate of  $f_{v,total}$  for both flames increase gradually from  $\phi = 108^\circ$  to  $324^\circ$ . The growth rate reaches a minimum where the total soot volume reaches a maximum. This suggests that the rate of oxidation reaches a maximum at this point, presumably due to the dynamics of the flame. Furthermore, consistent trends can be seen between the peak values of  $f_v$  and  $d_p$  through the phases, although their values are not linearly related. This is also consistent with the previous results.

Figure 4.13 presents a comparison between the radial profiles of  $T_g$ ,  $f_v$  and  $d_p$  for the three flames. To facilitate the comparison, only the measurements at the phase  $\phi = 288^\circ$  for the forced flames are chosen. For each flame, there are three  $f_v$  peaks across the axial direction. To better represent the  $f_v$  radial profile for the forced flames, the comparisons are made at these three  $x/D$  that exhibit the top three highest  $f_v$ . For the flame with  $St = 0.23$ , the selected heights are  $x/D = 7.76, 5.55$  and  $3.97$ . For the flame with  $St = 0.46$ , the selected heights are  $x/D = 6.91, 3.73$  and  $1.97$ . For the steady flame, the selected heights are  $x/D = 6, 5$  and  $4$ . The values of  $f_v$  and  $d_p$  are normalised by the maximum values as given in Table 4.1. The spatial locations of  $f_v/f_{v,max}$  and  $d_p/d_{p,max}$  do not coincide for all the cases. The peak values of  $d_p/d_{p,max}$  in all the regions are generally slightly on the oxidising side of the flame relative to the peak values of  $f_v/f_{v,max}$ . The exception is for the flame with  $St = 0.46$  in the mid and upper regions of the flame. The peak value of  $f_v/f_{v,max}$  increases with height together with the peak value of  $d_p/d_{p,max}$ . In contrast, the value of  $f_v/f_{v,max}$  for the flame with  $St = 0.46$  remains low at all three regions, while the value of  $d_p/d_{p,max}$  increases significantly with the height. Also, for the steady flame,  $d_p/d_{p,max}$  is relatively constant at three of the heights, while the change in  $f_v/f_{v,max}$  is more dramatic. Furthermore, it appears that forcing the flame increases the distance between the reaction zone and soot region, which may imply a increase in the time required for soot particles to reach the oxidation zone.



**Figure 4.11** Temporal evolution of the volume-integrated soot volume fraction and maximum diameter of primary particles for the flames with  $St = 0.23$  and  $St = 0.46$  during one period. The solid lines indicate the volume-integrated soot volume fraction, and the dashed lines represent the maximum diameter of primary particles.



**Figure 4.12** Growth rates of volume-integrated soot volume fraction at each phase for flame with  $St = 0.23$  and  $St = 0.46$ .

[This page is intentionally left blank]



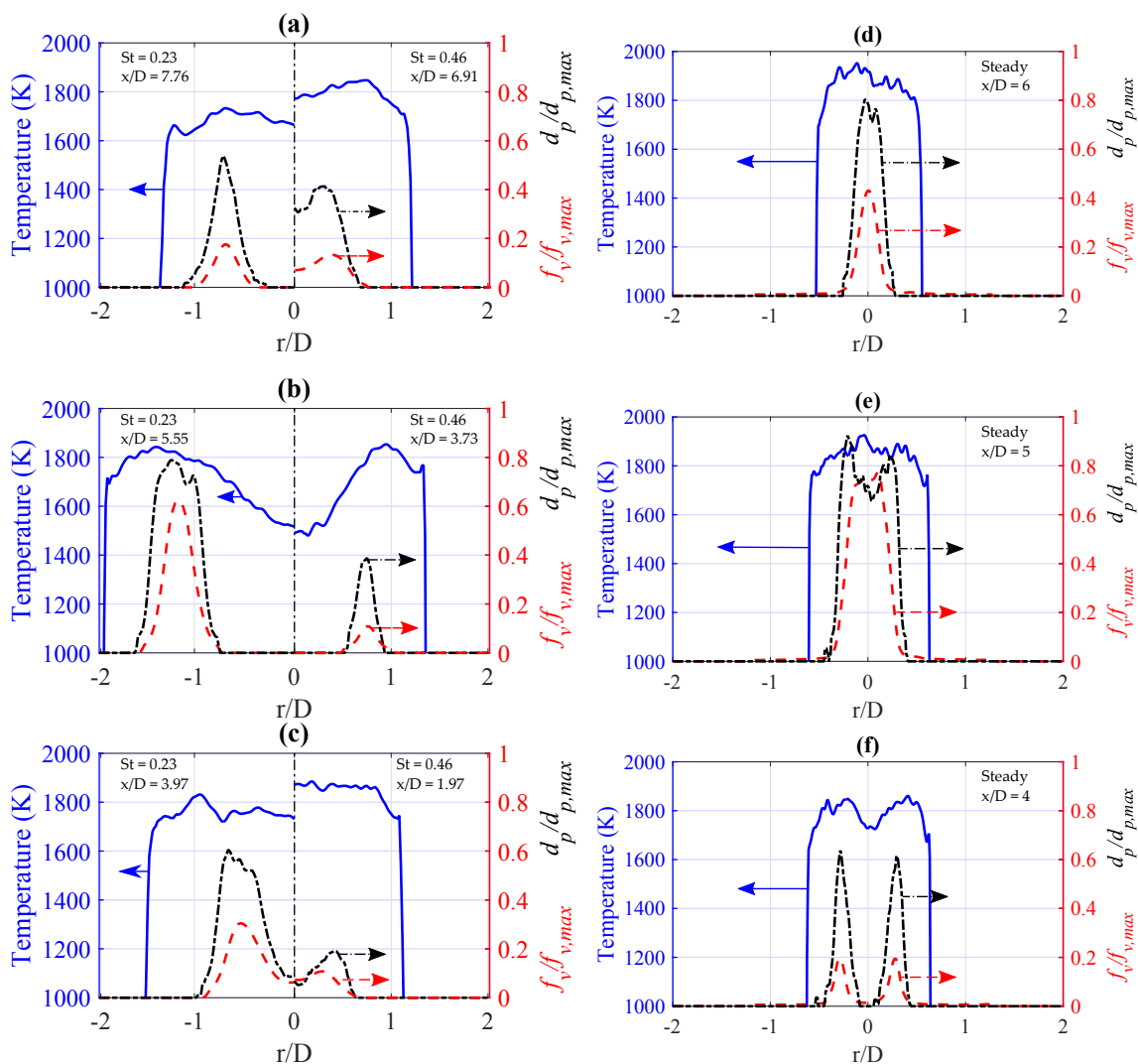


**Figure 4.13** A comparison between the radial profiles of the gas temperature (solid lines), the soot volume fraction (dashed lines) and the diameter of primary particles (dotted lines) for (a, b, c) the flames with  $St = 0.23$  (left half of the plots),  $St = 0.46$  (right half of the plots) and (d, e, f) the steady flame. The values of  $f_{v,max}$  and  $d_{p,max}$  for the flames are given in Table 4.1.

Table 4.2 summarises the flame length,  $L_{fl}$ , the flame width,  $W_{fl}$ , the time-averaged flame volume,  $\bar{V}_{fl,total}$  and the characteristic global residence time,  $\tau_G$  for each flame. The value of  $L_{fl}$  is defined to be the distance between the burner and the furthest downstream position of the time-averaged flame luminosity image (not shown here). The value of  $W_{fl}$  is defined to be the widest single row of the time-averaged flame luminosity image (not shown here). The value of  $\bar{V}_{fl,total}$  is calculated following a similar approaches as the Eq. 4.1. Firstly, the value of the flame volume at each HAB,  $V_{fl}$  is calculated at each phase, by performing a three-dimensional revolution around the axis. For each HAB,  $V_{fl}$  is averaged over one oscillation cycle and the sum of the values yields  $\bar{V}_{fl,total}$  for each flame.

The characteristic global residence time is defined as

$$\tau_G = \frac{\bar{V}_{fl,total}}{\dot{V}_{fuel}} \quad (4.2)$$

Here,  $\dot{V}_{fuel}$  for the forced flames are defined as the time-average volumetric flow rate of the fuel over one oscillation cycle, which is the same as that for the steady flame, 0.264 LPM or  $4.40 \times 10^{-6} \text{ m}^3/\text{s}$ .

**Table 4.2** Summary of the flame properties measured in steady and forced flames.

	Flame length, $L_{fl}$ (m)	Flame width, $W_{fl}$ (m)	Time- averaged total flame volume, $\bar{V}_{fl,total}$ ( $\text{m}^3$ )	Global residence time, $\tau_G$ (ms)
Steady	$3.01 \times 10^{-2}$	$0.97 \times 10^{-2}$	$1.59 \times 10^{-6}$	361
$St = 0.23$	$4.52 \times 10^{-2}$	$1.41 \times 10^{-2}$	$2.38 \times 10^{-6}$	541
$St = 0.46$	$4.03 \times 10^{-2}$	$1.02 \times 10^{-2}$	$1.84 \times 10^{-6}$	418

## 4.4 Discussion

The finding that the values of  $f_{v,max}$ ,  $\bar{f}_{v,total}$  and  $d_{p,max}$  for the two forced flames are higher than that of their steady counterpart stands in contrast with some previous investigations in which acoustic excitation is found to be associated with soot suppression due to an increased mixing rate [38, 39]. However, the finding is in consistent with other previous investigations [6, 7, 11]. The current results show that, at least for the present laminar flame, acoustic excitation at preferred-mode ( $St \simeq 0.3$ ) can lead to increased  $L_{fl}$  and  $W_{fl}$ , as shown in Table 4.1, which results in a larger  $\bar{V}_{fl,total}$ . The increase of  $\bar{V}_{fl,total}$  is also associated with increased  $\tau_G$ , which explains the enhanced soot production [18]. In addition, Fig. 4.12

shows that both the forced flames have similar growth rates of volume-integrated soot volume fraction at each phase, but the values of volume-integrated soot volume fraction for the flame with  $St = 0.23$  is larger than that for the flame with  $St = 0.46$ . That is, the present data are consistent with previous trends in which the  $\bar{f}_{v,total}$  in a flame scales with the residence time.

The available data shows that the two acoustically forced flames have similar qualitative features (i.e. the occurrence of necking and a hollow soot "shell" ) and can therefore be deduced to also have similar underlying vortex dynamics. It is also reasonable to deduce that the toroidal features reported by Papadopoulos et al. [15] for similar conditions are also present in these flames, although direct velocity measurements are needed to provide the details. The toroidal vortex is known to be responsible for the necking process observed here, and is evidently sufficiently strong to cause the observed pinch-off noted above. Hence, it is also reasonable to deduce that the neck region exhibits high strain rates that are likely to be unfavourable for soot formation [40], although new data are required to measure the local strain rates that correspond to the measured sooting parameters. This deduction is consistent with the absence of soot in the neck regions shown for both the  $St = 0.23$  and  $0.46$  cases (Figs. 4.6 and 4.8).

The shadowgraphs collected by Papadopoulos et al. [15] were used to deduce that heated region below the exit level of the fuel tube is present for their forced flames. The present measurements confirm there is combustion inside the fuel tube, rather than just a heated gas, as occur for the case of  $St = 0.23$ . Further investigations into the combustion region within the fuel tube is needed in order to achieve better understanding of coupling between the flame and time-varying flow field.

## 4.5 Conclusions

The present measurements have shown that acoustic forcing of the steady laminar non-premixed flame near to the preferred-mode ( $St = 0.23$  and  $0.46$ ) at 50% modulation of the centreline velocity increases  $f_{v,max}$ ,  $\bar{f}_{v,total}$  and  $d_{p,max}$  but result in overall decrease of  $T_g$  because of enhanced heat loss through soot radiation. In addition,  $f_{v,max}$ ,  $\bar{f}_{v,total}$  and  $d_{p,max}$  have been shown to scale approximately with  $\bar{V}_{fl,total}$  and  $\tau_G$ . This is consistent with previous trend reporting the scaling between the global residence time and soot production, but provide much more complete data than has previously been available. The results further suggest that the influence of acoustic forcing at the preferred-mode on  $f_{v,max}$  and  $d_{p,max}$  is amplitude dependent, given that some previous investigations have found it to increase mixing rates, reduce the flame volume and suppress soot, while others report the opposite trend.

New details have been revealed of the time-varying flow field, particularly with

regard to the influence of forcing on the hollow soot “shell” and the necking near to the burner exit. The soot region in the forced flames, although it is totally different from the steady flame, is confined to a restricted range of temperatures, namely 1700–1800 K. No soot was measured at the core of the forced flames, where temperatures are around 1500 K. This spatial relationship between temperature and soot region is well established in steady laminar flames, but the present investigation confirms that it also extends to unsteady flames. Furthermore, regions such as the neck zone near to the burner exit that are associated with high strain rates were found to exhibit a low soot loading, although the temperature is within the range favourable for soot formation.

The present measurements also reveal that the relationship between  $d_p$  and  $f_v$  is highly complex, implying that it also depends non-linearly on other parameters. Importantly, the relationship comprises a significant range that is approximately linear. However, for the flame with  $St = 0.23$  at  $\phi = 288^\circ$ , the slope varies significantly with axial position and also exhibits a second region that is characterised approximately by a plateau region. Furthermore, the trends are quite different for the flame with  $St = 0.46$  at the same phase where, although a strong linear regime is also found, it is offset by different amounts at different heights in the flame due to highly complex and non-linear relationships at low values of  $f_v / f_{v,max}$ .

The planar images of  $T_g$  and chemiluminescence reveal that the flame extends upstream into the burner for the forced flame with  $St = 0.23$ , although not for the  $St = 0.46$  case. The presence of the upstream combustion introduces strong coupling between the flame and time-varying flow field, which is much more difficult to characterise and adds greatly to the complexity of these flames. The presence or absence of this phenomenon should be carefully considered in future investigation of forced laminar flames.

## Acknowledgements

The authors gratefully acknowledge the Australian Research Council and the Australian Government Research Training Program Scholarship for their financial support. We also wish to thank Dr. Dahe Gu for his assistance in the experiments.

---

## References

- [1] M. Köhler, K. P. Geigle, W. Meier, B. M. Crosland, K. A. Thomson, and G. J. Smallwood, “Sooting turbulent jet flame: characterization and quantitative soot measurements”, *Applied Physics B* **104** (2011), pp. 409–425.
- [2] S. P. Kearney, D. R. Guildenbecher, C. Winters, T. W. Grasser, P. A. Farias, and J. C. Hewson, “Temperature, oxygen, and soot volume fraction measurements in a turbulent ethylene fuel jet flame”, tech. rep. Report No. SAND2015-7968, New Mexico and Livermore, CA, USA: Sandia National Laboratories, 2015.
- [3] S. M. Mahmoud, G. J. Nathan, P. R. Medwell, B. B. Dally, and Z. T. Alwahabi, “Simultaneous planar measurements of temperature and soot volume fraction in a turbulent non-premixed jet flame”, *Proceedings of the Combustion Institute* **35** (2015), pp. 1931–1938.
- [4] G. S. Lewis, B. J. Cantwell, U. Vandsburger, and C. T. Bowman, “An investigation of the structure of a laminar non-premixed flame in an unsteady vortical flow”, *Proceedings of the Combustion Institute* **22** (1988), pp. 512–522.
- [5] A. W. Strawa and B. J. Cantwell, “Investigation of an excited jet diffusion flame at elevated pressure”, *Journal of Fluid Mechanics* **200** (1989), pp. 309–336.
- [6] C. R. Shaddix, J. E. Harrington, and K. C. Smyth, “Quantitative Measurements of Enhanced Soot Production in a Flickering Methane/Air Diffusion Flame”, *Combustion and Flame* **99** (1994), pp. 723–732.
- [7] C. R. Shaddix and K. C. Smyth, “Laser-Induced Incandescence Measurements of Soot Production in Steady and Flickering Methane, Propane, and Ethylene Diffusion Flames”, *Combustion and Flame* **107** (1996), pp. 418–452.
- [8] O. A. Ezekoye, K. M. Martin, and F. Bisetti, “Pulsed flow modulation of soot production in a laminar jet-diffusion flame”, *Proceedings of the Combustion Institute* **30** (2005), pp. 1485–1492.
- [9] F. L. D. Oliveira, L. G. Barreta, and P. T. Lacava, “Experimental aspects of soot presence in pulsating diffusion flame”, *The Journal of the Brazilian Society of Mechanical Sciences and Engineering* **31** (2009), pp. 137–141.
- [10] H. S. Sapmaz, “Soot measurements in steady and pulsed ethylene/air diffusion flames using laser-induced incandescence”, Ph.D. dissertation, Florida International University, 2006.
- [11] J. Hentschel, R. Suntz, and H. Bockhorn, “Soot formation and oxidation in oscillating methane-air diffusion flames at elevated pressure”, *Applied Optics* **44** (2005), pp. 6673–6681.
- [12] G. Legros, T. Gomez, M. Fessard, T. Gouache, T. Ader, P. Guibert, P. Sagaut, and J. L. Torero, “Magnetically induced flame flickering”, *Proceedings of the Combustion Institute* **33** (2011), pp. 1095–1103.
- [13] M. Saito, M. Sato, and A. Nishimura, “Soot suppression by acoustic oscillated combustion”, *Fuel* **77** (1998), pp. 973–978.

## REFERENCES

---

- [14] T. C. Williams, C. R. Shaddix, R. W. Schefer, and P. Desgroux, “The response of buoyant laminar diffusion flames to low-frequency forcing”, *Combustion and Flame* **151** (2007), pp. 676–684.
- [15] G. Papadopoulos, R. A. Bryant, and W. M. Pitts, “Flow characterization of flickering methane/air diffusion flames using particle image velocimetry”, *Experiments in Fluids* **33** (2002), pp. 472–481.
- [16] P. J. Vermeulen, V. Ramesh, and W. K. Yu, “Measurements of entrainment by acoustically pulsed axisymmetric air jets”, *Journal of Engineering for Gas Turbines and Power* **108** (1986), pp. 479–484.
- [17] S. R. Turns and F. H. Myhr, “Oxides of nitrogen emissions from turbulent jet flames: Part I – fuel effects and flame radiation”, *Combustion and Flame* **87** (1991), pp. 319–335.
- [18] C. R. Kaplan, C. R. Shaddix, and K. C. Smyth, “Computations of enhanced soot production in time-varying ethylene/ air diffusion flames”, *Combustion and Flame* **106** (1996), pp. 89–115.
- [19] S. B. Dworkin, J. A. Cooke, B. A. V. Bennett, B. C. Connelly, M. B. Long, M. D. Smooke, R. J. Hall, and M. B. Colket, “Distributed-memory parallel computation of a forced, time-dependent, sooting, ethylene/air coflow diffusion flame”, *Combustion Theory and Modelling* **13** (2009), pp. 795–822.
- [20] A. S. Langman and G. J. Nathan, “Influence of a combustion-driven oscillation on global mixing in the flame from a refinery flare”, *Experimental Thermal and Fluid Science* **35** (2011), pp. 199–210.
- [21] S. B. Dworkin, B. C. Connelly, A. M. Schaffer, B. A. V. Bennett, M. B. Long, M. D. Smooke, M. P. Puccio, B. McAndrews, and J. H. Miller, “Computational and experimental study of a forced, time-dependent, methane-air coflow diffusion flame”, *Proceedings of the Combustion Institute* **31** (2007), pp. 971–978.
- [22] B. C. Connelly, M. B. Long, M. D. Smooke, R. J. Hall, and M. B. Colket, “Computational and experimental investigation of the interaction of soot and NO in coflow diffusion flames”, *Proceedings of the Combustion Institute* **32** (2009), pp. 777–784.
- [23] P. R. Medwell, Q. N. Chan, B. B. Dally, S. Mahmoud, Z. T. Alwahabi, and G. J. Nathan, “Temperature measurements in turbulent non-premixed flames by two-line atomic fluorescence”, *Proceedings of the Combustion Institute* **34** (2013), pp. 3619–3627.
- [24] P. R. Medwell, A. R. Masri, P. X. Pham, B. B. Dally, and G. J. Nathan, “Temperature imaging of turbulent dilute spray flames using two line atomic fluorescence”, *Experiments in Fluids* **55** (2014), pp. 1840–1851.
- [25] D. H. Gu, Z. W. Sun, G. J. Nathan, P. R. Medwell, and Z. T. Alwahabi, “Improvement of precision and accuracy of temperature imaging in sooting flames using two-line atomic fluorescence (TLAF)”, *Combustion and Flame* **167** (2016), pp. 481–493.
- [26] H. Haraguchi, B. Smith, S. Weeks, D. J. Johnson, and J. D. Winefordner, “Flame Diagnostics: Local Temperature Profiles and Atomic Fluorescence Intensity Profiles in Air-Acetylene Flames”, *Applied Spectroscopy* **31** (1977), pp. 195–200.

- 
- [27] D. H. Gu, Z. W. Sun, P. R. Medwell, Z. T. Alwahabi, B. B. Dally, and G. J. Nathan, “Mechanism for laser-induced fluorescence signal generation in a nanoparticle-seeded flow for planar flame thermometry”, *Applied Physics B* **118** (2015), pp. 209–218.
- [28] Q. N. Chan, P. R. Medwell, B. B. Dally, Z. T. Alwahabi, and G. J. Nathan, “New seeding methodology for gas concentration measurements”, *Applied Spectroscopy* (2012), pp. 803–809.
- [29] Q. N. Chan, “Development of Instantaneous Temperature Imaging in Sooty Flames”, PhD thesis, The University of Adelaide, 2011.
- [30] Z. W. Sun, D. H. Gu, G. J. Nathan, Z. T. Alwahabi, and B. B. Dally, “Single-shot, Time-Resolved planar Laser-induced Incandescence for soot primary particle sizing in flames”, *Proceedings of the Combustion Institute* **35** (2015), pp. 3673–3680.
- [31] Ÿ. University, “<http://guilford.eng.yale.edu/yalecoflowflames/flames.html>”, 2014.
- [32] J. J. Ye, P. R. Medwell, B. B. Dally, and M. J. Evans, “The transition of ethanol flames from conventional to MILD combustion”, *Combustion and Flame* **171** (2016), pp. 173–184.
- [33] A. E. E. Khalil and A. K. Gupta, “Hydroxyl radical distribution in distributed reaction combustion condition”, *Fuel* **122** (2014), pp. 28–35.
- [34] G. P. Smith, D. M. Golden, M. Frenklach, N. W. Moriarty, B. Eiteneer, M. Goldenberg, C. T. Bowman, R. K. Hanson, S. Song, W. C. Gardiner, V. V. Lissianski, and Z. W. Qin, 2016.
- [35] R. A. Dobbins, “Soot inception temperature and carbonization rate of precursor particles”, *Combustion and Flame* **130** (2002), pp. 204–214.
- [36] A. Gomez, M. G. Littman, and I. Glassman, “Comparative study of soot formation on the centerline of axisymmetric laminar diffusion flames: fuel and temperature effects”, *Combustion and Flame* **70** (1987), pp. 225–241.
- [37] B. C. Connelly, “Quantitative Characterization of Steady and Time-Varying, Sooting, Laminar Diffusion Flames using Optical Techniques”, Ph.D. dissertation, Yale University, 2009.
- [38] J. A. Lovett and S. R. Turns, “The structure of pulsed turbulent nonpremixed jet flames”, *Combustion Science and Technology* **94** (1993), pp. 193–217.
- [39] K. Lakshminarasimhan, M. D. Ryan, N. T. Clemens, and O. A. Ezekoye, “Mixing characteristics in strongly forced non-premixed methane jet flames”, *Proceedings of the Combustion Institute* **31** (2007), pp. 1617–1624.
- [40] D. Leipmann and M. Gharib, “The role of streamwise vorticity in the near-field entrainment of round jets”, *Journal of Fluid Mechanics* **245** (1992), pp. 643–668.

## Minor amendments to Chapter 4

Figure 4.14 presents normalised primary particle diameter,  $\hat{d}_p$ , as a function of normalised soot volume fraction,  $\hat{f}_v$ , at selected height above burner (HAB) for the flame with  $St = 0.23$ . Both quantities are normalised by the local maximums at each HAB. The curves exhibit two distinct regimes: (i) a linear slope and (ii) a "plateau" regime. It can be seen that the gradient in the linear regime increases as the probe moves from  $x/D = 3$  to 6, and it decreases as the HAB further increases to  $x/D = 8$ . This indicates that at lower HABs, large soot particles only appear in regions where soot is highly concentrated. At  $x/D = 6$ , however, large soot particles span across a wide range of soot concentration regions. It can be deduced that, under the influences of soot oxidation, the gradient decreases as the HAB increases.

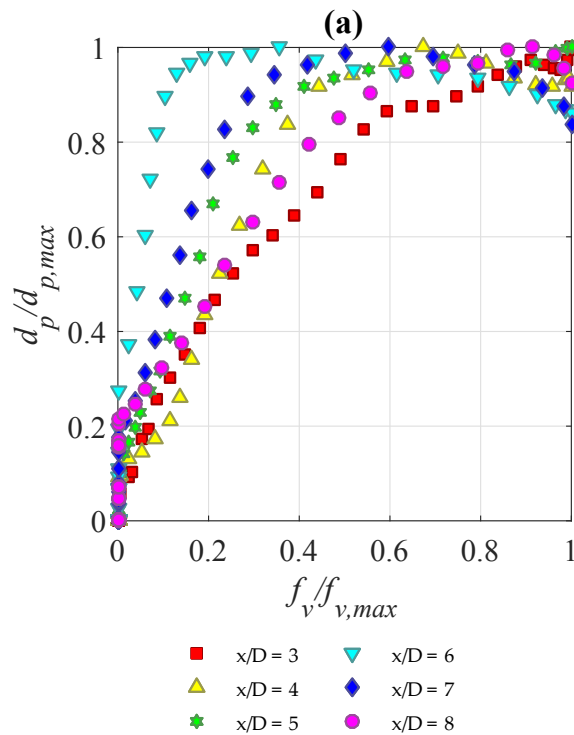


**Figure 4.14** The dependence of  $d_p/d_{p,max}$  upon  $f_v/f_{v,max}$  at selected HABs for the flames with  $St = 0.23$  (normalised to local maximum values) at  $\phi = 288^\circ$ . These data are obtained only from the left hand side of the flame.



Figure 4.15 presents normalised primary particle diameter,  $\hat{d}_p$ , as a function of normalised soot volume fraction,  $\hat{f}_v$ , at selected height above burner (HAB) for the flame with  $St = 0.46$ . Both quantities are normalised by the local maximums at each HAB. In contrast to Fig 4.14, there is no “plateau” regime, only the linear regime. Additionally, the gradient of the linear slope decreases as the HAB increases.

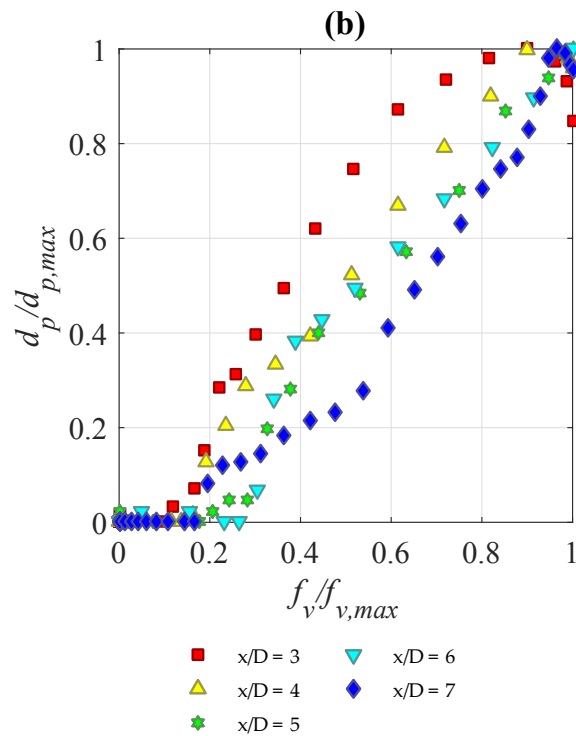


**Figure 4.15** The dependence of  $d_p/d_{p,max}$  upon  $f_v/f_{v,max}$  at selected HABs for the flames with  $St = 0.46$  (normalised to local maximum values) at  $\phi = 288^\circ$ . These data are obtained only from the left hand side of the flame.

[This page is intentionally left blank]

## Chapter 5

# Influence of nozzle diameter on soot evolution in acoustically forced laminar non-premixed flames

This chapter consists of the published journal article:

Kae Ken Foo, Zhiwei Sun, Paul R. Medwell, Zeyad T. Alwahabi, Graham J. Nathan and Bassam B. Dally, "Influence of nozzle diameter on soot evolution in acoustically forced laminar non-premixed flames", *Combustion and Flame* **194** (2018) pp. 376–386.

The content of this chapter is identical to that of the published article, with the following exceptions:

1. The typesetting and referencing style have been altered to maintain a consistent appearance within the thesis.
2. The numbering of tables, figures and equations has been changed to include the number of the chapter.

The article in its published format is available at:

<https://doi.org/10.1016/j.combustflame.2018.05.026>

## Statement of Authorship

Title of Paper	Influence of nozzle diameter on soot evolution in acoustically forced laminar non-premixed flames
Publication Status	<input checked="" type="checkbox"/> Published <input type="checkbox"/> Accepted for Publication <input type="checkbox"/> Submitted for Publication <input type="checkbox"/> Unpublished and Unsubmitted work written in manuscript style
Publication Details	K.K. Foo, Z.W. Sun, P.R. Medwell, Z.T. Alwahabi G.J. Nathan and B.B. Dally, "Influence of nozzle diameter on soot evolution in acoustically forced laminar non-premixed flames", <i>Combustion and Flame</i> 194 (2018) 376—386.

### Principal Author

Name of Principal Author (Candidate)	Kae Ken Foo
Contribution to the Paper	<p>I planned and proposed the experimental design matrix to the co-authors after a thorough literature review. Together with all the co-authors, we decided the experimental cases.</p> <p>I set up the experiments with the assistance provided by the second co-author, Z.W. Sun. We collected the experimental results together.</p> <p>I processed, analysed and interpreted all the experimental data. After some discussion with the co-authors regarding my interpretation of the experimental data, I wrote the manuscript. Furthermore, as the corresponding author, I responded to the reviewers' comments and recommendations.</p>
Overall percentage (%)	65%
Certification:	This paper reports on original research I conducted during the period of my Higher Degree by Research candidature and is not subject to any obligations or contractual agreements with a third party that would constrain its inclusion in this thesis. I am the primary author of this paper.
Signature	Digitally signed by Kae Ken Foo Date: 2018.08.20 09:34:38 +09'30'


### Co-Author Contributions


By signing the Statement of Authorship, each author certifies that:


- i. the candidate's stated contribution to the publication is accurate (as detailed above);
- ii. permission is granted for the candidate to include the publication in the thesis; and
- iii. the sum of all co-author contributions is equal to 100% less the candidate's stated contribution.

Name of Co-Author	Zhi Wei Sun
Contribution to the Paper	This co-author co-designed the experiments and provided aid collecting data. He helped to edit the experimental details section of the manuscript.
Signature	Digitally signed by Zhiwei Sun Date: 2018.08.21 11:00:12 +09'30'

Name of Co-Author	Paul R. Medwell
Contribution to the Paper	This co-author provided suggestions for the experimental set-up and data post-processing. He also helped evaluate and edit the manuscript.
Signature	<p style="text-align: center;"><b>Paul Medwell</b> 2018.08.23 11:12:20 +09'30'</p>

Name of Co-Author	Zeyad T. Alwahabi
Contribution to the Paper	This co-author provided suggestions for the experimental set-up. He also helped to evaluate and edit the manuscript.
Signature	<p style="text-align: center;">Digitally signed by Zeyad Alwahabi   DN: cn=Zeyad Alwahabi, o=Chem Eng, ou,  email=zeyad.alwahabi@adelaide.edu.au, c=AU  Date: 2018.08.21 14:07:55 +09'30'</p>

Name of Co-Author	Graham J. Nathan
Contribution to the Paper	This co-author co-supervised the development of the work. He also helped to evaluate and edit the manuscript.
Signature	<p style="text-align: center;">Digitally signed by Graham J   Nathan  Date: 2018.08.23 12:48:31 +09'30'</p>

Name of Co-Author	Bassam B. Dally
Contribution to the Paper	This co-author co-supervised the development of the work. He also helped to evaluate and edit the manuscript.
Signature	<p style="text-align: center;">Digitally signed by Bassam   Dally  Date: 2018.08.20 10:11:08  +09'30'</p>

## **Influence of nozzle diameter on soot evolution in acoustically forced laminar non-premixed flames**

Kae Ken Foo, Zhiwei Sun, Paul R. Medwell, Zeyad T. Alwahabi,  
Graham J. Nathan, Bassam B. Dally

### **Abstract**

The current study investigated the soot evolution in a series of acoustically forced laminar flames affected by the variations in the nozzle diameter, in-flame residence time and buoyancy. Measurements were performed for three laminar co-flowing non-premixed jet flames in which sinusoidal pressure fluctuations were imposed to the fuel stream. Non-linear excitation regime Two-Line Atomic Fluorescence (NTLAF), Laser-Induced Incandescence (LII), Time-Resolved Laser-Induced Incandescence (TiRe-LII) and Planar Laser-Induced Fluorescence of hydroxyl radicals (OH-PLIF) were performed simultaneously to acquire the phase-resolved measurements of temperature, soot concentration, primary particle size and the location of reaction zones. Additionally, Particle Imaging Velocimetry (PIV) was employed independently to characterise the velocity field. The peak soot concentrations in all the forced flames are double those measured in their steady counterparts, consistent with previous measurements, whereas the maximum particle size for the forced flames is only 10% larger than that for the steady flames and is independent of the nozzle diameter. Nevertheless, a systematic variation of the fuel tube diameter shows that the toroidal vortex scale affects the flame structure which leads to an impact on the spatial distribution and the total volume of soot. In addition, residence time analysis shows that the enhancement of the largest particle size, as well as the peak soot volume fraction, scales with the in-flame residence time.

## **5.1 Introduction**

Soot occurs naturally in many combustion devices, especially those which employ non-premixed combustion of hydrocarbon fuels. Driven by the desire to develop advanced combustion technologies that are highly efficient and produce low soot emissions, soot formation has been actively studied by the combustion research community for the past half-century [1–3]. Steady laminar flames have always been an attractive system in which to examine the fundamental physical and chemical processes involved in the soot evolution. These flames allow a variety of measurement techniques to be applied consecutively while providing a tractable system in which to examine the soot evolution in spatial and temporal

coordinates. Extensive studies on the soot formation processes have established that there is a close coupling between the soot particles, temperature [4, 5] and velocity fields [6]. The characteristics of these fields have significant influences on the spatial distribution of the soot, the rates of growth and the oxidation. However, almost all practical combustion systems involve turbulent flows [7]. Turbulent flames are challenging to resolve both experimentally and numerically because the reactions and flow are coupled non-linearly, while the flow and scalar fields fluctuate over time and length scales that span more than eight orders of magnitude. Nevertheless, soot formation in these flames can be characterised by controlling parameters of temperature, stoichiometry, strain rate and residence time [3, 8–10]. Numerous studies suggest that turbulent combustion can be viewed as a process dominated by the continuous distortion, extension, production and dissipation of the flame surface by a collection of vortices with a broad range of scales [11, 12]. However, complete information on all parameters that control the evolution of soot in a turbulent flame will not be available for many years, owing to the need for simultaneous measurement of them all. In this context, it is desirable to study unsteady laminar flames, which offer the ability to collect more complete data than is possible with turbulent flames and a broader range of variation in the controlling parameters than is possible to achieve with steady laminar flames.

In a non-premixed flame, vortices are developed from a modified Kelvin-Helmholtz-type instability [13], which originate within the shear layer between the flame sheet and the cold air. At sufficiently high flow rates, laminar flames exhibit a natural flicker, that occurs at a characteristic frequency but with significant cycle-to-cycle variations. These variations can be kept very low by acoustic forcing at a frequency close to its unforced natural frequency [11]. Acoustically forced non-premixed laminar flames have been extensively utilised to study the effects of time-varying flow field on the soot formation [14–16]. A significant body of work is attributable to Shaddix and co-workers [17–21]. Shaddix *et al.* [18] reported that the peak soot volume fraction measured in the forced flames can be 2–6 times greater than that of their steady counterpart, depending on the fuel type [18]. A computational study [19] suggests that the increased residence time is the dominant factor that contributes to the enhanced soot production. However, insufficient data are available in these flames to assess quantitatively the performance of soot evolution models, since such assessments also require measurements of temperature, velocity and as many other parameters as possible. The present paper aims to begin to fill this gap.

The natural instability evident in the flickering laminar flames has been studied explicitly using various measurement techniques including fast photography [22], light emission captured by a photodiode [23], and the combination of local temperature and velocity measurements [24]. Sato *et al.* [25] conducted a dimensional analysis of the flickering frequency,  $f$  of laminar flames and found the correlations

between the Strouhal number,  $St$ , and the Froude number,  $Fr$ . The dimensionless numbers are defined by

$$St = f \cdot D / U_f \quad \text{and} \quad Fr = U_f^2 / D \cdot g \quad (1) \text{ and } (2)$$

where  $D$  is the nozzle diameter,  $U_f$  is the jet exit velocity and  $g$  is the earth gravitational acceleration,  $9.8 \text{ m/s}^2$ . The  $St$ - $Fr$  relationship obtained at a wide range of experimental conditions could be summarised as  $St \propto Fr^n$ , where  $n$  varies between  $-0.41$  and  $-0.5$ . That is, the flickering is almost independent of velocity under some conditions and scales approximately with  $\sqrt{D}$ . The complex, non-linear nature of this relationship highlights the need for new, systematic data, while the stronger dependence of flicker frequency on  $D$  than  $U_f$  shows that it is more useful to vary  $D$  than  $U_f$ .

## 5.2 Experimental details

### 5.2.1 Burner

The experiment was conducted using a co-annular burner with three interchangeable fuel tubes, having inner diameters of 4.0, 5.6 and 8.0 mm. Figure 5.1 shows the schematic representation of the co-flow burner along with the coordinate orientation used in the study: other burner details have been described previously [26, 27]. The current design is based on the Yale Burner [15]. The fuel tubes were surrounded by a 74-mm-diameter co-flow annulus with dry air running through it. Beneath the fuel plenum, a loudspeaker was driven by a 10 Hz sine wave from a signal generator to impose pressure fluctuations on the fuel stream exciting the central jet. The relatively slow co-flow rolled up into a train of toroidal vortices with a torus diameter,  $D_v$ , proportional to the fuel tube diameter. The optical diagnostic systems were synchronised and phase-locked to the sinusoidal waves using a delay generator.

The fuel stream comprised 41.7% ethylene ( $\text{C}_2\text{H}_4$ ) and 58.3% nitrogen ( $\text{N}_2$ ), by volume. The fuel was diluted to limit the maximum amount of soot in the forced flame and thus minimise the level of interference from soot to the laser diagnostic measurements [28]. For all the studied cases, the volumetric flow rates of the fuel stream and the co-flow were kept constant at 0.31 and 60.0 standard litres per minute (SLPM), respectively. All flow rates were measured with mass flow controllers (Alicat Scientific) conditioned to a standard temperature and pressure, 293 K and 1 atm. The amplitudes of the forcing,  $\alpha$ , were defined as the ratio of the maximum centreline velocities,  $U_c$ , of the forced flames to their steady counterpart at the exit plane. The corresponding mean exit velocities and other dimensionless parameters for all three different burner jet diameter are shown in Table 5.1.



A high-speed silicon-based photodetector (DET110, Thorlabs) was used to record the fluctuations of luminosity intensity from the flickering flames. It was placed at a horizontal distance of 300 mm from the flame and at the same level as the mid-height of the flames to capture the dynamic response of the flickering flames. Since every flame has a well-defined characteristic frequency [25, 29], the height of the photodetector does not affect the measured frequency. The sampling rate was 1 kHz and for each flame, a total of 23000 data points were recorded, equivalent to 23 s.

**Table 5.1** Summary of test conditions

	Cases	$D$ (mm)	$U_f$ (m/s)	$U_c$ (m/s)	$\alpha$ (-)	$f$ (Hz)	$St$ (-)	$Fr$ (-)	$Re$ (-)
Steady	S-1	4.0	0.41	0.83	-	0	0	4.28	147
	S-2	5.6	0.21	0.36	-	0	0	0.80	104
	S-3	8.0	0.10	0.21	-	0	0	0.13	72
Forced	F-1	4.0	0.41	1.25	50%	10	0.10	4.28	147
	F-2	5.6	0.21	0.53	50%	10	0.27	0.80	104
	F-3	8.0	0.10	0.31	50%	10	0.80	0.13	72

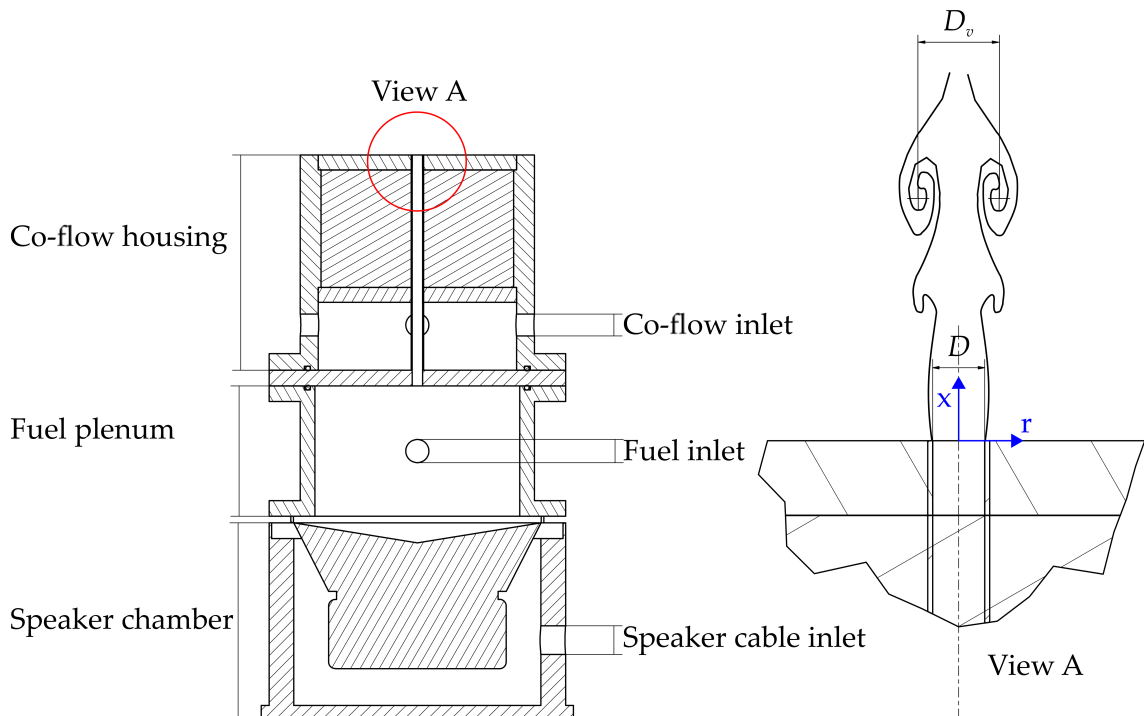


**Figure 5.1** Schematic representation of the co-flow burner [15], including coordinate orientation and a typical axisymmetric toroidal vortex structure.

## 5.2.2 Temperature measurement

The flame temperature was measured using the Non-linear excitation regime Two-Line Atomic Fluorescence (NTLAF) technique. The principle of the technique and the optical arrangement have been described previously [30–32]. The flames were seeded with indium, in the form of complex agglomerates of nano-sized primary particles of indium compounds and spherical micron-sized indium beads, through the fuel stream with an in-house-built ablation device [33, 34].

The system-dependent parameters of NTLAF were calibrated in an ethylene/air premixed flame with an equivalence ratio,  $\Phi = 2.0$  stabilised on a flat-flame burner. The burner was purpose-designed to produce a matrix of small laminar flames, which subsequently interact and combine to form a stable flat flame of uniform temperature [35]. The flat-flame temperature was measured using an R-type Pt/Pt-Rh 13% thermocouple with a 180- $\mu\text{m}$ -diameter bead (Omega, P13R-003). The thermocouple measurement was corrected for radiation heat loss ( $\sim 60$  K). In the present analysis, error due to the potential catalytic effect was assumed negligible because the influence is only significant at lower temperatures ( $T \approx 1000$  K) [36]. Overall, the phase-averaged images of gas temperature presented in the following sections have a typical signal-to-noise ratio (SNR) of 80 : 1. The overall uncertainty for the phase-averaged temperature is  $\pm 120$  K ( $1\sigma$ ).

## 5.2.3 Primary soot particles diameter measurement

The diameter of primary soot particle within the flames was measured using the Time-Resolved Laser-Induced Incandescence (TiRe-LII) technique. The soot particles were excited using a beam from an Nd:YAG laser at 1064 nm. The optical configuration and the theoretical model of the system have been presented previously [37]. The minimum measurable diameter is 5 nm and the uncertainty for the phase-averaged measurement is  $\pm 4$  nm ( $1\sigma$ ).

## 5.2.4 Soot volume fraction measurement

The prompt LII signal was used to evaluate the soot volume fraction,  $f_v$  and was calibrated via performing laser extinction measurements in a steady ethylene/air non-premixed flame. The calibration flame has a visible flame length of 72 mm and is surrounded by a co-flow velocity of 0.642 m/s. The uncertainty and the lower limit of detection for the soot volume fraction are  $\pm 0.03$  ppm ( $1\sigma$ ) and 0.01 ppm (where the SNR is lower than 10:1), respectively.

## 5.2.5 Hydroxyl radical concentration measurement

The planar Laser-Induced Fluorescence of the hydroxyl radical (OH-PLIF) was excited using a single ultraviolet (UV) laser beam tuned to the  $Q_1(8)$  transition (283.5 nm) of the  $A^2\Sigma^+ \leftarrow X^2\Pi_i(1,0)$  system. This is a strong fluorescence line

with little temperature dependence of the population, less than 5% over the range 1400 to 2100 K [38]. The OH fluorescence was imaged onto an ICCD camera (Princeton Instruments ICCD-576) equipped with a 105 mm  $f/1.2$  UV lens after transmission through a UV filter centred at 310 nm with an FWHM of 10 nm. Since the measurements of OH-PLIF are not quantitative, the results are presented in arbitrary units in the following sections.

### 5.2.6 Velocity measurement

The flow velocity field was measured using the Particle Image Velocimetry (PIV) technique. The light source was a frequency-doubled, double-cavity Nd:YAG laser (Quantel BrilliantB) operating at a wavelength of 532 nm (180 mJ per pulse) and a pulse rate of 10 Hz. The time interval between the pulses was 100  $\mu$ s. The region of interest (ROI) was illuminated with a 1-mm-thick laser sheet. Recording of the particle image pairs was accomplished using two double-frame CCD cameras (Princeton Instruments, Megaplus II ES4020) stacked one on top of the other. Each viewing area was approximately 70.4 mm  $\times$  70.4 mm which translated into a spatial resolution of 29.4 pixel/mm. Each CCD camera was equipped with a 70–300 mm 1:4–5.6 D zoom lens (Nikon, AF Nikkor) and a 532 nm bandpass filter (Andover) with an FWHM of 1 nm to reduce the flame luminosity interference on the image pairs.

Both the fuel and co-flow streams were seeded with 1- $\mu$ m-diameter titanium dioxide (TiO<sub>2</sub>) particles using separate cyclone seeders located downstream of the mass-flow controllers. In the experiment, the Stokes number ( $Sk$ ) ranges from  $10^{-4}$  to  $10^{-3}$  which satisfy the criterion,  $Sk \ll 0.1$ , for an acceptable flow tracing accuracy with errors below 1% [39]. To avoid the accumulation of particles and minimise the blockage effect on the co-flow uniformity, the burner was regularly flushed with clean air during the experiments.

The PIV image ensembles were batch processed with PIVlab 1.41 [40, 41]. A multi-pass (sequential interrogation window sizes of 256, 128, 64 and 32 pixels, 50% overlap), standard FFT was used to calculate the particle displacement vector fields. For each flame condition and at each phase, an ensemble of 50 instantaneous, phase-resolved measurements was averaged to construct the phase profiles of the velocity fields. In general, PIV in sooting flames is quite challenging and often encounters limitations. In the current study, the velocity field in the soot regions cannot be resolved due to the interference from soot scattering and the low seeding density in these regions. This is because the hot gas expands approximately seven times due to thermal expansion [42] and the seeding density scales with the gas density. The missing data due to the soot scattering interference are replaced by values estimated by a robust interpolation algorithm proposed by Garcia [43]. To illustrate the effectiveness of the algorithm, Fig 5.2 compares the interpolated results with the original data where the sooting region is masked.

Here, the velocity field measurement for the steady flame S-1 ( $D = 4.0$  mm) is shown as an example. Besides, thermophoresis is a major source of error at the reaction zone where the temperature gradients are steep, the maximum thermophoretic drift velocity is assumed to be  $0.1$  m/s [44] which is approximately 10% of the typical gas velocities ( $\sim 1.1$  m/s) at the reaction zone. The typical velocity uncertainty outside the reaction zone is approximately  $\pm 0.08.0$  m/s ( $1\sigma$ ).

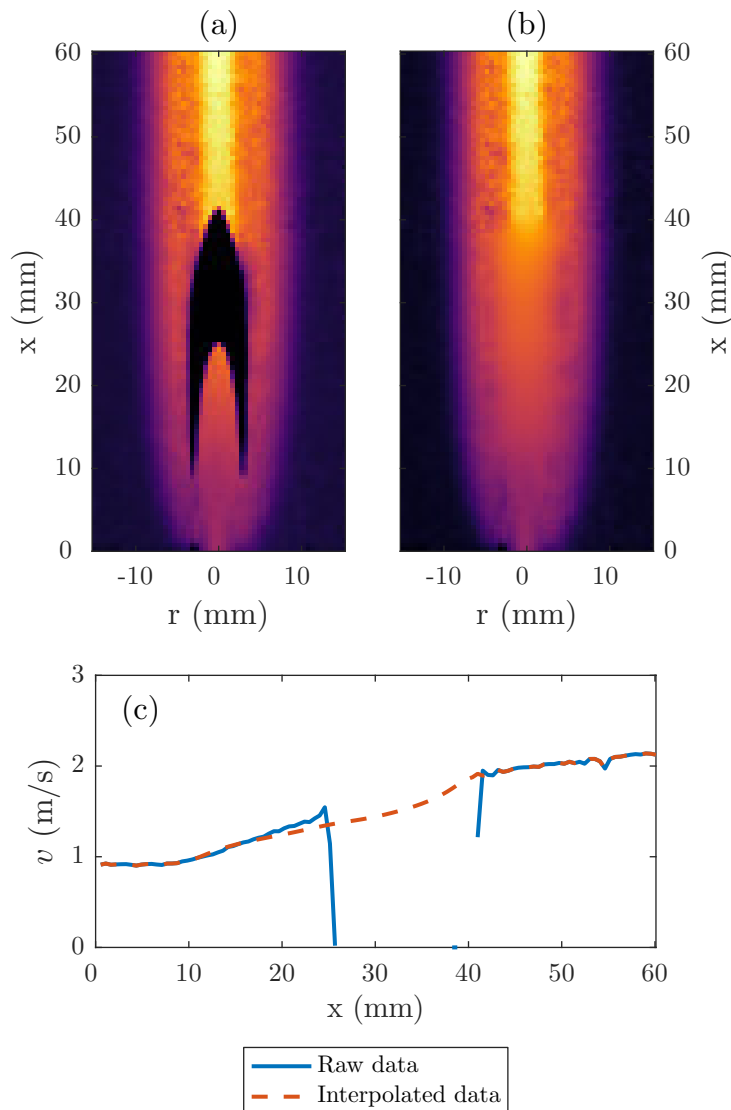


**Figure 5.2** Comparison of (a) soot interfered axial velocity field and (b) interpolated velocity field for the steady flame S-1 ( $D = 4.0$  mm). The axial velocities along the centreline for both cases are plotted in panel (c) for a better comparison.

## 5.3 Results and discussion

### 5.3.1 Natural flickering frequency

The time-evolving flame luminosity signals acquired via photodetector are converted into the frequency domain by performing a Fast Fourier Transformation (FFT) of the signals. Figure 5.3 illustrates the resultant Power Spectral Density (PSD) distribution for the flames S-1 ( $D = 4.0$  mm), S-2 ( $D = 5.6$  mm) and S-3 ( $D = 8.0$  mm) in the natural flickering mode without a co-flow. The PSDs are normalised with respect to the peak values of approximately 10 Hz. The dominant frequencies are defined as the natural flickering frequencies of the flames, which are 9.8 Hz, 10.3 Hz and 10.5 Hz for S-1, S-2 and S-3, respectively. In addition to the dominant frequency, higher harmonics are present for each signal. To enforce the coupling between the flame response and the flickering motion, the frequencies of the sinusoidal forcing were maintained at 10 Hz.

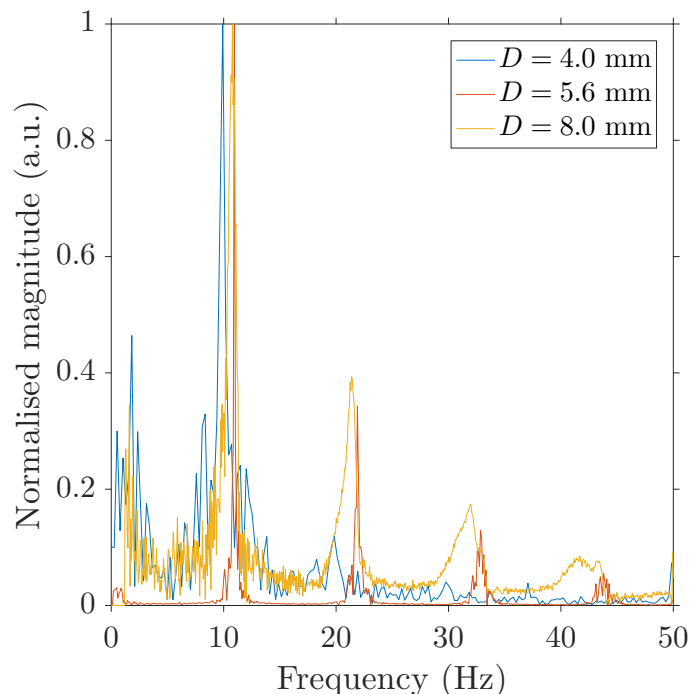


**Figure 5.3** Normalised power spectral density of the flame luminosity signals acquired for S-1 ( $D = 4.0$  mm), S-2 ( $D = 5.6$  mm) and S-3 ( $D = 8.0$  mm) at natural flickering mode without a co-flow.

### 5.3.2 Steady flames

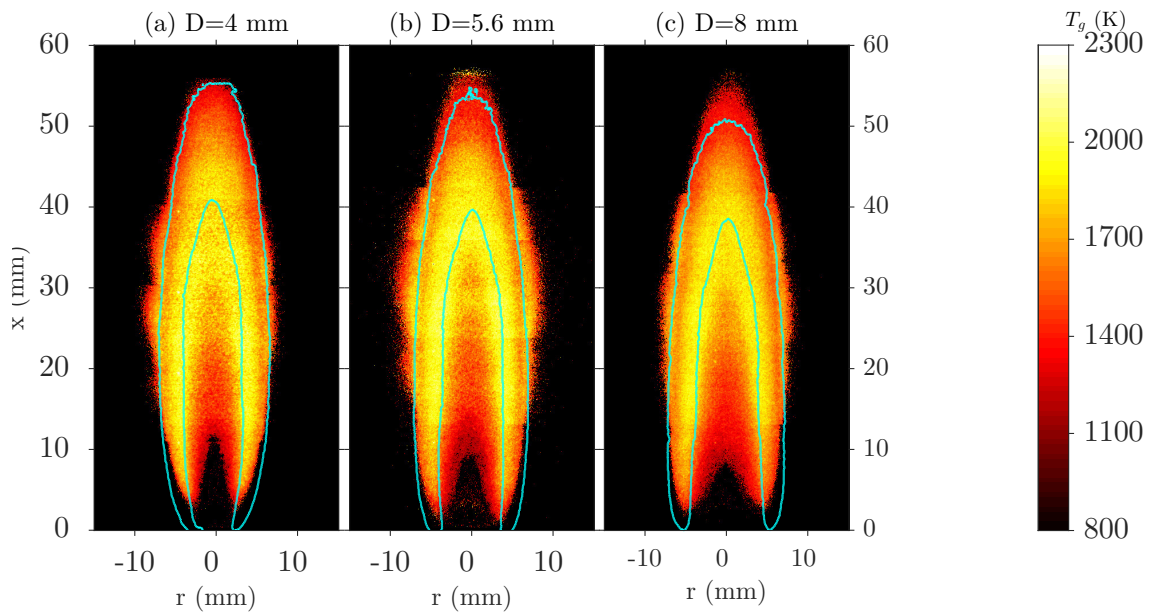
The length of a laminar jet flame can be described as:

$$L_f \approx \frac{3}{8\pi} \frac{Q_f}{\mathcal{D} Y_{f,stoic}} \quad (5.1)$$

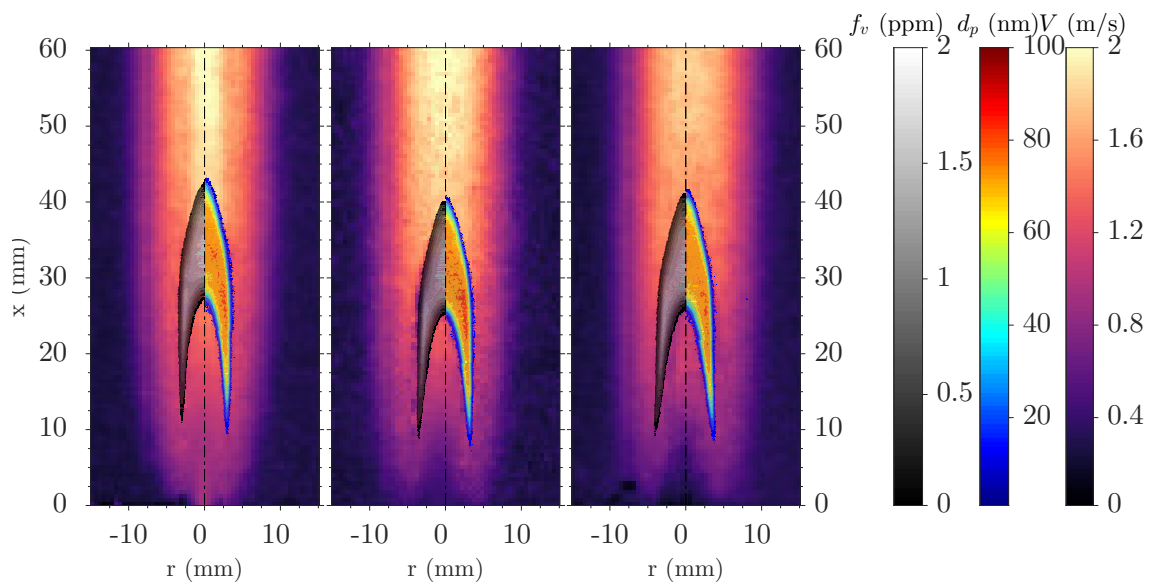
where  $\mathcal{D}$  is the diffusion coefficient and  $Y_{f,stoic}$  is the stoichiometric fuel mass fraction. Equation 5.1 shows that, for the same fuel type, the flame length is solely dependent on the fuel volumetric flow rate,  $Q_f$ . Here,  $L_f$  is defined as the axial distance between the burner exit and the farthest point along the centreline where the gas mixture is stoichiometric.

Figure 5.4 shows the planar temperature distribution for all the three steady flames along with the envelope of the normalised intensity of OH-PLIF ( $0.01 \leq I_{OH}/I_{OH,max} \leq 0.99$ ), which serves as a qualitative marker of the reaction zone. The figure shows that all three steady flames have an almost identical flame length  $L_f \approx 37.6$  mm. This is consistent with the measurement of almost identical flickering frequency and previous understanding that the flames are all dominated by buoyancy.

Figure 5.5 presents the velocity fields for all the three steady flames. In addition, superimposed on Fig. 5.5 are the planar distributions of  $f_v$  on the left hand side (LHS) and of the particle primary diameter,  $d_p$  on the right hand side (RHS). The exit velocity profiles are significantly different for the three jets, as can be seen from Fig. 5.5. Steady flame S-1 exhibits the highest centreline velocity at the exit plane ( $U_c = 0.79$  m/s), followed by S-2 ( $U_c = 0.40$  m/s) and S-3 ( $U_c = 0.19$  m/s). However, the distinctions in the fuel exit profiles do not extend to the downstream, which clearly indicates that all the flames are buoyancy-dominated. The soot fields in all the flames exhibit a similar appearance: high soot concentration ( $f_v \geq 1.2$  ppm) is located at the centreline and more large soot particles ( $d_p \geq 70$  nm) are accumulated in the wings of the flame, instead of at the centreline. Despite the volumetric flow rate of the fuel being constant, each of the three steady flames, S-1, S-2 and S-3 has a slightly different maximum soot volume fraction,  $f_{v,max} = 1.60, 1.43$  and  $1.40$  ppm, respectively. Within the soot region, F-1 exhibits the highest maximum temperature, 80 K more than F-2 and 170 K more than F-3. In addition, the largest measured largest primary particle diameter is,  $d_{p,max} = 78$  nm for all three flames.



**Figure 5.4** Planar measurements of flame temperature for the steady flames S-1 ( $D = 4.0$  mm), S-2 ( $D = 5.6$  mm) and S-3 ( $D = 8.0$  mm) superimposed with isopleths of corresponding OH-PLIF marking the location of the reaction zones. Five images at different heights have been stacked together to constitute the full-field images presented here.



**Figure 5.5** Velocity fields for the steady flames S-1 ( $D = 4.0$  mm), S-2 ( $D = 5.6$  mm) and S-3 ( $D = 8.0$  mm) superimposed with contours of soot volume fraction and diameter of primary soot particle on the left half and right half of the plots, respectively.

### 5.3.3 Forced flames

In addition to velocity measurements, the two-dimensional strain and vorticity fields were also calculated from the axial ( $u_x$ ) and radial ( $u_r$ ) velocities. Using the two velocity components, two important fluid dynamic quantities, the shear-strain rate and vorticity field, can be computed by:

$$|S_{rx}| = \frac{1}{2} \left| \left( \frac{\partial u_r}{\partial x} + \frac{\partial u_x}{\partial r} \right) \right| \quad (5.2)$$

$$\omega = \frac{\partial u_x}{\partial r} - \frac{\partial u_r}{\partial x} \quad (5.3)$$

Since the axial-velocity-gradient term,  $\partial u_x / \partial r$  is dominant in Eqs. 5.2 and 5.3, it is expected that the profile of the vorticity field would appear qualitatively similar to the corresponding shear-strain rate field. Strain rates on the flame surface are responsible for transporting the fresh reactants into the reaction zone and enhance the burning rate unless the strain rate exceeds the extinction limit. Thus, it is widely recognised that the strain-rate structure is responsible for the distortion of flame surface [45]. On the other hand, high vorticity without strain rate has no effect on the deformation of fluid elements and is not expected to enhance the rate of combustion [46].

Figure 5.6 presents the envelope of the OH-PLIF superimposed on the phase-averaged planar images of  $T_g$  superimposed for all three forced flames studied, F-1 ( $D = 4.0$  mm), F-2 ( $D = 5.6$  mm) and F-3 ( $D = 8.0$  mm). The OH serves as a useful marker for the reaction zone, which is found to align with regions of high temperature. The flame oscillation cycle is equally divided into eight phases ( $45^\circ$  of separation), equivalent to a time interval of 12.5 ms between the phases. During the phases from  $\phi = 0^\circ$  to  $180^\circ$  (or  $225^\circ$  for F-2 and F-3) the attached flames are quite similar to laminar steady flames. In the lower part of the flames, the high-temperature reaction zone occurs in the annular region of the flames. Under the influence of buoyancy, the reaction zone shifts toward the centreline as it approaches the flame tip. In contrast to a laminar steady flame, a bulge in the flame is visible at the mid-height (most obvious in flame F-1) which is the result of flame interaction with the toroidal vortex. At  $\phi = 225^\circ$  for F-1 and  $\phi = 270^\circ$  for F-2 and F-3, the region upstream of the flame bulge is strained by the toroidal vortex where it brings fuel and oxidiser together. As a result, the rates of strain and reaction are increased in this region, which is consistent both with the presence of low soot volume fraction and high local temperatures there. At the instant of pinch-off, the flame tip separates from the attached flame and is isolated from the flammable mixture in the flamelet upstream. The only fuel source for the pinched-off flame is at its core. The fuel diffuses radially outward



due to thermal expansion, while the oxidiser diffuses radially inward. Meanwhile, the toroidal vortex upstream of the pinched-off flame entrains more oxidiser into the base of the flame. Consequently, the base of the pinched-off flame exhibits a lower soot volume fraction, higher temperature and a thicker OH layer relative to the annular region and tip of the flame.

In most unsteady flows, the presence of vortical structures is often masked by the relatively high flow mean velocity. To unveil the presence of the vortical structures, mean-bulk Galilean decomposition is applied to the velocity fields. A constant convection velocity calculated by averaging over the whole flow field ( $\bar{u} \sim 0.8$  m/s) is subtracted from all the velocity vectors [47]. Figure 5.7 shows the Galilean-transformed velocity magnitudes ( $|u| - \bar{u} = \sqrt{u_r^2 + u_x^2} - \bar{u}$ ) superimposed onto the soot concentration,  $f_v$  (LHS) and primary particle size,  $d_p$  (RHS) for forced flames F-1, F-2 and F-3. The black stripe at the top part of the plots represents no data because it is beyond the field of view of the camera. The shear layers, represented by the dark region between the hot gases of combustion and the cold co-flow air are visible in this frame of reference. The shear layer gives rise to the Kelvin-Helmholtz instability, which further develops into a sequence of vortex shedding.

Figure 5.8 presents the streamlines derived from the Galilean-transformed velocity components superimposed onto the contour of shear-strain rate and the soot field,  $f_v$  (LHS) together with  $d_p$  (RHS). As mentioned above, both the shear-strain rate and vorticity fields have a similar distribution, the vorticity field is represented by the streamlines derived from the PIV measurements (the core of vortex have the highest vorticity). Also, the OH layer (*i.e.*, the reaction zone) aligns with the high-strain structure, showing that the distortion of the flame surface is associated with the fluid-dynamic shear strain [45, 46]. In addition, the flame bulge observed in Fig. 5.6 is a result of the toroidal vortex compressing the upstream flow and thinning the flame core. The lateral compression on the flame stem eventually leads to a pinch-off. Lewis et al. [48] suggest that the flame pinch-off is a result of a local extinction induced by high-strain rate along the centreline. For the current study, however, the shear-strain rates at the base of the pinch-off flames are approximately  $100 \text{ s}^{-1}$  ( $|S_{rx}| = 103, 130$  and  $109 \text{ s}^{-1}$  for flames F-1, F-2 and F-3), which are an order of magnitude lower than the extinction strain rate for ethylene-air flames,  $1186 \text{ s}^{-1}$  [49]. Hence, for these cases, it is more likely that the lateral compression induced by the toroidal vortex and the decrease in the fuel velocity temporally cut-off the fuel supply to the tip of the flame and results in flame separation. Nevertheless, the local strain rate is within the range of limiting strain rate for soot suppression,  $S = 60\text{--}175 \text{ s}^{-1}$  [50, 51], which contributes to the locally low soot volume fraction.

[This page is intentionally left blank]

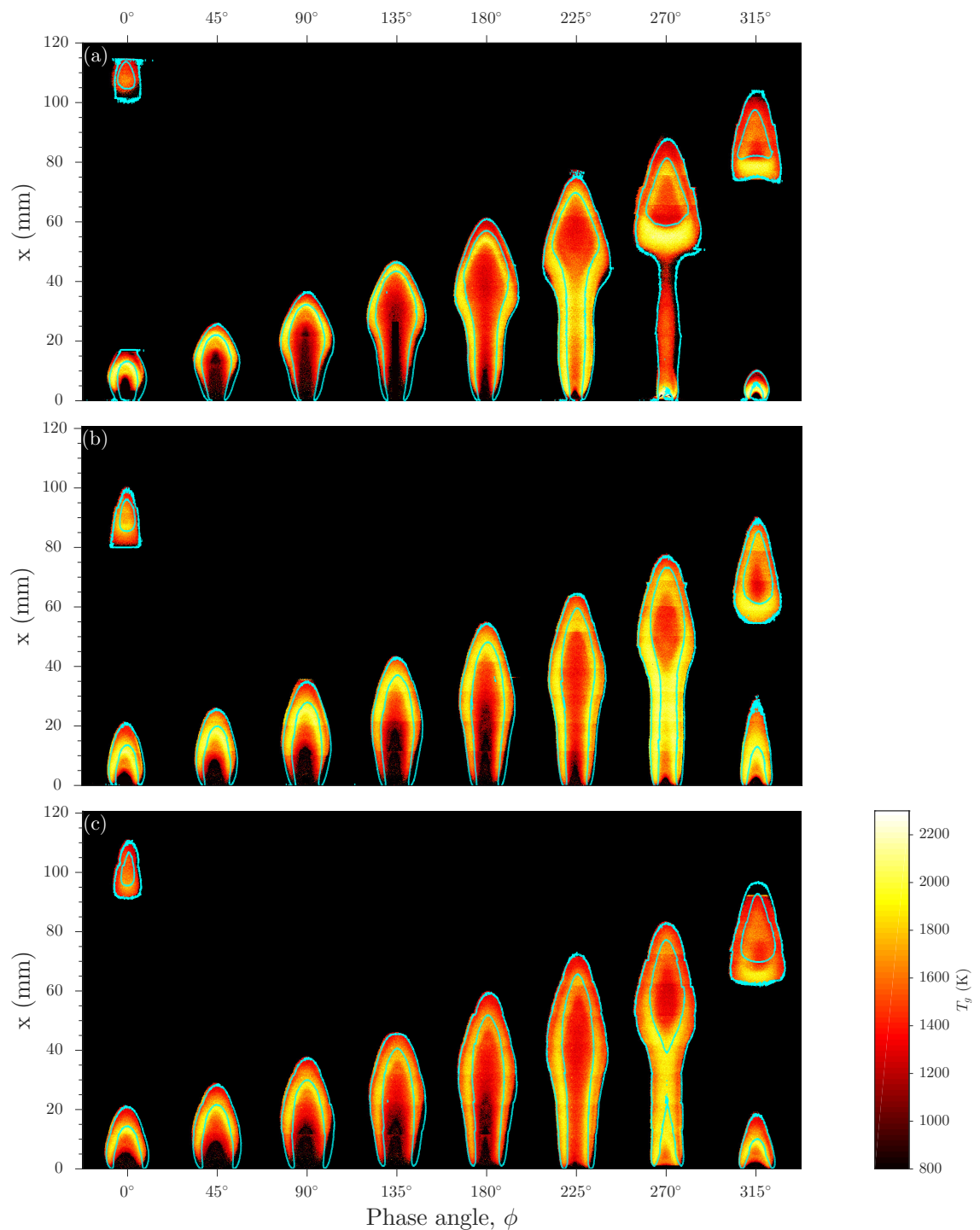


**Figure 5.6** Planar measurements of gas temperature,  $T_g$ , superimposed with the corresponding OH layer collected for the forced flames (a) F-1 with  $D = 4.0$  mm, (b) F-2 with  $D = 5.6$  mm and (c) F-3 with  $D = 8.0$  mm. The flames are forced at 10 Hz 50% amplitude. The oscillation cycle is divided into eight phases with  $45^\circ$  phase angle difference, equivalent to a time interval of 12.5 ms.

[This page is intentionally left blank]

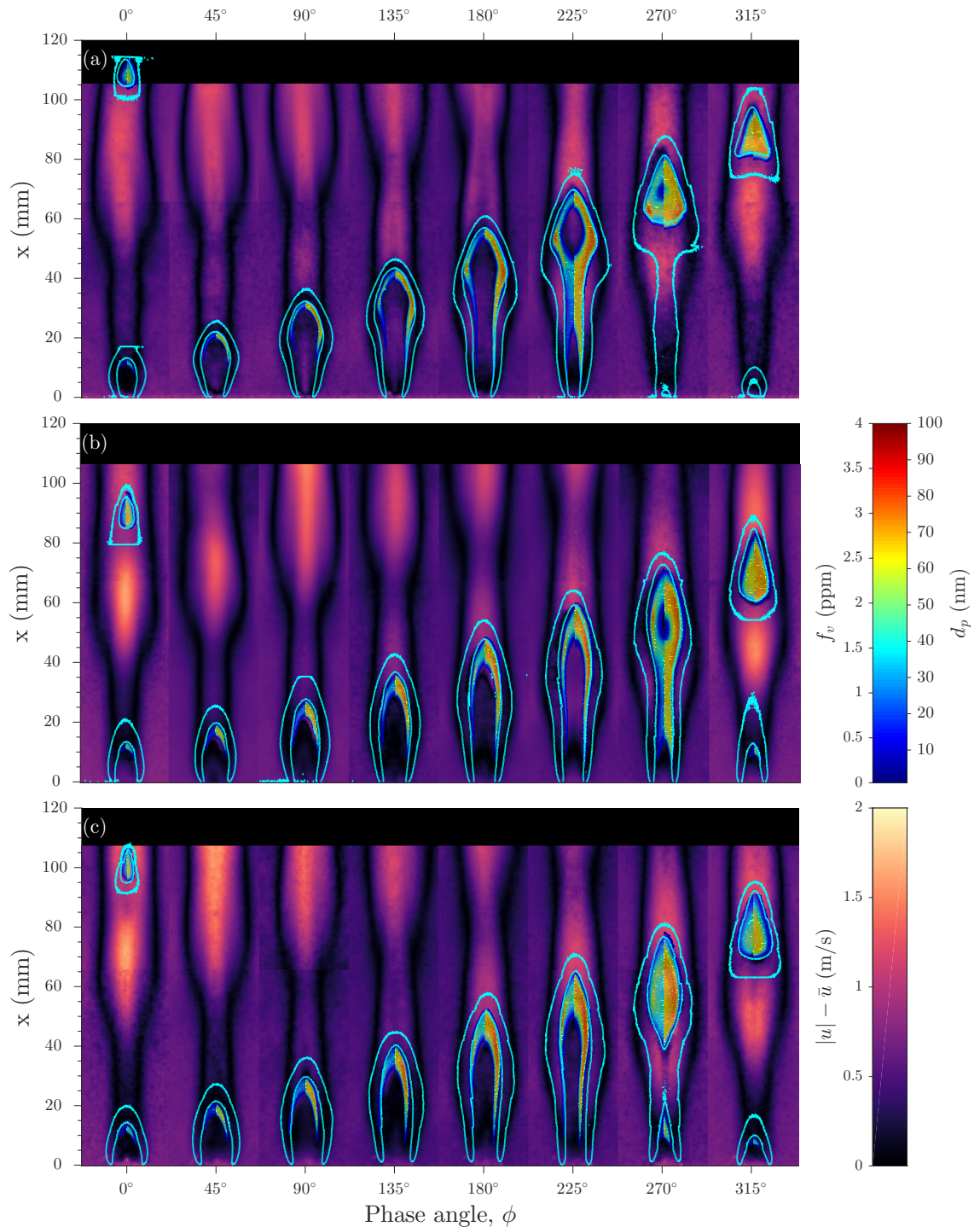


**Figure 5.7** Contour of Galilean-transformed velocity magnitudes superimposed with the OH layer indicating the reaction zone and the planar measurements of soot volume fraction,  $f_v$  (LHS), and diameter of primary soot particle,  $d_p$  (RHS), collected for the forced flames (a) F-1 with  $D = 4.0$  mm, (b) F-2 with  $D = 5.6$  mm and (c) F-3 with  $D = 8.0$  mm. In the velocity contour, the mean flow velocity ( $\bar{u} \sim 0.8$  m/s) is subtracted from all the velocity magnitudes. The black stripe at the top part of the plots represents no data as it is beyond the field of view of the PIV camera.

[This page is intentionally left blank]

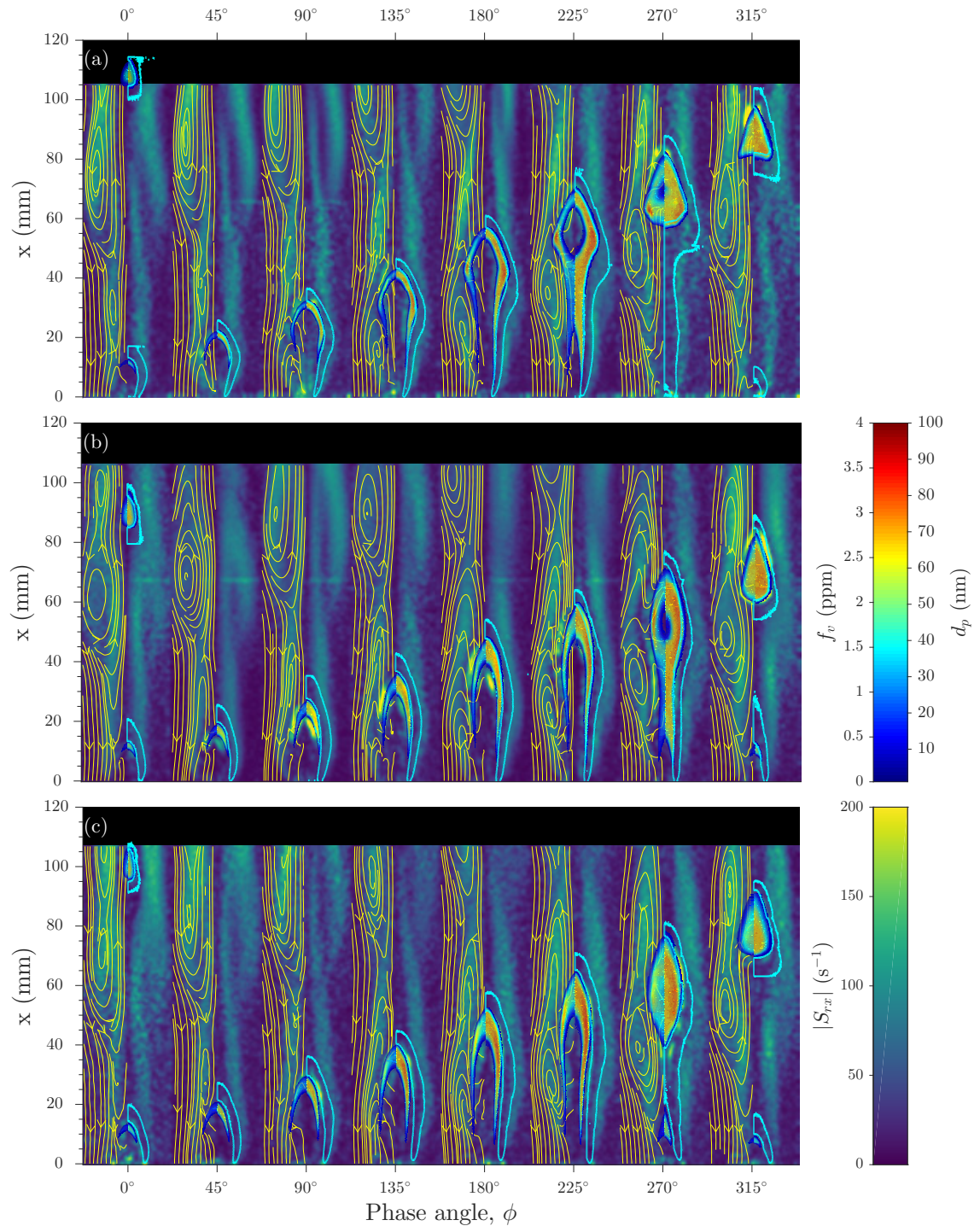


**Figure 5.8** Contour of shear strain rate superimposed with vorticity fields presented in the form of streamlines derived from the Galilean-transformed velocity fields, the OH layer and the planar measurements of soot volume fraction,  $f_v$  (LHS), and diameter of primary soot particle,  $d_p$  (RHS), collected for the forced flames (a) F-1 with  $D = 4.0$  mm, (b) F-2 with  $D = 5.6$  mm and (c) F-3 with  $D = 8.0$  mm. The black stripe at the top part of the plots represents no data as it is beyond the field of view of the PIV camera.

All three forced flames clearly exhibit a strong enhancement in the soot production relative to their unforced counterparts. The maximum soot volume fraction,  $f_{v,max}$ , and the largest primary particle diameter,  $d_{p,max}$ , measured in forced flames F-1, F-2 and F-3 are 3.48, 3.22 and 3.24 ppm and 83, 84 and 86 nm, correspondingly. The increase in  $d_{p,max}$  for the forced flames, relative to the steady flames, is only  $\sim 10\%$ , insignificant in comparison to the peak soot concentration, which shows an enhancement of  $\sim 110\%$ . These findings are consistent with previous studies [17, 18]. Comparing the spatial distributions of  $f_v$  and  $d_p$ , it is apparent that the large  $d_p$  has a more gradual distribution relative to the steep-gradient  $f_v$  profile. This non-linear spatial relationship between  $f_v$  and  $d_p$  could probably be explained by the physical processes involved in the soot growth. Coalescent collisions between particles are predominant during the early stage of particle growth. In a coalescence-dominated regime, the primary particle size grows as the soot volume fraction increases. At a later stage when collisions are no longer coalescence-dominated, chain-forming collisions become predominant, *i.e.*, growth in soot primary diameter is replaced by aggregation [52]. Additionally, due to the variations in the fuel velocity [2], all three forced flames exhibit the periodic transitions of  $f_{v,max}$  and  $d_{p,max}$  between the centreline and the annular regions of the flames at different phases of the oscillation cycles. This transition causes the soot fields in F-1 and F-2 to form a hollow shell of unburned fuel at the central region. However, the hollow shell does not occur in the soot field of F-3. This suggests that the increase in jet diameter is sufficient to increase the scale of the large eddies and the residence time within this flamelet to the point where the entire region is filled with soot. The diameter of the toroidal vortex increases with the nozzle diameter but has not been measured previously. However, the diameters of the toroidal vortices here are  $D_v = 16.9, 18.6$  and  $19.6$  mm for flames F-1, F-2 and F-3. While this dependence is relatively weak, the overall result is nevertheless significant.

To compare the total amount of soot produced in the steady and forced flames, the volume-integrated soot volume fraction,  $f_{v,total}$  is computed using the following expression

$$f_{v,total}(t) = 2\pi \int_0^{x_{max}} \int_0^{r_{max}} f_v(r, x, t) \cdot r \cdot dr \cdot dx \quad (5.4)$$

where  $f_v(r, x)$  is the local soot volume fraction at a coordinate specified by the radial distance,  $r$ , and the axial distance,  $x$ . Figure 5.9 shows the volume-integrations,  $f_{v,total}$ , and  $d_{p,max}$  at each phase for the forced flames and compared with those of the steady flames. F-1 shows the greatest degree of enhancement, by a factor of 9, while F-2 and F-3 exhibit factors of 8 and 6 increase relative to the steady counterpart, respectively. The variations of  $d_{p,max}$  are not as dramatic as that of  $f_{v,total}$ . Overall, the temporal profiles of  $d_{p,max}$  for the three forced flames are similar and their maximums are only  $\sim 10$  nm larger than  $d_{p,max}$  of their stationary counterparts. It appears that the "mature" soot particles have a well



characterised diameter that asymptotes to a near-constant value independent of further increases in residence time.

Previous computational studies [3, 19, 53] have highlighted the decisive role of in-flame residence time in determining the maximum soot volume fraction in a flame. To quantify the in-flame residence time,  $t_{res}$ , imaginary fluid parcels are tracked as they followed the streamlines in the steady and forced flames. Figure 5.10 illustrates the time-dependent positions of a fluid parcel, denoted  $A$ , prescribed by the Cartesian  $(r, x)$  and the streamline  $(n, s)$  coordinate systems. The coordinate along the streamlines is denoted  $s$ , and the second coordinate normal to the streamlines is denoted  $n$ . For a given fluid parcel, the value of  $s$  changes with time while  $n$  is constant because the fluid parcel can only flow along the streamline. Hence, the velocity is always tangent to the  $s$  direction,  $u_s = \sqrt{u_r^2 + u_x^2}$ .

The tracing of fluid parcel  $A$  is started at position  $(n = n, s = 0)$  at the nozzle exit at time  $t_0$ . Its next position at time  $t_1 = t_0 + \Delta t$  is traced along a streamline  $(n = n, s = s_0 + u_s \cdot \Delta t)$ . Here we choose  $\Delta t = f/8 = 0.0125$  s, where  $f$  is the 10 Hz frequency and the cycle is divided into 8 phases. The position of  $A$  at  $t_1$  is then transferred to the next panel, to form  $t_0$  of the next phase in the phase-locked imaged series, and so on. The process is continued until the fluid parcel enters the soot oxidation layer, determined from the position of the OH layer. Since the wings of the flames exhibit a higher soot concentration than that along the centreline, the fluid parcels are tracked as they enter the annular regions of the flames through the edge of the fuel stream (on the rich side of the OH layer).

[This page is intentionally left blank]

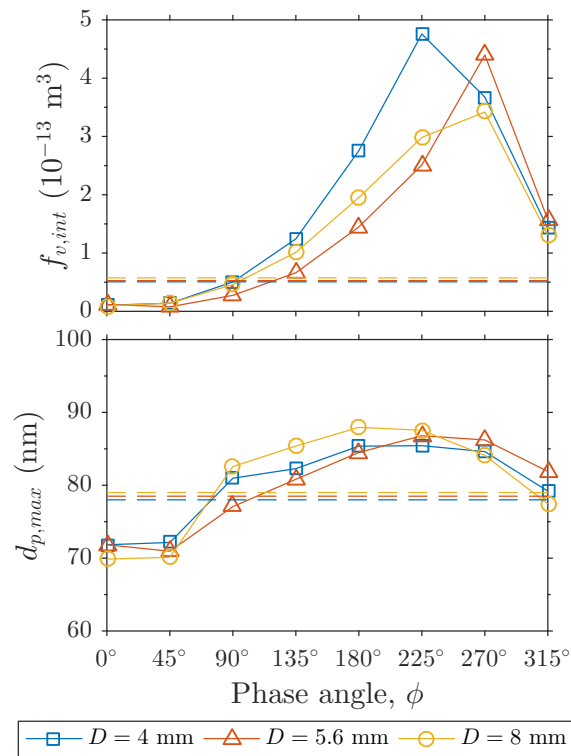


**Figure 5.9** Temporal evolution of the volume-integrated soot volume fraction ( $f_{v,int}$ ) and the local maximum diameter of primary soot particle ( $d_{p,max}$ ) for steady (dashed lines) and forced flames, F-1 ( $D = 4.0 \text{ mm}$ ), F-2 ( $D = 5.6 \text{ mm}$ ) and F-3 ( $D = 8.0 \text{ mm}$ ).

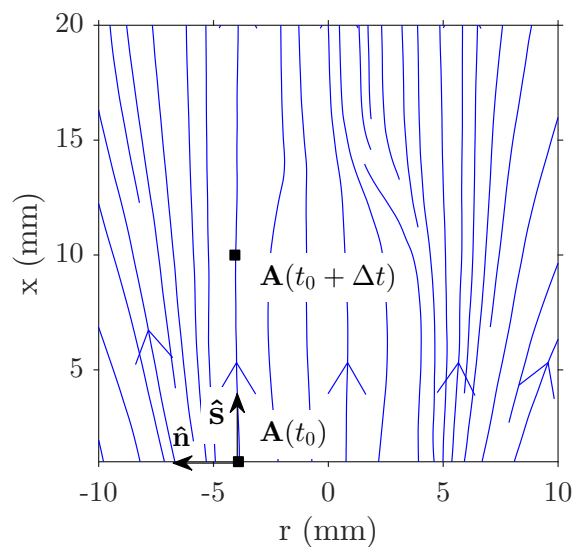


**Figure 5.10** A fluid parcel traced along a streamline as a function of time ( $t$ ) in the Cartesian ( $r, x$ ) and streamline ( $s, n$ ) coordinate systems.

Figure 5.11 presents the histories of  $f_v$ ,  $d_p$  and  $T_g$  as functions of the total residence time for the steady and forced flames. The pathlines show the temporal evolution of the soot concentration and the primary particle size at the tracked fluid parcels as they travel through the flames. Since all the steady flames have soot fields with similar spatial distributions, it is unsurprising that the times for soot inception for all the steady flames are similar,  $t_{res} \sim 14$  ms. For the forced flames, however, the temporal resolution of the phase-locked measurements is not sufficient to identify the exact time for soot inception. Nevertheless, the results show that at  $t_{res} = 12.5$  ms, the tracked fluid parcels in all three forced flames are prior to entering the corresponding soot fields and at  $t_{res} = 25$  ms, the tracked fluid parcels are deep inside the wings of the soot fields. Thus, it is reasonable to assume that the range of times for soot inception for the forced flames is close to that of the steady flames, which is consistent with the finding by Kaplan *et al.* [19]. In addition, the temperatures for soot inception are measured to be 1300–1500 K, although steady flames exhibit temperatures slightly lower than those of forced flames. This finding is consistent with the previous study reported by Santoro *et al.* [6], who observed initial soot formation at temperatures near to 1300 K in laminar non-premixed flames. Furthermore, the total in-flame residence time for the steady flames are similar as well,  $t_{res} \approx 48$  ms. In contrast to the steady conditions, the total in-flame residence times for the forced flames are twice as long, with  $t_{res} \approx 100$  ms. This increased residence time provides an explanation for the increased values of  $f_{v,max}$ ,  $f_{v,total}$  and  $d_{p,max}$ .

## 5.4 Conclusions

These new measurements have identified important new features of time-varying laminar flames and confirmed the values of more detailed investigations of acoustically forced laminar jet flames of different diameter. These time-varying laminar flames generate a range of residence time, temperature and mixture-fraction histories that vary with a factor of three over the steady counterparts, providing a much more versatile testing ground for soot models than steady laminar flames alone. These measurements have also shown that:

- varying the nozzle diameter by a factor of two causes the total volume of soot in the time-varying flame to increase by 50%;
- the pinching-off in the neck region in the flame is associated with consumption of the fuel there, rather than sufficiently high strain for extinction. Nevertheless, the strain rate is sufficiently high to be likely to contribute to the low soot volume fraction there, a feature that is also not present in steady flames;
- For F-1 with the smallest nozzle diameter (and hence smaller vortex diameter), the pinch-off occurs  $\sim 10$  ms earlier compared to F-2 and F-3. The

earlier pinch-off leads to the formation of a hollow soot shell observed in the forced flames F-1 and F-2, but not in F-3. The hollow soot shell is formed by a relatively large amount of unburned fuel and is convected into the core of the flame.

- The peak soot volume fractions in the forced flames are enhanced by  $\sim 110\%$  relative to their unforced counterparts. On the other hand, the maximum primary particle diameters reach  $\sim 85$  nm in the forced flames compared with 78 nm in the steady laminar flames, which is only  $\sim 10\%$  increase;
- In-flame residence time is identified as the decisive factor that is responsible for the soot enhancement in the forced flames relative to their stationary counterparts. The times for soot inception are similar for the steady and forced flames, regardless of the nozzle diameter. Tracking the imaginary fluid parcels as they travel through the whole flame shows that forcing the flames extends the in-flame residence time by a factor of two, relative to the steady conditions. The increased residence time not only expands the lifespan of soot but also allows more soot particles to form.

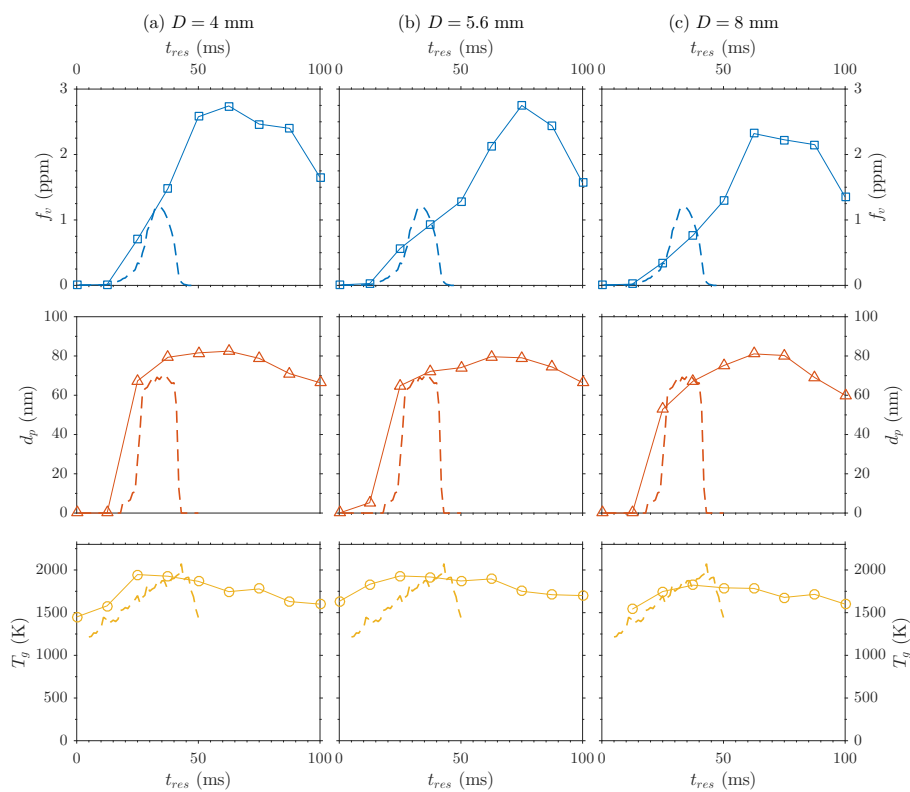


**Figure 5.11** Measurements of soot volume fraction ( $f_v$ ), diameter of primary soot particle ( $d_p$ ) and flame temperature ( $T_g$ ) along the tracked fluid parcel pathlines as a function of the total residence time for the steady (dashed lines) and forced flames (open symbols).

## Acknowledgement

The authors gratefully acknowledge the University of Adelaide and the financial support of the Australian Research Council (ARC Discovery grant DP130100198). The authors also thank Dr Timothy Lau and Dr Michael Evans for their help in the PIV experiments.

## References

- [1] P. Dearden and R. Long, “Soot formation in ethylene and propane diffusion flames”, *Journal of Chemical Technology & Biotechnology* **18** (8 1968), pp. 243–251.
- [2] R. J. Santoro, H. G. Semerjian, and R. A. Dobbins, “Soot particle measurements in diffusion flames”, *Combustion and Flame* **51** (1983), pp. 203–218.
- [3] M. D. Smooke, M. B. Long, B. C. Connelly, M. B. Colket, and R. J. Hall, “Soot formation in laminar diffusion flames”, *Combustion and Flame* **143** (2005), pp. 613–628.
- [4] R. Santoro and H. Semerjian, “Soot formation in diffusion flames: flow rate, fuel species and temperature effects”, *Proceedings of the Combustion Institute* **20** (1984), pp. 997–1006.
- [5] M. Smooke, C. McEnally, L. Pfefferle, R. Hall, and M. Colket, “Computational and experimental study of soot formation in a coflow, laminar diffusion flame”, *Combustion and Flame* **117** (1999), pp. 117–139.
- [6] R. Santoro, T. Yeh, J. Horvath, and H. Semerjian, “The transport and growth of soot particles in laminar diffusion flames”, *Combustion Science and Technology* **53** (1987), pp. 89–115.
- [7] K. Bray, “The challenge of turbulent combustion”, *Proceedings of the Combustion Institute* **26** (1996), pp. 1–26.
- [8] A. Gomez, G. Sidebotham, and I. Glassman, “Sooting behavior in temperature-controlled laminar diffusion flames”, *Combustion and Flame* **58** (1984), pp. 45–57.
- [9] I. Glassman, O. Nishida, and G. Sidebotham, “Critical Temperatures of Soot Formation”, *Soot Formation in Combustion: Mechanisms and Models*, ed. by H. Bockhorn, Berlin, Heidelberg: Springer Berlin Heidelberg, 1994, pp. 316–324.
- [10] N. Qamar, G. J. Nathan, Z. T. Alwahabi, and K. D. King, “The effect of global mixing on soot volume fraction: measurements in simple jet, precessing jet and bluff body flames”, *Proceedings of the Combustion Institute* **30** (2005), pp. 1493–1500.
- [11] P. H. Renard, D. Thévenin, J. C. Rolon, and S. Candel, “Dynamics of flame/vortex interactions”, *Progress in Energy and Combustion Science* **26** (2000), pp. 225–282.
- [12] S. R. Turns, “An introduction to combustion: concepts and applications”, 3rd ed., New York, United States: McGraw-Hill, 2012.

- 
- [13] J. Buckmaster and N. Peters, “The infinite candle and its stability – a paradigm for flickering diffusion flame”, *Proceedings of the Combustion Institute* **21** (1988), pp. 1829–1836.
- [14] O. A. Ezekoye, K. M. Martin, and F. Bisetti, “Pulsed flow modulation of soot production in a laminar jet-diffusion flame”, *Proceedings of the Combustion Institute* **30** (2005), pp. 1485–1492.
- [15] S. B. Dworkin, B. C. Connelly, A. M. Schaffer, B. A. V. Bennett, M. B. Long, M. D. Smooke, M. P. Puccio, B. McAndrews, and J. H. Miller, “Computational and experimental study of a forced, time-dependent, methane-air coflow diffusion flame”, *Proceedings of the Combustion Institute* **31** (2007), pp. 971–978.
- [16] R. Chrystie and S. H. Chung, “Response to acoustic forcing of laminar coflow jet diffusion flames”, *Combustion Science and Technology* **186** (2014), pp. 409–420.
- [17] C. R. Shaddix, J. E. Harrington, and K. C. Smyth, “Quantitative Measurements of Enhanced Soot Production in a Flickering Methane/Air Diffusion Flame”, *Combustion and Flame* **99** (1994), pp. 723–732.
- [18] C. R. Shaddix and K. C. Smyth, “Laser-Induced Incandescence Measurements of Soot Production in Steady and Flickering Methane, Propane, and Ethylene Diffusion Flames”, *Combustion and Flame* **107** (1996), pp. 418–452.
- [19] C. R. Kaplan, C. R. Shaddix, and K. C. Smyth, “Computations of enhanced soot production in time-varying ethylene/ air diffusion flames”, *Combustion and Flame* **106** (1996), pp. 89–115.
- [20] K. C. Smyth, J. E. Harrington, E. L. Johnsson, and W. M. Pitts, “Greatly enhanced soot scattering in flickering CH<sub>4</sub> Air diffusion flames”, *Combustion and Flame* **95** (1993), pp. 229–239.
- [21] K. C. Smyth, C. R. Shaddix, and D. A. Everest, “Aspects of soot dynamics as revealed by measurements of broadband fluorescence and flame luminosity in flickering diffusion flames”, *Combustion and Flame* **111** (1997), pp. 185–207.
- [22] D. S. Chamberlin and A. Rose, “The flicker of luminous flames”, *Industrial & Engineering Chemistry Research* **20** (1928), pp. 1013–1016.
- [23] A. J. Grant and J. M. Jones, “Low-frequency diffusion flame oscillations”, *Combustion and Flame* **25** (1975), pp. 153–160.
- [24] D. F. G. Durão and J. H. Whitelaw, “Instantaneous velocity and temperature measurements in oscillating diffusion flames”, *Proc. R. Soc. Lond. A.* **338** (1974), pp. 479–501.
- [25] H. Sato, K. Amagai, and M. Arai, “Diffusion flames and their flickering motions related with Froude numbers under various gravity levels”, *Combustion and Flame* **123** (2000), pp. 107–118.
- [26] A. Jocher, K. K. Foo, Z. W. Sun, B. B. Dally, H. Pitsch, Z. T. Alwahabi, and G. J. Nathan, “Impact of acoustic forcing on soot evolution and temperature in ethylene-air flames”, *Proceedings of the Combustion Institute* **36** (2017), pp. 781–788.

## REFERENCES

---

- [27] K. K. Foo, Z. W. Sun, P. R. Medwell, Z. T. Alwahabi, B. B. Dally, and G. J. Nathan, “Experimental investigation of acoustic forcing on temperature, soot volume fraction and primary particle diameter in non-premixed laminar flames”, *Combustion and Flame* **181** (2017), pp. 270–282.
- [28] Z. W. Sun, B. B. Dally, and Z. T. A. G. J. Nathan, “Effects of hydrogen and nitrogen on soot volume fraction, primary particle diameter and temperature in laminar ethylene/air diffusion flames”, *Combustion and Flame* **175** (2017), pp. 270–282.
- [29] L. D. Chen, J. P. Seaba, W. M. Roquemore, and L. P. Goss, “Buoyant diffusion flames”, *Proceedings of the Combustion Institute* **22** (1988), pp. 677–684.
- [30] P. R. Medwell, Q. N. Chan, B. B. Dally, S. Mahmoud, Z. T. Alwahabi, and G. J. Nathan, “Temperature measurements in turbulent non-premixed flames by two-line atomic fluorescence”, *Proceedings of the Combustion Institute* **34** (2013), pp. 3619–3627.
- [31] P. R. Medwell, A. R. Masri, P. X. Pham, B. B. Dally, and G. J. Nathan, “Temperature imaging of turbulent dilute spray flames using two line atomic fluorescence”, *Experiments in Fluids* **55** (2014), pp. 1840–1851.
- [32] D. H. Gu, Z. W. Sun, G. J. Nathan, P. R. Medwell, and Z. T. Alwahabi, “Improvement of precision and accuracy of temperature imaging in sooting flames using two-line atomic fluorescence (TLAF)”, *Combustion and Flame* **167** (2016), pp. 481–493.
- [33] P. R. Medwell, Q. N. Chan, B. B. Dally, Z. T. Alwahabi, G. F. Metha, and G. J. Nathan, “Flow seeding with elemental metal species via an optical method”, *Applied Physics B* **107** (2012), pp. 665–668.
- [34] D. H. Gu, Z. W. Sun, P. R. Medwell, Z. T. Alwahabi, B. B. Dally, and G. J. Nathan, “Mechanism for laser-induced fluorescence signal generation in a nanoparticle-seeded flow for planar flame thermometry”, *Applied Physics B* **118** (2015), pp. 209–218.
- [35] Q. N. Chan, “Development of Instantaneous Temperature Imaging in Sooty Flames”, PhD thesis, The University of Adelaide, 2011.
- [36] P. Freeze, D. Thomas, S. Edelman, and J. Stern, “Study of performance characteristics of noble metal thermocouple materials to 2000°C”, NASA, 1972.
- [37] Z. W. Sun, D. H. Gu, G. J. Nathan, Z. T. Alwahabi, and B. B. Dally, “Single-shot, Time-Resolved planar Laser-induced Incandescence for soot primary particle sizing in flames”, *Proceedings of the Combustion Institute* **35** (2015), pp. 3673–3680.
- [38] R. Puri, M. Moser, R. J. Santoro, and K. C. Smyth, “Laser-induced fluorescence measurements of OH concentrations in the oxidation region of laminar hydrocarbon diffusion flames”, *Proceedings of the Combustion Institute* **24** (1992), pp. 1015–1022.
- [39] B. J. McKeon, G. Comte-Bellot, J. F. Foss, F. S. J. Westerwell, C. Tropea, J. F. Meyers, J. W. Lee, A. A. Cavone, R. Schodl, M. M. Koochesfahani, D. G. Nocera, Y. Andreopoulos, W. J. A. Dahm, J. A. Mullin, J. M. Wallace, P. V. Vukoslavčević, S. C. Morris, E. R. Pardyjak, and A. Cuerva, “Velocity, Vorticity and Mach Number”, *Springer Handbook of Experimental Fluid Mechanics*, ed. by C. Tropea, A. L. Yarin, and J. F. Foss, Springer, Heidelberg, Germany, 2007.



- 
- [40] W. Thielicke and E. J. Stamhuis, “PIVlab - Time-resolved digital particle image velocimetry tool for MATLAB (version: 1.41)”, *J. Open Res. Softw.* **2** (2014), e30.
- [41] W. Thielicke, “The Flapping Flight of Birds - Analysis and Application”, PhD thesis, Rijksuniversiteit Groningen, 2014.
- [42] D. L. Reuss, R. J. Adrian, and C. C. Landreth, “Two-Dimensional Velocity Measurements in a Laminar Flame Using Particle Image Velocimetry”, *Combustion Science and Technology* **67** (1989), pp. 73–83.
- [43] D. Garcia, “A fast all-in-one method for automated post-processing of PIV data”, *Experiments in Fluids* **50** (2011), pp. 1247–1259.
- [44] C. J. Sung, C. K. Law, and R. L. Axelbaum, “Thermophoretic effects on seeding particles in LDV measurements of flames”, *Combustion Science and Technology* **99** (1994), pp. 119–132.
- [45] Adam M. Steinberg and James F. Driscoll, “Straining and wrinkling processes during turbulence-premixed flame interaction measured using temporally-resolved diagnostics”, *Combustion and Flame* **156** (2009), pp. 2285–2306.
- [46] D. Han and M. G. Mungal, “Simultaneous measurements of velocity and CH distributions. Part 1: jet flames in co-flow”, *Combustion and Flame* **132** (2003), pp. 565–590.
- [47] J. V. Lukowicz and J. Köngeter, “Experimental Investigation of Coherent Structures using Digital Particle Image Velocimetry”, ed. by W. Rodi and D. Laurence, Oxford: Elsevier Science Ltd, 1999, pp. 361–370.
- [48] G. S. Lewis, B. J. Cantwell, U. Vandsburger, and C. T. Bowman, “An investigation of the structure of a laminar non-premixed flame in an unsteady vortical flow”, *Proceedings of the Combustion Institute* **22** (1988), pp. 512–522.
- [49] B.G. Sarnacki, G. Esposito, R.H. Krauss, and H.K. Chelliah, “Extinction limits and associated uncertainties of nonpremixed counterflow flames of methane, ethylene, propylene and n-butane in air”, *Combustion and Flame* **159** (2012), pp. 1026–1043.
- [50] J. Du and R. Axelbaum, “The Effect of Flame Structure on Soot-Particle Inception in Diffusion Flames”, *Combustion and Flame* **100** (1995), pp. 367–375.
- [51] M. E. Decroix and W. L. Roberts, “Transient flow field effects on soot volume fraction in diffusion flames”, *Combustion Science and Technology* **160** (2000), pp. 165–189.
- [52] G. Prado and J. Lahaye, “Physical Aspects of Nucleation and Growth of Soot Particles”, *Particulate Carbon: Formation During Combustion*, ed. by D. C. Siegla and G. W. Smith, Boston, MA: Springer US, 1981, pp. 143–175.
- [53] S. B. Dworkin, J. A. Cooke, B. A. V. Bennett, B. C. Connelly, M. B. Long, M. D. Smooke, R. J. Hall, and M. B. Colket, “Distributed-memory parallel computation of a forced, time-dependent, sooting, ethylene/air coflow diffusion flame”, *Combustion Theory and Modelling* **13** (2009), pp. 795–822.

[This page is intentionally left blank]

## Chapter 6

# Soot evolution and flame response to acoustic forcing of laminar non-premixed jet flames at varying amplitudes

This chapter consists of the published journal article:

Kae Ken Foo, Zhiwei Sun, Paul R. Medwell, Zeyad T. Alwahabi, Graham J. Nathan and Bassam B. Dally, "Soot evolution and flame response to acoustic forcing of laminar non-premixed jet flames at varying amplitudes", *Combustion and Flame* **198** (2018) pp. 249–259.

The content of this chapter is identical to that of the published article, with the following exceptions:

1. The typesetting and referencing style have been altered to maintain a consistent appearance within the thesis.
2. The numbering of tables, figures and equations has been changed to include the number of the chapter.

The article in its published format is available at:

<https://doi.org/10.1016/j.combustflame.2018.09.022>

## Statement of Authorship

Title of Paper	Soot evolution and flame response to acoustic forcing of laminar non-premixed jet flames at varying amplitudes
Publication Status	<input type="checkbox"/> Published <input type="checkbox"/> Accepted for Publication <input checked="" type="checkbox"/> Submitted for Publication <input type="checkbox"/> Unpublished and Unsubmitted work written in manuscript style
Publication Details	K.K. Foo, Z.W. Sun, P.R. Medwell, Z.T. Alwahabi, G.J. Nathan and B.B. Dally, "Soot evolution and flame response to acoustic forcing of laminar non-premixed jet flames at varying amplitudes", <i>Combustion and Flame</i> (under review).

### Principal Author

Name of Principal Author (Candidate)	Kae Ken Foo
Contribution to the Paper	<p>I planned and proposed the experimental design matrix to the co-authors after a thorough literature review. Together with all the co-authors, we decided the experimental cases.</p> <p>I set up the experiments with the assistance provided by the second co-author, Z.W. Sun. We collected the experimental results together.</p> <p>I processed, analysed and interpreted all the experimental data. After some discussion with the co-authors regarding my interpretation of the experimental data, I wrote the manuscript.</p>
Overall percentage (%)	65%
Certification:	This paper reports on original research I conducted during the period of my Higher Degree by Research candidature and is not subject to any obligations or contractual agreements with a third party that would constrain its inclusion in this thesis. I am the primary author of this paper.
Signature	Digitally signed by Kae Ken Foo Date: 2018.08.20 09:37:36 +09'30'

### Co-Author Contributions

By signing the Statement of Authorship, each author certifies that:

- i. the candidate's stated contribution to the publication is accurate (as detailed above);
- ii. permission is granted for the candidate to include the publication in the thesis; and
- iii. the sum of all co-author contributions is equal to 100% less the candidate's stated contribution.

Name of Co-Author	Zhi Wei Sun
Contribution to the Paper	This co-author co-designed the experiments and provided aid collecting data. He helped to edit the experimental details section of the manuscript.
Signature	Digitally signed by Zhiwei Sun Date: 2018.08.21 11:00:56 +09'30'

Name of Co-Author	Paul R. Medwell
Contribution to the Paper	This co-author provided suggestions for the experimental set-up and data post-processing. He also helped evaluate and edit the manuscript.
Signature	Paul Medwell 2018.08.23 11:13:06 +09'30'

Name of Co-Author	Zeyad T. Alwahabi
Contribution to the Paper	This co-author provided suggestions for the experimental set-up. He also helped to evaluate and edit the manuscript.
Signature	Digitally signed by Zeyad Alwahabi DN: cn=Zeyad Alwahabi, o=Chem Eng, ou, email=zeyad.alwahabi@adelaide.edu.au, c=AU Date: 2018.08.21 14:07:22 +09'30'

Name of Co-Author	Graham J. Nathan
Contribution to the Paper	This co-author co-supervised the development of the work. He also helped to evaluate and edit the manuscript.
Signature	Digitally signed by Graham J Nathan Date: 2018.08.23 12:49:27 +09'30'

Name of Co-Author	Bassam B. Dally
Contribution to the Paper	This co-author co-supervised the development of the work. He also helped to evaluate and edit the manuscript.
Signature	Digitally signed by Bassam Dally Date: 2018.08.20 10:11:54 +09'30'

## Soot evolution and flame response to acoustic forcing of laminar non-premixed jet flames at varying amplitudes

Kae Ken Foo, Zhiwei Sun, Paul R. Medwell, Zeyad T. Alwahabi,  
Graham J. Nathan, Bassam B. Dally

### Abstract

New details regarding the soot evolution and its controlling parameters in steady and forced flames have been studied using high spatial resolution laser diagnostic techniques. Steady laminar non-premixed ethylene/nitrogen flames with three different diameter burners were acoustically forced using a loudspeaker. 10-Hz-sinusoidal signals of different amplitudes were transmitted to the loudspeaker to drive the flames. The results reveal that the spatial correlation between the soot field and the temperature profile is influenced by the burner diameter and forcing conditions. The soot field in steady laminar flames is confined to a relatively narrow temperature range, 1500–2000 K. In contradiction, the soot field in forced flames spread across a wider range of temperature, 1400–2100 K. Furthermore, the spatial correlation between the normalised soot concentration and primary particle size can be described with an exponential function. While it is observed that the exponential coefficients vary with burner diameter and forcing conditions, further study is necessary for a better understanding. In general, laminar flames forced at a lower amplitude ( $\alpha = 25\%$ ) tend to produce less soot than moderately forced ( $\alpha = 50\%$ ) flames. Further increasing the forcing amplitude to  $\alpha = 75\%$  does not increase the soot production in laminar flames; conversely, lower peak and volume-integrated soot volume fraction are observed in the strongly forced flame ( $\alpha = 75\%$ ) as relative to the moderately forced counterpart. These findings shed new light on the seemingly contradictory results published in the literature regarding the effect of the forcing intensity on the soot production.

## 6.1 Introduction

There is an ongoing need to increase the understanding of soot evolution in flames. Soot formation and oxidation have practical significance in the development of technologically advanced combustion devices that are highly efficient while producing low emissions, as well as its influences on public health [1–4] and ecology [5, 6]. The development of these devices can be accelerated with the aid of robust and predictive soot models. However, despite advanced computational power, the ability to adequately model the complex chemical and physical

processes that constitute the soot evolution remains limited [7, 8]. To address this issue, systematic experimental data of the parameters controlling soot formation is essential for the development of affordable and accurate soot models. Key scalars that are accessible using non-intrusive techniques include particle size distribution, the volume fraction of soot, along with the governing variables such as temperature and flow field.

Time-varying laminar flames are an intermediate class of flame that bridge the gap between steady laminar and turbulent flames. They exemplify the complex flame–vortex interactions exhibited in turbulent flames. Additionally, due to their cyclic temporal nature, time-varying laminar flames are also particularly valuable as a platform to study flame development and soot evolution in a time-varying flow field. Several experimental [9–15] and numerical studies [16–18] have revolved around time-varying laminar flames. The interest in this subject stems from the fact that time-varying laminar flames provide a broader range of flame conditions than that are available under steady-state conditions. Laser-Induced Incandescence (LII) measurements have shown that acoustically pulsing a laminar steady flame with a frequency of 10 Hz (near to the natural flickering frequency) increases the soot production [10]. Furthermore, Shaddix and Smyth [11] reported that while the effect of pulsing on soot enhancement varies with the fuel type (*i.e.*, methane, ethylene and propane), the qualitative intensity of flame flickering has a limited effect on the soot production. However, Connelly [19] provided a contrasting view on the relationship of the soot production with the forcing level via quantifying the modulation of centreline velocity using Particle Image Velocimetry (PIV). While the peak soot concentration increases with the forcing level, the spatial area of the soot field also expands which leads to a substantial rise in the volume-integrated soot volume fraction. Additionally, a numerical study conducted by Kaplan et al. [16] has shown that the peak soot concentration in the forced methane flames increases with the amplitude of the 10-Hz sinusoidal forcing. The study [16] also attributed the augmented soot production under forcing conditions to the lengthening of soot growth residence time in the time-varying flow field as compared to the steady-state. However, Shaddix and Smyth [11] also reported that the peak soot levels measured in ethylene forced flames to decrease as the flame flickering intensity increases, which appears to contradict the trend shown by Connelly [19]. It is worth noting that the burners utilised in [11] and [19] have different diameters, 11.0 and 4.0 mm, respectively and it is unclear how jet diameter affects these processes. A previous study [20] has investigated the soot fields of flames with different diameters to the same forcing conditions, at a frequency of 10 Hz and 50% amplitude (defined as the maximum centreline velocity of forced flames compared to that of steady counterparts). The results show that while the difference in the burner size has an insignificant effect on the peak soot level, it affects the flame structure and hence the spatial distribution of soot. Hence, a larger diameter burner results in a decreased volume-integrated soot volume fraction.

The discrepancy between [11] and [19] motivates the current study to investigate time-varying laminar flames of ethylene in more details. The present study extends the previous measurements in flames with different diameter burners [20] to other forcing amplitudes. The present paper aims to shed new light on the mechanisms that affect the soot evolution in time-varying flames in more details. Furthermore, these measurements for three different burner diameters under both steady and forced conditions constitute a comprehensive database for supporting the development and verification of predictive soot models.

## 6.2 Experimental details

### 6.2.1 Burner configuration

Figure 6.1 presents the cross-sectional view of the co-flow burner used in the current study. The burner was designed and built based on the configurations of the Yale Burner [17]. It consists of three interchangeable fuel tubes, with inner diameters of 4.0, 5.6 and 8.0 mm, and a concentric 74-mm-diameter co-flow air passage. A loudspeaker was installed in the plenum below the fuel tube and it was driven by a signal generator to impose a 10 Hz periodic pressure fluctuation on the fuel stream. The frequency of the forcing was chosen to be 10 Hz because it is close to the natural frequencies of all of the three steady laminar flames, and therefore provides the most effective coupling between the flame structure and the flow field [20, 21]. The optical diagnostics were phase-locked to the 10 Hz sinusoidal oscillation to acquire phase-resolved measurements.

The fuel stream comprised 41.7% ethylene ( $C_2H_4$ ) and 58.3% nitrogen ( $N_2$ ), by volume. The fuel was diluted to limit the maximum amount of soot in the forced flame and thus minimise the level of interference from soot on the laser diagnostic measurements [22]. To isolate the effect of C/O ratio on soot production, the volumetric flow rates of the fuel stream and the co-flow for all the studied cases were kept constant at 0.31 and 60.0 standard litres per minute (SLPM), respectively. All flow rates were measured with mass flow controllers (Alicat Scientific) conditioned to a standard temperature and pressure, 293 K and 1 atm. The normalised amplitude,  $\alpha$ , is defined as

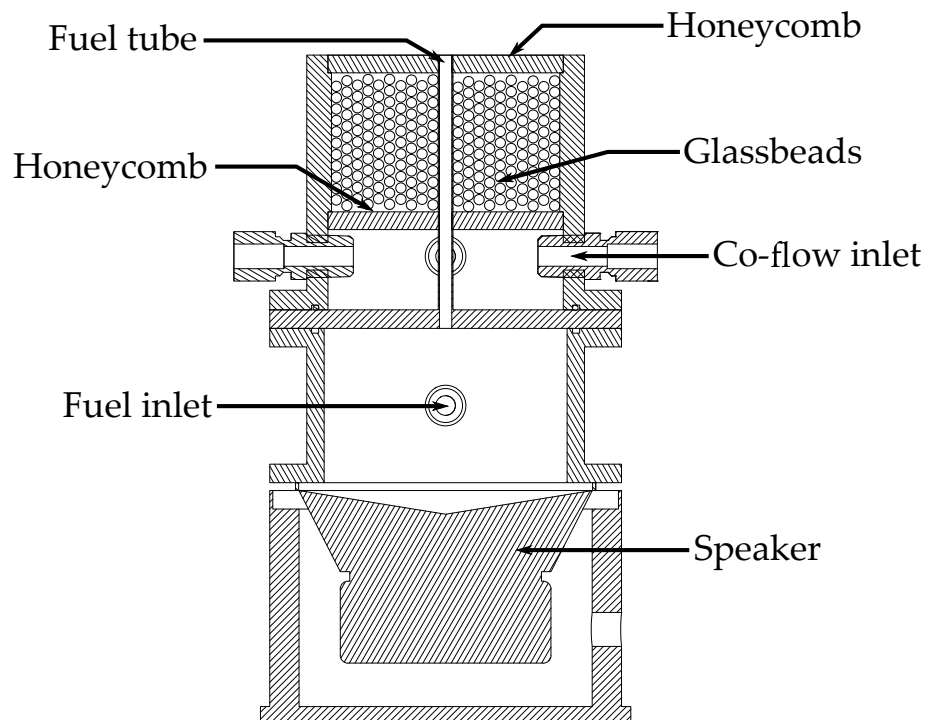
$$\alpha = \frac{U_{c,forced} - U_{c,steady}}{U_{c,steady}} \quad (6.1)$$

where  $U_c$  is the centreline velocity and the subscript denotes whether it is for steady or forced flame. Flow conditions for all the flames studied, including the fuel bulk velocity,  $U_f$ , and dimensionless parameters (Strouhal, Froude and Reynolds numbers) are given in Table 6.1.



**Table 6.1** Summary of test conditions

	Cases	$D$ (mm)	$U_f$ (m/s)	$U_c$ (m/s)	$\alpha$ (-)	$f$ (Hz)	$St$ (-)	$Fr$ (-)	$Re$ (-)
Steady	S-1	4.0	0.41	0.83	-	0	0	4.28	147
	S-2	5.6	0.21	0.36	-	0	0	0.80	104
	S-3	8.0	0.10	0.21	-	0	0	0.13	72
Forced	F-1	4.0	0.41	1.25	50%	10	0.10	4.28	147
	F-2	5.6	0.21	0.53	50%	10	0.27	0.80	104
	F-3	8.0	0.10	0.31	50%	10	0.80	0.13	72
	F-4	4.0	0.41	1.04	25%	10	0.10	4.28	147
	F-5	5.6	0.21	0.62	75%	10	0.27	0.80	104
	F-6	8.0	0.10	0.27	25%	10	0.80	0.13	72

**Figure 6.1** Cross-sectional diagram of the co-flow burner, which is identical to that of Dworkin et al. [17].

## 6.2.2 Temperature measurement

Temperature ( $T_g$ ) profiles were obtained using the Non-linear excitation regime Two-Line Atomic Fluorescence (NTLAF) technique. The principle of this technique is based on the optical excitation of two neighbouring electronic ground states to a common excited state and the sequential detection of the fluorescence. The flame temperature is then derived from the ratio between the two laser-induced fluorescence signals using an equation described previously [23, 24]. The flames were seeded with indium, in the form of complex agglomerates of nano-sized primary particles of indium compounds and spherical micron-sized indium beads, through the fuel stream with an in-house-built ablation device [25, 26].

The system-dependent parameters of NTLAF were calibrated in an ethylene/air premixed flame with an equivalence ratio,  $\Phi = 2.0$  stabilised on a flat-flame burner. The burner was purpose-designed to produce a matrix of small laminar flames, which subsequently interact and combine to form a stable flat flame of uniform temperature [27]. The flat-flame temperature was measured using an R-type Pt/Pt-Rh 13% thermocouple with a 180- $\mu\text{m}$ -diameter bead (Omega, P13R-003). A correction of 60 K was added to the thermocouple measurements to account for the radiation heat loss from the thermocouple bead to the surrounding [28]. The phase-averaged images of gas temperature presented in the following sections have a typical signal-to-noise ratio (SNR) of 80:1. The overall uncertainty for the phase-averaged temperature is  $\pm 120$  K ( $1\sigma$ ).

## 6.2.3 Soot volume fraction and primary particle diameter measurements

Soot volume fraction ( $f_v$ ) and primary particle diameter ( $d_p$ ) were both measured using the Time-Resolved Laser-Induced Incandescence (TiRe-LII) technique. A fundamental output, 1064 nm, from an Nd:YAG laser (Quantel, Brilliant B) was used to perform the measurements of the soot field. The technique utilises the prompt LII signal as a means of quantifying the soot volume fraction. The gate width of the ICCD camera was set to 40 ns. The collected LII signal was calibrated by performing a comparison with soot volume fraction profiles obtained from an extinction measurement in a well-characterised steady ethylene non-premixed flame burned on a Santoro-type burner. A value of the extinction coefficient,  $K_e = 5.66$  was chosen to determine the soot volume fraction [29]. The uncertainty and the lower limit of detection for the soot volume fraction are  $\pm 10\%$  ( $1\sigma$ ) [30] and 0.01 ppm (where SNR is lower than 10:1), respectively.

The primary particle diameter measurement was obtained by comparing the ratios of four subsequently collected LII signals (delayed by 0, 40, 80 and 120 ns) with the estimated values provided by an LII model [31]. This model assumed the soot particles to be non-aggregated and the size distribution of primary

particles to be mono-disperse which leads to an overestimation of the primary particle diameter by up to a factor of two [28]. Due to the low intensity level, the minimum measurable diameter is 5 nm, while the uncertainty for the phase-averaged measurement is  $\pm 4$  nm ( $1\sigma$ ). The absolute accuracy of the measurement is limited by the selected LII model, nevertheless, the relatively high precision provides a good resolution of the spatial gradient of the primary particle diameter in the flames.

#### 6.2.4 Hydroxyl radical concentration measurement

The planar Laser-Induced Fluorescence of the hydroxyl radical (OH-PLIF) was excited using a single ultraviolet (UV) laser beam tuned to the  $Q_1(8)$  transition (283.5 nm) of the  $A^2\Sigma^+ \leftarrow X^2\Pi_i(1,0)$  system. This is a strong fluorescence line with little temperature dependence of the population, less than 5% over the temperature range of interest, 1400 to 2100 K [32]. The OH fluorescence was imaged onto an ICCD camera (Princeton Instruments ICCD-576) equipped with a 105 mm  $f/1.2$  UV lens after transmission through a UV filter centred at 310 nm with an FWHM of 10 nm. Since the intensity of OH-PLIF ( $I_{OH}$ ) is not quantified, the results are presented in arbitrary units.

#### 6.2.5 Velocity measurement

The Particle Imaging Velocimetry (PIV) technique was used to characterise the dynamics and the flow fields of the forced flames. The light source was a frequency-doubled, double-cavity Nd:YAG laser (Quantel BrilliantB) operating at a wavelength of 532 nm (180 mJ per pulse) and a pulse rate of 10 Hz. The time interval between the pulses was 100  $\mu$ s. The region of interest (ROI) was illuminated with a 1-mm-thick laser sheet. The particle image pairs were recorded with two double-frame CCD cameras (Princeton Instruments, Megaplus II ES4020) stacked one on top of the other. Each viewing area was approximately 70.4 mm  $\times$  70.4 mm, which translates into an in-plane spatial resolution of 29.4 pixel/mm. Each CCD camera was equipped with a 70–300 mm 1:4–5.6 D zoom lens (Nikon, AF Nikkor) and a 532 nm bandpass filter (Andover) with an FWHM of 1 nm to reduce the flame luminosity interference on the image pairs.

Both the fuel and co-flow streams were seeded with 1- $\mu$ m-diameter titanium dioxide ( $\text{TiO}_2$ ) particles using separate cyclone seeders located downstream from the mass-flow controllers. In the experiment, the Stokes number ( $Sk$ ) ranges from  $10^{-4}$  to  $10^{-3}$  which satisfies the criterion,  $Sk \ll 0.1$ , for an acceptable flow tracing accuracy with errors below 1% [33]. To avoid the accumulation of particles and minimise the blockage effect on the co-flow uniformity, the burner was regularly flushed with clean air during the experiments.

The PIV image ensembles were batch processed with PIVlab 1.41 [34, 35]. A

multi-pass (sequential interrogation window sizes of 256, 128, 64 and 32 pixels, 50% overlap), standard FFT was used to calculate the particle displacement vector fields. For each case and at each phase, an ensemble of 50 instantaneous, phase-resolved measurements was averaged to construct the phase profiles of the velocity fields. The PIV measurement is challenging in the regions of sooting flames due to the combined effects of gas expansion and interference. In the current study, the velocity field could not be resolved in the regions of highest soot concentration due to these two effects. For these affected regions, values were interpolated using the Discrete Cosine Transform based on the penalised least squares approach (DCT-PLS) described in [36]. Velocities measured in the reaction zone where steep temperature gradients occur,  $\nabla T \sim 300$  K/mm, are affected by the thermophoresis effect. The magnitude of the thermophoresis velocity,  $U_t$  can be expressed as

$$U_t = -\frac{3}{4(1 + \pi A/8)} \frac{\nu}{T} \nabla T \quad (6.2)$$

where  $\nu$  is the kinematic viscosity,  $T$  is the temperature and  $A$  is the accommodation coefficient which usually is taken to be 0.9 [37]. Assuming a temperature of 1800 K as characteristic for the reaction zone, the resulting  $U_t$  can be as large as  $0.37 \text{ m}\cdot\text{s}^{-1}$  toward the lower temperature. Outside of this region, the typical velocity uncertainty is approximately  $\pm 0.08 \text{ m}\cdot\text{s}^{-1}$  ( $1\sigma$ ).

## 6.3 Results and discussion

### 6.3.1 Laminar steady flames

Velocity measurements were used to determine the streaklines of virtual fluid particles in the flames and to follow the evolution of pseudo-soot particles along these paths. Initially, at  $t_0 = 0$  s, the fluid particle  $A$  at the exit plane ( $x_0 = 0$  mm,  $r$ ) has a velocity expressed in axial and radial components ( $u_x$ ,  $u_r$ ). The next position of  $A$  at time  $t_1 = t_0 + \Delta t$  is ( $x_0 + u_x \cdot \Delta t$ ,  $r + u_r \cdot \Delta t$ ), and so on.

In Fig. 6.2, the contours of residence time,  $\tau$ , are plotted at 10-ms intervals superimposed on the spatial distribution of the  $f_v$  and  $I_{OH}$  envelope isopleths indicating the location of the reaction zone. They are different for each of the three flames, consistent with the different jet exit velocities. However, the soot distributions and the peak soot volume fractions are similar.

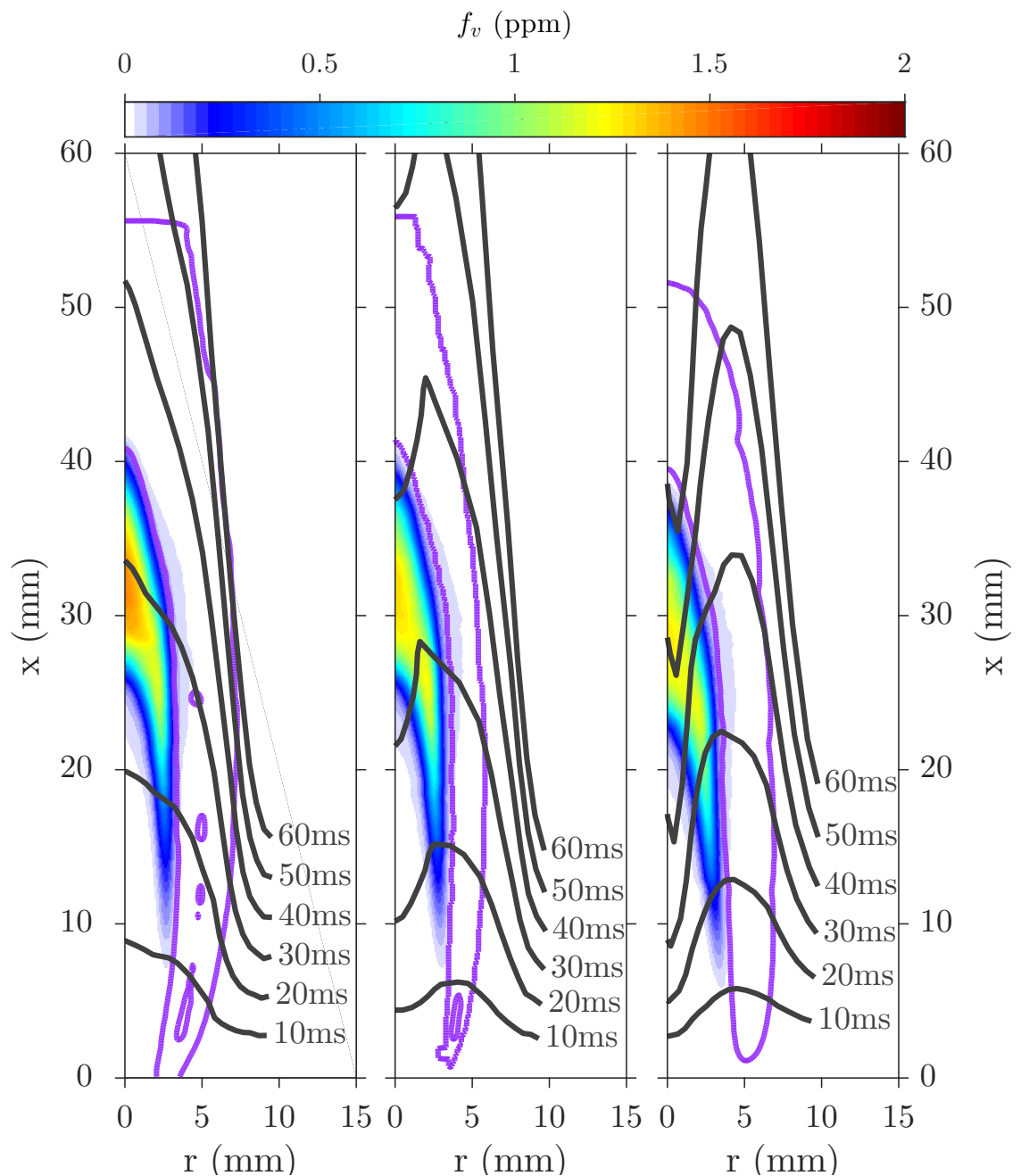


**Figure 6.2** Isopleths of the residence time superimposed on the spatial distribution of soot volume fraction in pseudo-colour for laminar steady flames, from left to right, S-1 ( $D = 4.0$  mm), S-2 ( $D = 5.6$  mm) and S-3 ( $D = 8.0$  mm). For reference, the location of the OH-PLIF is plotted in purple.

Figure 6.3(a) presents  $f_v$  along the centreline as a function of  $\tau$  for the three steady flames S-1 ( $U_c = 0.83 \text{ m}\cdot\text{s}^{-1}$ ), S-2 ( $U_c = 0.36 \text{ m}\cdot\text{s}^{-1}$ ) and S-3 ( $U_c = 0.21 \text{ m}\cdot\text{s}^{-1}$ ). Because the LII technique only measures graphitic soot particles, pseudo-soot inception,  $\tau_{i,ps}$  is defined here to correspond to  $f_v = 0.02 \text{ ppm}$  [16]. The values of  $\tau_{i,ps}$  along the centreline are 23, 31 and 45 ms for the flames S-1, S-2 and S-3, respectively. These trends are consistent with those in temperature, with the corresponding values of  $T_{i,ps}$  being 1688, 1657 and 1525 K, respectively. That is, a longer residence time is required where the temperature is lower. Fig. 6.3(c) presents the corresponding values of  $d_p$ . By comparing Figs. 6.3(a) and (c), it can be seen that the growth of  $d_p$  almost coincides with that of  $f_v$ . However, in contrast with the literature in which the primary particles are typically 20–40 nm in average diameter [38–40], the largest  $d_p$  measured in the current steady flames are approximately 78 nm. In addition, the maximum values of  $f_v$  measured here are slightly different, 1.44, 1.31 and 1.28 ppm for S-1, S-2 and S-3, respectively. Temperatures corresponding to these  $f_{v,max}$  decrease from 1863, 1841 and 1704 K as the burner diameter is increased from 4.0, 5.6 and 8.0 mm. While these trends are consistent with each other, they are the opposite to those of the pseudo inception point, highlighting the complexity of these flames.

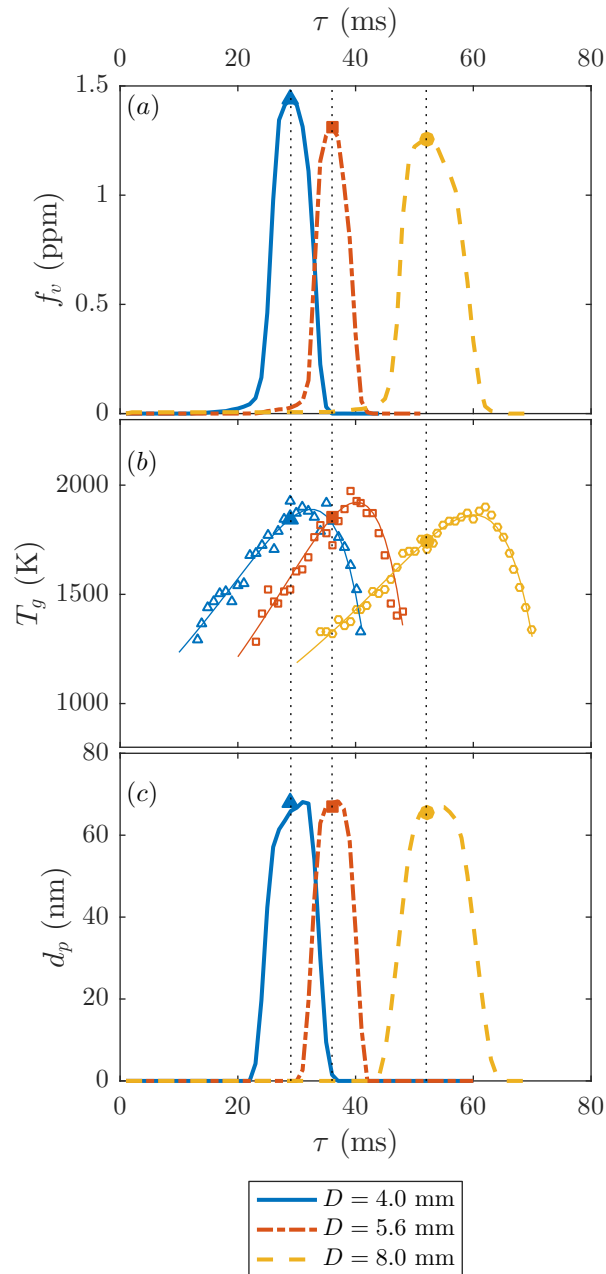
Figure 6.4, 6.5 and 6.6 present the trivariate distributions of spatially-correlated  $f_v$ ,  $d_p$  and  $T_g$  for steady laminar flames S-1, S-2 and S-3, respectively. Due to the overestimation of  $d_p$  with the present TiRe-LII method, measurements of the soot concentration and the primary particle diameter are normalised by the local maximum values shown in Figs. 6.3(a) and (c), respectively ( $\hat{f}_v = f_v / f_{v,max}$  and  $\hat{d}_p = d_p / d_{p,max}$ ). The spatial correlation of  $\hat{f}_v$  and  $\hat{d}_p$  shows a common trend for all three steady flames. Primary soot particles with diameters less than half of the maximum value ( $\hat{d}_p < 0.5$ ) can be found in regions of relatively low soot concentration ( $\hat{f}_v < 0.4$ ). In contrast, larger primary soot particles ( $\hat{d}_p \geq 0.5$ ) are commonly found in regions of a broader range of soot concentrations ( $0.4 \leq \hat{f}_v \leq 1.0$ ). Furthermore, it can be seen that the soot field is constrained in a relatively narrow temperature range,  $1500 < T_g < 2000 \text{ K}$ , which is consistent with previous studies [41, 42]. However, the distribution of large soot particle is skewed toward the high-temperature region, while a low-density region is found at  $T \sim 1750 \text{ K}$  which as can be seen from Figs. 6.5 and 6.6.

Figure 6.7 presents the spatial correlation between  $\hat{f}_v$  and  $\hat{d}_p$ . The  $\hat{f}_v$ - $\hat{d}_p$  correlation can be described using an exponential relation (shown with black solid line), with an uncertainty of  $\pm 9\%$  (confidence bounds of 99%), as follows:

$$\hat{f}_v = a \cdot e^{n \cdot \hat{d}_p} \quad (6.3)$$

where  $a$  is the  $\hat{d}_p$ -intercept and  $n$  is the growing coefficient, both are dependent on the flame, as shown in the figure. The growing coefficient,  $n$ , appears to decrease

with the increased burner diameter. In addition, while the trends are similar for the three flames, some significant differences can also be seen, with S-3 having the greatest population of large particles, for example.



**Figure 6.3** Soot volume fractions along the centreline as a function of residence time. Filled markers represent the temperatures and diameters of primary particle corresponding to the maximum soot volume fraction.

[This page is intentionally left blank]



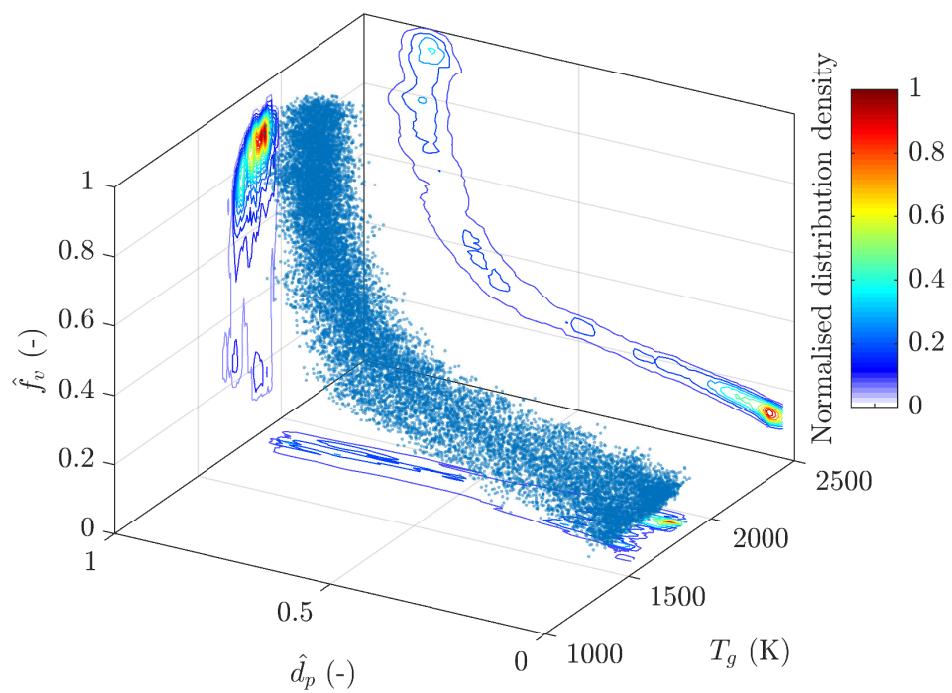


**Figure 6.4** Interdependence of the normalised soot volume fraction,  $\hat{f}_v$  and primary particle diameter,  $\hat{d}_p$ , and the temperature,  $T_g$ , for the steady laminar flame S-1 ( $D = 4.0$  mm).

[This page is intentionally left blank]

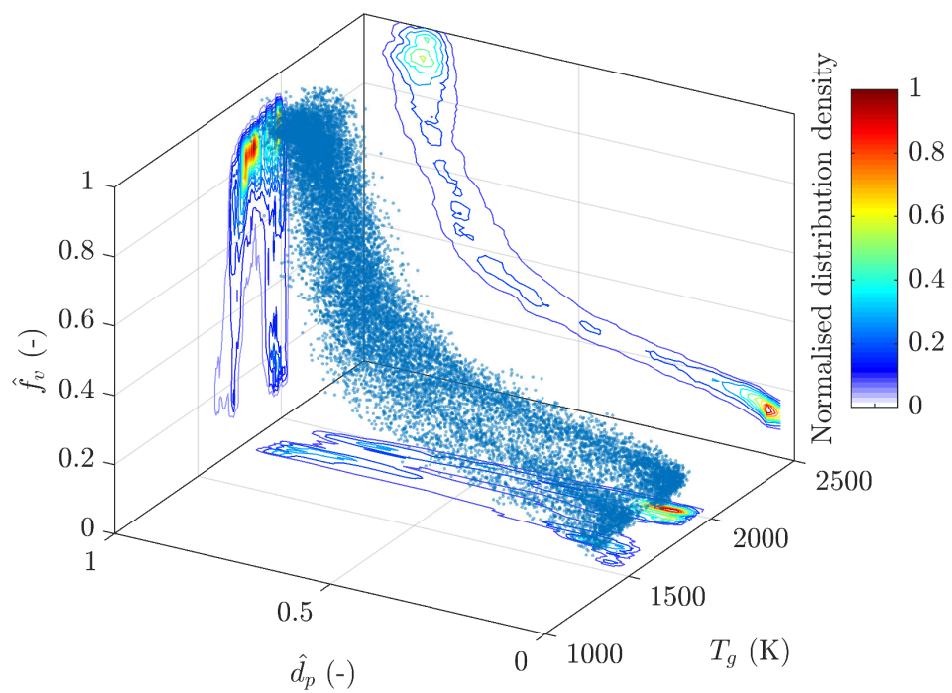


**Figure 6.5** Interdependence of the normalised soot volume fraction,  $\hat{f}_v$  and primary particle diameter,  $\hat{d}_p$ , and the temperature,  $T_g$ , for the steady laminar flame S-2 ( $D = 5.6$  mm).

[This page is intentionally left blank]

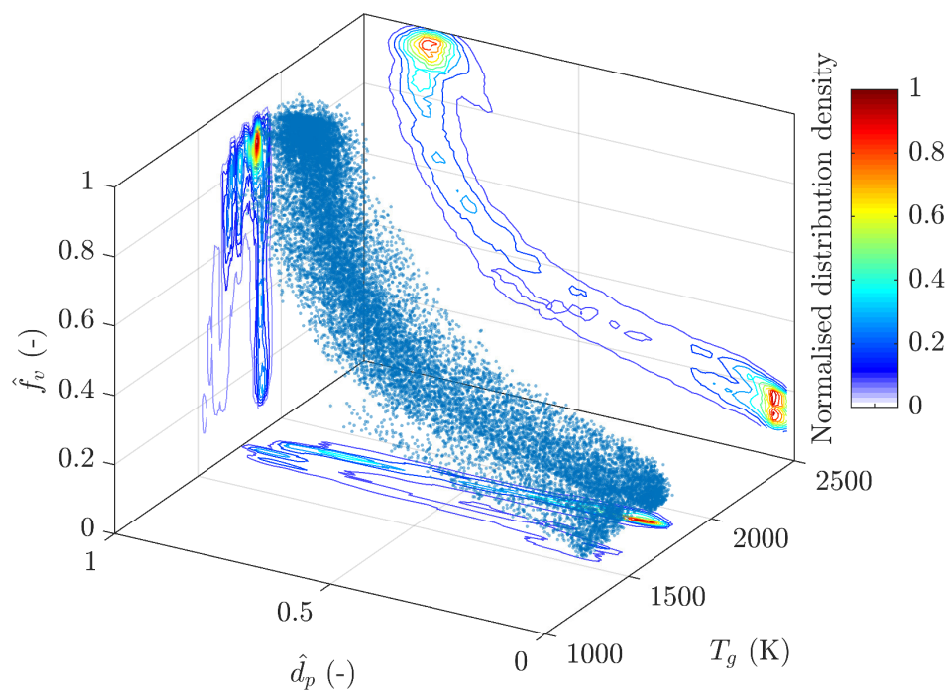


**Figure 6.6** Interdependence of the normalised soot volume fraction,  $\hat{f}_v$  and primary particle diameter,  $\hat{d}_p$ , and the temperature,  $T_g$ , for the steady laminar flame S-3 ( $D = 8.0$  mm).

[This page is intentionally left blank]

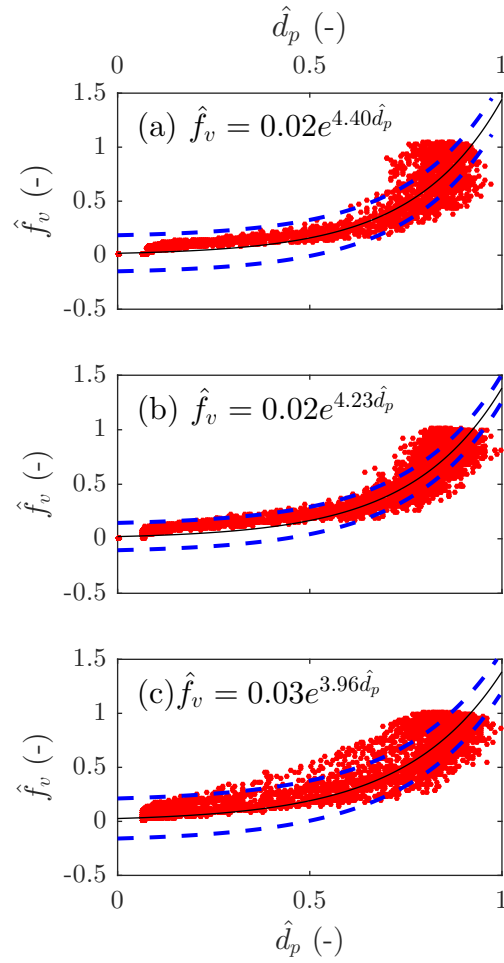


**Figure 6.7** Bivariate correlation between the normalise soot volume fraction,  $\hat{f}_v$  and primary particle diameter,  $\hat{d}_p$  for the three steady flames (a) S-1 ( $D = 4.0$  mm), (b) S-2 ( $D = 5.6$  mm) and (c) S-3 ( $D = 8.0$  mm). The black solid line corresponds to an exponential function fitted from experimental data,  $\hat{f}_v = a \cdot e^{n \cdot \hat{d}_p}$ , while the blue dashed lines represent the 99% confidence bounds.

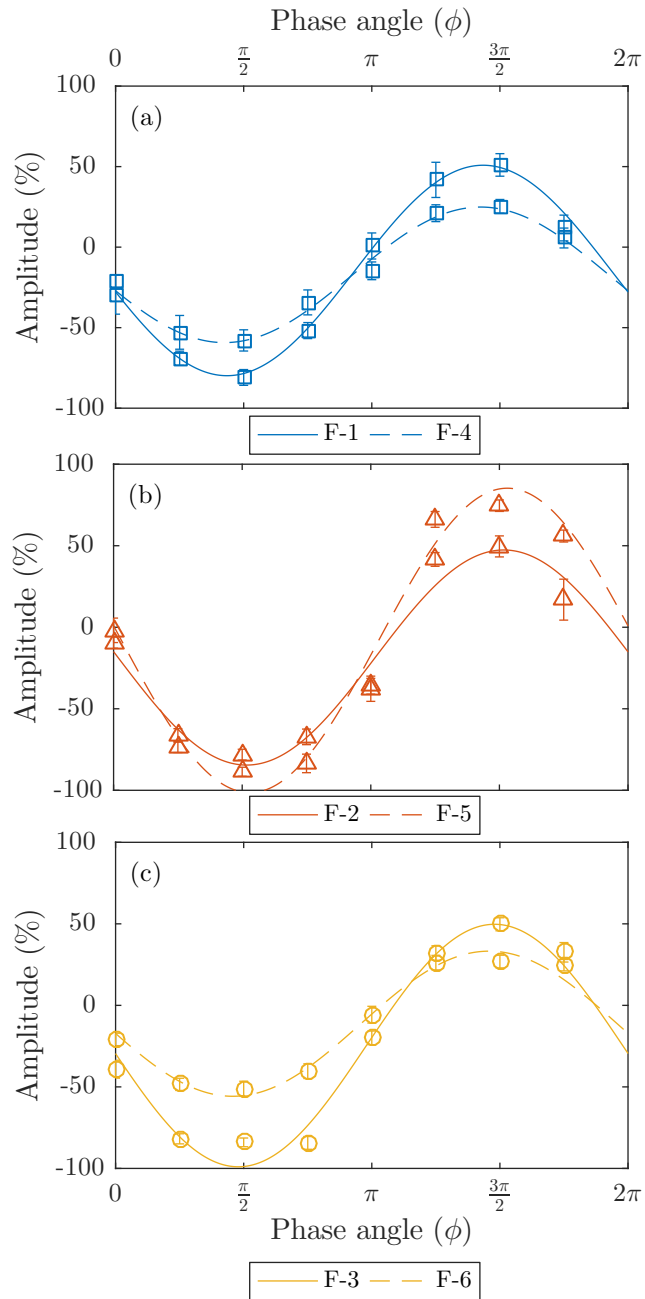
### 6.3.2 Forced flames

Figure 6.8 presents the evolution of the centreline velocity measured with PIV as a function of phase angle. The modulation of the fuel flow is characterised by the amplitude of the time-dependent centreline velocity at an axial height,  $x = 0.5$  mm, under non-reacting condition. While all the speaker driving signals are sinusoidal, the flow response is not perfectly sinusoidal, indicating the non-linear relationship between the modulation of the fuel flow and the electrical signal input. Hence, in the current study, the forcing amplitudes are defined using PIV measurements, rather than peak-to-peak voltages.

Two different forcing amplitude were applied to each forced flame: 25% and 50% for the (a) 4.0- and (c) 8.0-mm-diameter burners, while 50% and 75% for the (b) 5.6-mm-diameter burner. The flame with 4.0-mm-diameter could not be forced by a forcing amplitude larger than 50% as it led to blow-off. Furthermore, the magnitudes of the positive and negative phases of the oscillation are asymmetric. As a result, a forcing amplitude larger than 50% is also unsuitable for the forced flames with 8.0-mm-diameter burner since it can lead to a negative flow during part of the cycle, which is undesired.

Figure 6.9, 6.10 and 6.11 presents the isopleths for constant residence time at 12.5 ms intervals for 4-, 5.6- and 8.0-mm-diameter burners, respectively, superimposed on  $f_v$ , together with  $d_p$ . The images of  $d_p$  are presented on the left hand side (LHS) of each image, while  $f_v$  is on the right hand side (RHS). Also shown are the contours of OH-PLIF for the forced flames. The precision of the residence time measurement is affected by the uncertainty of the velocity measurements and the relatively large time intervals between the phase-resolved measurements. Nevertheless, it does provide a direct measurement of the evolution of soot tracers through the flame. The isopleths of constant residence time first reach the soot fields in the wings at between  $\tau = 12.5$  and 25 ms, which explains why the soot volume fraction peaks in the annular regions for all of the forced flames. The width of the soot field and the volume of the detached flames both increase as the forcing amplitude is increased. For forced flames with 4-mm-diameter burner, a void present in the soot field of the detached flamelet both pre- and post-detachment at  $\tau = 50$  and 62.5 ms when the forcing amplitude is approximately 50%. At a lower forcing amplitude,  $\alpha = 25\%$ , the flame stem closes in at a later phase which results in sufficient residence time for all of the fuel along the axis to be converted to soot. A similar trend can be seen in forced flames with 8-mm-diameter burner, probably due to the low jet velocity: both flames have sufficiently long residence time and temperature to convert some of the fuel to soot through the history of the detached flamelet. Once the constant residence time lines reach the OH layer, the soot oxidation process dominates, which is consistent with the measured consumption of the soot fields for times greater than  $\tau = 50$  to 62.5 ms (as later shown in Fig. 6.12).





**Figure 6.8** Amplitudes of the centreline velocity,  $\alpha = (U_{c,forced} - U_{c,steady})/U_{c,steady}$ , measured with PIV technique under cold-flow condition at  $x = 0.5$  mm as a function of phase angle,  $\phi$ , for (a) 4.0-mm-diameter-burner, (b) 5.6-mm-diameter-burner and (c) 8.0-mm-diameter-burner.

[This page is intentionally left blank]

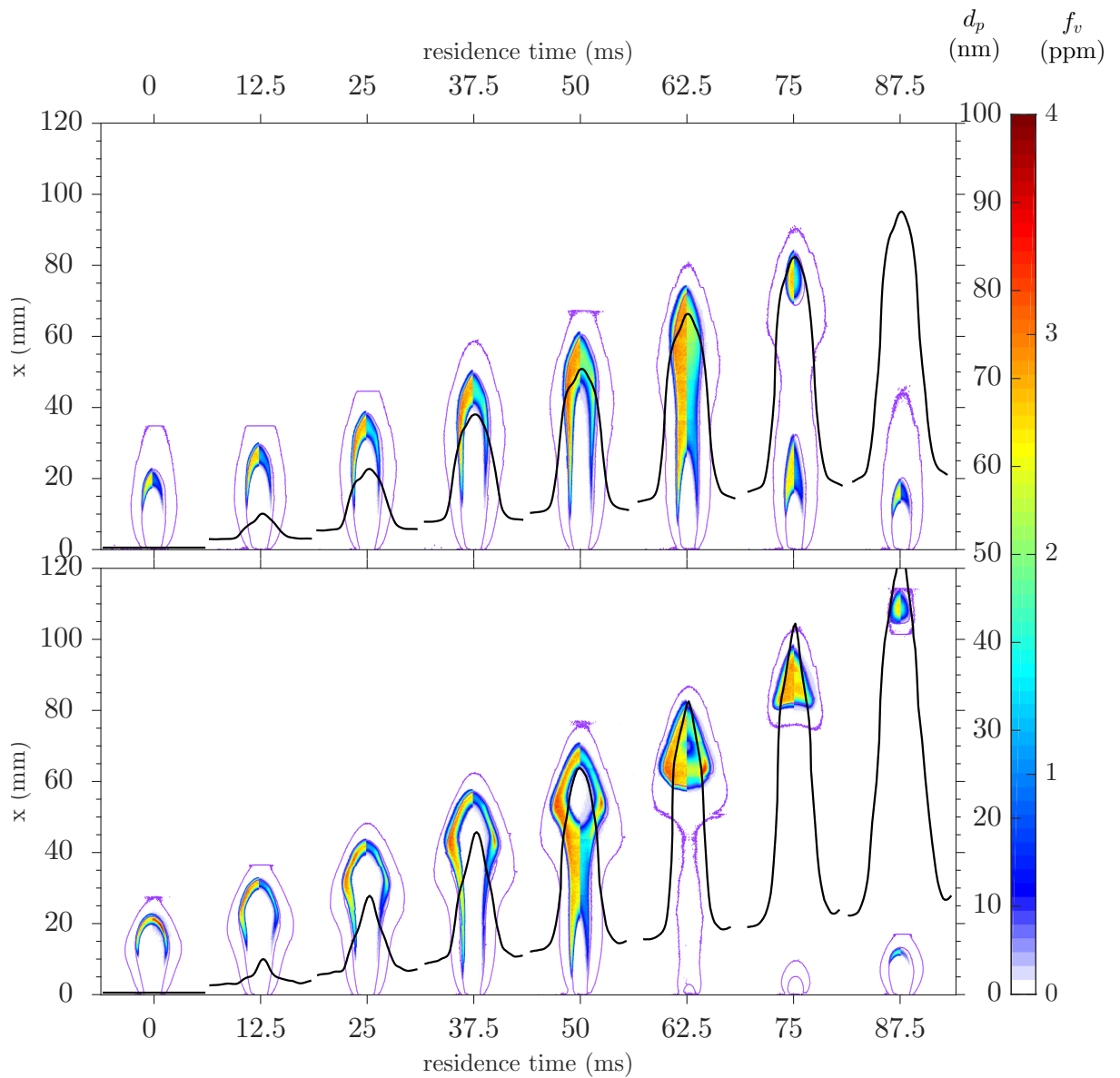


**Figure 6.9** Level of residence times superimposed on planar measurements of diameter of primary particle (LHS) and soot volume fraction (RHS) for the laminar flames with a 4.0-mm-diameter burner, F-4 and F-1, forced at  $\alpha = 25$  and 50%, respectively. For reference, the location of the OH-PLIF is plotted in purple.

[This page is intentionally left blank]

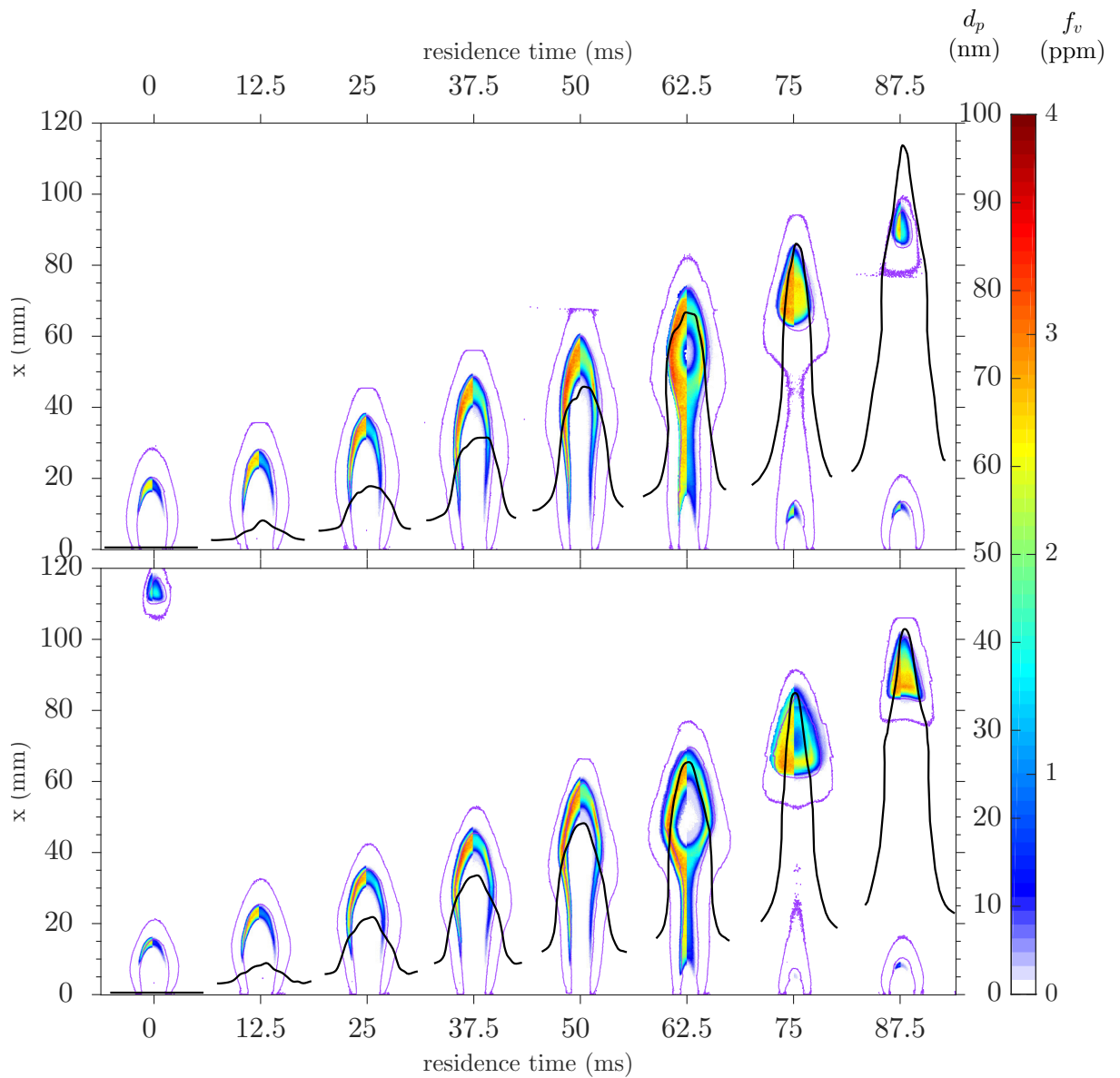


**Figure 6.10** Level of residence times superimposed on planar measurements of diameter of primary particle (LHS) and soot volume fraction (RHS) for the laminar flames with a 5.6-mm-diameter burner, F-2 and F-5, forced at  $\alpha = 50$  and 75%, respectively. For reference, the location of the OH-PLIF is plotted in purple.

[This page is intentionally left blank]

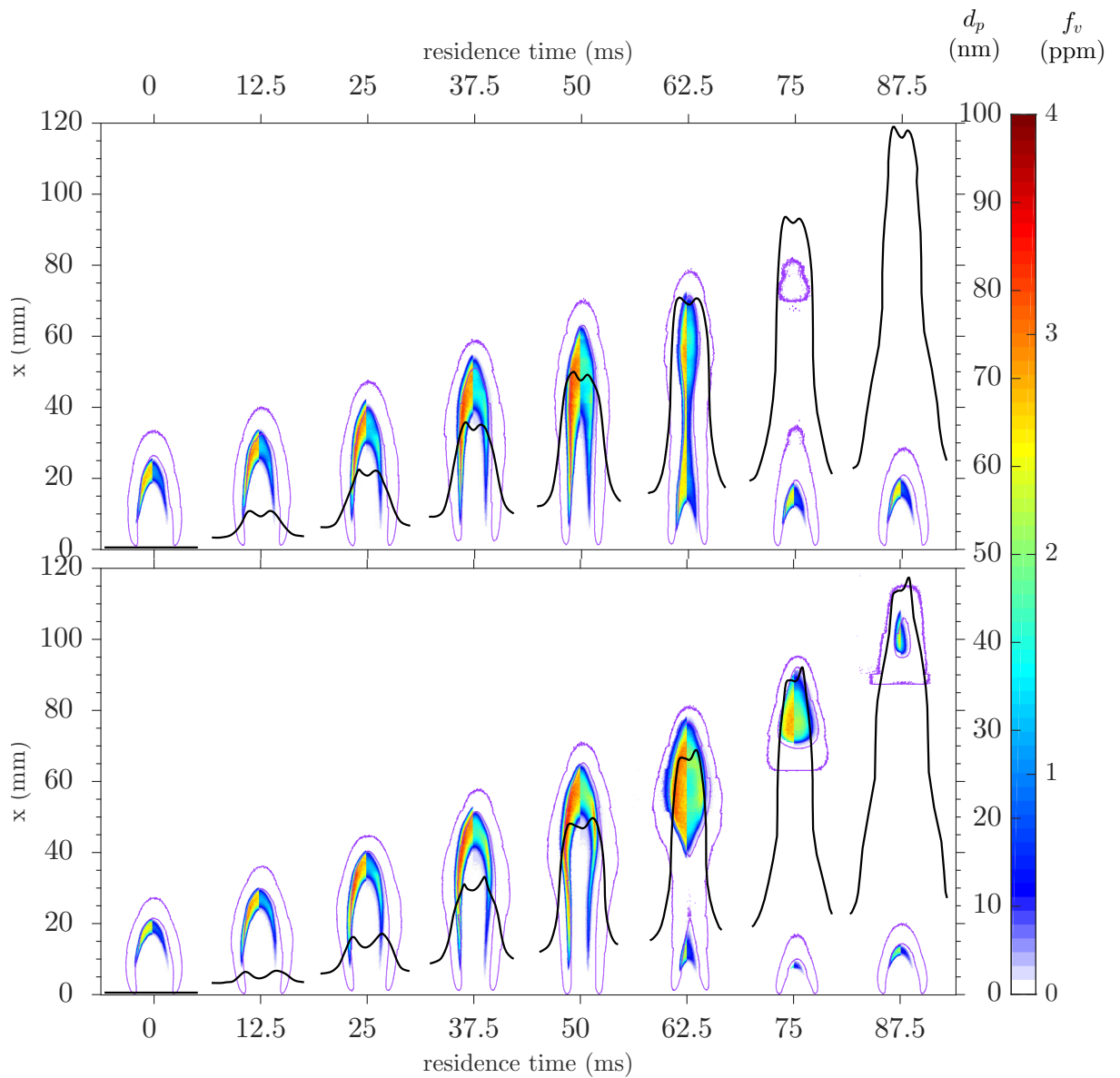


**Figure 6.11** Level of residence times superimposed on planar measurements of diameter of primary particle (LHS) and soot volume fraction (RHS) for the laminar flames with an 8.0-mm-diameter burner, F-6 and F-3, forced at  $\alpha = 25$  and 50%, respectively. For reference, the location of the OH-PLIF is plotted in purple.

Figure 6.12 presents a plot of the integrated soot volume fraction,

$$f_{v,int} = 2\pi \int_0^{x_{max}} \int_0^{r_{max}} f_v(r, x) \cdot r \cdot dr \cdot dx \quad (6.4)$$

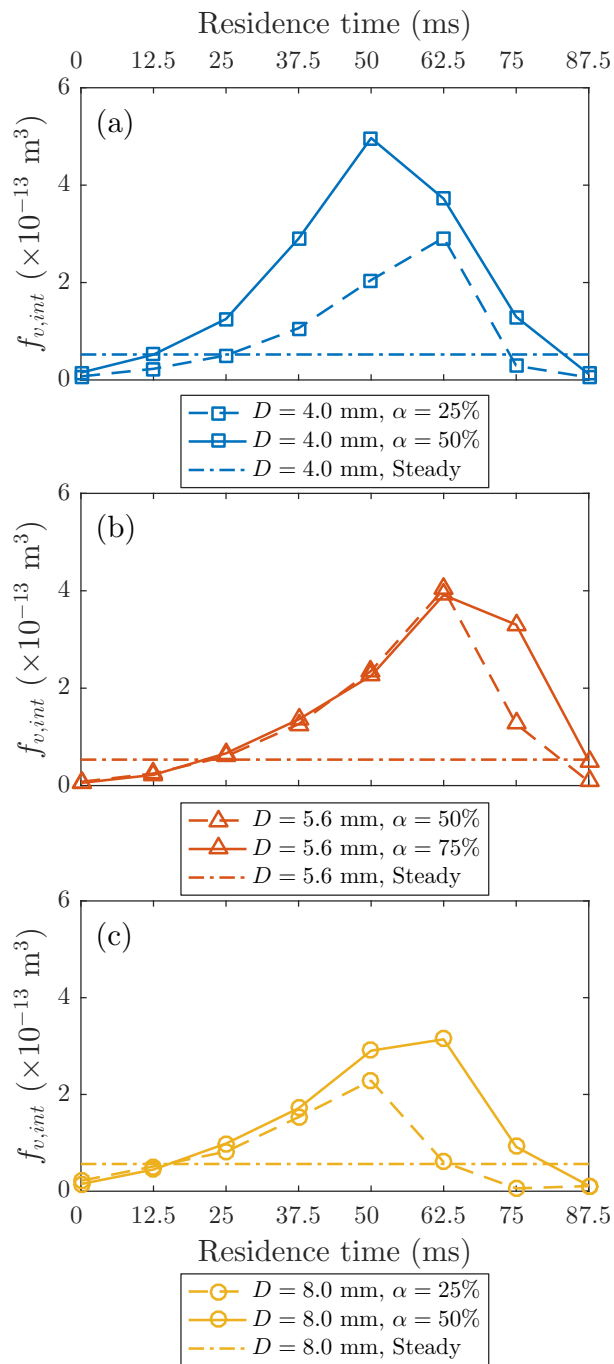
as a function of residence time for each forced flame. For the 4.0- and 8.0-mm-diameter burners, an increase in the forcing amplitude from  $\alpha = 25\%$  to  $50\%$  causes a corresponding increase in the maximum  $f_{v,int}$  from  $2.92 \times 10^{-13}$  to  $4.97 \times 10^{-13} \text{ m}^3$  and  $2.29 \times 10^{-13}$  to  $3.14 \times 10^{-13} \text{ m}^3$ , respectively. In contrast, for the 5.6-mm-diameter burner, the maximum  $f_{v,int}$  and even its evolution do not differ much with the change in forcing amplitude, except during the declining periods ( $\tau = 75$  to  $87.5$  ms). This can help to explain the apparent contradiction in earlier investigations. While Shaddix and Smyth [11] concluded that the forcing intensity has no significant effect on  $f_{v,int}$ , Connelly [19] reported that the soot production increases as the forcing intensity is increased from 20 to 50%. Together, the previous and present results suggest that there is a limit to the extent to which the amplitude of forcing a laminar steady non-premixed flame enhances the soot production. The present results show that the differences correlate with the variation in the residence time at the tip of the flame. However, the details of the physics that cause these differences are difficult to decouple and requires further investigation.

Table 6.2 summarises the peak soot volume fraction, maximum volume-integrated soot volume fraction and largest primary particle diameter for each of the flames. It is interesting to note that for the 5.6-mm-diameter burner, forced flame F-5 ( $\alpha = 75\%$ ) has a lower peak  $f_v$  and maximum  $f_{v,int}$ , relative to F-2 ( $\alpha = 50\%$ ). This is consistent with Shaddix and Smyth [11], where a strongly flickering ethylene flame exhibited lower peak  $f_v$  and  $f_{v,int}$  than its moderately flickering counterpart.

**Table 6.2** Soot measurements in steady and forced flames of different burners at various forcing amplitudes

Cases	$D$ (mm)	$\alpha$ (-)	Peak $f_v$ (ppm)	Maximum $f_{v,int}$ ( $\times 10^{-13} \text{ m}^3$ )	Largest $d_p$ (nm)
S-1	4.0	-	1.60	0.52	78
S-2	5.6	-	1.43	0.53	78
S-3	8.0	-	1.40	0.56	78
F-1	4.0	50%	3.48	4.97	83
F-2	5.6	50%	3.22	4.03	84
F-3	8.0	50%	3.24	3.14	86
F-4	4.0	25%	2.65	2.92	80
F-5	5.6	75%	3.15	3.91	83
F-6	8.0	25%	2.33	2.29	84





**Figure 6.12** Volume-integrated soot volume fraction as a function of residence time measured for all six forced flames at various forcing amplitudes.

Figure 6.13 compares the forced flames F-2 and F-5 ( $D = 5.6$  mm), for  $\tau = 62.5$  ms. The velocity fields are Galilean-transformed relative to the mean flow ( $u_r^* = u_r - \bar{u}_r$  and  $u_x^* = u_x - \bar{u}_x$ ) to reveal the vortical structure in the co-flow region. The resultant streamlines are superimposed on the soot volume fraction profiles to visualise the location of the vortex relative to the soot field. For clarity, only the streamlines in the co-flow are shown. For each forced flame, three transects normal to the soot sheet are presented on the right side of each image, together with the corresponding measurements of soot concentration, primary particle diameter, temperature and OH intensity along these transects. The measurements of  $d_p$  and  $f_v$  normalised by the peak values that are listed in Table 6.2, while the temperature is normalised by the adiabatic flame temperature,  $T_{ad} = 2280$  K, calculated using CHEMKIN code with GRI-Mech 3.0 kinetic mechanisms [43]. The intensity of OH-PLIF is normalised by its local maximum count and because it serves as a qualitative marker of the reaction zone, its location is more important than its intensity.

For the forced flame F-5, a higher forcing amplitude ( $\alpha = 75\%$ ) creates a larger toroidal vortex in the co-flow, than that of flame F-2 with a lower forcing amplitude ( $\alpha = 50\%$ ). Consequently, the larger vortex results in a greater distortion of the shape of the flame, resulting in a more obvious bulge at the position where the soot volume fraction peaks. This lateral expansion also translates into a shorter soot field than flame F-2. Although the soot field structures are quite different, the peak soot volume fractions are comparable. Temperatures across the soot sheet are relatively uniform, however. Nevertheless, there is a subtle decrease near to the fuel-rich region (centreline). The peak in the temperature profile is found in between the peaks of soot volume fraction (fuel-rich side) and OH-PLIF (fuel-lean side), consistent with expectation from the structure of a laminar steady non-premixed flame [44].

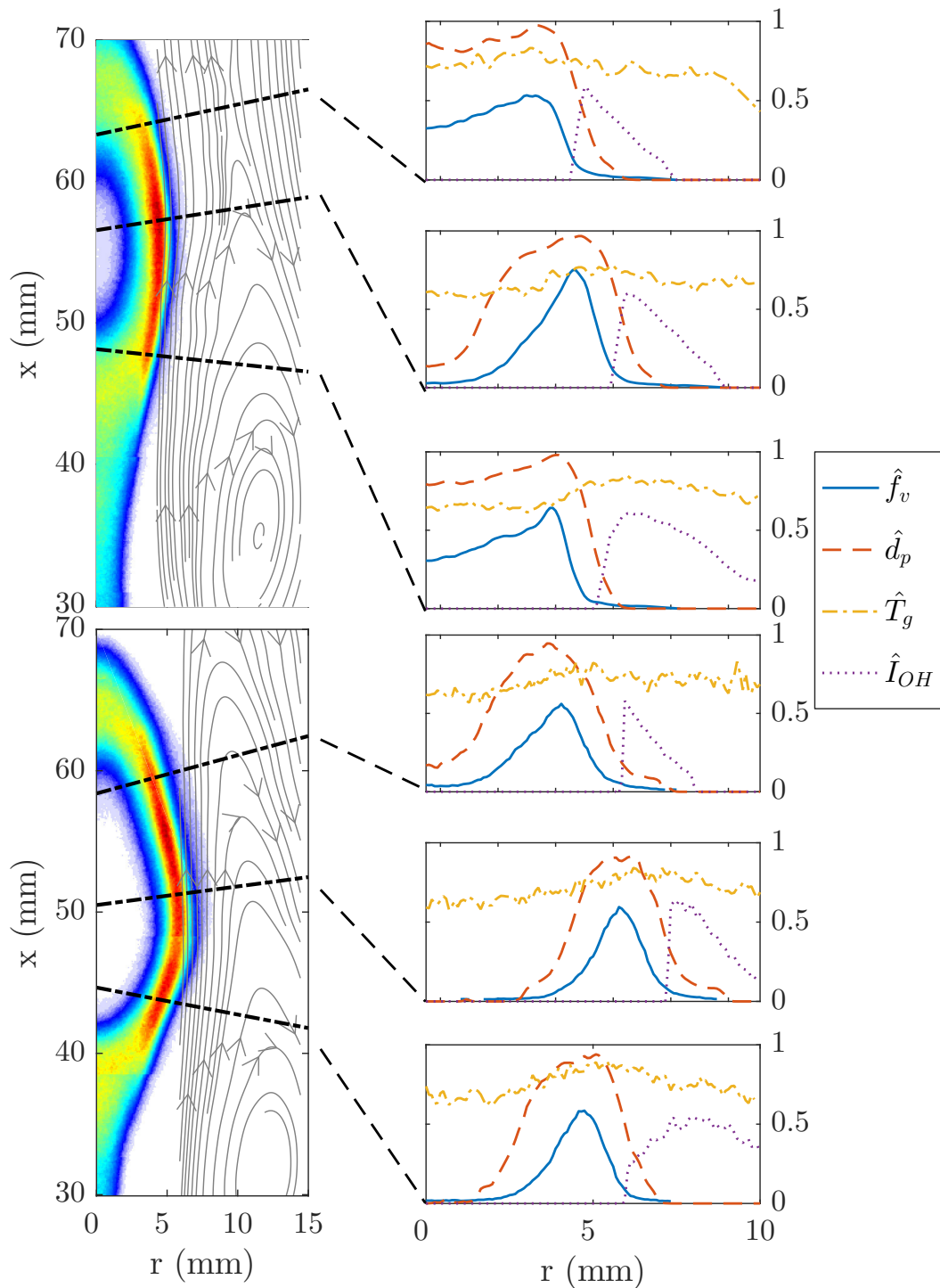


**Figure 6.13** Galilean-transformed streamlines relative to the mean flow, superimposed on the soot volume fraction profiles for forced flames F-2 and F-5 ( $D = 5.6$  mm), at  $\alpha = 50\%$  (upper) and  $75\%$  (lower) while both at  $\tau = 62.5$  ms. Only the streamlines in the co-flow region are shown for clarity. Three arbitrary lines normal to the soot sheet are selected for each flame. Normalised quantities (soot volume fraction,  $\hat{f}_v$ , diameter of primary particle,  $\hat{d}_p$ , temperature,  $T_g$ , and OH intensity,  $\hat{I}_{OH}$ ) are plotted along the normal transects.

Figures 6.14 and 6.15 present the interdependence of  $\hat{f}_v$ ,  $\hat{d}_p$  and  $T_g$  for the forced flames F-2 and F-5, respectively, at  $\tau = 62.5$  ms. Both flames have distributions of high soot concentrations spread across a wider range of temperatures, 1400–2100 K, compared with the steady cases. However, F-2 has a higher population of larger soot particles in the low-temperature region, whereas F-5 has more large soot particles distributed in the low-temperature region and more smaller soot particles in the high-temperature region.

Referring back to Fig 6.7, the relationship between  $\hat{d}_p$ – $\hat{f}_v$  can also be expressed as  $\hat{f}_v = a \cdot e^{n \cdot \hat{d}_p}$ . There is a trend where  $a$  increases with the increased burner diameter. Furthermore, the growing coefficient,  $n$ , appears to decrease with an increased forcing amplitude, except for the forced flame F-4 ( $D = 4.0$  mm;  $\alpha = 25\%$ ) which  $n = 3.94$  is lower than that of F-1 ( $D = 4.0$  mm;  $\alpha = 50\%$ ),  $n = 4.05$ . It requires further investigation to explain the trend and the outlier. Nevertheless, it is clear that the trends in spatial correlations found in steady laminar flames can be extended to time-varying forced laminar flames.

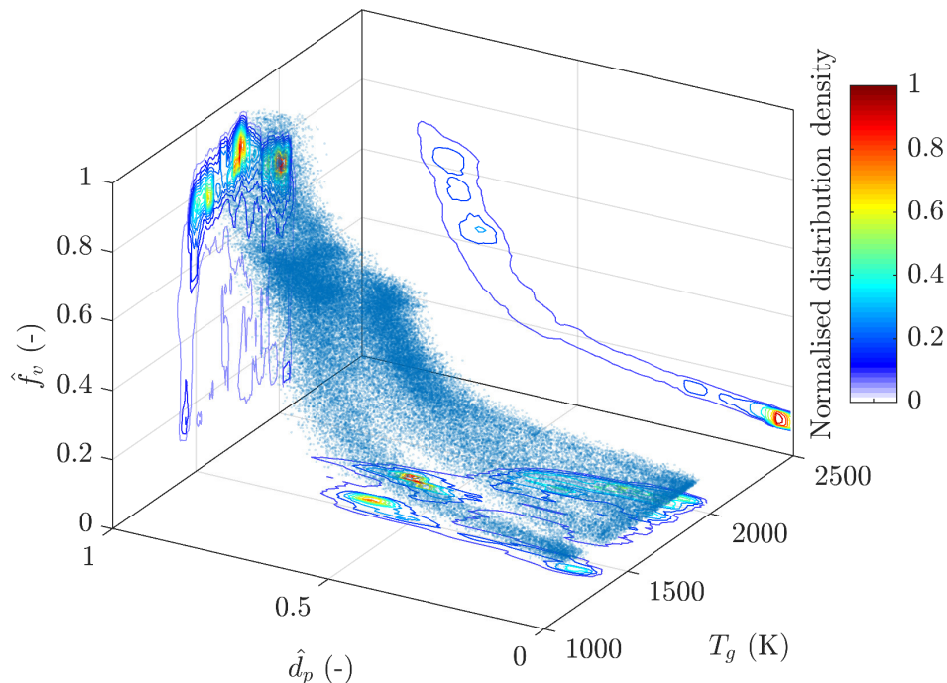


**Figure 6.14** Interdependence of the normalised soot volume fraction,  $\hat{f}_v$  and primary particle diameter,  $\hat{d}_p$ , and the temperature,  $T_g$ , for the forced flame F-2 ( $D = 5.6$  mm,  $\alpha = 50\%$ ) at  $\tau = 62.5$  ms.

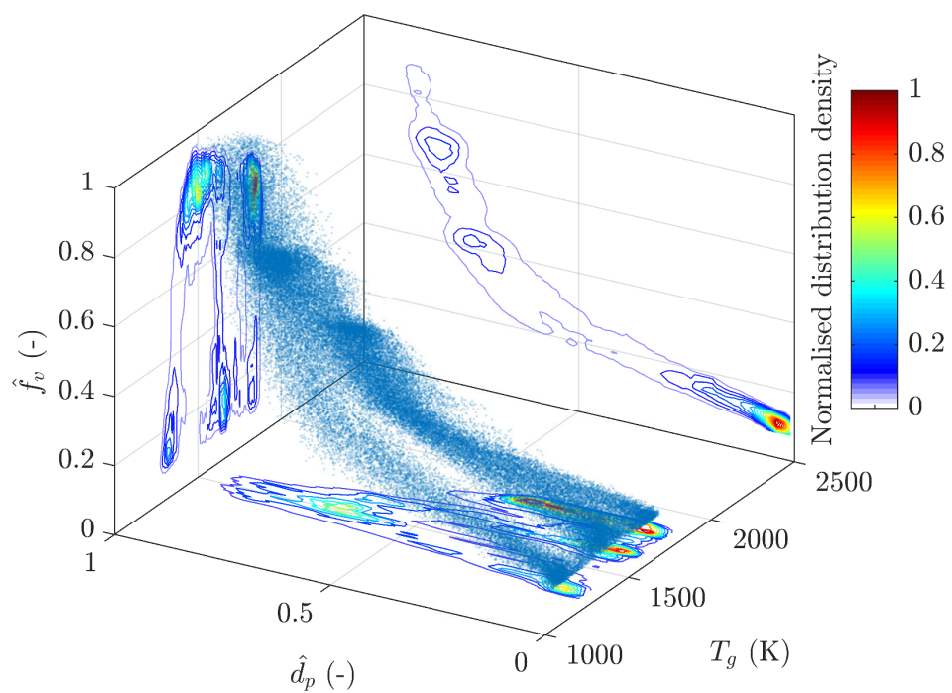


**Figure 6.15** Interdependence of the normalised soot volume fraction,  $\hat{f}_v$  and primary particle diameter,  $\hat{d}_p$ , and the temperature,  $T_g$ , for the forced flame F-5 ( $D = 5.6$  mm,  $\alpha = 75\%$ ) at  $\tau = 62.5$  ms.

[This page is intentionally left blank]

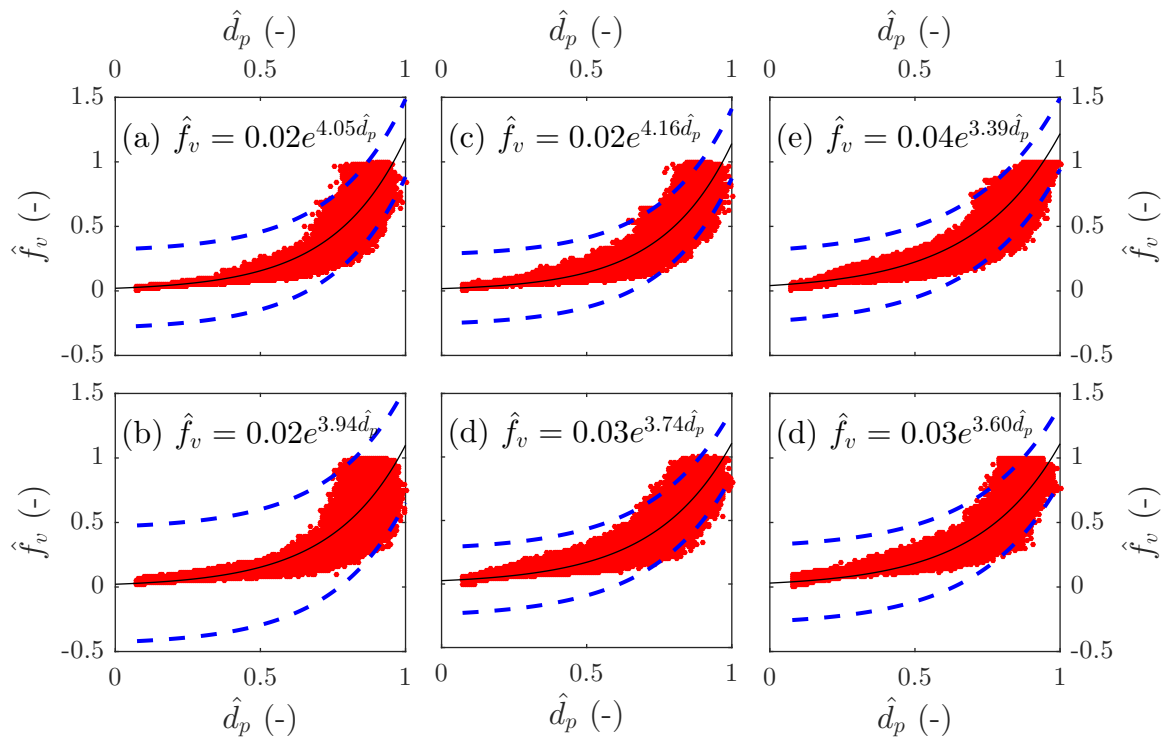


**Figure 6.16** Bivariate correlation between normalised soot volume fraction and primary particle for six of the forced flames (a) F-1 ( $D = 4.0$  mm;  $\alpha = 50\%$ ), (b) F-4 ( $D = 4.0$  mm;  $\alpha = 25\%$ ), (c) F-2 ( $D = 5.6$  mm;  $\alpha = 50\%$ ), (d) F-5 ( $D = 5.6$  mm;  $\alpha = 75\%$ ), (e) F-3 ( $D = 8.0$  mm;  $\alpha = 50\%$ ) and (f) F-6 ( $D = 8.0$  mm;  $\alpha = 25\%$ ). The phase chosen is  $\tau = 62.5$  ms. The black solid line corresponds to an exponential function fitted from experimental data,  $\hat{f}_v = a \cdot e^{n \cdot \hat{d}_p}$ , while the blue dashed lines represent the 99% confidence bounds.

## 6.4 Conclusions

In summary, new details regarding the non-linear relationships between the forcing conditions and the parameters controlling the soot evolution have been revealed. Increasing the forcing amplitude from low to moderate intensities (from  $\alpha = 25\%$  to  $50\%$ ), the maximum volume-integrated soot volume fraction is increased by  $50\%$  for the 4.0- and 8.0-mm-diameter burners. For the 5.6-mm-diameter burner, a further increase of the forcing amplitude (from  $\alpha = 50\%$  to  $75\%$ ), however, does not increase the soot production significantly. These findings explain the seeming contradiction found in the literature.

The residence time analysis shows that soot particles form early in the annular region of the flame, typically between  $\tau = 12.5$  to  $25$  ms, which leads to soot volume fraction peaks at the wings of the flame between  $\tau = 37.5$  to  $62.5$  ms. In addition, the soot oxidation process dominates for  $\tau \geq 50$  ms. It appears that forcing at a lower amplitude (for the 4.0-mm-diameter burner) or low jet velocity (for the 8.0-mm-diameter burner), the flames have sufficiently long residence time and temperature to convert some of the fuel to soot throughout the history of the detached flamelet, resulting in a relatively low volume-integrated soot volume fraction.

Comparing the spatial correlation between the soot volume fraction, primary particle size and temperature for steady and forced flames reveals a strong exponential correlation between soot concentration and particle diameter. However, even though the soot field is confined to a narrow temperature range,  $1400$ – $2100$  K, the correlation between temperature and soot distribution is rather weak. This is because the temperature gradients through the reaction zone are gradual, but does not suggest that temperature is not important. In addition, the  $\hat{d}_p$ – $\hat{f}_v$  correlation appears to vary with the variations in the burner geometry and forcing conditions. However, the correlations found in steady flames can be extended into time-varying, vortex-influenced flames.

## Acknowledgements

The authors gratefully acknowledge the University of Adelaide and the financial support of the Australian Research Council (ARC Discovery grant DP130100198). The authors also thank Dr Timothy Lau and Dr Michael Evans for their help in the PIV experiments.



---

## References

- [1] D. Dockery, C. Pope, X. Xu, J. Spengler, J. Ware, M. Fay, B. F. Jr., and F. Speizer, “An association between air pollution and mortality in six U.S. cities”, *The New England Journal of Medicine* **329** (1993), pp. 1753–1759.
- [2] D. Dockery, “Epidemiologic evidence of cardiovascular effects of particulate air pollution”, *Environmental Health Perspectives* **109** (2001).
- [3] A. J. Cohen, H. R. Anderson, B. Ostro, K. D. Pandey, M. Krzyzanowski, N. Künzli, K. Gutschmidt, A. Pope, I. Romieu, J. M. Samet, and K. Smith, “The Global Burden of Disease Due to Outdoor Air Pollution”, *Journal of Toxicology and Environmental Health, Part A* **68** (2005), pp. 1301–1307.
- [4] F. Caiazzo, A. Ashok, I. A. Waitz, S. H. Yim, and S. R. Barrett, “Air pollution and early deaths in the United States. Part I: Quantifying the impact of major sectors in 2005”, *Atmospheric Environment* **79** (2013), pp. 198–208.
- [5] T. C. Bond et al., “Bounding the role of black carbon in the climate system: A scientific assessment”, *Journal of Geophysical Research: Atmospheres* **118**.11 (2013), pp. 5380–5552.
- [6] D. Shindell, J. C. I. Kuylenstierna, E. Vignati, R. van Dingenen, M. Amann, Z. Klimont, S. C. Anenberg, N. Muller, G. Janssens-Maenhout, F. Raes, J. Schwartz, G. Faluvegi, L. Pozzoli, K. Kupiainen, L. Höglund-Isaksson, L. Emberson, D. Streets, V. Ramanathan, K. Hicks, N. T. K. Oanh, G. Milly, M. Williams, V. Demkine, and D. Fowler, “Simultaneously Mitigating Near-Term Climate Change and Improving Human Health and Food Security”, *Science* **335**.6065 (2012), pp. 183–189, DOI: 10.1126/science.1210026.
- [7] Z. A. Mansurov, “Soot formation in combustion processes (review)”, *Combustion, Explosion, and Shock Waves* **41** (2005), pp. 727–744.
- [8] H. Omidvarborna, A. Kumar, and D.-S. Kim, “Recent studies on soot modeling for diesel combustion”, *Renewable and Sustainable Energy Reviews* **48** (2015), pp. 635–647.
- [9] G. S. Lewis, B. J. Cantwell, U. Vandsburger, and C. T. Bowman, “An investigation of the structure of a laminar non-premixed flame in an unsteady vortical flow”, *Proceedings of the Combustion Institute* **22** (1988), pp. 512–522.
- [10] C. R. Shaddix, J. E. Harrington, and K. C. Smyth, “Quantitative Measurements of Enhanced Soot Production in a Flickering Methane/Air Diffusion Flame”, *Combustion and Flame* **99** (1994), pp. 723–732.
- [11] C. R. Shaddix and K. C. Smyth, “Laser-Induced Incandescence Measurements of Soot Production in Steady and Flickering Methane, Propane, and Ethylene Diffusion Flames”, *Combustion and Flame* **107** (1996), pp. 418–452.
- [12] J. Zhang and C. M. Megaridis, “Soot microstructure in steady and flickering laminar methane/air diffusion flames”, *Combustion and Flame* **112** (1998), pp. 473–484.

## REFERENCES

---

- [13] R. K. Mohammed, M. A. Tanoff, M. D. Smooke, A. M. Schaffer, and M. B. Long, “Computational and experimental study of a forced, time-varying, axisymmetric, laminar diffusion flame”, *Proceedings of the Combustion Institute* **27** (1998), pp. 693–702.
- [14] R. Chrystie and S. H. Chung, “Response to acoustic forcing of laminar coflow jet diffusion flames”, *Combustion Science and Technology* **186** (2014), pp. 409–420.
- [15] O. A. Ezekoye, K. M. Martin, and F. Bisetti, “Pulsed flow modulation of soot production in a laminar jet-diffusion flame”, *Proceedings of the Combustion Institute* **30** (2005), pp. 1485–1492.
- [16] C. R. Kaplan, C. R. Shaddix, and K. C. Smyth, “Computations of enhanced soot production in time-varying ethylene/air diffusion flames”, *Combustion and Flame* **106** (1996), pp. 89–115.
- [17] S. B. Dworkin, B. C. Connelly, A. M. Schaffer, B. A. V. Bennett, M. B. Long, M. D. Smooke, M. P. Puccio, B. McAndrews, and J. H. Miller, “Computational and experimental study of a forced, time-dependent, methane-air coflow diffusion flame”, *Proceedings of the Combustion Institute* **31** (2007), pp. 971–978.
- [18] S. B. Dworkin, J. A. Cooke, B. A. V. Bennett, B. C. Connelly, M. B. Long, M. D. Smooke, R. J. Hall, and M. B. Colket, “Distributed-memory parallel computation of a forced, time-dependent, sooting, ethylene/air coflow diffusion flame”, *Combustion Theory and Modelling* **13** (2009), pp. 795–822.
- [19] B. C. Connelly, “Quantitative Characterization of Steady and Time-Varying, Sooting, Laminar Diffusion Flames using Optical Techniques”, Ph.D. dissertation, Yale University, 2009.
- [20] K. K. Foo, Z. W. Sun, P. R. Medwell, Z. T. Alwahabi, G. J. Nathan, and B. B. Dally, “Influence of nozzle diameter on soot evolution in acoustically forced laminar non-premixed flames”, *Combustion and Flame* **194** (2018), pp. 376–386.
- [21] K. K. Foo, Z. W. Sun, P. R. Medwell, Z. T. Alwahabi, B. B. Dally, and G. J. Nathan, “Experimental investigation of acoustic forcing on temperature, soot volume fraction and primary particle diameter in non-premixed laminar flames”, *Combustion and Flame* **181** (2017), pp. 270–282.
- [22] Z. W. Sun, B. B. Dally, and Z. T. A. G. J. Nathan, “Effects of hydrogen and nitrogen on soot volume fraction, primary particle diameter and temperature in laminar ethylene/air diffusion flames”, *Combustion and Flame* **175** (2017), pp. 270–282.
- [23] P. R. Medwell, Q. N. Chan, B. B. Dally, S. Mahmoud, Z. T. Alwahabi, and G. J. Nathan, “Temperature measurements in turbulent non-premixed flames by two-line atomic fluorescence”, *Proceedings of the Combustion Institute* **34** (2013), pp. 3619–3627.
- [24] P. R. Medwell, A. R. Masri, P. X. Pham, B. B. Dally, and G. J. Nathan, “Temperature imaging of turbulent dilute spray flames using two line atomic fluorescence”, *Experiments in Fluids* **55** (2014), pp. 1840–1851.
- [25] P. R. Medwell, Q. N. Chan, B. B. Dally, Z. T. Alwahabi, G. F. Metha, and G. J. Nathan, “Flow seeding with elemental metal species via an optical method”, *Applied Physics B* **107** (2012), pp. 665–668.

- [26] D. H. Gu, Z. W. Sun, P. R. Medwell, Z. T. Alwahabi, B. B. Dally, and G. J. Nathan, “Mechanism for laser-induced fluorescence signal generation in a nanoparticle-seeded flow for planar flame thermometry”, *Applied Physics B* **118** (2015), pp. 209–218.
- [27] Q. N. Chan, “Development of Instantaneous Temperature Imaging in Sooty Flames”, PhD thesis, The University of Adelaide, 2011.
- [28] D. Gu, Z. Sun, B. Dally, P. Medwell, Z. Alwahabi, and G. Nathan, “Simultaneous measurements of gas temperature, soot volume fraction and primary particle diameter in a sooting lifted turbulent ethylene/air non-premixed flame”, *Combustion and Flame* **179** (2017).
- [29] C. Schulz, B. F. Kock, M. Hofmann, H. Michelsen, S. Will, B. Bougie, R. Suntz, and G. Smallwood, “Laser-induced incandescence: recent trends and current questions”, *Applied Physics B* **83** (2006), pp. 333–354.
- [30] Z. Sun, B. Dally, G. Nathan, and Z. Alwahabi, “Effects of hydrogen and nitrogen on soot volume fraction, primary particle diameter and temperature in laminar ethylene/air diffusion flames”, *Combustion and Flame* **175** (2017), pp. 270–282.
- [31] Z. W. Sun, D. H. Gu, G. J. Nathan, Z. T. Alwahabi, and B. B. Dally, “Single-shot, Time-Resolved planar Laser-induced Incandescence for soot primary particle sizing in flames”, *Proceedings of the Combustion Institute* **35** (2015), pp. 3673–3680.
- [32] R. Puri, M. Moser, R. J. Santoro, and K. C. Smyth, “Laser-induced fluorescence measurements of OH concentrations in the oxidation region of laminar hydrocarbon diffusion flames”, *Proceedings of the Combustion Institute* **24** (1992), pp. 1015–1022.
- [33] B. J. McKeon, G. Comte-Bellot, J. F. Foss, F. S. J. Westerwell, C. Tropea, J. F. Meyers, J. W. Lee, A. A. Cavone, R. Schodl, M. M. Koochesfahani, D. G. Nocera, Y. Andreopoulos, W. J. A. Dahm, J. A. Mullin, J. M. Wallace, P. V. Vukoslavčević, S. C. Morris, E. R. Pardyjak, and A. Cuerva, “Velocity, Vorticity and Mach Number”, *Springer Handbook of Experimental Fluid Mechanics*, ed. by C. Tropea, A. L. Yarin, and J. F. Foss, Springer, Heidelberg, Germany, 2007.
- [34] W. Thielicke and E. J. Stamhuis, “PIVlab - Time-resolved digital particle image velocimetry tool for MATLAB (version: 1.41)”, *J. Open Res. Softw.* **2** (2014), e30.
- [35] W. Thielicke, “The Flapping Flight of Birds - Analysis and Application”, PhD thesis, Rijksuniversiteit Groningen, 2014.
- [36] D. Garcia, “A fast all-in-one method for automated post-processing of PIV data”, *Experiments in Fluids* **50** (2011), pp. 1247–1259.
- [37] R. Santoro, T. Yeh, J. Horvath, and H. Semerjian, “The transport and growth of soot particles in laminar diffusion flames”, *Combustion Science and Technology* **53** (1987), pp. 89–115.
- [38] B. S. Haynes and H. G. Wagner, “Soot formation”, *Progress in Energy and Combustion Science* **7** (1981), pp. 229–273.
- [39] A. D’Anna, A. Rolando, C. Allouis, P. Minutolo, and A. D’Alessio, “Nano-organic carbon and soot particle measurements in a laminar ethylene diffusion flame”, *Proceedings of the Combustion Institute* **30** (2005), pp. 1449–1456.

- [40] P. H. Joo, B. Gigone, E. A. Griffin, M. Christensen, and Ö. L. Gülder, “Soot primary particle size dependence on combustion pressure in laminar ethylene diffusion flames”, *Fuel* **220** (2018), pp. 464–470.
- [41] I. Glassman, O. Nishida, and G. Sidebotham, “Critical Temperatures of Soot Formation”, *Soot Formation in Combustion: Mechanisms and Models*, ed. by H. Bockhorn, Berlin, Heidelberg: Springer Berlin Heidelberg, 1994, pp. 316–324.
- [42] R. Santoro and H. Semerjian, “Soot formation in diffusion flames: flow rate, fuel species and temperature effects”, *Proceedings of the Combustion Institute* **20** (1984), pp. 997–1006.
- [43] G. P. Smith, D. M. Golden, M. Frenklach, N. W. Moriarty, B. Eiteneer, M. Goldenberg, C. T. Bowman, R. K. Hanson, S. Song, W. C. Gardiner, V. V. Lissianski, and Z. W. Qin, 2016.
- [44] T. Cheng, C.-Y. Wu, Y.-H. L. C.-P. Chen, Y.-C. Chao, T. Yuan, and T. Leu, “Detailed measurement and assessment of laminar hydrogen jet diffusion flames”, *Combustion and Flame* **146** (2006), pp. 268–282.

## Minor amendments to Chapter 6

Figure 6.17 presents the soot volume fraction,  $f_v$ , gas temperature,  $T_g$ , and primary particle diameter,  $d_p$  as functions of dimensionless axial coordinate,  $x/x_{T,max}$ , normalised by the axial location of the maximum  $T_g$ . The quantities presented are measured at the axis for three steady flames with different nozzle diameters,  $D = 4.0, 5.6$  and  $8.0$  mm. The figure shows that, in each plot, all three curves collapse into one trend. The axial profile of  $T_g$  at the axis can be treated as the approximation of the flame length and the three laminar flames have a similar flame length. This is consistent with the fact that the length of a laminar flame is only affected by the volumetric flow rate of the fuel. Since these three laminar flames have the same fuel flow rate, it is expected that they share a similar flame length and structure, including the soot field. However, the laminar flame with the smallest diameter,  $D = 4.0$  mm, exhibits the highest peak soot concentration,  $f_{v,max} = 1.44$  ppm, followed by 1.31 and 1.28 ppm measured in the laminar flames with 5.6- and 8.0-mm-diameter-nozzle, respectively. Nevertheless, the largest primary particles measured in these three laminar flames are similar in size, approximately 78 nm.

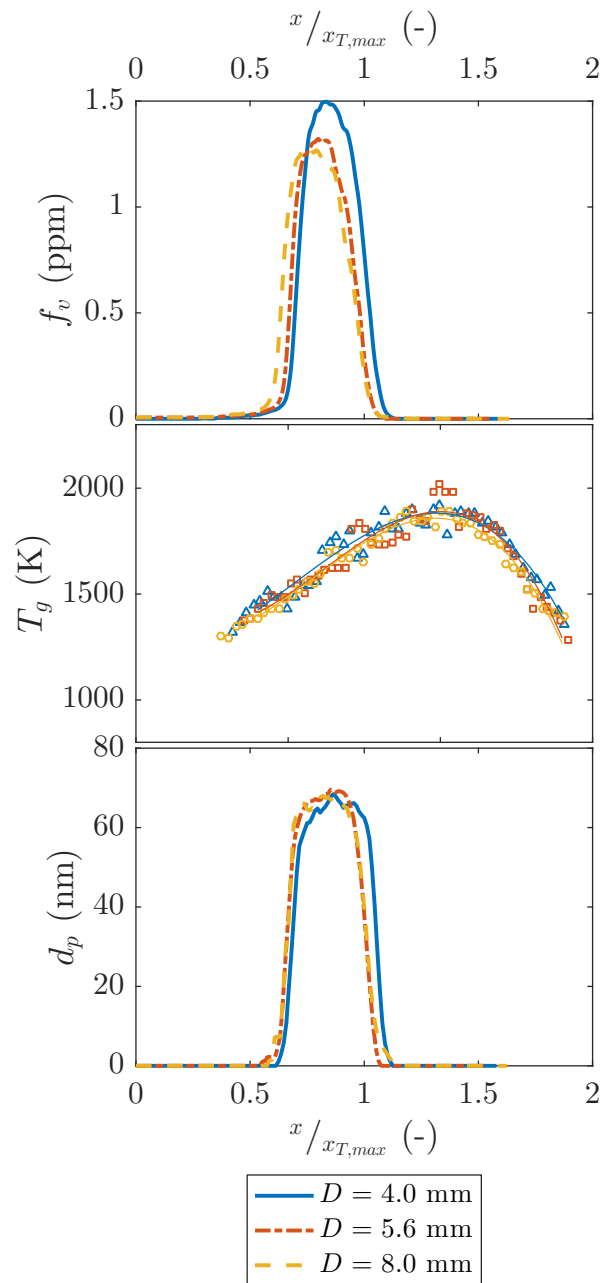


**Figure 6.17** Soot volume fraction,  $f_v$ , temperature,  $T_g$ , and primary particle diameter,  $d_p$ , are presented as functions of dimensionless axial coordinate ( $x/x_{T,max}$ , where  $x_{T,max}$  is the location of the maximum  $T_g$ ) for steady laminar flames with burner diameters,  $D = 4.0, 5.6$  and  $8.0$  mm.

[This page is intentionally left blank]

# Chapter 7

## Calculated concentration distributions and time histories of key species in an acoustically forced laminar flame

This chapter contains the submitted article:

Kae Ken Foo, Michael J. Evans, Zhiwei Sun, Paul R. Medwell, Zeyad T. Alwahabi, Graham J. Nathan and Bassam B. Dally, "Calculated radial profiles and time histories of major species on concentrations in an acoustically forced laminar flame", submitted to *Combustion and Flame* on August 21, 2018.

The content of this chapter is identical to that of the submitted manuscript, with the following exceptions:

1. The typesetting and referencing style have been altered to maintain a consistent appearance within the thesis.
2. The numbering of tables, figures and equations has been changed to include the number of the chapter.

## Statement of Authorship

Title of Paper	Calculated radial profiles and time histories of major species concentrations in an acoustically forced laminar flame
Publication Status	<input type="checkbox"/> Published <input type="checkbox"/> Accepted for Publication <input checked="" type="checkbox"/> Submitted for Publication <input type="checkbox"/> Unpublished and Unsubmitted work written in manuscript style
Publication Details	K.K. Foo, M.J. Evans, Z.W. Sun, P.R. Medwell, Z.T. Alwahabi, G.J. Nathan and B.B. Dally, "Calculated radial profiles and time histories of major species concentrations in an acoustically forced laminar flame", <i>Combustion and Flame</i> (under review).

### Principal Author

Name of Principal Author (Candidate)	Kae Ken Foo
Contribution to the Paper	I processed, analysed and interpreted all the experimental and computational data. I validated the computational results with the experimental measurements. After some discussion with the co-authors regarding my interpretation of the computational data, I wrote the manuscript.
Overall percentage (%)	55%
Certification:	This paper reports on original research I conducted during the period of my Higher Degree by Research candidature and is not subject to any obligations or contractual agreements with a third party that would constrain its inclusion in this thesis. I am the primary author of this paper.
Signature	Digitally signed by Kae Ken Foo Date: 2018.08.20 09:45:10 +09'30'

### Co-Author Contributions

By signing the Statement of Authorship, each author certifies that:

- i. the candidate's stated contribution to the publication is accurate (as detailed above);
- ii. permission is granted for the candidate to include the publication in the thesis; and
- iii. the sum of all co-author contributions is equal to 100% less the candidate's stated contribution.

Name of Co-Author	Michael J. Evans
Contribution to the Paper	This co-author designed the simulations. He helped to edit the numerical method section of the manuscript. He also assisted in the interpretation of computational data.
Signature	Digitally signed by Michael Evans Date: 2018.08.21 14:24:06 +09'30'



Name of Co-Author	Zhi Wei Sun
Contribution to the Paper	This co-author co-designed the experiments and provided aid collecting data. He helped to edit the experimental details section of the manuscript.
Signature	Digitally signed by Zhiwei Sun Date: 2018.08.21 11:01:35 +09'30'

Name of Co-Author	Paul R. Medwell
Contribution to the Paper	This co-author provided suggestions for the experimental set-up and data post-processing. He also helped evaluate and edit the manuscript.
Signature	Paul Medwell 2018.08.23 11:13:50 +09'30'

Name of Co-Author	Zeyad T. Alwahabi
Contribution to the Paper	This co-author provided suggestions for the experimental set-up. He also helped to evaluate and edit the manuscript.
Signature	Digitally signed by Zeyad Alwahabi DN: cn=Zeyad Alwahabi, o=Chem Eng, ou, email=zeyad.alwahabi@adelaide.edu.au, c=AU Date: 2018.08.21 14:06:50 +09'30'

Name of Co-Author	Graham J. Nathan
Contribution to the Paper	This co-author co-supervised the development of the work. He also helped to evaluate and edit the manuscript.
Signature	Digitally signed by Graham J Nathan Date: 2018.08.23 12:50:21 +09'30'

Name of Co-Author	Bassam B. Dally
Contribution to the Paper	This co-author co-supervised the development of the work. He also helped to evaluate and edit the manuscript.
Signature	Digitally signed by Bassam Dally Date: 2018.08.20 10:12:33 +09'30'

## Calculated concentration distributions and time histories of key species in an acoustically forced laminar flame

Kae Ken Foo, Michael J. Evans, Zhiwei Sun, Paul R. Medwell,  
Zeyad T. Alwahabi, Graham J. Nathan, Bassam B. Dally

### Abstract

A numerical study on fluid-chemical interactions in the steady and time-varying laminar non-premixed jet flames was conducted to advance the understanding of the complex interplay between the flame chemistry, fluid dynamics and soot evolution. The results show that the increased residence time in the neck-zone of the time-varying flame leads to the increase in soot production due to more prolonged ethylene pyrolysis. However, the residence time analysis indicates that fuel flow modulation has only a modest influence on early stages of flame development. Acoustic forcing significantly increases the residence time at which the concentration of acetylene is relatively high, despite the peak mole fraction of acetylene not changing much. The numerical study also finds that the “pinch-off” of the flickering tip is a result of the role of buoyancy amplifying the modulation to the fuel flow-rate to increase the consumption rate of the fuel-rich region. It is also found that the assumption that the fuel exit velocity profile oscillates sinusoidally as a parabolic profile about an average velocity, which has typically been employed previously, produces a different time-varying flame than that observed in the experiment.

## 7.1 Introduction

Vortices are of significant practical importance in most combustion devices because they influence both the flame chemistry and the mixing processes, particularly in flames containing soot. However, the interplay between vortices, flame chemistry and soot evolution in turbulent flames is challenging, both to understand and to measure because of the non-linear coupling between them and the interference of soot on most measurement techniques. One approach to advance understanding of these flames is to employ time-varying laminar flames because they reduce the complexity both of the analysis and of the measurement process. These flames generate a wider range of histories of residence time, temperature, local stoichiometry (mixture fraction) and strain rate than is found in steady laminar flames, while also allowing the acquirement of comprehensive data sets than is possible in turbulent flames because they are both highly repeatable and more readily controlled. Because of these advantages, time-varying laminar flames have been the central theme of numerous studies [1–17] in the past. Table 7.1

summarises the configuration of time-varying laminar flames and parameters that have been investigated, selecting those most relevant to the present work. This shows that forced flames tend to exhibit a higher soot production than their steady counterparts. Furthermore, the degree of enhancement in soot production is affected by the fuel type [4], the forcing frequency [15], the nozzle diameter [16] and the amplitude of the fuel flow modulation [17, 18].

Previous experimental studies have investigated the influences of forcing frequency [15], nozzle diameter [16] and amplitude of fuel flow modulation [17] on the flame shape and soot production. This has characterised and quantified the soot volume fraction and primary particle diameter using Laser-Induced Incandescence (LII) and Time-resolved LII, respectively [15–17], together with the conditional temperature profile using Non-linear excitation regime Two-Line Atomic Fluorescence (NTLAF). Foo et al. [15] reported that the extent of soot augmentation decreases as the forcing frequency is shifted away from the natural flickering frequency of the flame, in this case, it was 10 Hz. The maximum and integrated soot volume fractions measured in the 40-Hz forced flame are similar to those of the steady counterpart. Foo and co-workers [16, 17] also employed Planar Laser-Induced Fluorescence of hydroxyl radicals (OH-PLIF) to identify the location of the reaction zone. This, together with measurements of the velocity field measured with Particle Image Velocimetry (PIV) found that the nozzle diameter influences the generation of toroidal vortices which, in turn, affects the pinch-off and amount of soot production. They also showed that increasing the amplitude of fuel flow modulation from 25% to 50% enhances the soot production [17]. However, no further enhancement occurs when the amplitude is increased from 50% to 75%. Nevertheless, despite the value of these data, no measurements of mixture fraction or of the distribution of the major species are available in these flames. To meet this need, therefore, the present investigation aims to advance understanding of these parameters using numerical simulations and to gain insights into the basic physical and chemical processes.

Small laminar flames forced at 10- and 20-Hz frequencies have been found to exhibit a pinch-off at the flame tip, which is associated with the toroidal vortex enhanced by acoustic forcing [8, 16, 19]. In naturally flickering flames, this vortex is also a product of a buoyancy-induced instability [20, 21]. However, the role of buoyancy in the oscillation and pinch-off in the acoustically forced flames has yet to be assessed. Hence, a further aim of the present investigation is to assess this influence by comparing the time-varying laminar flames under normal- and zero-gravity conditions.

In light of the gaps in understanding identified above, the aim of the present investigation is to apply well-established models and chemical kinetic mechanisms from the literature to study the fluid-chemical interactions that generate the experimentally observed enhanced soot production in time-varying laminar

flames. Noteworthy is that the present work does not aim to develop or assess the soot models themselves. Instead, the focus is on the complex flow-field and chemistry interactions that change the distribution of major species, together with the shape of the flames and the vortices.

## 7.2 Methodology

### 7.2.1 Experimental

Experimental data sets from previous studies [16, 17] were selected for the validation of the numerical approach for the current study. The experimental burner consists of a 5.6-mm-inner-diameter fuel tube and it was concentrically surrounded by a 74-mm-diameter co-flow. The fuel tube was connected to a cylindrical plenum equipped with a loudspeaker to superimpose a sinusoidal pressure perturbation on the fuel stream at 10 Hz.

The fuel stream, comprised 41.7% of ethylene and 58.3% of nitrogen, by volume, has a total flow rate of 0.31 standard litre per minute (SLPM), equivalent to a bulk exit velocity of 0.21 m/s, also following Foo et al. [16, 17]. This condition avoids smoking under the acoustically forced conditions. The air co-flow was conditioned using layers of glass beads sandwiched between a pair of honeycomb to generate a uniform plug flow with a velocity of 0.23 m/s (60 SLPM). Temperatures of the fuel and co-flow streams were measured at 294 K using mass flow controllers.

Due to the nature of the NTLAF technique, the temperature measurements reported here and previously [16, 17] are both conditional. This is because the NTLAF technique has a lower temperature threshold at 800 K because of the low population density ( $\leq 3\%$ ) of thermally excited indium at this temperature [22]. Additionally, the NTLAF measurements also conditioned based on the local equivalence ratio,  $\Phi$ . In regions with  $\Phi \leq 0.8$  [23], the signal-to-noise ratio (SNR) is too low to consider the measurement trustworthy. Hence, the current work treats the maximum intensity of OH-PLIF as a surrogate for the threshold and disregards all temperature measurements on the lean side. The uncertainty for the time-averaged NTLAF measurement is about  $\pm 120$  K [16, 17]. Additionally, the uncertainty and the lower limit of detection for LII are estimated to be  $\pm 10\%$  and 0.01 ppm, where SNR is lower than 10:1, respectively [16, 17]. One of the limiting factors in performing PIV in sooting flames is that the scattering of the laser from soot particles overwhelms the Mie scattering from the seed particles [24]. As a result, velocity vectors in the regions of high soot concentration were unresolvable. Previous studies [16, 17] interpolated the unresolved PIV measurements using neighbouring vectors. However, the current work has rejected all the interpolated data to perform a more reliable model validation.

**Table 7.1** Measurements reported with different kinds of time-varying laminar flames.

Author(s)	Flame type	Measurement(s)
Smyth et al. [2]	10.13-Hz methane flame	OH distribution and soot scattering
Shaddix et al. [3]	10-Hz methane flames	Soot volume fraction, primary particle diameter and number density
Shaddix and Smyth [4]	10-Hz methane, propane and ethylene flames	Soot volume fraction, primary soot particle diameter and number density
Zhang and Megaridis [6]	10-Hz methane flame	Soot volume fraction, primary soot particle diameter, soot surface area and number density
Mohammed et al. [7]	20-Hz methane flame	Temperature, flow velocity and CH* distribution
Dworkin et al. [10]	20-Hz methane flame	Temperature, isothermal velocity profile and mole fractions of N <sub>2</sub> , CO <sub>2</sub> , CH <sub>4</sub> , H <sub>2</sub> , O <sub>2</sub> , CO and H <sub>2</sub> O
Dworkin et al. [11]	20-Hz ethylene flame	Soot volume fraction
Papadopoulos et al. [8]	10-Hz methane flames	Flow velocity
Chrystie and Chung [13]	10-Hz propane flame	Flow velocity
Joher et al. [14]	20-Hz ethylene flame	Soot volume fraction
Foo et al. [15]	20-and 40-Hz ethylene flames	Temperature, soot volume fraction and primary particle diameter
Foo et al. [16, 17]	10-Hz ethylene flames	Temperature, soot volume fraction, primary soot particle diameter, OH distribution and flow velocity
Present work	10-Hz ethylene flame	Mixture fraction, distribution of major species and the role of buoyancy

## 7.2.2 Computational

The same steady and forced laminar flames were simulated using ANSYS Fluent 17.2 [25]. Figure 7.1 presents the axisymmetric computational domain employed in the simulation, which includes the fuel plenum, a central fuel jet with a concentric co-flow and the combustion region downstream from the jet exit plane. The structured mesh comprised 26,000 nodes, which was chosen following a mesh independence study. The time-averaged bulk flow rate and fuel compositions were matched to the experimental values. The co-flow was surrounded by quiescent air, while the opening boundaries were placed sufficiently far away from the reaction zone to avoid any significant interference. The fuel inlet was specified upstream from the jet exit, at a location corresponded to the speaker in the burner body. Both fuel and co-flow streams were modelled with an initial temperature of 294 K to match the experiment.

To simulate the experimental forcing conditions, a sum of sinusoids was obtained to fit the measured data and used to specify the fuel inflow boundary condition via a user-defined function. The flow field was solved using the SIMPLEC algorithm, with second-order spatial discretisation for all variables. The transient case was solved using implicit, bounded second-order time-stepping in steps of 10  $\mu$ s starting from the steady-state case. While the experimental results were sampled at eight phases of the 10-Hz cycle, the numerical sampling rate is ten times of that in the experimental study, which is 800 Hz, equivalent to a time interval of 1.25 ms. Streams of inert tracer particles were injected at the jet exit plane to track the temporal evolution of the concentration of major species and to calculate in-flame residence times along different trajectories.

The simulation employed a skeletal mechanism with 32 species and 206 reactions [26], including limited  $C_3$  species, and an *in-situ* adaptive tabulation (ISAT) approach [27] for chemical reactions. The chemical species transport included a full multicomponent diffusion and thermal diffusivity, with the primary interest in assessing the role of soot precursors. Soot was also modelled, primarily with a view to correcting for radiation, using a method-of-moments (MOM) model based on  $C_2H_2$  as the soot precursor species and OH from the skeletal mechanism as the oxidising agent [28]. The MOM model is computationally less expensive than the Monte Carlo method and it can be solved simultaneously with the gas-phase chemistry, which is optimal for the objective of the current paper [29]. An optically thin radiation model [30] was included in simulations to account for the thermal radiation for the steady and transient case. However, the predicted soot volume fraction distribution had significant errors in both cases. Consequently, these errors lead to the over-prediction of radiative heat losses. The peak of the calculated soot volume fraction was scaled to match the experimental data to reduce the errors. The convergence criteria for all species, the momentum and continuity were set to an absolute value of  $1 \times 10^{-5}$ , with  $1 \times 10^{-6}$  for the energy and radiation. Given the following stoichiometric mixture of a hydrocarbon fuel:

$a_i C_{m_i} H_{n_i} O_{p_i} + \nu O_2$ , where  $\sum_{i=1}^N a_i = 1$ . Then, the mixture fraction,  $Z$ , is defined, following earlier work [31] as:

$$Z = \frac{\frac{Z_C - Z_{C,ox}}{a_i \cdot m_i \cdot W_C} + \frac{Z_H - Z_{H,ox}}{a_i \cdot n_i \cdot W_H} - \frac{Z_O - Z_{O,ox}}{\nu \cdot W_O}}{\frac{Z_{C,f} - Z_{C,ox}}{a_i \cdot m_i \cdot W_C} + \frac{Z_{H,f} - Z_{H,ox}}{a_i \cdot n_i \cdot W_H} - \frac{Z_{O,f} - Z_{O,ox}}{\nu \cdot W_O}}. \quad (7.1)$$

Here,  $Z_i$  is the atomic mixture fraction,  $W_i$  is the atomic weight, with  $f$  and  $ox$  denoting the fuel and oxidiser streams, respectively. For the current case, the stoichiometric mixture fraction is  $Z_{stoic} = 0.142$ .

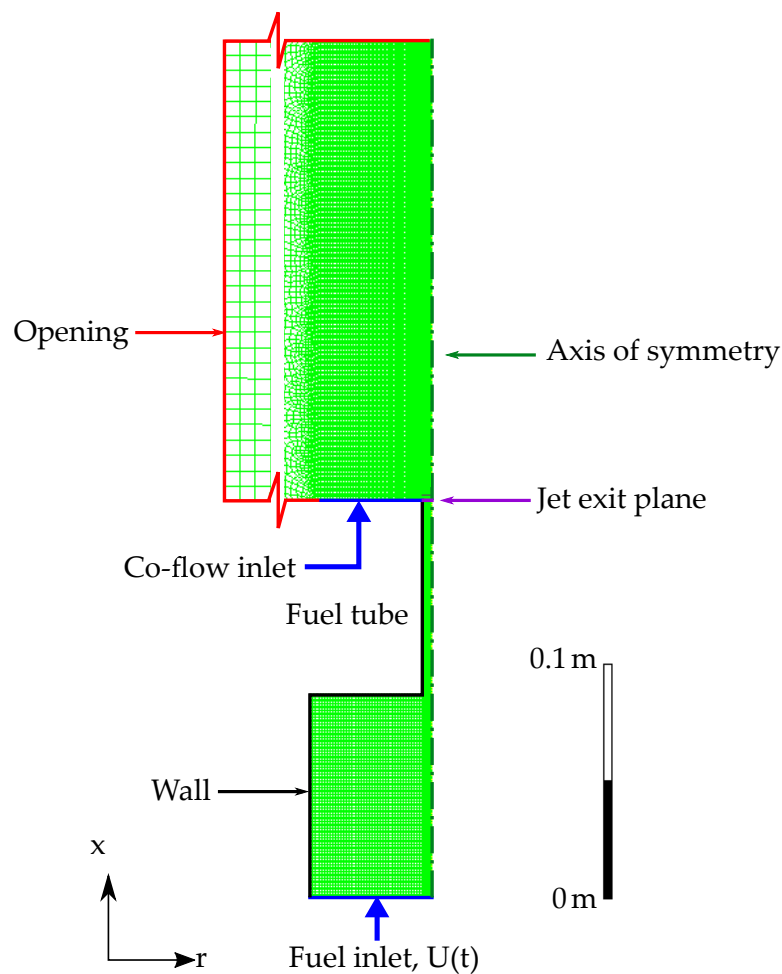


**Figure 7.1** Cross-sectional diagram of the computational domain of the axisymmetric nozzle for steady and forced laminar flames simulations. Boundaries include inlets for fuel and co-flow (blue), no-slip wall (black), jet exit plane (purple), axis of symmetry (dark green) and opening (red). For the transient case, the temporal profile of the time-dependent fuel inlet velocity,  $U(t)$ , is defined as a sum of sinusoids.

## 7.3 Results and discussion

### 7.3.1 Steady laminar flame

Figure 7.2 presents the comparisons between (a) the normalised measured and calculated values of OH concentrations,  $\hat{I}_{OH,E}$  [16, 17] and  $\hat{n}_{OH,C}$ , respectively, (b) the measured and calculated velocities,  $U_E$  [16, 17] and  $U_C$ , respectively, and (c) the measured and calculated temperatures,  $T_{g,E}$  [16, 17] and  $T_{g,C}$ , respectively. Here, the subscripts  $E$  and  $C$  denote the experimental and computational quantities, respectively. It is worth mentioning that the experimental data for OH-PLIF is qualitative hence it has been normalised by the maximum intensity. The hatched region in the PIV measurement shown in (b) represents no data due to the interference from soot scattering. It is important to recall that the NTLAF technique is only valid for fuel-rich regions where temperatures are above 800 K.

All comparisons exhibit good qualitative agreement, particularly the flame length which agrees within 4% of the total flame length, as evidenced by the OH distributions. The predicted velocity field qualitatively agrees with the measured velocity field. Additionally, the qualitative comparison between the profiles of  $T_{g,E}$  and  $T_{g,C}$  reveals an excellent agreement within 0.5 to 2 mm for the radial location of the peak temperature at all heights (outlined by black dashed lines). The largest discrepancy occurs near to the tip of the flame where the measurement is affected by the relatively lean mixture fraction.

Figure 7.3 presents comparisons between experimental [16, 17] and computed axial profiles at the centreline for the steady flame:  $T_{g,C}$  versus  $T_{g,E}$  and  $\hat{n}_{OH,C}$  versus  $\hat{I}_{OH,E}$ . The axial profiles of the normalised measured and computed soot volume fractions,  $\hat{f}_{v,E}$  [16, 17] and  $\hat{f}_{v,C}$ , respectively, at the centreline are included for reference. The axial profile of  $T_{g,E}$  exhibits a drop at  $x \approx 25$ –40 mm, due to the radiative heat loss from the concentrated soot region [32]. Without the radiation model, a maximum  $T_{g,C}$  of 2194 K is predicted at the centreline. At low heights,  $x = 10$ –30 mm, the simulation under-predicts  $T_{g,C}$  by  $\sim 260$  K for  $x \leq 15$  mm and  $\sim 130$  K for  $15 < x < 30$  mm, presumably due to the overestimation in thermal radiation of predicted soot. Nonetheless, the agreement is good within the high-temperature zone  $20 \leq x \leq 45$  mm. Nevertheless, the differences in temperature do not have any significant impact on the mixture fraction, as evidenced by the good match between  $\hat{n}_{OH,C}$  and  $\hat{I}_{OH,E}$ , especially for the location of the peak, which agrees to within 2 mm (4% of the total flame length).

Table 7.2 presents Reactions (R1)–(R9) which are considered as key steps. The first seven reactions describe the thermal decomposition of ethylene, to the intermediate species, vinyl with the formation and consumption of acetylene. Additionally, the last two being key heat release reactions in the flame region.



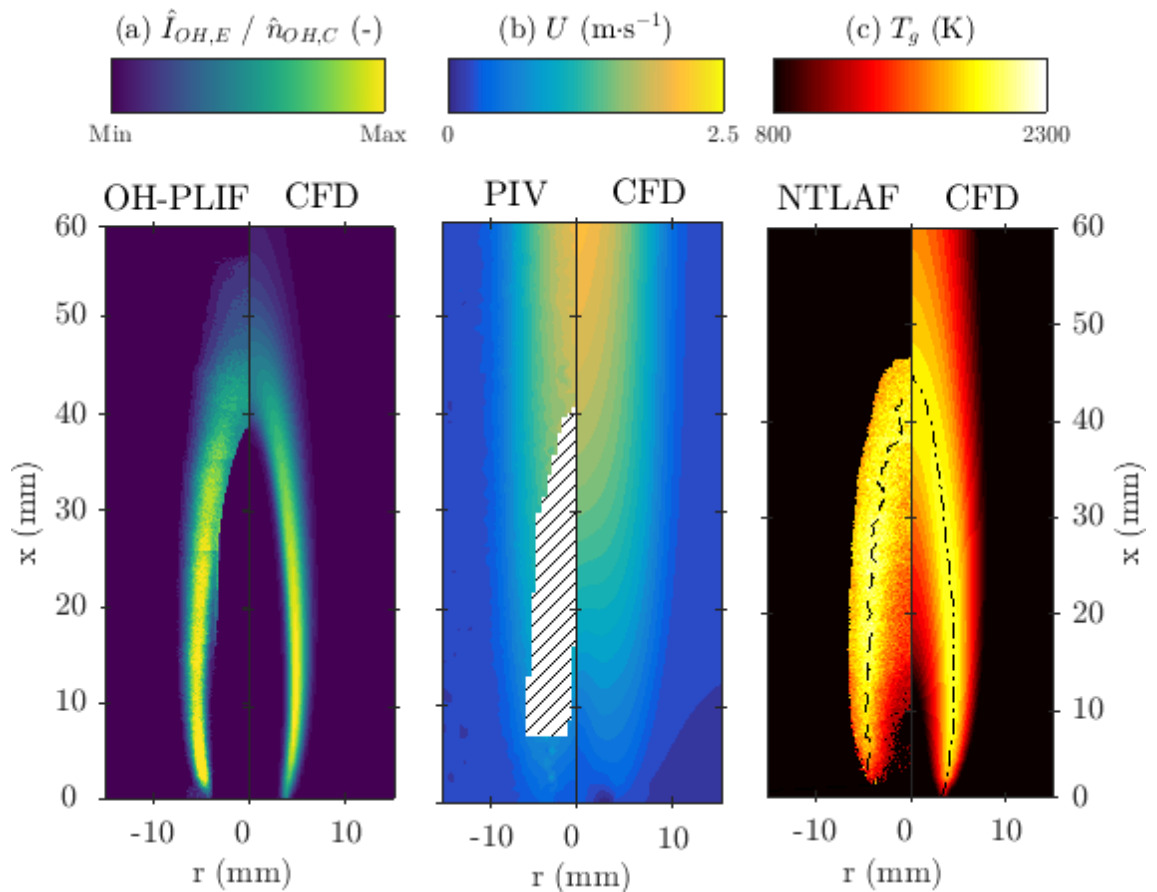


**Figure 7.2** Comparisons between the planar cross-sections of the experimental (left) [16, 17] and numerical data (right) for the steady laminar  $C_2H_4/N_2$  non-premixed flame: (a) normalised OH distribution, (b) velocity,  $U$ , and (c) flame temperature,  $T_g$ . The black dashed lines in (c) represent the radial location of peak values of  $T_{g,E}$  and  $T_{g,C}$  at all heights.

[This page is intentionally left blank]

**Table 7.2** Key reactions that involved in the ethylene  $\rightarrow$  vinyl  $\rightarrow$  acetylene processes and key heat release reactions.

$C_2H_4 + M \rightleftharpoons C_2H_2 + H_2 + M$	(R1)
$C_2H_4 + M \rightleftharpoons C_2H_3 + H + M$	(R2)
$C_2H_4 + H \rightleftharpoons C_2H_3 + H_2$	(R3)
$C_2H_3 + H \rightleftharpoons C_2H_2 + H_2$	(R4)
$C_2H_2 + O \rightleftharpoons HCCO + H$	(R5)
$C_2H_2 + O \rightleftharpoons CH_2 + CO$	(R6)
$C_2H_2 + OH \rightleftharpoons CH_2CO + H$	(R7)
$OH + H_2 \rightleftharpoons H + H_2O$	(R8)
$CO + OH \rightleftharpoons CO_2 + H$	(R9)

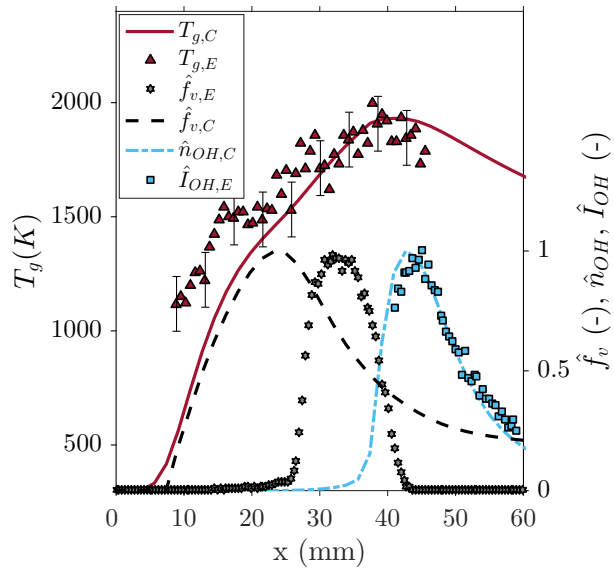
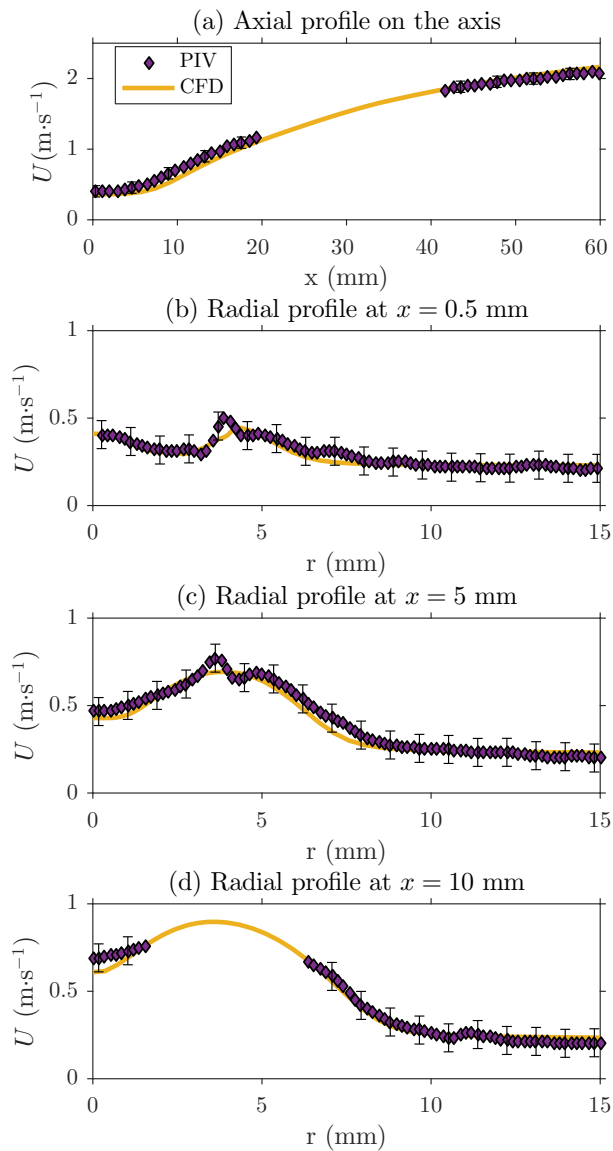


**Figure 7.3** Comparisons between experimental (symbols) [16, 17] and computed (lines) axial profiles of temperature,  $T_g$ , at the centreline. Additionally, the normalised computed number density of OH,  $\hat{n}_{OH,C}$ , is compared with the normalised experimental OH-PLIF intensity,  $\hat{I}_{OH,E}$ . For reference, the location of measured and computed normalised soot volume fraction,  $\hat{f}_{v,E}$  and  $\hat{f}_{v,C}$ , respectively, at the centreline is included.

Figure 7.4 presents quantitative comparisons between the axial profiles of (a)  $U_C$  and  $U_E$  [16, 17] at the centreline and for radial profiles at (b)  $x = 0.5$  mm, (c)  $x = 5$  mm and (d)  $x = 10$  mm. The comparison between the axial profiles of  $U_C$  and  $U_E$  shows an agreement within 20% of the experimental measurement. The radial profiles of  $U_C$  at  $x = 0.5, 5$  and  $10$  mm agree with  $U_E$  to within the experimental uncertainty,  $\pm 0.08 \text{ m}\cdot\text{s}^{-1}$ . This level of agreement is deduced to be sufficient both to calculate mixture fraction with good accuracy and to provide reasonable estimates of the concentration of key gas-phase species influencing early stages of soot production.

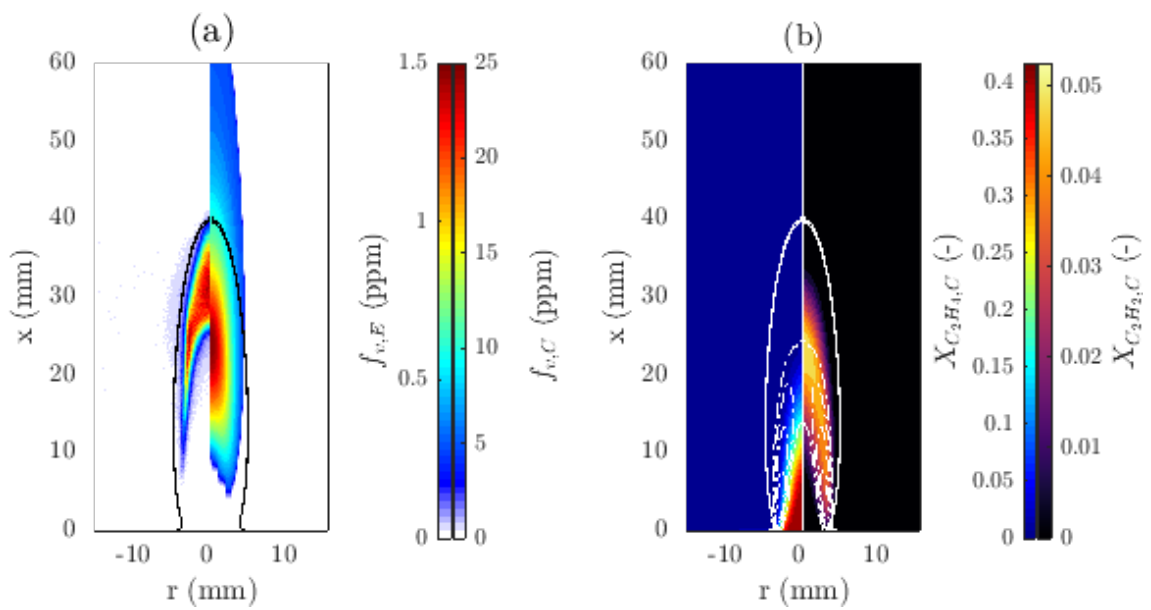
Figure 7.5(a) compares the experimental and computational soot volume fraction,  $f_{v,E}$  (left) [16, 17] and  $f_{v,C}$  (right), respectively. The predicted isopleths of  $Z_{stoic}$  are also shown for reference. The agreement between the predicted soot and the experiment is not good, demonstrating the need for further development of the soot model. The peak value of  $f_{v,C}$  is over-estimated by one order of magnitude. Furthermore, the soot model over-predicts the spatial extent of the soot region, especially in the region downstream from the isopleth of  $Z_{stoic}$ . Nevertheless, notwithstanding these limitations in certain regions of the flame, the position of the predicted soot in the wings, which first appears at  $x = 5.5$  mm, is similar to that at which soot is first detected experimentally,  $x = 6.0$  mm. This similarity provides confidence in the distribution of major species and the chemical processes upstream from the soot zone. However, the soot prediction at the centreline exhibits significant disagreement with the experiment. While the peaks of both  $f_{v,E}$  and  $f_{v,C}$  are located at the centreline, the peak  $f_{v,C}$  is found at  $x = 23$  mm, whereas that of the experiment is located at  $x = 32$  mm.

Fig. 7.5(b) presents the contours of the computed mole fractions of ethylene,  $X_{C_2H_4,C}$ , and acetylene,  $X_{C_2H_2,C}$ . Since acetylene-based growth is the dominant contributor to soot volume fraction [33, 34], the current work treats acetylene as an approximation of soot precursor in the absence of PAHs. The pyrolysis of ethylene is shown by the gradual decrease in  $X_{C_2H_4,C}$  as the axial height increases. Two pathways occur for ethylene decomposition: (R1) and (R2) [35], with the molecular path being predominant. It either directly decomposes into acetylene or through the intermediate species, vinyl. The contour (white dashed lines) of the mole fraction of vinyl,  $X_{C_2H_3,C}$ , is superimposed on the contours of  $X_{C_2H_4,C}$  and  $X_{C_2H_2,C}$ . The region of concentrated vinyl is located between those of ethylene and acetylene, consistent with its role as a key intermediate species. The vinyl radical can be produced through the three-body reaction (R2) and H-abstraction mechanism (R3) [35, 36].



**Figure 7.4** Quantitative comparisons between the experimental (symbols) [16, 17] and numerical (lines) results: (a) the axial profiles of velocity,  $U$ , on the axis (for clarity, only every tenth point is shown) and the radial profiles of the jet exit velocity probed at selected axial heights,  $x =$  (b) 0.5 mm, (c) 5 mm and (d) 10 mm.

[This page is intentionally left blank]



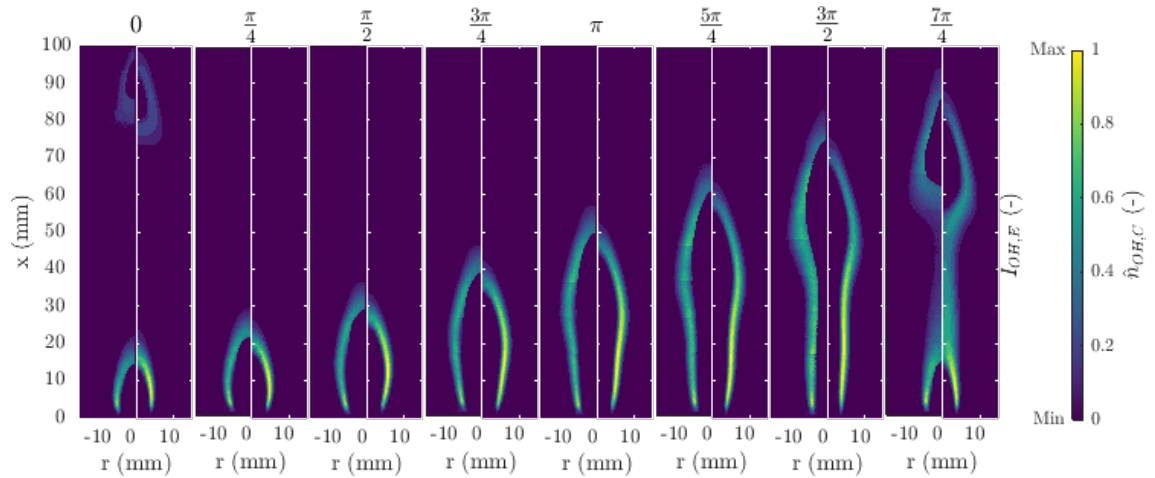
**Figure 7.5** Two-dimensional cross-sections for the steady laminar  $C_2H_4/N_2$  non-premixed flame: (a) the measured and computed soot volume fraction,  $f_{v,E}$  (left) [16, 17] and  $f_{v,C}$  (right), respectively; (b) the calculated contours of mole fractions of ethylene,  $X_{C_2H_4,C}$  (left) and acetylene,  $X_{C_2H_2,C}$  (right). The isopleth of the stoichiometric mixture fraction,  $Z_{stoisic}$ , is presented in black and white colours in panels (a) and (b), respectively. The white dashed contour in (b) represents the location of the computed mole fraction of vinyl,  $X_{C_2H_3,C}$ .

### 7.3.2 Time-varying laminar flame

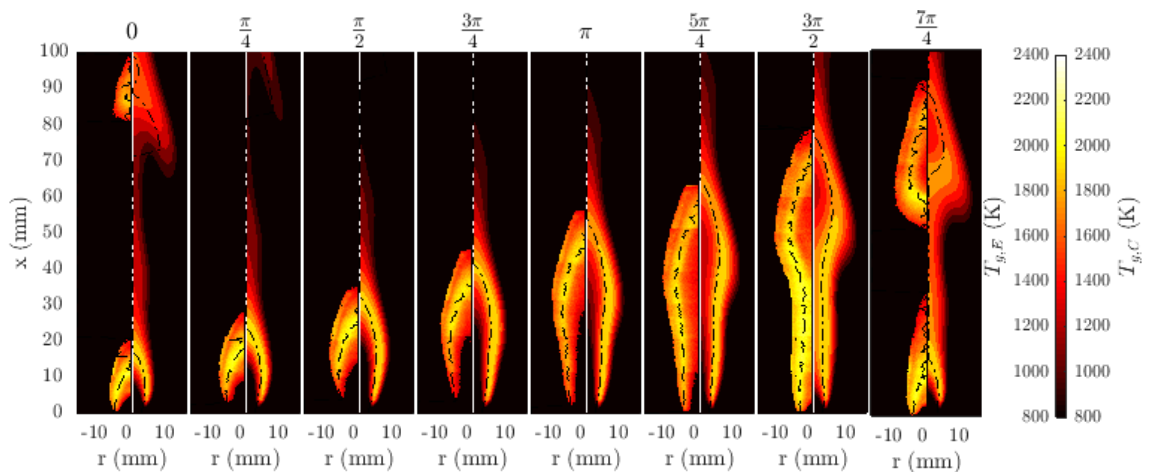
Figure 7.6 presents a comparison between the planar cross-sectional images of the measured and calculated OH distributions,  $\hat{I}_{OH,E}$  (left) [16, 17] and  $\hat{n}_{OH,C}$  (right), respectively. The figure shows eight phase angles of the forcing cycle, which is equivalent to 12.5 ms intervals. The comparison shows that the spatial features of the simulated flame qualitatively agree with the experiments. However, the length of the simulated flame is noticeably lower than that of the experimental flame due to the over-estimation of radiative heat loss. Nevertheless, the good agreement indicates that the numerical model reproduces the flame dynamics: the lateral compression on the flame stem, followed by the necking and the pinch-off. This agreement provides further confidence in the calculated values of the mixture fraction.

Figure 7.7 presents the comparison between the experimental and computed temperatures,  $T_{g,E}$  (left) [16, 17] and  $T_{g,C}$  (right), respectively. Due to the limitation of the NTLAF technique, the temperature measurements are conditional which explains the absence of data for comparisons in the necking region ( $\phi = 7\pi/4$ ) and the burnt gas roll-up at the base of the detached flame ( $\phi = 0$  to  $\pi/2$ ). It is important to keep in mind that the soot radiation is over-predicted which leads to the mismatch between the numerical and experimental temperatures at the upper part of the flames at  $\phi = 3\pi/2$  and  $7\pi/4$ . The qualitative comparison between  $T_{g,E}$  and  $T_{g,C}$  exhibit a good agreement of the spatial distributions, to within 2 mm for the overall flame shape and the locations of high-temperature regions (outlined by black dash-lines) at all heights. The good agreement provides further confidence in the usefulness of the model.





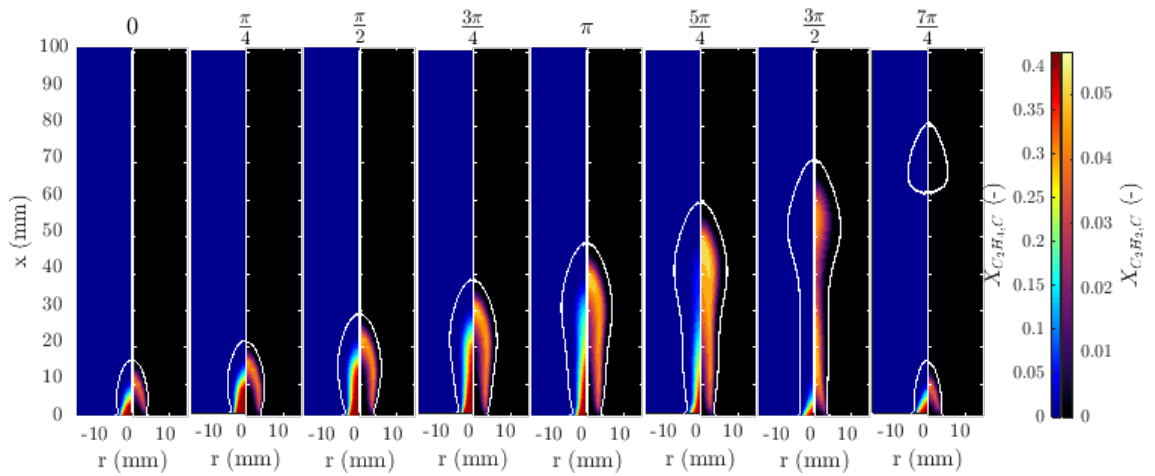
**Figure 7.6** Pseudo-colour images of OH-PLIF with normalised intensity,  $\hat{I}_{OH,E}$  (left) [16, 17], and the normalised computed number density of OH,  $\hat{n}_{OH,C}$  (right), for the time-varying laminar  $C_2H_4/N_2$  non-premixed flame in which the inlet fuel flow rate is varied with a 10-Hz sinusoidal wave with a 50% amplitude (defined as the ratio between the maximum jet exit velocity at the exit plane of the time-varying and steady laminar flames). The images are obtained at 12.5-ms intervals.



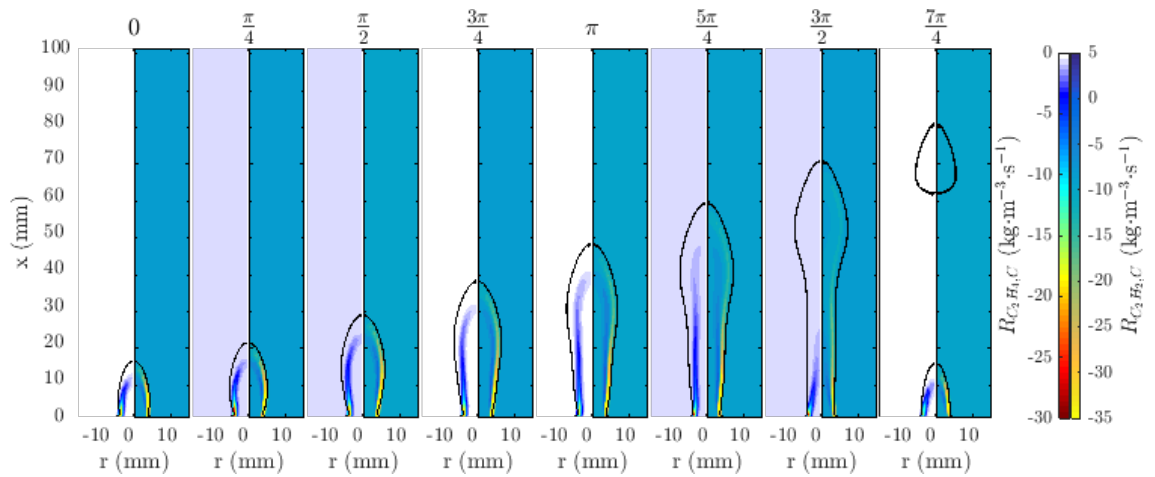
**Figure 7.7** Pseudo-colour images of the measured temperature,  $T_{g,E}$  (left) [16, 17], and the computed temperature,  $T_{g,C}$  (right), for the time-varying laminar  $C_2H_4/N_2$  non-premixed flame obtained at 12.5-ms intervals. Black dashed-lines represent the radial location of peak values of  $T_{g,E}$  and  $T_{g,C}$  at all heights.

Figure 7.8 presents the corresponding calculated pseudo-colour maps of  $X_{C_2H_4,C}$  and  $X_{C_2H_2,C}$ , together with the calculated isopleths of  $Z_{stoic}$  presented in white solid lines. It can be seen that the volume of the region containing unburned ethylene first grows and then shrinks through the full cycle, consistent with the corresponding increase and decrease in the exit velocity of the fuel (Fig. 7.4). Comparison with Figure 7.7 also reveals that the position of ethylene correlates with the low-temperature region of the flame. The acetylene is distributed radially outside and downstream from that of the ethylene, consistent with the process of decomposition. However, its axial extent is much greater, particularly for  $5\pi/4 \leq \phi \leq 3\pi/2$ . The value of  $X_{C_2H_2,C}$  reaches its maximum at  $\phi = 5\pi/4$ , with its peak on the centreline. Even though the peak  $X_{C_2H_2,C}$  is only 8.0% higher than that of the steady flame, the spatial extent of the region containing high  $X_{C_2H_2}$  in the time-varying flame is twice that of the unforced counterpart. The findings suggest that the additional acetylene contributes to the enhanced soot production in the time-varying laminar flame.

Figure 7.9 presents the corresponding calculated values of net molar reaction rate for ethylene,  $R_{C_2H_4,C}$ , and acetylene,  $R_{C_2H_2,C}$ . The regions with the highest production and consumption rates typically occur in a thin layer just inside the flame front (denoted by  $Z_{stoic}$ ). Since acetylene is the major product of ethylene pyrolysis (with vinyl as the primary intermediate species), it is not unreasonable that the regions of acetylene production and ethylene consumption partially overlap. At  $\phi = 3\pi/2$ , both regions of high ethylene consumption rates and high acetylene production rates are confined to the lower part of the flame near to the nozzle exit, whereas the region of high acetylene consumption rate extends into the neck of the flame.



**Figure 7.8** Pseudo-colour images of computed mole fractions of ethylene,  $X_{C_2H_4}$  (left), and acetylene,  $X_{C_2H_2}$  (right), for the time-varying laminar  $C_2H_4/N_2$  non-premixed flame for time-steps of 12.5 ms. The calculated isopleth of the stoichiometric mixture fraction,  $Z_{stoic}$ , is presented in white solid lines.



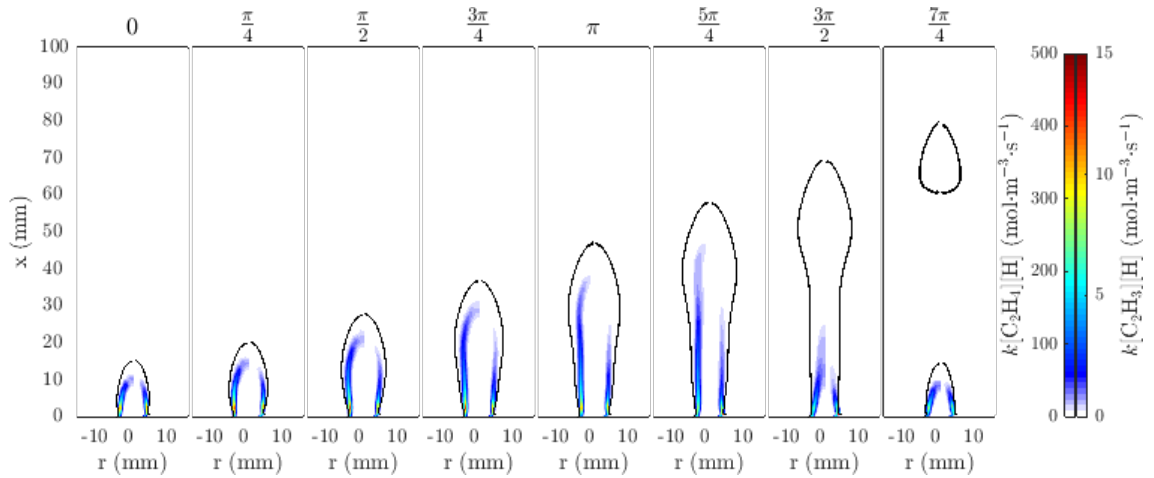
**Figure 7.9** Pseudo-colour images of computed net molar reaction rates of ethylene,  $R_{C_2H_4,C}$  (left), and acetylene,  $R_{C_2H_2,C}$  (right), for the time-varying laminar  $C_2H_4/N_2$  non-premixed flame, also at 12.5-ms intervals. The calculated isopleth of the stoichiometric mixture fraction,  $Z_{stoic}$ , is presented in black solid lines.

Figure 7.10 presents the contours of kinetic rates of (R3),  $k[\text{C}_2\text{H}_4][\text{H}]$ , (left) and (R4),  $k[\text{C}_2\text{H}_3][\text{H}]$  (right). The kinetic rates of (R3) is two orders of magnitude higher than those of (R1) and (R2), which implies that (R3) is the predominant pathway for ethylene consumption. It extends well into the upper part of the flame at  $\phi = 5\pi/4$  before the vortex suppresses the reaction in the neck of the flame. In contrast, the region of high  $k[\text{C}_2\text{H}_3][\text{H}]$  appears smaller than the region of high  $R_{\text{C}_2\text{H}_2,\text{C}}$  in Fig. 7.9, which indicates that although the dominant pathway of acetylene formation is through vinyl, other minor reactions, such as (R1), also contribute to the additional acetylene formation.

Figure 7.11 presents the corresponding computed images of strain rate,  $S_{rx,C}$  (left) and heat release rate, HRR (right) for the time-varying laminar non-premixed flame. The fluid dynamic strain rate is defined as:

$$S_{rx} = \frac{1}{2} \left( \frac{\partial u_r}{\partial x} + \frac{\partial u_x}{\partial r} \right) \quad (7.2)$$

where  $u_r$  and  $u_x$  are the radial and axial velocity components. Since the strain rate is responsible for the deformation of fluid elements, it is expected that the reaction zone, as denoted by the isopleth of  $Z_{stoic}$ , closely follows the high-strain-rate region. The trend is consistent with the expectation that the high-temperature reaction zone marked by the calculated isopleth of  $Z_{stoic}$  coincides with the region of high heat release rate. The negative HRR region is located on the fuel-rich side of the stoichiometric, which is coincident with the endothermic process of H-abstraction from vinyl to acetylene [37]. It can also be seen that a high-strain rate region progressively grows at mid-flame height and pinches the flame surface towards the centreline. However, the magnitude of  $S_{rx,C}$  near to the neck of the flame is in the range of 250 to 300  $\text{s}^{-1}$ , which is significantly lower than the estimated extinction strain rate for ethylene-air flames, 1186  $\text{s}^{-1}$  [38]. Nevertheless, the relatively high level of strain in this region is consistent with high rates of mixing-induced oxidation that consume any soot particles in the neck. Additionally, regions of the highest soot, within the detached flamelet, correspond to the regions of lowest strain, which is consistent with previous work [39–43].



**Figure 7.10** Pseudo-colour images of the computed kinetic rate of reaction of  $C_2H_4 + H \rightarrow C_2H_3 + H_2$  (left) and  $C_2H_3 + H \rightarrow C_2H_2 + H_2$  (right) for the time-varying laminar  $C_2H_4/N_2$  non-premixed flame for time-steps of 12.5 ms. The calculated isopleth of the stoichiometric mixture fraction,  $Z_{stoic}$ , is presented in black solid line.

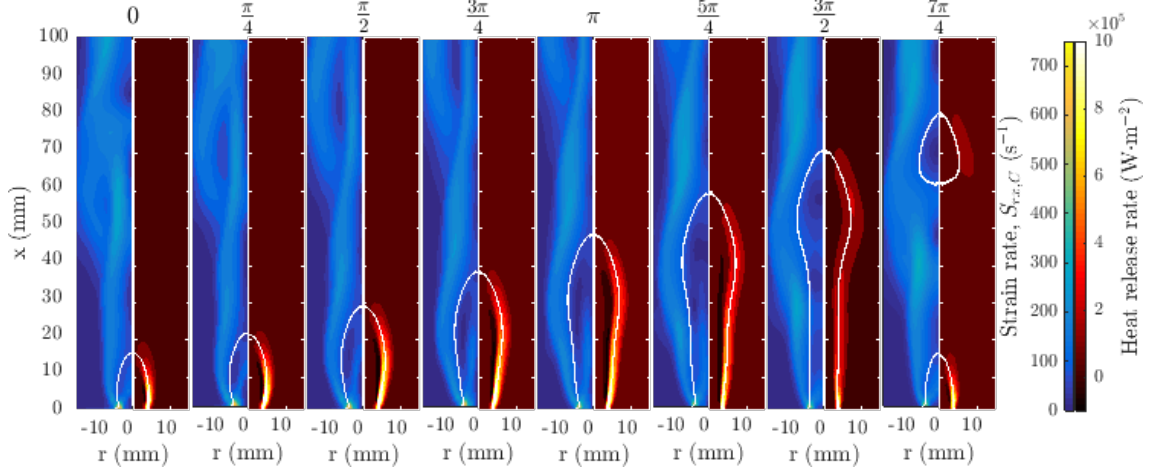


**Figure 7.11** Pseudo-colour images of computed strain rate,  $S_{rx,C}$  (left), and heat release rate (right) for the time-varying laminar non-premixed flame at 12.5-ms intervals. The calculated isopleth of stoichiometric mixture fraction,  $Z_{stoic}$ , is presented in white solid lines.

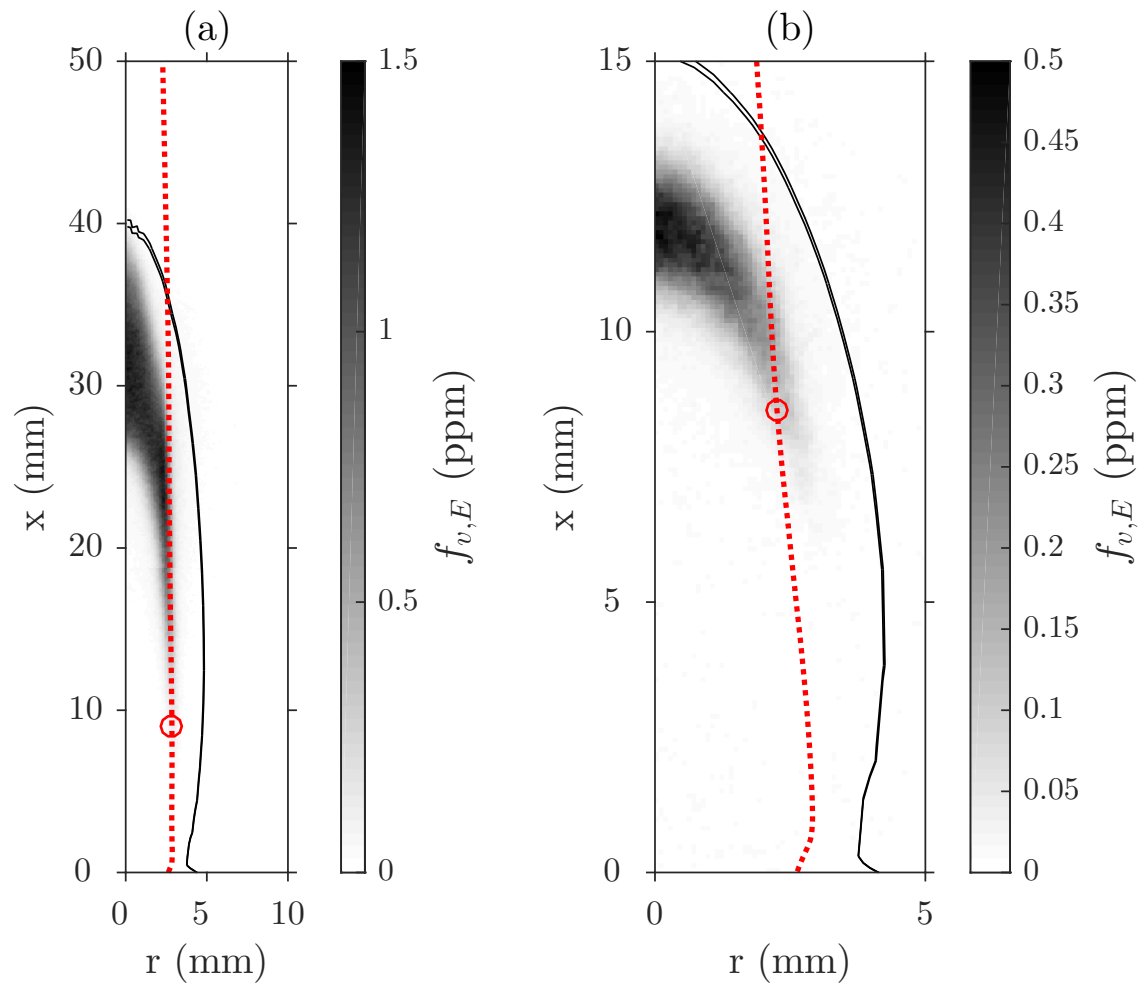
### 7.3.3 Residence time analysis

Residence time is calculated by tracking massless inert particles that follow the convective pathlines through the steady and time-varying flames, particularly on the streamlines that pass through the locations where soot is first detected and where the maximum soot volume fraction occurs.

Figure 7.12 presents the contours of  $f_{v,E}$  [16, 17] for (a) the steady and (b) time-varying laminar flames at  $\phi = 0$  when the attached flame is at its earliest stage of development. The figure also includes the isopleths of  $Z_{stoic}$  for reference. The dashed lines indicate the convective trajectories, while the red circular markers denote the locations where the minimum  $f_{v,E}$  was first encountered along the trajectories.

Figure 7.13 presents the time histories of  $Z$  and  $X_{C_2H_4,C}$ ,  $X_{C_2H_3,C}$ ,  $X_{C_2H_2,C}$ ,  $X_{CO,C}$ ,  $X_{H,C}$  and  $X_{OH,C}$  along trajectories described in Fig. 7.12 for (a) the steady-state and (b) time-varying laminar flames. The figure presents the temporal evolution of quantities as a function of a dimensionless residence time,  $\hat{\tau}$ , normalised by the time required to reach the peak of  $X_{OH,C}$ , which is 42.94 and 30.70 ms for the steady and time-varying flames, respectively. The vertical dotted lines denote the residence times,  $\tau = 20.13$  and 21.95 ms, corresponding to the red circular markers in Fig 7.12(a) and (b), respectively.

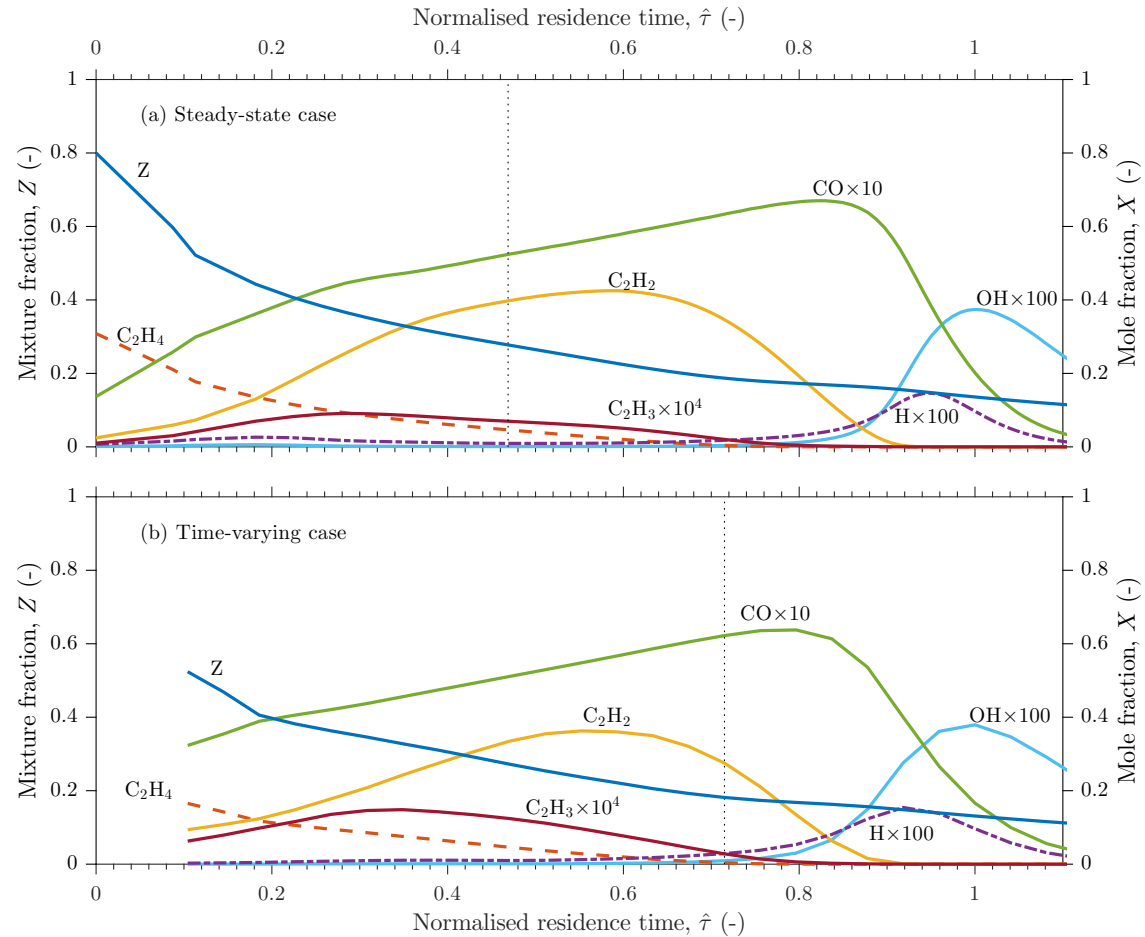
The time histories in the steady-state case are qualitatively similar to those in the transient case, although the residence time between the first soot detection and the peak of  $X_{OH,C}$  is different. This indicates that the soot in the early stages of the steady laminar flame a has longer time to form and grow than does the forced counterpart. Another interesting point is that there is more  $X_{C_2H_3,C}$  in the time-varying flame than for the steady-state counterpart.



**Figure 7.12** Images of the measured soot volume fraction,  $f_{v,E}$  [16, 17], showing the position of the representative trajectories that were tracked throughout the flames, namely the height where soot is first detected in (a) the steady and (b) time-varying laminar flames at  $\phi = 0$  using the LII technique. The calculated isopleths of the stoichiometric mixture fraction,  $Z_{stoisic} = 0.142$ , are presented in black solid lines. The red circular markers correspond to the locations where minimum soot volume fractions were first detected along the trajectories.

[This page is intentionally left blank]

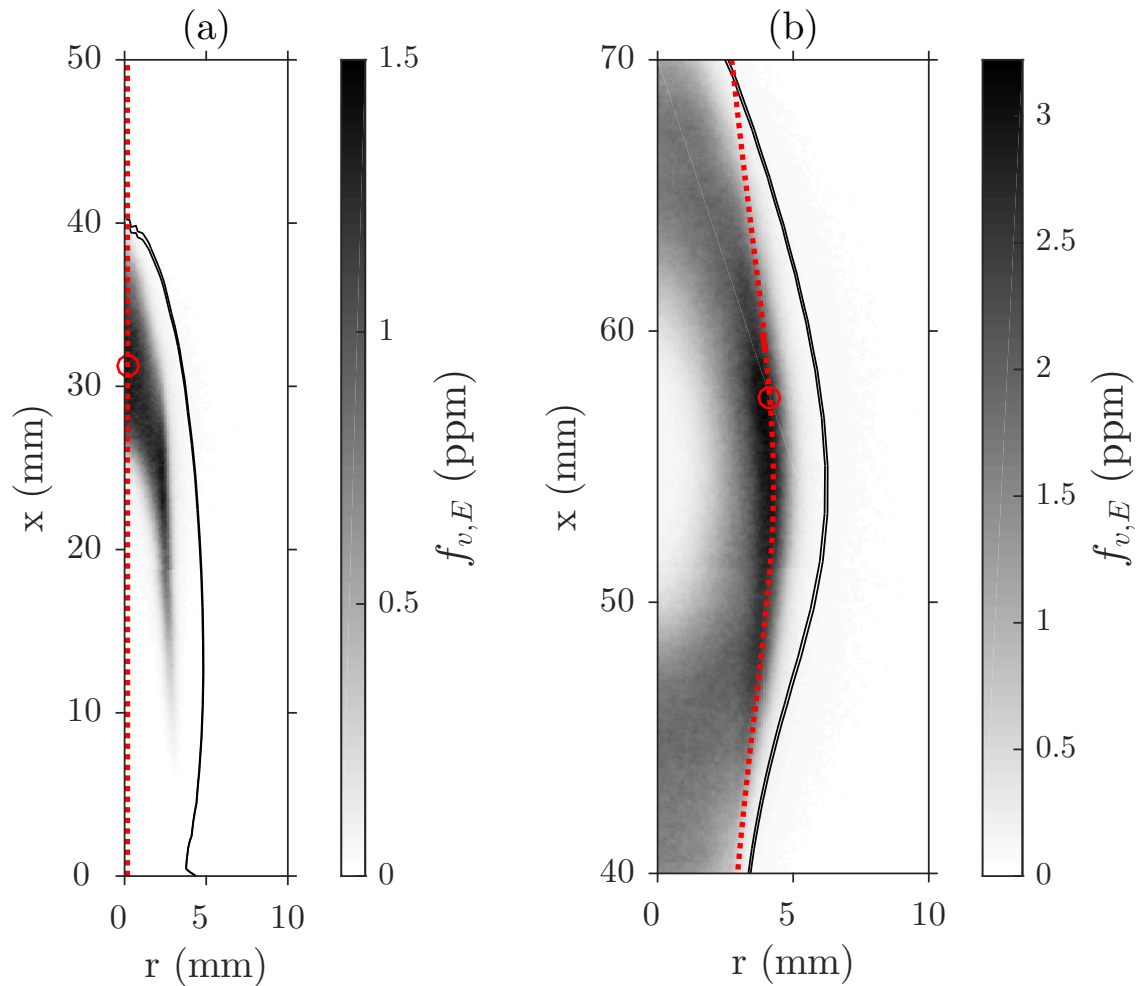




**Figure 7.13** Calculated mixture fraction,  $Z$ , and mole fractions of ethylene,  $X_{C_2H_4,C}$ , vinyl,  $X_{C_2H_3,C}$ , acetylene,  $X_{C_2H_2,C}$ , carbon monoxide,  $X_{CO,C}$ , hydrogen atoms,  $X_{H,C}$ , and hydroxyl radicals,  $X_{OH,C}$ , as functions of dimensionless residence time,  $\hat{\tau}$  (normalised by the time particles require to reach the peak of  $X_{OH,C}$ ), along trajectories described in Fig. 7.12 for (a) the steady-state and (b) time-varying laminar flames. The vertical dotted lines represent the residence time required for the virtual inert particles released at the jet exit plane to reach the locations marked by the red circular markers in Fig. 7.12.

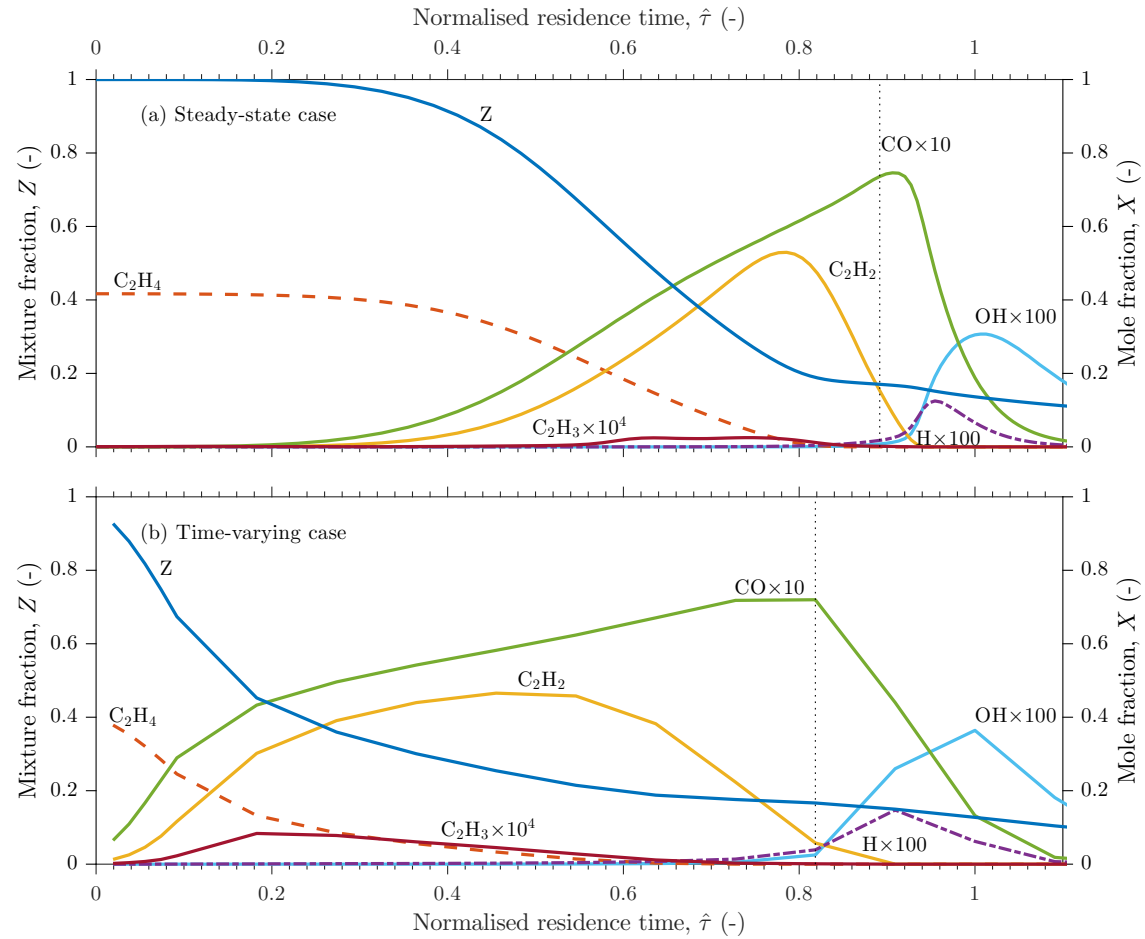
Figure 7.14 presents the contours of  $f_{v,E}$  [16, 17] for (a) the steady and (b) time-varying laminar flames at  $\phi = 3\pi/2$  when the maximum  $f_{v,E}$  occurs. The figure also includes the isopleths of  $Z_{stoic}$  for reference. The dashed lines represent the convective trajectories, while the red circular markers denote the locations of maximum  $f_{v,E}$  along these trajectories. It can be readily seen that the peak on  $f_{v,E}$  for the forced flame is found in the wings, which contrasts the steady flame where it is found on the axis. Furthermore, the magnitude of the peak  $f_{v,E}$  for the forced flame is 125% greater than that for the steady counterpart [16, 17].

Figure 7.15 presents the corresponding time histories along trajectories described in Fig. 7.14 for (a) the steady-state and (b) time-varying laminar flames. The total residence times needed to reach the peak of  $X_{OH,C}$  is 50.39 and 68.83 ms for the steady and time-varying flame, respectively. The vertical dotted lines denote the residence times,  $\tau = 44.93$  and 56.33 ms, respectively, required for the fuel parcel to reach the locations of the maximum  $f_{v,E}$  for the steady-state and transient cases. Furthermore, the duration between the maximum  $f_{v,E}$  and the peak  $X_{OH,C}$  is 8 ms longer for the time-varying flame than for the steady laminar flame. In contrast to Fig 7.13, the time histories in the steady-state and transient cases are significantly different. The fuel concentration for the time-varying flame decays faster than for the steady-state case. Although the peak value of  $X_{C_2H_2,C}$  for the transient case ( $X_{C_2H_2,C} = 0.47$ ) is slightly lower than for the steady counterpart ( $X_{C_2H_2,C} = 0.53$ ), it remains at a high level  $>30$  ms longer. This greater time with high  $C_2H_2$  concentration explains the higher soot concentration. The value of  $X_{C_2H_3,C}$  is also greater for the time-varying flame, consistent with the trends in Fig. 7.13.



**Figure 7.14** Images of the measured soot volume fraction,  $f_{v,E}$  [16, 17], showing the position of the representative trajectories that were tracked throughout the flames, namely the maximum sooting region in (a) the steady and (b) time-varying laminar flames at  $\phi = 3\pi/2$  using the LII technique. The calculated isopleths of the stoichiometric mixture fraction,  $Z_{stoic} = 0.142$ , are presented in black solid lines. The red circular markers correspond to the locations of maximum soot volume fractions.

[This page is intentionally left blank]

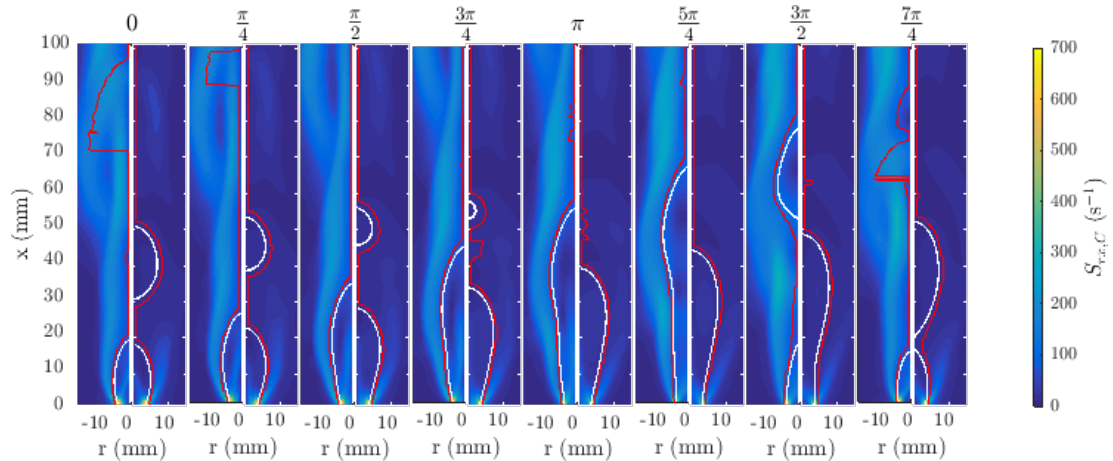


**Figure 7.15** Calculated mixture fraction,  $Z$  and mole fractions of ethylene,  $X_{C_2H_4,C}$ , vinyl,  $X_{C_2H_3,C}$ , acetylene,  $X_{C_2H_2,C}$ , carbon monoxide,  $X_{CO,C}$ , hydrogen atoms,  $X_{H,C}$ , and hydroxyl radicals,  $X_{OH,C}$  as functions of a dimensionless residence time,  $\hat{\tau}$  (normalised by the time particles require to reach the peak of  $X_{OH,C}$ ), along trajectories described in Fig. 7.14 for (a) the steady-state and (b) time-varying laminar flames. The vertical dotted lines represent the residence time required for the virtual inert particles released at the jet exit plane to reach the locations marked by the red circular markers in Fig. 7.14.

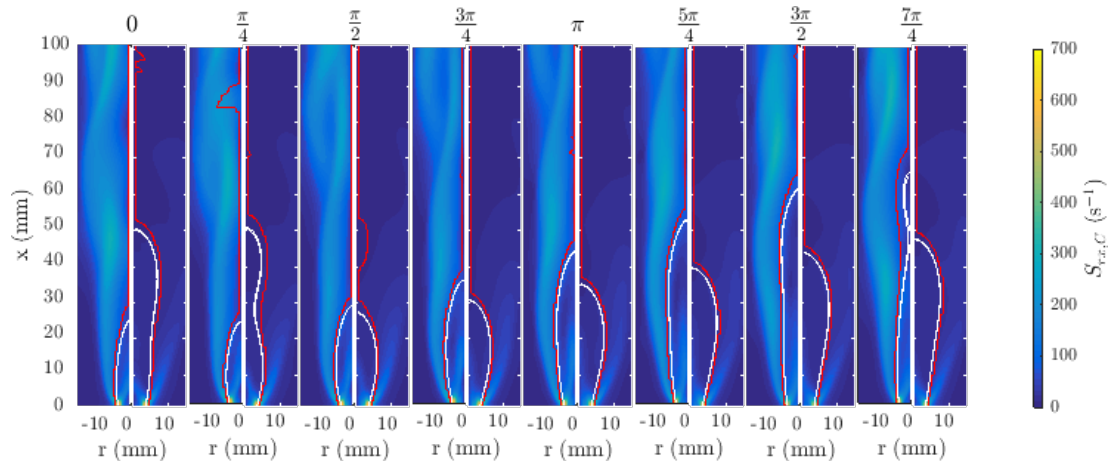
### 7.3.4 Flame response to external forcing in zero-gravity

Figure 7.16 presents a side-by-side comparison of the distribution of  $S_{rx,C}$  for time-varying laminar flames under normal conditions (left) and zero-gravity environment (right). The locations of the maximum calculated number density of OH and  $Z_{stoic}$  are also shown with red and white isopleths, respectively. It can be seen that the case without buoyancy results in a significantly lower magnitude of  $S_{rx,C}$  than that does normal gravity. Furthermore, the layer of high strain appears to decouple from the isopleth of  $Z_{stoic}$ . However, the flame pinch-off is observed in both cases. While the necking and pinch-off regions in the buoyant flame are associated with a localised region of high-strain rate, the conditions are very different for the non-buoyant flame. Under normal-gravity conditions, the spatial extent of the high-strain region ( $S_{rx,C} \approx 280 \text{ s}^{-1}$ ) increases and moves toward the centreline as the phase of the cycle progresses. This can be inferred to contribute to the necking and pinch-off of the flame. In contrast, while the zero-gravity flame exhibits a pinch-off event at  $\phi = 7\pi/4$  that is clearly not strain-induced. The detached fuel-rich pocket under zero-gravity conditions also has a larger volume than that of the normal-gravity counterpart. As a result, it survives after the pinch-off approximately 50 ms longer than the detached fuel-rich pocket of the normal-gravity time-varying flame. However, at the phase immediately after the pinch-off, the heights of the attached flames in both cases are approximately the same. The results suggest that the pinch-off is primarily a consequence of the fuel flow fluctuation, although buoyancy has a role in convecting the pinched-off fuel-rich pocket further downstream and accelerating the consumption of the remaining fuel.

Figure 7.17 presents the contours of  $S_{rx,C}$  for the time-varying flames with fuel flow modulations specified by a 10-Hz pure sinusoidal function with an amplitude of 50% under normal- and zero-gravity conditions. Even though the amplitude of the fuel flow modulation is also 50%, the flame pinch-off is not as evident for the case with a sum-of-sinusoidal function. In both normal- and zero-gravity cases, the fuel-rich region in the upper part of the flame is consumed before it is pinched-off. These results indicate that the purely sinusoidal forcing does not increase the residence time as much as does the sum-of-sinusoidal forcing, even though the frequency and amplitude are the same. This questions the accuracy of previous numerical studies of time-varying laminar flames that have assumed a sinusoidal variation in a parabolic profile of the fuel inlet velocity [11, 14, 44] despite previous experimental studies showing that the temporal evolution of the jet centreline velocity is not purely sinusoidal [8, 17, 45]. Furthermore, at some phases of the forcing cycle, the velocity profiles near to the jet exit is not parabolic [8]. This highlights the importance of accurately matching the jet exit profiles throughout time-varying flames in a numerical model.



**Figure 7.16** Pseudo-colour contours for the computed strain rate,  $S_{rx,C}$  for the normal- (left) and zero-gravity (right) time-varying laminar non-premixed flames. The fuel flow modulation is determined by a 10-Hz sum-of-sinusoidal function with an amplitude of 50%. Red and white isopleths represent the locations of the maximum calculated number density of OH,  $n_{OH,C}$ , and the stoichiometric mixture fraction,  $Z_{stoic}$ .



**Figure 7.17** Pseudo-colour contours for the computed strain rate,  $S_{rx,C}$  for the normal- (left) and zero-gravity (right) time-varying laminar non-premixed flames. The fuel flow modulation is determined by a 10-Hz pure sinusoidal function with an amplitude of 50%. Red and white isopleths represent the locations of the maximum calculated number density of OH,  $n_{OH,C}$ , and the stoichiometric mixture fraction,  $Z_{stoic}$ .

## 7.4 Conclusions

The numerical study of the fluid-chemical interactions in steady and time-varying  $C_2H_4/N_2$  non-premixed laminar flames has provided new insights and quantitative data of the influence of forcing on a laminar sooting flame. The model predicts the overall flame shape and the time-dependent flame response, together with the OH contour and the velocity field with sufficient accuracy to give confidence in the values of mixture fraction in regions except where soot is present. The agreement with temperature in these regions was also sufficient to have confidence in the trends of the key gas phase species in the early stage of soot production, although the absolute accuracy of these calculated parameters is not yet known.

The results of these calculations reveal that, during phases of the cycle when the jet exit velocity is increasing, the flame is momentum-dominated. As a result, the time-varying laminar flame is fuelled with a larger amount of ethylene compared to its steady counterpart. The subsequent decrease in the jet exit velocity causes the fuel to be consumed there, pinching off the flame front. These effects are augmented by the presence of buoyancy which stretches the flame stem to prolong the residence time within the hot, fuel-rich reacting gases. This high-temperature region promotes the thermal decomposition of the ethylene into acetylene, which is the principal ingredient for soot growth by the HACA mechanism. Although the peak value of acetylene concentration does not increase much in the time-varying laminar flame, its spatial extent is significantly increased by the forcing. This explains the increase in the peak soot volume fraction in the time-varying laminar flame relative to its steady equivalent. At a later phase in the cycle, even though the magnitude of the vortex-induced strain rate is not sufficient to extinguish the local reaction zone, it promotes soot oxidation by enhancing the local mixing rates in the neck of the time-varying laminar flame. After the pinching, the isolated flame pocket comprises mostly combustion products and about 0.05% of acetylene, in addition to the nitrogen. This is consistent with the uniformly distributed large primary soot particles within the pinched-off flame.

The residence time analysis shows that the fuel flow modulation has a significant effect on the total residence time, but has only a modest influence on the distribution of major species during the early stages of flame development. Tracking the inert particles which pass through the location where soot is first detected in both the steady and time-varying flames reveals that the distributions of ethylene, vinyl, acetylene, carbon monoxide, hydrogen atoms and hydroxyl radicals are qualitatively similar. However, the results also suggest that the forcing has an effect on the pathways of ethylene decomposition since the time-varying flame exhibits a higher concentration of vinyl. The effect of the forcing is obvious by comparing the distribution of major species along trajectories which pass through the maximum sooting region in both the steady and time-varying flames. The



total residence time in the time-varying flame is approximately 50% longer than that in the steady counterpart. Even though the peak concentration of acetylene of time-varying flame does not differ much from that of the steady-state case, the residence time in the region of high acetylene concentration is significantly longer than that of the steady flame. Finally, an increase in the concentration of vinyl is also observed.

The pinch-off phenomenon is a consequence of fuel flow fluctuation with buoyancy accelerating the process. While buoyancy allows the pinch-off occurs earlier in the forcing cycle, it also hastens the consumption of the detached fuel-rich pocket. Under zero-gravity conditions, the pinched-off fuel-rich pocket survives longer into the next forcing cycle. However, these phenomena only occur when the fuel flow modulation is described by a sum-of-sinusoidal function. Under either normal- or zero-gravity conditions, the flames determined by a purely sinusoidal function do not exhibit an obvious pinch-off, even though the frequency and amplitudes are the same as the sum-of-sinusoidal function. These results highlight the complex interactions between the acoustic forcing and the reacting flow. This understanding would be further advanced by a more detailed characterisation of the temporal evolution of the jet exit velocity profile. Furthermore, the study shows that there is a risk in assuming the initial and boundary conditions of time-varying laminar flames are purely sinusoidal and parabolic, without matching the experimental data.

## Acknowledgement

The authors gratefully acknowledge the University of Adelaide and the financial support of the Australian Research Council (ARC Discovery grant DP130100198).

## References

- [1] A. W. Strawa and B. J. Cantwell, "Visualization of the structure of a pulsed methane-air diffusion flame", *Phys. Fluids* **28** (1985), pp. 2317–2320.
- [2] K. C. Smyth, J. E. Harrington, E. L. Johnsson, and W. M. Pitts, "Greatly enhanced soot scattering in flickering CH<sub>4</sub> Air diffusion flames", *Combustion and Flame* **95** (1993), pp. 229–239.
- [3] C. R. Shaddix, J. E. Harrington, and K. C. Smyth, "Quantitative Measurements of Enhanced Soot Production in a Flickering Methane/Air Diffusion Flame", *Combustion and Flame* **99** (1994), pp. 723–732.
- [4] C. R. Shaddix and K. C. Smyth, "Laser-Induced Incandescence Measurements of Soot Production in Steady and Flickering Methane, Propane, and Ethylene Diffusion Flames", *Combustion and Flame* **107** (1996), pp. 418–452.

## REFERENCES

---

- [5] K. C. Smyth, C. R. Shaddix, and D. A. Everest, “Aspects of soot dynamics as revealed by measurements of broadband fluorescence and flame luminosity in flickering diffusion flames”, *Combustion and Flame* **111** (1997), pp. 185–207.
- [6] J. Zhang and C. M. Megaridis, “Soot microstructure in steady and flickering laminar methane/air diffusion flames”, *Combustion and Flame* **112** (1998), pp. 473–484.
- [7] R. K. Mohammed, M. A. Tanoff, M. D. Smooke, A. M. Schaffer, and M. B. Long, “Computational and experimental study of a forced, time-varying, axisymmetric, laminar diffusion flame”, *Proceedings of the Combustion Institute* **27** (1998), pp. 693–702.
- [8] G. Papadopoulos, R. A. Bryant, and W. M. Pitts, “Flow characterization of flickering methane/air diffusion flames using particle image velocimetry”, *Experiments in Fluids* **33** (2002), pp. 472–481.
- [9] O. A. Ezekoye, K. M. Martin, and F. Bisetti, “Pulsed flow modulation of soot production in a laminar jet-diffusion flame”, *Proceedings of the Combustion Institute* **30** (2005), pp. 1485–1492.
- [10] S. B. Dworkin, B. C. Connelly, A. M. Schaffer, B. A. V. Bennett, M. B. Long, M. D. Smooke, M. P. Puccio, B. McAndrews, and J. H. Miller, “Computational and experimental study of a forced, time-dependent, methane-air coflow diffusion flame”, *Proceedings of the Combustion Institute* **31** (2007), pp. 971–978.
- [11] S. B. Dworkin, J. A. Cooke, B. A. V. Bennett, B. C. Connelly, M. B. Long, M. D. Smooke, R. J. Hall, and M. B. Colket, “Distributed-memory parallel computation of a forced, time-dependent, sooting, ethylene/air coflow diffusion flame”, *Combustion Theory and Modelling* **13** (2009), pp. 795–822.
- [12] B. C. Connelly, “Quantitative Characterization of Steady and Time-Varying, Sooting, Laminar Diffusion Flames using Optical Techniques”, Ph.D. dissertation, Yale University, 2009.
- [13] R. Chrystie and S. H. Chung, “Response to acoustic forcing of laminar coflow jet diffusion flames”, *Combustion Science and Technology* **186** (2014), pp. 409–420.
- [14] A. Jocher, K. K. Foo, Z. W. Sun, B. B. Dally, H. Pitsch, Z. T. Alwahabi, and G. J. Nathan, “Impact of acoustic forcing on soot evolution and temperature in ethylene-air flames”, *Proceedings of the Combustion Institute* **36** (2017), pp. 781–788.
- [15] K. K. Foo, Z. W. Sun, P. R. Medwell, Z. T. Alwahabi, B. B. Dally, and G. J. Nathan, “Experimental investigation of acoustic forcing on temperature, soot volume fraction and primary particle diameter in non-premixed laminar flames”, *Combustion and Flame* **181** (2017), pp. 270–282.
- [16] K. K. Foo, Z. W. Sun, P. R. Medwell, Z. T. Alwahabi, G. J. Nathan, and B. B. Dally, “Influence of nozzle diameter on soot evolution in acoustically forced laminar non-premixed flames”, *Combustion and Flame* **194** (2018), pp. 376–386.
- [17] K. K. Foo, Z. W. Sun, P. R. Medwell, Z. T. Alwahabi, G. J. Nathan, and B. B. Dally, “Soot evolution and flame response to acoustic forcing of laminar non-premixed jet flames at varying amplitudes”, *Combustion and Flame* **198** (2018), pp. 249–259.

- [18] B. C. Connelly, M. B. Long, M. D. Smooke, R. J. Hall, and M. B. Colket, “Computational and experimental investigation of the interaction of soot and NO in coflow diffusion flames”, *Proceedings of the Combustion Institute* **32** (2009), pp. 777–784.
- [19] L. D. Chen, J. P. Seaba, W. M. Roquemore, and L. P. Goss, “Buoyant diffusion flames”, *Proceedings of the Combustion Institute* **22** (1988), pp. 677–684.
- [20] D. S. Chamberlin and A. Rose, “The flicker of luminous flames”, *Industrial & Engineering Chemistry Research* **20** (1928), pp. 1013–1016.
- [21] K. R. V. Manikantachari, V. Raghavan, and K. Srinivasan, “Natural flickering of methane diffusion flames”, *International Journal of Mechanical, Aerospace, Industrial, Mechatronic and Manufacturing Engineering* **5** (2011), pp. 2423–2428.
- [22] P. R. Medwell, Q. N. Chan, B. B. Dally, S. Mahmoud, Z. T. Alwahabi, and G. J. Nathan, “Temperature measurements in turbulent non-premixed flames by two-line atomic fluorescence”, *Proceedings of the Combustion Institute* **34** (2013), pp. 3619–3627.
- [23] P. R. Medwell, Q. N. Chan, P. A. M. Kalt, Z. T. Alwahabi, B. B. Dally, and G. J. Nathan, “Instantaneous temperature imaging of diffusion flames using Two-Line Atomic Fluorescence”, *Applied Spectroscopy* **64** (2010), pp. 173–176.
- [24] M. Köhler, I. Boxx, K. Geigle, and W. Meier, “Simultaneous planar measurements of soot structure and velocity fields in a turbulent lifted jet flame at 3 kHz”, *Applied Physics B* **103** (2011), pp. 271–279.
- [25] ANSYS Fluent, “Release 17.2”.
- [26] Z. Luo, C. Yoo, E. S. Richardson, J. Chen, C. Law, and T. Lu, “Chemical explosive mode analysis for a turbulent lifted ethylene jet flame in highly-heated coflow”, *Combustion and Flame* **159** (2012), pp. 265–274.
- [27] S. Adhikari, A. Sayre, and A. J. Chandy, “*In situ* adaptive tabulation (ISAT) for combustion chemistry in a network of perfectly stirred reactors (PSRs)”, *Computers & Chemical Engineering* **97** (2017), pp. 124–134.
- [28] M. Frenklach, “Method of moments with interpolative closure”, *Chemical Engineering Science* **57.12** (2002), pp. 2229–2239.
- [29] M. Mueller, G. Blanquart, and H. Pitsch, “A joint volume-surface model of soot aggregation with the method of moments”, *Proceedings of the Combustion Institute* **32** (2009), pp. 785–792.
- [30] F. Liu, H. Guo, G. J. Smallwood, and Ö. L. Gülder, “Effects of gas and soot radiation on soot formation in a coflow laminar ethylene diffusion flame”, *Journal of Quantitative Spectroscopy & Radiative Transfer* **73** (2002), pp. 409–421.
- [31] M. J. Evans, C. Petre, P. R. Medwell, and A. Parente, “Generalisation of the eddy-dissipation concept for jet flames with low turbulence and low Damköhler number”, *Proceedings of the Combustion Institute* **37** (2018), pp. 1–9.
- [32] K. A. Thomson, Ö. L. Gülder, E. J. Weckman, R. A. Fraser, G. J. Smallwood, and D. R. Snelling, “Soot concentration and temperature measurements in co-annular, nonpremixed CH<sub>4</sub>/air laminar flames at pressure up to 4 MPa”, *Combustion and Flame* **140** (2005), pp. 222–232.

## REFERENCES

---

- [33] S. T. Chong, M. Hassanaly, H. Koo, M. E. Mueller, V. Raman, and K.-P. Geigle, “Large eddy simulation of pressure and dilution-jet effects on soot formation in a model aircraft swirl combustor”, *Combustion and Flame* **192** (2018), pp. 452–472.
- [34] K. C. Kalvakala, V. R. Katta, and S. K. Aggarwal, “Effects of oxygen-enrichment and fuel unsaturation on soot and NO<sub>x</sub> emissions in ethylene, propane, and propene flames”, *Combustion and Flame* **187** (2018), pp. 217–229.
- [35] C. K. Westbrook and F. L. Dryer, “Chemical kinetics and modelling of combustion processes”, *Proceedings of the Combustion Institute* **18** (1981), pp. 749–767.
- [36] C. K. Westbrook, “Chemical kinetics of hydrocarbon oxidation in gaseous detonations”, *Combustion and Flame* **46** (1982), pp. 191–210.
- [37] M. J. Evans, P. R. Medwell, Z. F. Tian, J. Ye, A. Frassoldati, and A. Cuoci, “Effects of oxidant stream composition on non-premixed laminar flames with heated and diluted coflows”, *Combustion and Flame* **178** (2017), pp. 297–310.
- [38] B.G. Sarnacki, G. Esposito, R.H. Krauss, and H.K. Chelliah, “Extinction limits and associated uncertainties of nonpremixed counterflow flames of methane, ethylene, propylene and n-butane in air”, *Combustion and Flame* **159** (2012), pp. 1026–1043.
- [39] W. L. Roberts, “Soot, temperature, and OH Measurements in a Unsteady Counterflow Diffusion Flame”, tech. rep. ARO34438.5-EG-YIP, North Carolina State University, Raleigh, NC, USA: North Carolina State University, 1998.
- [40] M. E. Decroix and W. L. Roberts, “Transient flow field effects on soot volume fraction in diffusion flames”, *Combustion Science and Technology* **160** (2000), pp. 165–189.
- [41] N. Qamar, G. J. Nathan, Z. T. Alwahabi, and K. D. King, “The effect of global mixing on soot volume fraction: measurements in simple jet, precessing jet and bluff body flames”, *Proceedings of the Combustion Institute* **30** (2005), pp. 1493–1500.
- [42] V. Narayanaswamy and N. Clemens, “Simultaneous LII and PIV measurements in the soot formation region of turbulent non-premixed jet flames”, *Proceedings of the Combustion Institute* **34** (2013), pp. 1455–1463.
- [43] S. M. Mahmoud, G. J. Nathan, Z. T. Alwahabi, Z. W. Sun, P. R. Medwell, and B. B. Dally, “The effect of exit strain rate on soot volume fraction in turbulent non-premixed jet flames”, *Proceedings of the Combustion Institute* **36** (2017), pp. 889–897.
- [44] C. R. Kaplan, C. R. Shaddix, and K. C. Smyth, “Computations of enhanced soot production in time-varying ethylene/ air diffusion flames”, *Combustion and Flame* **106** (1996), pp. 89–115.
- [45] J. Hentschel, R. Suntz, and H. Bockhorn, “Soot formation and oxidation in oscillating methane-air diffusion flames at elevated pressure”, *Applied Optics* **44** (2005), pp. 6673–6681.

# Chapter 8

## Conclusions and outlook

### 8.1 Conclusions

In conclusion, the present thesis shows that the variations in the forcing frequency and the fuel flow modulation result in the change in the in-flame residence time, which directly affects the ethylene pyrolysis in the neck of the flames, ultimately contributing to the soot growth. The difference in the burner diameter has a less significant effect on the peak soot concentration in time-varying flames, but it affects the structure of the soot fields and thus the volume-integrated soot volume fraction. The study has also found that the flame oscillation has a more significant effect on the particle growth during the later stages of soot evolution than the soot inception stage.

The first part of the experiments shows that the 20-Hz flame exhibits an increase in soot production relative to the 40-Hz and steady flames, where the trend qualitatively correlates with the global residence time. The soot measurements show that the peak soot concentration in the 20-Hz flame is 87% larger than that measured in the steady flame, whereas the enhancement for the 40-Hz flame is only 10%. The same qualitative trend is also observable in the comparisons of the diameter of primary soot particles between the 20-, 40-Hz and steady flames. The temperature measurements reveal significant differences in the structure of the steady and time-varying flames which leads to the difference in global residence times. Since the soot field closely follows the flame structure, the 20-Hz flame which has a wider flame width exhibits a larger maximum volume-integrated soot volume fraction compared with the 40-Hz flame and the steady counterpart.

Previous experimental studies [1, 2] suggest that the frequency,  $f$ , of the naturally flickering flames correlates with the diameter,  $D$ , of the burner:  $f \propto D^{-1/2}$ . However, characterising the frequency of the natural flickering flames using a photodetector shows that the oscillation frequency is approximately 10 Hz regardless of the burner diameter. Combining the observation of soot productions in 20- and 40-Hz flames with those measured in the 10-Hz flames, these findings indicate that laminar flames oscillate at their natural flickering frequencies enhances the soot production to the largest extent and it decreases with the increase in frequency.

For the steady laminar flames, the variation in the burner diameter does not greatly affect the flame structure and the soot field. However, distinct features are observable in the soot field of time-varying flames at the same forcing frequency, 10 Hz, and flow modulation amplitude,  $\alpha = 50\%$ . One of them is the presence of a low-soot region, encompassed by high soot concentrations, found on the centreline of the time-varying flames with the 4.0- and 5.6-mm-diameter burners. In contrast, the distributions of soot concentration and primary particle diameter in the secondary soot region of the time-varying flame with an 8.0-mm-diameter burner appear relatively uniform. The differences in the degree of enhancement in relative soot production between time-varying and steady flames with 4.0-, 5.6- and 8.0-mm-diameter burners are insignificant. However, variations in the spatial extent of the soot region result in the difference in the volume-integrated soot volume fraction between the time-varying flames. Doubling the nozzle diameter from 4.0 to 8.0 mm causes the maximum volume-integrated soot volume fraction to increase by 50%.

The current experimental study identifies two distinct regimes in the effect of forcing magnitude on the enhancement of soot production. Reducing the amplitude of fuel flow modulation from 50% to 25% leads to a decrease in the degree of enhancement in soot concentrations between steady and time-varying flames, from more than 125% to approximately 65%. This trend qualitatively agrees with the findings reported by Connelly et al. [3]. In contrast, increasing the forcing amplitude from 50% to 75% results in a slight decline in the peak soot concentration between the time-varying flames, which is consistent with previous work [4]. This trend is not observed in methane flames [4, 5]. These findings suggest that there is a limit to the enhancement of soot production for ethylene flames. Nevertheless, the physics involved require further investigation.

The current numerical analysis shows that the time-varying flame is momentum-dominated during the phases of the cycle when the jet exit velocity is increasing. As a result, a region of high ethylene concentration significantly increases as compared with its steady equivalent. The subsequent decrease in the jet exit velocity causes the flame to become buoyancy-dominated. The buoyant force stretches the flame stem and prolongs the residence time in the flame neck zone. As a result, the additional ethylene thermally decomposes into acetylene during the extended residence time, which leads to the occurrence of a high-soot region in the flame neck. However, the buoyancy-induced toroidal vortex keeps pinching the flame surface towards the centreline, which promotes soot oxidation by enhancing the local mixing rates. The vortex separates the flame tip from the burner-attached flame. The separated flame primarily contains combustion products and a low concentration of acetylene. The calculated composition is consistent with the uniformly distributed large primary soot particles within the isolated flame.

The residence time analysis conducted in the simulations shows that the time-varying flame offers a much wider range of trajectories of time–temperature–mixture fraction histories than those available in the steady flame. The simulation suggests that the soot growth rate at the early stages of the time-varying flame are similar or even slower than that in the steady flame. Additionally, the earlier occurrence of soot oxidation also contributes to the lower soot concentration during the early stages of the time-varying flame. In contrast, the trajectories that pass through the region of the maximum soot volume fraction exhibit extended residence time during which the acetylene concentration is high and temperatures that favour soot growth in the time-varying flame compared with the steady counterpart. Furthermore, during the later stages of the time-varying flame, the soot formation rate is higher on the centreline than those pass through the annular region of the flame.

## 8.2 Outlook

Soot evolution is an extremely complex process that involves chemical and physical interactions. This thesis merely provides new insights into the macroscopic phenomena observed in time-varying laminar non-premixed flames. There remain some issues that are worthy of further investigation. Suggestions for future work are presented in the following section to improve the understanding of this topic beyond this thesis.

The renewed interest of time-varying laminar flames has increased the knowledge of soot evolution in controllable time-dependent environments considerably. The research has laid the foundation for a systematic study of sooting time-varying laminar flames. This experimental data set describes the flame behaviour and its complex interdependence with soot evolution as a function of the flow field characteristics. However, the experimental data set is far from comprehensive. It is possible to expand on this work in an increasingly comprehensive manner by combining it with future measurements. For example, the polarisation spectroscopy in the mid-infrared is one of the techniques that provides the concentration of acetylene molecules. Since acetylene is a critical intermediate species in combustion and soot formation, the information of its concentration can correlate with the mixture fraction, which is highly desirable for model validation. Furthermore, the repeatable nature of these flames provides a suitable environment for assessing the reliability of different techniques. Consequently, it would either make improvements to the diagnostic methods or refine the existing measurements.

Soot evolution is a complicated process, especially the transition from gas-phase molecules to solid particles which involves a wide variety of species. Experimentally probing those representative gas-phase species, for example, PAH and acetylene, is always desirable. Accurately describing the coupling between the soot particles, gas-phase species, and temperature and velocity fields is necessary

for advancing the understanding of soot inception mechanisms, thereby enabling a more realistic soot model to be developed. It would be beneficial to measure all the major species and deduce the mixture fraction in one or many of the time-varying laminar flames that have been investigated in this work. Additionally, the wide ranges of flame conditions provided by the experimental data set can be utilised to validate and improve the existing soot models.

Extending the research to higher hydrocarbon fuels could be an interesting topic that has practical relevance and may shed some light on the interplay between the soot chemistry and residence time. Furthermore, developing a modified system that enables high intensity forcing may be useful to the development of active-control strategies for reducing soot emission.

## References

- [1] A. Hamins, J. C. Yang, and T. Kashiwagi, “An experimental investigation of the pulsation frequency of flames”, *Proceedings of the Combustion Institute* **24** (1992), pp. 1695–1702.
- [2] C. R. Shaddix, J. E. Harrington, and K. C. Smyth, “Quantitative Measurements of Enhanced Soot Production in a Flickering Methane/Air Diffusion Flame”, *Combustion and Flame* **99** (1994), pp. 723–732.
- [3] B. C. Connelly, M. B. Long, M. D. Smooke, R. J. Hall, and M. B. Colket, “Computational and experimental investigation of the interaction of soot and NO in coflow diffusion flames”, *Proceedings of the Combustion Institute* **32** (2009), pp. 777–784.
- [4] C. R. Shaddix and K. C. Smyth, “Laser-Induced Incandescence Measurements of Soot Production in Steady and Flickering Methane, Propane, and Ethylene Diffusion Flames”, *Combustion and Flame* **107** (1996), pp. 418–452.
- [5] C. R. Kaplan, C. R. Shaddix, and K. C. Smyth, “Computations of enhanced soot production in time-varying ethylene/ air diffusion flames”, *Combustion and Flame* **106** (1996), pp. 89–115.



# Appendix A

## List of publications

1. Agnes Jocher, Kae Ken Foo, Zhiwei Sun, Bassam Dally, Heinz Pitsch, Zeyad Alwahabi and Graham Nathan, "Impact of acoustic forcing on soot evolution and temperature in ethylene-air flames", *Proceedings of the Combustion Institute* **36** (2017), pp. 781–788.
2. Kae Ken Foo, Zhiwei Sun, Paul R. Medwell, Zeyad T. Alwahabi, Bassam B. Dally and Graham J. Nathan, "Experimental investigation of acoustic forcing on temperature, soot volume fraction and primary particle diameter in non-premixed laminar flames", *Combustion and Flame* **181** (2017), pp. 270–282.
3. Kae Ken Foo, Zhiwei Sun, Paul R. Medwell, Zeyad T. Alwahabi, Graham J. Nathan and Bassam B. Dally, "Characteristics of an acoustically forced non-premixed jet flame", *11<sup>th</sup> Asian-Pacific Conference on Combustion* (2017)
4. Kae Ken Foo, Zhiwei Sun, Paul R. Medwell, Zeyad T. Alwahabi, Graham J. Nathan and Bassam B. Dally, "Influence of nozzle diameter on soot evolution in acoustically forced laminar non-premixed flames", *Combustion and Flame* **194** (2018) pp. 376–386.
5. Kae Ken Foo, Zhiwei Sun, Paul R. Medwell, Zeyad T. Alwahabi, Graham J. Nathan and Bassam B. Dally, "Soot evolution and flame response to acoustic forcing of laminar non-premixed jet flames at varying amplitudes", *Combustion and Flame* **198** (2018) pp. 249–259.
6. Kae Ken Foo, Michael J. Evans, Zhiwei Sun, Paul R. Medwell, Zeyad T. Alwahabi, Graham J. Nathan and Bassam B. Dally, "Calculated radial profiles and time histories of major species on concentrations in an acoustically forced laminar flame", submitted to *Combustion and Flame* on August 21, 2018.